KU LEUVEN

ARENBERG DOCTORAL SCHOOL
Faculty of Engineering Science

Filament stabilisation in free-surface flows of complex fluids

Wouter Mathues

Supervisor:
Prof. dr. C. Clasen

Dissertation presented in partial fulfillment of the requirements for the degree of Doctor in Chemical Engineering

August 2015

Filament stabilisation in free-surface flows of complex fluids

Wouter MATHUES

Examination committee:
Prof. dr. ir. P. Wollants, chair
Prof. dr. C. Clasen, supervisor
Prof. dr. ir. J. Vermant
Prof. dr. ir. P. Van Puyvelde
Prof. dr. ir. I. Verpoest
Prof. dr. O. G. Harlen
(University of Leeds)
Prof. dr. ir. J. P. Rothstein
(University of Massachusetts)

Dissertation presented in partial fulfillment of the requirements for the degree of Doctor in Chemical Engineering

August 2015

Uitgegeven in eigen beheer, Wouter Mathues, Celestijnenlaan 200F box 2424, B-3001 Heverlee, Belgium (Belgium)

There is a way out of every box,
a solution to every puzzle;
it's just a matter of finding it.

JEAN-LUC PICARD

Preface

You are now holding the final result of my years as a PhD student. It was an intense period with great satisfaction of solving the scientific puzzles and some frustration when reaching my scientific boundaries. I have had the time to study complex fluids and rheology, which is a multidisciplinary field at the intersection of physics, chemistry and mathematics. It is a wonderful playground for a chemical engineer and I have built up the scientific foundations where I can rely on in my future career. Needless to say, research is never finished and hopefully other people can benefit from this work to discover new theories and applications. But first, I would like to thank some people who have made an invaluable contribution to the successful completion of this study.

First of all, I would like to thank my adviser prof. Christian Clasen for giving me the opportunity to start a PhD. You have given me the time and freedom to investigate an interesting and challenging topic. We have had stimulating scientific discussions that kept me motivated to continue searching for explanations for my observations. Moreover, I would like to thank prof. Peter Van Puyvelde, whose support and confidence in my abilities were crucial in completing this work. Furthermore, I want to thank my collaborators Mariano Rubio, Claire McIlroy and prof. Oliver Harlen for the interesting scientific discussions. Their complementary view on the subject has undoubtedly improved the quality of this work. I also thank the other members of the jury for their constructive feedback on the manuscript.

Next, I would like to thank all my colleagues from the Soft Matter Rheology and Technology group for creating a very pleasant work atmosphere. You are a group of fun, talented people and I have learned a lot from all of you. I especially want to mention my master-colleagues Tom, Rob and Pieter, who started their PhD at the same time and who have even become better friends during our PhD years. And of course thanks to my office mates Stijn, Josefina

and Mathieu for their friendship and the many relaxing talks.

I also want to thank my other friends for the fun distractions (the dinners, the concerts and other pleasant evenings and weekends) and for the interesting conversations that broaden my view in life. Thanks for your interest in my work and for finding the most unconventional links between my research and everyday life.

Finally, my uttermost gratitude goes to my family for their love and encouragements. I especially want to thank my parents for their unconditional support and belief in me. And finally, I want to thank Flore for giving me a home where I can forget my worries and just be me.

Wouter

Abstract

This doctoral dissertation discusses the capillary-driven breakup of various low viscous non-Newtonian liquid filaments. A liquid filament is destabilised by surface tension that drives the free surface to minimise its surface energy by forming spherical droplets. The thinning dynamics during this free-surface flow are determined by the dominant resisting stress, which depends on the relative magnitude of fluid properties such as density, viscosity and elasticity.

Since a homogeneous uniaxial extensional flow field is generated during the pinching process, free-surface flows are used as a characterisation method for the extensional rheological properties of low viscous liquids. We have enhanced the performance of the commercial Capillary Breakup Extensional Rheometer (CaBER) that creates an unstable liquid bridge by rapidly stretching a droplet of fluid between two plates and monitors the filament radius with a laser micrometer. The spatial and temporal resolution of the setup is improved by using a high-speed camera equipped with a custom-made microscopic tube lens to follow the filament thinning. Moreover, the image processing routines are substantially improved by employing advanced edge detection techniques to locate the position of the filament edges with sub-pixel accuracy. The code is used to determine polymer relaxation behaviour during the pinching of inkjet printing model fluids performed with an extensional rheometer at Cambridge University. The software was able to quantify the relaxation times in these fluids of $\lambda = O(100\ \mu\text{s})$, which are the smallest relaxation times that have been reliably obtained in capillary breakup experiments.

The CaBER setup is further used to study two model complex fluids that display an opposite stabilisation effect on a filament. First, we examine the breakup dynamics of long stable jets of weak viscoelastic fluids. Unforced jets of three model polymer solutions are studied over a range of jet velocities, which all display a similar temporal evolution of the capillary instabilities. The

instabilities arise in a stable zone after the nozzle at wave numbers that are in line with predictions from linear stability analysis. This zone is followed by a short inertia-capillary regime where the flexible polymer chains are efficiently unraveled, resulting in strong non-linear elastic stresses that stabilise the filament during the important elasto-capillary regime. In this regime, the minimal filament radius decreases exponentially in time with a time scale that is proportional to the relaxation time λ of the fluid. By comparing the thinning dynamics during jetting and static CaBER experiments we observe a new time scale $\theta = 2\lambda$, which implies that jets breakup faster than static liquid bridges of the same elastic fluid. This new scaling is theoretically explained with a stress balance over the filament, where the creation of surface below the nozzle generates a constant tensile force in the jet. Numerical simulations of the jet breakup with a non-linear dumbbell model (FENE) are in agreement with the experimental observation by selecting a proper value for the initial deformation of the polymer molecules.

The drop formation of non-colloidal suspensions in a Newtonian matrix is examined as a second model system, in which the filament is locally destabilised during the pinching process. Experiments are performed on suspensions with varying particle radius and volume fraction and the dynamics are explained by dividing the process into four stages. Initially, the suspension behaves as a homogeneous fluid and the suspension viscosity dominates the thinning, resulting in a linear decrease of the filament radius in time. As the filament thins, local particle density fluctuations are amplified and the filament becomes heterogeneous with diluted zones that exhibit faster thinning rates due to the local decrease in viscosity. The onset of this concentration fluctuaction regime is defined with a transition radius R_{T1} and a scaling for this radius is proposed based on the standard deviation of the mean inter-particle distance and the relative dependence of the viscosity to small changes the volume fraction. Third regime starts when a particle-free section is formed between two particle clusters. The breakup resembles a small-scale filament stretching experiment and the thinning rate reaches a maximum. Finally, a deceleration is detected before breakup, where the depleted filament becomes slender again and the thinning rate approaches that of the pure medium fluid.

Samenvatting

Dit proefschrift bestudeert de wijze waarop druppels gevormd worden onder invloed van oppervlaktespanning bij verschillende laag viskeuze, niet-Newtoniaanse vloeistoffen. Dit proces wordt veroorzaakt door de thermodynamische instabiliteit van een langgerekt vloeistoffilament. Door de aanwezigheid van de oppervlaktespanning aan de vloeistof-luchtinterfase verkleint de oppervlakte-energie bij de overgang van een langgerekt filament naar sferische druppels. De dynamica van dergelijke vrije-oppervlakstromingen wordt bepaald door de dominante spanning in de vloeistof die de oppervlaktespanning in balans houdt. Zowel inertiële, viskeuze als elastische spanningen kunnen aanwezig zijn in een complexe vloeistof en de overheersende spanning wordt bepaald door de inherente vloeistofeigenschappen.

Aangezien er een homogene, uniaxiale rekstroming ontstaat tijdens het opbreekproces, worden gecontroleerde vrije-oppervlakstromingen bestudeerd om de reologische eigenschappen van laag viskeuze vloeistoffen onder rek te bepalen. Het meest gebruikte apparaat voor deze karakterisatie is de Capillary Breakup Extensional Rheometer (CaBER), dat een onstabiel filament creëert door een vloeistofdruppel snel uit te rekken tussen twee plaatjes en vervolgens de straal van het filament te volgen met een lasermicrometer. We hebben de ruimtelijke en temporele resolutie van dit toestel verbeterd door het te combineren met een hogesnelheidscamera die uitgerust is met een zelf ontworpen microscopische lens. De beeldverwerking is eveneens substantieel verbeterd door de randen van het filament met sub-pixel nauwkeurigheid te lokaliseren met behulp van geavanceerde detectiealgoritmes. Deze code wordt gebruikt om snelle relaxatieprocessen van polymeren te detecteren tijdens de druppelvorming bij printerinkten. Deze experimenten zijn uitgevoerd met een speciale rekreometer op Cambridge University. De software is in staat om relaxatietijden van een grootteorde $\lambda = O(100\ \mu\text{s})$ in deze vloeistoffen te detecteren. Dit zijn de kortste relaxatietijden die ooit bepaald zijn in een dergelijk experiment.

De verbeterde CaBER-opstelling is gebruikt voor de studie van twee soorten complexe vloeistoffen die een tegengesteld stabilisatie-effect op het filament vertonen. Eerst wordt het opbreekgedrag van lange, stabiele jets van een licht visco-elastische vloeistof bestudeerd, waarbij de snelheid van de jet en de concentratie van het opgeloste polymeer stelselmatig gewijzigd worden. De capillaire instabiliteiten vertonen voor alle jets een vergelijkbare evolutie. De instabiliteiten ontstaan in het rechte deel van de jet na de spuitopening en verschijnen met een frequentie die ook theoretisch voorspeld wordt door een lineaire stabiliteitsanalyse. Vervolgens worden de polymeermolecules uitgerekt tijdens een kort inertie-capillair regime, wat leidt tot grote elastische spanningen in de vloeistof die het filament stabiliseren. In dit elasto-capillair regime daalt de straal van het filament exponentieel in de tijd met een tijdschaal die evenredig is met de relaxatietijd van de vloeistof. De opbreeksnelheid van een dergelijk filament is groter in een jet dan in de CaBER en door het vergelijken van de dynamica van beide stromingen is een nieuwe tijdschaal $\theta = 2\lambda$ voor de jet ontdekt. Deze nieuwe tijdschaal wordt theoretisch verklaard met behulp van een krachtenbalans in het filament, waarin een extra constante kracht verschijnt als gevolg van de vorming van nieuw oppervlak onder de spuitopening. De experimentele bevindingen stemmen overeen met numerieke simulaties met een niet-lineaire bewegingsvergelijking (FENE).

Als een tweede modelsysteem wordt de druppelvorming bij suspensies van niet-colloïdale deeltjes in een Newtoniaanse matrix bestudeerd. Deze complexe vloeistof zorgt voor een lokale destabilisatie van het filament en dit fenomeen wordt bestudeerd bij suspensies met verschillende concentraties en deeltjesgroottes. Het opbreekproces wordt verklaard door een opsplitsing in vier regimes. Aanvankelijk gedraagt de suspensie zich als een homogene vloeistof waarin de viskeuze spanningen zorgen voor een constante opbreeksnelheid. Wanneer het filament dun genoeg is, wordt het filament heterogeen door de toename van lokale densiteitsverschillen. Deze evolutie resulteert in zones met minder deeltjes waar het filament sneller dunner wordt door een lokale daling van de viscositeit. De start van dit verdunningsregime wordt gekwantificeerd met een overgangsstraal R_{T1}. Deze straal wordt voorspeld op basis van de standaardafwijking van de gemiddelde afstand tussen de deeltjes en de relatieve gevoeligheid van de viscositeit voor kleine concentratieveranderingen. Het derde regime start wanneer een kleine hoeveelheid matrixvloeistof zichtbaar wordt tussen twee deeltjesclusters. Op dit punt bereikt de opbreeksnelheid een maximum en lijkt de matrixvloeistof actief uitgerekt te worden tussen de deeltjes. Tenslotte wordt een vertraging waargenomen vlak voor het opbreken waardoor de snelheid deze van de zuivere matrixvloeistof benadert.

List of symbols

Symbols in arabic letters

Symbol	Description	Units
a	Mark-Houwink exponent	[–]
$\mathbf{A}$	conformation tensor	[–]
A_{rr}	radial normal chain conformation	[–]
A^0_{rr}	initial radial chain conformation	[–]
A_{zz}	axial normal chain conformation	[–]
A^0_{zz}	initial normal chain conformation	[–]
Bo	Bond number	[–]
c	concentration	[g/ml]
c^*	critical overlap concentration	[g/ml]
C_∞	characteristic ratio of polymer-solvent system	[–]
De	Deborah number	[–]
$\mathbf{D}$	rate of stain tensor	[s^{-1}]
E_s	surface energy	[Nm]
Ec	elasto-capillary number	[–]
f	image	[–]
	focal length	[m]
F_z	tensile force in the thread	[N]
$\bar{F}_z$	dimensionless tensile force in the thread	[–]
g	gravitational constant	[m/s^2]
	image gradient	[–]
G	elastic modulus	[Pa·s]
	Gaussian function	[–]
H_p	probability density function	[m^{-1}]
h	dimensionless filament radius	[–]
I_0	modified Bessel function of 0th order	[–]

Symbol	Description	Units
I_1	modified Bessel function of 1st order	[–]
$\mathbf{I}$	identity tensor	[–]
$\mathrm{II}_{\mathbf{2D}}$	second invariant of the rate of strain tensor	[–]
j	number of bonds of a polymer monomer	[m]
k	wavenumber	[m^{-1}]
k_B	Boltzmann constant	[J/K]
k_m	wavenumber associated with the highest growth rate	[m^{-1}]
K	curvature term	[–]
K_H	Huggins constant	[–]
K_M	Martin coefficient	[–]
K_n	constancy factor	[$\mathrm{Pa{\cdot}s}^n$]
$K_{[\eta]}$	Mark-Houwink parameter	[$\mathrm{Pa{\cdot}s}^n$]
L	sample length	[m]
	finite extensibility parameter	[–]
L_0	initial gap between the plates	[m]
L_1	final gap between the plates	[m]
L_p	breakup distance of a jet	[m]
ℓ_r	radial length scale	[m]
ℓ_v	internal length scale	[m]
ℓ_z	axial length scale	[m]
M	gradient magnitude	[–l]
M_u	molar mass of a monomer	[g/mol]
M_w	weight average molecular weight	[g/mol]
n	power law exponent	[–]
	refractive index	[–]
n_p	number density of the polymer chains	[m^{-3}]
N_A	Avogadro constant	[mol^{-1}]
N_b	number of bins	[–]
N_p	number of particles	[–]
$\mathbf{n}$	normal unit vector	[–]
Oh	Ohnesorge number	[–]
Oh^*	critical Ohnesorge number	[–]
Oh_i	local Ohnesorge number	[–]
Oh_s	solvent-based Ohnesorge number	[–]
P	pressure	[Pa]

Symbol	Description	Units
Pe	Péclet number	[–]
$\dot{Q}$	flow rate	[ml/s]
Q_{ev}	dumbbell equilibrium size	[–]
$\mathbf{Q}$	dumbbell connection vector	[–]
r_{lens}	lens resolution	[m]
$\langle r \rangle$	mean nearest-neighbour distance	[m]
R	radius	[m]
R^*	scaled filament radius	[–]
R_0	reference radius	[m]
	radius of the geometry	[m]
R_g	radius of gyration	[m]
R_m	minimal filament radius	[m]
R_n	nozzle radius	[m]
R_p	particle radius	[m]
R_s	length scale for transition radius	[m]
R_{T1}	first transition radius	[m]
R_{T2}	second transition radius	[m]
Re	Reynolds number	[–]
Re_p	particle Reynolds number	[–]
S	surface area	[m^2]
t	time	[s]
$t^{'}$	reduced time	[–]
t_c	reference time	[s]
t_η	viscous time scale	[s]
t_p	pinching time	[s]
$t_{p,v}$	pinching time for viscous fluid	[s]
t_R	Rayleigh time	[s]
t_v	internal time scale	[s]
T	absolute temperature	[K]
Tr	Trouton ratio	[–]
$\mathbf{t}$	tangent unit vector	[–]
$\mathbf{T}$	stress tensor	[Pa]
$U_{\eta\tau}$	universal ratio	[–]
v	velocity	[m/s]
$\bar{v}$	dimensionless velocity	[–]
v_0	jet velocity	[m/s]

Symbol	Description	Units
v_c	capillary velocity	[m/s]
v_n	average velocity in the nozzle	[m/s]
v_r	radial velocity	[m/s]
v_s	sedimentation velocity	[m/s]
$v_{s,0}$	sedimentation velocity for low concentrations	[m/s]
v_z	axial velocity	[m/s]
V_h	hydrodynamic volume	[m^3]
V_p	particle volume	[m^3]
V_{tot}	total volume	[m^3]
$\mathbf{v}$	velocity vector	[m/s]
We	Weber number	[–]
Wi	Weissenberg number	[–]
z	axial coordinate	[m]
$\bar{z}$	dimensionless axial coordinate	[–]
$z^{'}$	reduced axial coordinate	[–]
z^*	scaled axial coordinate	[–]
z_0	axial coordinate of the minimal diameter	[m]
Z	correction term in FENE model	[–]

Greek symbols

Symbol	Description	Units
α	gradient direction	[–]
	half angle of the light cone	[–]
α_1	similarity scaling exponent	[–]
α_2	similarity scaling exponent	[–]
β	similarity scaling exponent	[–]
$\dot{\gamma}$	shear rate	[s^{-1}]
γ	surface tension	[N/m]
Γ	gamma function	[–]
δ	shift factor	[-]
ε	small perturbation	[–]
ϵ_H	Hencky strain	[–]
$\dot{\epsilon}$	extension rate	[s^{-1}]
ζ	Riemann zeta function	[–]
η	dynamic viscosity	[Pa·s]

Symbol	Description	Units
$[\eta]$	intrinsic viscosity	[ml/g]
η_E	extensional viscosity	[Pa·s]
$\eta_{E,app}$	apparent extensional viscosity	[Pa·s]
η_{fit}	fitted viscosity	[Pa·s]
η_m	medium viscosity	[Pa·s]
η_p	polymeric viscosity	[Pa·s]
η_r	relative viscosity	[–]
η_{red}	reduced viscosity	[–]
η_s	solvent viscosity	[Pa·s]
η_{sp}	specific viscosity	[dl/g]
θ	characteristic elastic time scale	[s]
θ_b	average bond angle	[–]
κ	mean curvature of the filament	[m^{-1}]
λ	relaxation time	[s]
λ_i	mode in relaxation spectrum	[s]
λ_w	wave length	[m]
λ_z	Zimm relaxation time	[s]
λ_η	characteristic theoretic relaxation time	[s]
λ_ξ	blob relaxation time	[s]
ν	excluded volume exponent	[m^2/s]
ξ	similarity variable	[–]
ξ_h	correlation length	[m]
ρ	density	[kg/m^3]
ρ_c	polymer coil density	[kg/m^3]
ρ_N	particle number density	[m^{-3}]
σ	stress	[Pa]
	standard deviation	[–]
$\sigma_{p,rr}$	radial polymeric normal stress	[Pa]
$\sigma_{p,zz}$	axial polymeric normal stress	[Pa]
$\Delta\sigma_p$	polymeric normal stress difference	[Pa]
$\boldsymbol{\sigma}$	extra stress tensor	[Pa]
$\boldsymbol{\sigma_p}$	polymeric contribution to the extra stress tensor	[Pa]
τ	dimensionless time	[–]
ϕ	volume fraction	[–]
	similarity function (radius)	[–]
ϕ_{Av}	average volume fraction	[–]

Symbol	Description	Units
ϕ_m	maximum packing volume fraction	[–]
ϕ_{St}	Stokes similarity function	[–]
Φ	numerical factor for power-law	[–]
Φ_0	Flory constant	[mol^{-1}]
ψ	similarity function (velocity)	[–]
ω	growth rate	[s^{-1}]
Ω	angular velocity	[s^{-1}]
$\mathbf{\Omega}$	vorticity tensor	[s^{-1}]

List of abbreviations

BDF	backward differentiation formula
BOAS	beads-on-a-string
CaBER	Capillary Breakup Extensional Rheometer
CMOS	Complementary Metal-Oxide Semiconductor
DEP	diethyl phtalate
EC	elasto-capillary
EVF	Extensional Viscosity Fixture
FENE	Finitely Extensible Non-linear Elastic
IC	inertia-capillary
IV	inertia-viscous
LDPE	low-density polyethylene
LoG	Laplacian of Gaussian
MHS	Mark-Houwink-Sakurada
NA	numerical aperture
PDMS	polydimethylsiloxane
PEO	poly(ethylene oxide)
PMMA	poly(methyl methacrylate)
PP	polypropylene
PS	polystyrene
ROJER	Rayleigh Ohnesorge Jet Extensional Rheometer
SER	Sentmanat Extension Rheometer
UCM	Upper-convected Maxwell

Contents

Chapter 1

Introduction

1.1 Motivation

Imagine a large fountain on a beautiful square in a city, preferably on a hot summer day. Water jets appear from many points, intertwine and form a nebula of small droplets. This scene is not only aesthetically pleasing, it also bears a fascinating phenomenon that has been a playground for physicists and mathematicians for centuries. The instability of a liquid jet and its spontaneous breakup into droplets is a classical physical problem that was first correctly described by Belgian physicist Joseph Plateau [1]. He recognised the fundamental role of surface tension as a driving force in the droplet formation. The mere fact that a cohesive force such as surface tension is responsible for the breakup of a liquid cylinder, might appear counterintuitive at first, but Plateau showed that perturbations of long wavelength reduce the surface area and thus lower the surface energy of the system, leading to a thermodynamically favoured state. Later, Lord Rayleigh included fluid dynamics in the description of the jet and predicted the most unstable perturbation wavelength of an inviscid liquid jet using linear stability analysis [2]. This breakthrough allowed determining the final droplet size and the jet perturbations are generally called Plateau-Rayleigh instabilities.

Surface tension-driven flows are not only encountered in the form of liquid jets, but for instance a dripping faucet and the stretching of a liquid filament are essentially similar axisymmetric free-surface flows. These flows are omnipresent in daily life and are encountered in various technological applications such

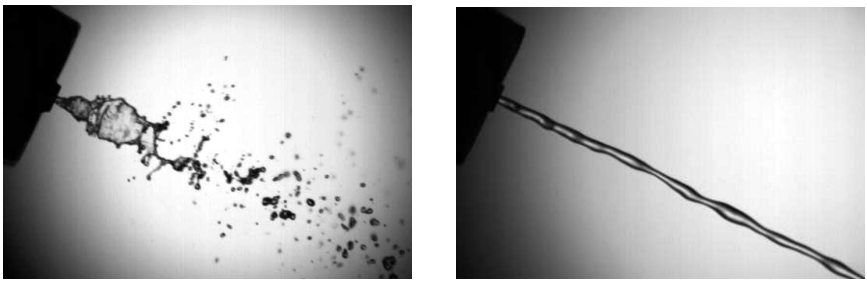

(a) (b)

Figure 1.1: Visualisation of a spray of (a) a Newtonian solvent and (b) a viscoelastic polymer solution.

as liquid jet propulsion, agricultural spraying of fertilisers and pesticides, inkjet printing, food dispensing operations, pharmaceutical sprays and liquid dispensers [3,4]. For all these applications it is crucial to know whether capillary stresses are sufficient to break the filament and to identify the time scale for the pinching process. Moreover, the size and size distribution of the emerged droplets is key to assessing spray patterns and printing quality. The original linear stability theory is unable to describe many important features of the breakup process, since non-linear effects are dominant when the pinching point is approached. The additional degrees of freedom, inherent to the free surface, makes numerical modelling of these flows an extremely hard problem. However, as a result of the absence of external forcing and an associated length scale, concepts of scaling and self-similarity are successfully employed to understand the breakup process [5].

In general, the capillary thinning of a fluid filament is resisted by inertia, viscosity and additional stresses resulting from the deformation of the fluid microstructure. In many processes, the fluid undergoing breakup is non-Newtonian and hence displays a complex rheological behaviour due to the presence of dissolved polymers, suspended particles or other micro-structural constituents. The extensional flow field in the filament is for instance very efficient in unraveling flexible polymer molecules, resulting in strong non-linear elastic stresses and a corresponding increase of the transient extensional viscosity. This localised strain hardening stabilises the thin fluid thread and this behaviour is desired in many applications such as fiber spinning and drag reduction. In other applications, such as dispensing operations, long stable threads are undesirable and a local destabilisation of the filament is preferred to induce

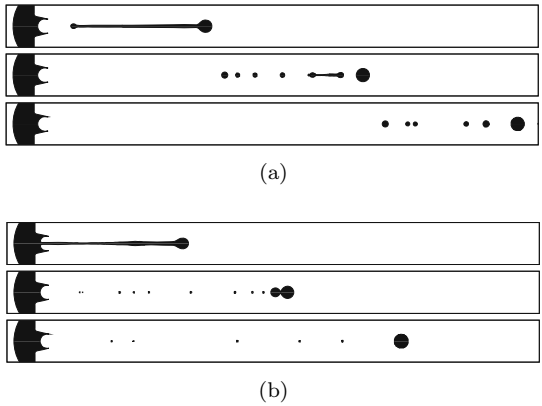

Figure 1.2: Characteristic snapshots of modelled drop-on-demand inkjet printing of (a) a Newtonian solvent and (b) a viscoelastic polymer solution. [9]

fast rupture. In some cases, extra components are specifically added to tailor the breakup process and the droplet formation. Figure 1.1 illustrates the change in atomisation dynamics when a small amount of high molecular weight polymers is dissolved into a Newtonian solvent. The Newtonian jet disintegrates close to the nozzle, creating a wide spraying pattern of droplets with a large size distribution. The viscoelastic jet, on the other hand, is stabilised due to the high resistance of the macromolecules to the extensional deformation, resulting in a dramatical increase of the spraying distance and a more localised spraying pattern. Moreover, the polymers also suppress the formation of micron-sized droplets and are therefore used as an anti-misting additive in pesticides to increase the spraying efficiency [6], in machining fluids in metal working operations to reduce inhalation hazards [7] and in jet fuels to reduce the potential of post-crash fire hazard [8].

The presence of a small amount of polymers in printing inks can also be beneficial for the printing quality in inkjet printing. In drop-on-demand (DOD) printing, which is the dominant technique in graphics and text printing, a printer head generates individual ink drops that are deposited on the substrate. Drops are formed by propagating a pressure pulse in the fluid that is held in a chamber behind the printing nozzle. The pressure pulse is generated either with a thin-film heater that periodically forms a small vapour bubble by heating the fluid above its boiling temperature or with direct mechanical actuation by a piezoelectric transducer [10]. If the pulse exceeds some threshold at the nozzle, a drop is ejected. Figure 1.2 shows the modelling of this process by

Morrison and Harlen [9] for a Newtonian and a viscoelastic liquid. The ejected fluid forms an initial liquid column that thins to define a leading droplet and the elongated tail or ligament. Due to Rayleigh instabilities, this ligament subsequently breaks up into several small droplets, known as satellite drops (see Figure 1.2a). These drops often catch up and merge with the main large drop in flight, prior to impact, in which case their presence is irrelevant. However, if they are still present at impact, they cause non-circular impact footprints of the drop, reducing the deposit precision, resolution and accuracy [10]. As illustrated in Figure 1.2b, the size of the satellite drops is drastically reduced by adding polymer to the ink. The elastic polymeric stresses pull the ligament back into the main droplet before capillary breakup occurs. However, elasticity can also reduce the drop velocity and the break-off of the drop from the ink reservoir can even be prevented when the polymer concentration is too high [11]. The elasticity of such dilute polymer solutions is generally expressed with an extensional relaxation time of the fluid. The optimal model inkjet printing fluids exhibit relaxation times below 100 μs, which is unfortunately below the detection limit of any commercially available rheometer [12].

1.2 Aim and approach

Although the breakup of a Newtonian jet into a series of droplets is a classical physical problem, the behaviour of complex liquids is still not well understood. The extensional fluid motion gives rise to strong non-linear effects in these fluids, that can either have stabilising or destabilising effect on the fluid column. In the last decade, there have been lots of studies on free-surface flows of complex fluids, both from a modelling as from an experimental perspective. Nevertheless, experimental studies on complex fluid jets are often limited to testing linear stability theories [13, 14] or examining final droplet size distribution [15, 16]. For the much-studied case of solutions of flexible polymers, the non-linear dynamics are rarely quantified because strain hardening creates long stable jets (see Figure 1.1b) and it is very challenging to follow the small threads over a long distance. Hence, experimental studies of the non-linear dynamics are generally executed with other free-surface flows, such as a dripping setups or with capillary thinning devices that employ an unstable liquid bridge geometry. As a result, non-Newtonian constitutive laws are not well tested for jetting flows [17].

The first part of this work concentrates on obtaining quantitative jetting experiments for the interesting case of dilute polymer solutions. The thinning

dynamics of an undisturbed jet are visualised with a new high-speed, high-resolution optical setup and advanced edge detection routines are written to follow a single instability from its formation in the linear stability regime until breakup into droplets. Additionally, the non-linear deformation is compared with static capillary thinning in an unstable liquid bridge, because at present, no direct comparison of the breakup dynamics of the same fluid in these two setups has been reported. In order to quantify the relaxation processes in both setups, the selected model fluids should exhibit relaxation times near the detection limit of the capillary thinning device. By determining the filament diameters with sub-pixel precision, the lower detection boundary of the latter setup is substantially enhanced. We show that these improvements allow the assessment of extremely fast relaxation processes in uniaxial extension with relaxation times that are in the range of the values expected for inkjet printing fluids.

The second part of this work investigates complex fluids that have an opposite or destabilising effect on the liquid filament. For this a suspension of non-colloidal spherical particles in a Newtonian medium was chosen as a model system, also because particle-laden threads are frequently observed in dispensing operations. Contrary to polymer solutions, filaments of non-Brownian particles are generally inelastic and display a faster and more localised pinching than a viscous oil with the same bulk viscosity. This accelerated breakup is the subject of various studies [18–21], however a fundamental understanding of the origin of the acceleration has not been found. In order to achieve this goal, the static capillary breakup of these suspensions is studied by systematically varying the key parameters such as concentration, particle size and medium viscosity. The extracted thinning curves are compared with the self-similar scaling laws for viscous fluids as well as for power-law liquids to assess whether the initial destabilisation is either caused by an extensional thinning effect due to particle alignment or by the fact that local variations in the particle density render the continuum approximation obsolete. The onset and the speed of the destabilisation are systematically quantified and a framework is developed to understand the divergent breakup behaviour. Finally, the experiments are compared with modelled filament thinning by Claire McIlroy and Oliver Harlen [22] from Leeds University to perceive the correlation between changes in the thinning dynamics and the particle distribution in the filament.

1.3 Outline

The thesis is organised in seven Chapters. Chapter 2 starts with an overview of the state of the art concerning extensional rheology and free-surface flows. We first review the fundamental concepts and the importance of extensional rheology and discuss the experimental challenges of characterising the uniaxial extensional deformation of a liquid. The second part of the chapter focusses on the free-surface flows of low viscous liquids. Important concepts such as linear stability analysis and self-similarity are introduced and the breakup dynamics of various complex fluids is discussed. In Chapter 3 the materials are described and the experimental methods are explained. The modifications that were made to the optical setup of the capillary breakup rheometer are introduced in Chapter 4. This chapter also discusses the different image processing routines that are employed to extract information from the images of the free-surface flows. In Chapter 5, jets of dilute polymer solutions are examined and the different stages in the breakup process are discussed. We mainly focus on the characteristic elasto-capillary balance where the surface tension is resisted by the elastic stresses of the deforming polymer molecules. The pinching dynamics of the model solutions are compared with static capillary breakup experiments and we show some remarkable differences between these two free-surface flows. Chapter 6 discusses the second model system of suspensions of non-colloidal spheres. We define a set thinning stages in the breakup process and obtain a better understanding of the destabilisation mechanism with the use of the self-similar scaling laws. Finally, Chapter 7 summarises the main conclusions of this study and some suggestions for further work are given.

Chapter 2

State of the art

This chapter provides an overview of the state of the art concerning the extensional flow behaviour of complex liquids. Section 2.1 demonstrates the importance of extensional rheology and highlights the differences from shear rheology, which is more commonly employed. We mainly consider uniaxial extensional deformation because this flow type is generally encountered during the experimental work presented in the following chapters. We give a summary of the available techniques to characterise the flow properties of various liquids in extension. Section 2.2 focuses on free-surface flows of low viscous fluids, in which surface tension creates an extensional flow field before generating a drop. The traditional linear analysis of this hydrodynamic stability problem is discussed and the recent advances in non-linear analysis using self-similarity are introduced. Finally, we review the breakup dynamics of different material classes, including the remarkable effects of viscoelasticity on filament thinning.

Additional mathematical background to this chapter is provided in the first three appendices. Some basic rheological definitions are summarised in Appendix A, Appendix B focusses on uniaxial extensional flow and Appendix C gives supplementary information on the slenderness assumption.

2.1 Extensional rheology

2.1.1 Introduction

Within the last two decades, there has been an increased interest in the measurement and understanding of extensional deformations of non-Newtonian liquids. Pure extensional flows typically originate from a tensile force on the material in the absence of a stationary boundary and the associated no slip boundary condition. These flows are defined by a symmetric velocity gradient tensor $\nabla \mathbf{v}$. Strong extensional flows are essential in many polymer processing operations. Fiber spinning, thermoforming, film blowing, blow moulding and foam production consist predominantly of extensional deformations [23]. Significant extensional components are also generated by any reasonably sudden change in geometry, such as converging or diverging regions of dies and moulds, as well as during flow out of an orifice.

Other applications, such as coating operations, inkjet printing, turbulent drag reduction, agricultural spraying and anti-misting of jet fuels, can benefit from the specific extensional rheological properties of polymer solutions [9, 24–26]. Solutions of very flexible polymers can have extensional viscosities that are orders of magnitude higher than those expected for a Newtonian liquid. Such large extensional viscosities cause the 'Tubeless Siphon' effect, which is used to examine the thread forming capacity or the spinnability of a material [27, 28]. The extensional rheological properties are also important in polymer flooding in enhanced oil recovery (EOR). Adding a flexible polymer to the pumping water stabilises the water-oil interface and thereby suppresses the unwanted fingering, reducing pressure losses [24]. Moreover, the extensional properties are also important for the food industry in various stages of the product life cycle, from the initial stage of formulation and process design, to process and quality control of products, to the final stage of sensory perception of the product by the consumer [29, 30].

The importance of the extensional flow behaviour can be illustrated by the fiber spinning process of a polymeric liquid [24]. To attain a stable spinning process, the tension along the thread-line is chosen to prevent fracture under normal operation conditions. However, small disturbance along thread-line are nearly unavoidable in this physical process and the propagation and magnification of these instabilities should be minimised [31]. The extensional rheology of the polymeric liquid can play an important role in this stability issue. Let us speculate that for some reason a local change in diameter occurs. Based on

the continuity equation, the narrower part of the filament should move faster than the rest of the thread-line, indicating that the strain rate is higher in the narrower part. If the polymeric liquid is strain thinning, the resistance to extension is reduced in the narrow part and motion in this part of the thread-line is further accelerated. It becomes thinner and will ultimately break. If the polymeric liquid is on the contrary strain hardening, the resistance in the narrow part of the filament will now be increased. The flow in the filament will slow down, the radius will increase and may be expected to return to that of the remainder of the thread-line. Strain hardening is therefore a stabilising influence in this process and the spinnability of a polymeric liquid is closely related to this extensional rheological property.

However, this non-linear extensional response of a viscoelastic material cannot be predicted from shear rheological characterisation. Whereas a polymeric liquid is often shear thinning at higher rate, strain hardening is typically observed under extensional deformation [23]. Shear flows are quite weak in the sense that material elements in the fluid separate linearly with time, and vorticity ensures that the fluid microstructure is simultaneously rotated away from the principal axes of stretching ($\mathbf{\Omega} \neq 0$). Extensional flows, on the other hand, are irrotational ($\mathbf{\Omega} = 0$) and extremely efficient at unraveling flexible macromolecules or orienting rigid molecules [25]. De Gennes [32] proved that the extensional viscosity of a dilute polymer solution grows without bound for a Weissenberg number $Wi = \lambda\,\dot{\epsilon} > 0.5$, where λ is the dominant relaxation time of polymer chain. This value corresponds to the coil-stretch transition of the polymer molecule, which has been confirmed by single-molecule imaging of a DNA chain [33, 34]. Shear flows are however unable to force the same level of molecular unraveling even at very large Weissenberg numbers [35]. Extensional flows are therefore expected to induce different fluid responses from simple shear flow.

2.1.2 Classification of extensional flows

Different elongational flows can be classified according to the system proposed by Meissner et al. [36]. A coordinate system is chosen to make the velocity gradient tensor diagonal with the main strain rates ordered such that $\dot{\epsilon} = \dot{\epsilon}_{11} \geq \dot{\epsilon}_{22} \geq \dot{\epsilon}_{33}$. A general incompressible extensional flow is characterised by the maximal positive strain rate $\dot{\epsilon} > 0$ and the ratio $m = \dot{\epsilon}_{22}/\dot{\epsilon}_{11}$. With these parameters, the rate of deformation tensor of an extensional flow is written as

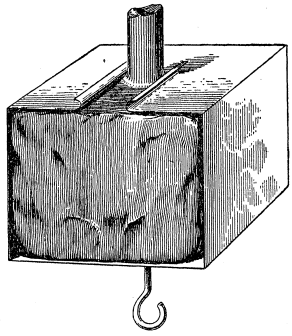

Figure 2.1: Sketch of the original experimental setup of Trouton [37].

$$\mathbf{2D} = 2\dot{\epsilon} \begin{bmatrix} 1 & 0 & 0 \\ 0 & m & 0 \\ 0 & 0 & -(1+m) \end{bmatrix}. \tag{2.1}$$

This representation considers the conservation of the total amount of mass in an incompressible fluid because the trace $\mathrm{tr}\,(\mathbf{2D}) = 0$. The most common extensional deformation is simple uniaxial extension, which is for instance encountered in fiber spinning. It is characterised by a positive extensional deformation in only one coordinate. As consequence of the contraction in an incompressible material, the second and third components are negative. From symmetry $\dot{\epsilon}_{22} = \dot{\epsilon}_{33}$, so $\dot{\epsilon}_{22} = -\dot{\epsilon}_{11}/2$, so that the general representation is satisfied with $m = -1/2$. The rate of deformation tensor thus becomes

$$\mathbf{2D} = \begin{bmatrix} 2\dot{\epsilon} & 0 & 0 \\ 0 & -\dot{\epsilon} & 0 \\ 0 & 0 & -\dot{\epsilon} \end{bmatrix}. \tag{2.2}$$

Uniaxial extension is also the predominantly encountered flow type in extensional rheometry. The easiest way to imagine the generation of a uniaxial extension is to grab both ends of a rod of fluid and pull on it. This setup was already used by Trouton for his groundbreaking rheological experiments on rods of very viscous pitch [37]. The flow properties of this very viscous material have recently gained some renewed attention due to the pitch drop experiment at the University of Queensland. In Trouton's experiment, the pitch rod was thickened at the end and shaped into an almost cubical block, as shown in Figure 2.1. This block was fitted into a small metal box, at which extra weights were hung with a hook to obtain a variety of stresses. Trouton found that the ratio of stress and velocity

gradient was constant in a tensional test, but it was approximately three times larger than the value he measured in shear. This observation is confirmed with the three dimensional form of Newton's law (see Eq. A.7), using the rate of deformation tensor for uniaxial extension. By neglecting surface tension effects, the boundary conditions on the free surface are $T_{22} = T_{33} = 0$, so

$$T_{11} = 3\eta\dot{\epsilon}. \tag{2.3}$$

The difference in the ratio between stress and strain rate in shear and extension results in the definition of an extensional viscosity. This new material parameter is generally defined as the ratio of the net tensile stress $T_{11} - T_{22}$ to the rate of strain [38]

$$\eta_E\left(\dot{\epsilon}, t\right) = \frac{T_{11} - T_{22}}{\dot{\epsilon}}. \tag{2.4}$$

The normal stress difference $T_{11} - T_{22}$ is used to avoid any dependence on the hydrostatic pressure. In honour of the contribution of Trouton, the extensional viscosity is sometimes expressed with the Trouton ratio, which is the ratio of the extensional to the shear viscosity of a fluid

$$Tr = \frac{\eta_E}{\eta}. \tag{2.5}$$

The Trouton ratio of a Newtonian liquid has a constant value of 3 and this value even holds true for polymer melts in the limit of small deformation rates [23]. However, strain hardening can occur at larger deformations due to changes in the structure of the material. Polymer melts can exhibit an increase of Tr with several orders of magnitude. Hence, the value $Tr = 3$ is often chosen as a lower limit for these non-Newtonian liquids. Contrary to the stress-controlled measurements of Trouton, it is presently more conventional to control the strain rate during an extensional measurement. More information on such steady uniaxial extension of a cylindrical sample is presented in Appendix B. The most important conclusion is that an exponential increase of the sample length L is required to obtain a steady deformation

$$L = L_0\, e^{\dot{\epsilon}t}, \tag{2.6}$$

where L_0 is the initial length. Hence, the strain in extensional deformations is generally measured on a logarithmic scale and is referred to as the Hencky strain:

$$\epsilon_H = \dot{\epsilon}\, t = \ln\left(\frac{L}{L_0}\right). \tag{2.7}$$

Another important extensional flow is biaxial stretching that is for instance used in the production of polymer sheets. This flow consists of an extensional flow in two directions and $\dot{\epsilon}_{11} = \dot{\epsilon}_{22}$, so the parameter $m = 1$. This implies that a contraction is acting in the third direction $\dot{\epsilon}_{33} = -2\dot{\epsilon}_{11}$. This flow type is also encountered in lubricated uniaxial compression, which can be used as a rheological technique [39]. Biaxial extension flow is not as strongly orienting as uniaxial flow and is therefore less sensitive to structural changes in the material. Hence, it gives different material functions from uniaxial extension [40, 41]. The third important extensional flow is planar extension, where $\dot{\epsilon}_{11} = -\dot{\epsilon}_{33}$ and $\dot{\epsilon}_{22} = 0$, so the parameter $m = 0$. This flow is for instance created by impinging two liquid streams creating a planar stagnation flow with for instance a four-roll mill [42] or a cross-slot apparatus [43]. Both devices create a well defined extensional flow in the centre point and birefringence can be used to directly measure the tensile stress difference [44].

2.1.3 Experimental methods

It is generally agreed that it is far more difficult to measure extensional viscosity than shear viscosity [23–25, 45]. Firstly, it is rather difficult to generate a homogeneous extensional flow, especially for low viscous liquids. The basic problem is that it is hard to control the deformation of a low viscous fluid without the presence of boundaries, whereas flow over such boundaries results in shear stresses. Surface tension, gravity, and inertia can alter the deformation of such fluids. Furthermore, the determination of a steady state extensional viscosity $\eta_E(\dot{\epsilon})$ is practically impossible. Large strains are often required before stresses in viscoelastic fluids can reach their steady stress limit. Since the streamlines are parallel in rotational shearing flows, large strains can be achieved after long residence times. The streamlines in extensional flow are, however, diverging, which implies that a sample will become very thin in one direction to achieve large strains and might rupture or deform non-uniformly before a steady state is reached. Although the transient extensional viscosity might appear to approach a steady state value at large extensions, careful experiments on LDPE by Meissner et al. [46] have shown that this plateau might be a stress overshoot. In these experiments, a steady state value was not achieved at a Hencky strain $\epsilon_H = 7$, meaning that the sample is stretched to 1100 times its original length. Moreover, even if a steady state extensional viscosity could be measured, it would not necessarily be directly industrially relevant, because a material element

in a processing flow is unlikely to see a steady extensional flow that persists long enough for a steady state to be approached. On the other hand, nearly steady state shearing does occur in various processing flows, such as moulding, extrusion, and transport through ducts and dies [23].

Despite the many challenges in measuring the extensional flow properties of a viscoelastic liquid, many different methods have been tried to circumvent these difficulties and generate purely extensional flows. In this section we will limit ourselves to measurement techniques that use a uniaxial extensional flow field. Unlike shear measurements, where a single rotational rheometer can measure viscosities with a range of 8 orders of magnitude, extensional rheometers are only suited for a particular viscosity range. Consequently, we have classified the experimental methods according to the sample viscosity starting with methods for very viscous polymer melts and ending with techniques suited for water-like samples.

Rotating fixtures for polymer melts

The investigation of polymer melt elongation started around 1970. In general, both ends of a molten polymer sample are connected to an extensional rheometer that imposes a steady extensional deformation to the sample. One of the clamps is connected to a force transducer that continuously monitors the stretching force. The normal stress in the sample is typically calculated by assuming an exponential decrease of the cross-sectional area of the molten polymer specimen (see Eq. B.11). This allows determining the evolution of the transient extensional viscosity $\eta_E(\dot{\epsilon}, t)$, according to Eq. 2.4. One of the challenges in extensional rheometry lies in properly holding the sample ends and many options have been proposed. Originally, the best results were achieved with bonding cylindrical samples with adhesive to a metal base and with mechanical clamps for rectangular samples [23]. However, the fact that the velocity of the translating block must vary exponentially with time (see Eq. 2.6) remains a barrier in acquiring good extensional data.

An alternate method for pulling samples is the rotating clamp, developed by Meissner [47]. The sample is held and stretched between two pairs of rotating gears or cylinders. It is much easier to program a constant extension rate with this rotating clamp than with the translating clamp. The length of the sample remains equal to the distance between the cylinder pairs L_0 during the experiment, resulting in a constant velocity at the end of the sample. This

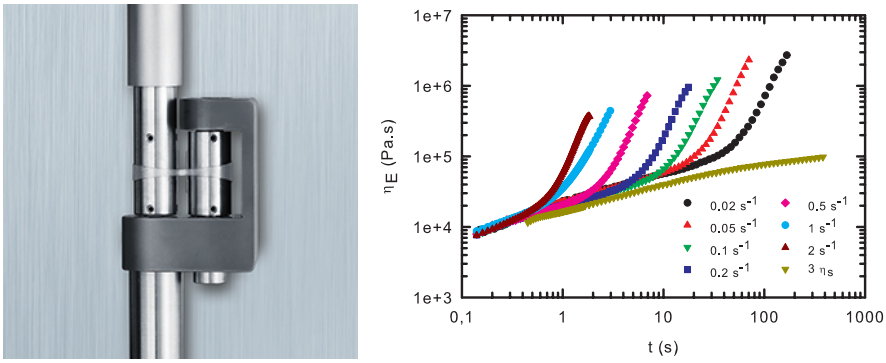

(a) (b)

Figure 2.2: (a) Extensional viscosity fixture (EVF) mounted on ARES strain-controlled rheometer. (b) Strain hardening of a PP melt at different strain rates.

implies that the strain rate is proportional to the imposed angular velocity Ω and can be expressed as

$$\dot{\epsilon} = \frac{2\Omega R_0}{L_0}, \tag{2.8}$$

where R_0 is the radius of the rotating clamp. This design was improved in the following decades allowing more accurate measurements at higher temperatures on smaller samples [48]. In the last decade, smaller rotating fixtures emerged that can be mounted on a conventional rotational rheometer. The original design was the Sentmanat Extension Rheometer (SER) fixture [49] that is based on the fiber windup technique first described by Macosko and Lorntson [50]. The SER uses a pair of counterrotating rollers to wind up a thin rectangular sheet of polymer melt. The Extensional Viscosity Fixture (EVF) is a similar design where only one of the two drums is fixed and the other one is making a double rotation. Figure 2.2a shows the EVF connected to a strain-controlled rheometer. The sample is connected to the drums with two metal clamps and it wraps around both the fixed and the rotating drum during the measurement. However, after one revolution, the sample will wind up on top of itself and the force signal becomes unusable. This results in a maximum Hencky strain $\epsilon_H = 4.3$, which is significantly lower than for the Meissner design. Figure 2.2b shows the detection of strain hardening in a PP melt at different strain rates

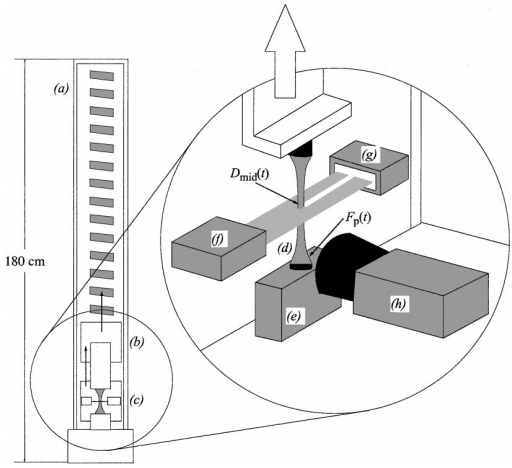

Figure 2.3: Schematic view of a filament stretching device [51].

during measurements with the EVF-geometry. The transient shear viscosity multiplied by the Newtonian Trouton ratio $Tr = 3$ (yellow triangles) is included as a lower reference.

Filament stretching

The previous techniques cannot be used to characterise the transient extensional flow behaviour of polymer solutions, due to gravitational sagging. Filament stretching rheology emerged in the early nineties as an alternative method for fluids with a lower viscosity, such as polymer solutions. In filament stretching devices, the sample forms a cylindrical liquid bridge between two rigid endplates, which are actively stretched. The first design was presented by Matta and Tytus [52] as a falling plate device, where the stretching was achieved by allowing the bottom plate to fall under gravity. This constant force extensional rheometer could generate a nearly pure extensional flow and the authors were able to calculate the tension in the filament. With some modifications, the original setup was even used to determine the finite extensibility parameters of polymer molecules [53]. More importantly, these constant force measurements inspired Sridhar and co-workers [54, 55] to make the prototypical design of a filament stretching rheometer (see Figure 2.3). The plates are connected to a motion control system that exponentially separates the plates to ensure a constant strain rate $\dot{\epsilon}_0$ (see Eq. 2.6). One plate is connected to a force transducer

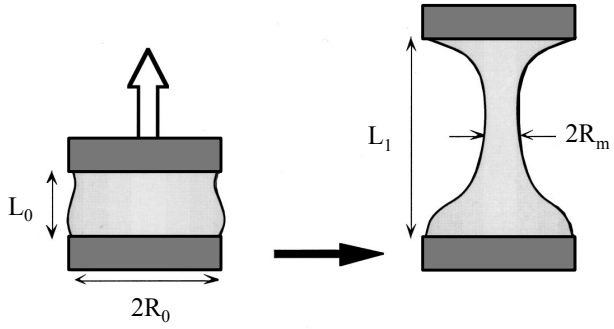

Figure 2.4: Schematic diagram of a capillary breakup experiment.

to measure the tensile force and the mid-filament diameter is actively monitored.

Unfortunately, an ideal filament stretching experiment is practically difficult to implement. A perfect homogeneous uniaxial extensional flow cannot be imposed throughout the entire fluid filament, because the no-slip boundary condition at the endplates introduces local shearing [56]. The optimal endplate separation should therefore be corrected to a more complex motion in order to achieve the desired exponential decay of the filament diameter at the midpoint (see Eq. B.9) [51, 57–60]. Moreover, gravitational sagging [61] or elastic instabilities [56] can provide additional measurement problems for some materials at certain strain rates. Furthermore, the maximum achievable Hencky strain ϵ is limited by the specifications of the device, i.e. either position-limited by the maximal vertical displacement or velocity-limited by the maximal velocity of the motor. Nevertheless, an inter-laboratory comparison of filament stretching data for three common test fluids was presented, in which the authors demonstrated that the agreement between different designs of filament stretching rheometers is excellent [62]. More information on filament stretching can be found in an extensive review by McKinley and Sridhar [25].

Capillary breakup

As the viscosity of the sample liquid decreases, surface tension tends to destabilise the slender fluid filament and obtaining good measurements with a filament stretching device becomes difficult [62,63]. Capillary breakup rheometry provides an alternative measurement technique for low viscous fluids that exploits surface

tension to create a uniaxial extensional flow [64, 65]. Similar to filament stretching, the fluid is placed between two cylindrical endplates, however, these plates are rapidly separated in this technique and then held at a fixed axial separation (see Figure 2.4). The subsequent evolution of the minimal filament radius is monitored during the process of surface-tension-driven necking and breakup. Unlike previous methods, this technique does not involve active stretching and stress measurement. Consequently, axial stress and strain rate are estimated from the evolution of the minimal radius and an apparent extensional viscosity $\eta_{E,app}$ is determined. Contrary to filament stretching, a capillary breakup experiment is relatively simple to perform. However, since the fluid column is allowed to spatially rearrange and select its own time scales, the dynamics of the fluid response can be quite complicated and the kinematics are typically time dependent. Analysis and interpretation of filament thinning data is therefore not as straightforward as that of filament stretching data. [61,66]

The temporal evolution of the filament profile depends the relative importance of inertial, viscous and elastic contributions balancing the surface tension. As a result of the absence of external forcing, the dynamics of the necking process are often self-similar and various scaling laws have been established to predict the non-linear dynamics near pinch-off depending on the dominant resisting stress [3, 4]. These scaling laws can be used to identify material classes and extract other material properties of the fluid besides an apparent extensional viscosity. In order to obtain useful material information, it is thus essential to thoroughly understand this visco-elasto-capillary balance. In Section 2.2, we present an overview of the fluid dynamics in capillary-driven free-surface flows. Because this technique will be used in main part of this study, more practical information is given in the Chapter 3.

2.2 Free-surface flows

2.2.1 Introduction

In order to use capillary breakup rheometry, it is crucial to comprehend the physics of free-surface flows. Surface-tension-driven flows and their tendency to spontaneously form droplets have fascinated scientists for centuries. A major breakthrough in the description of this phenomenon was made by Plateau [1] and Rayleigh [2] at the end of the 19th century. Rayleigh introduced the concept of linear stability analysis on a liquid column to predict the onset of jet breakup. He was capable of identifying the most unstable perturbation wavelength and

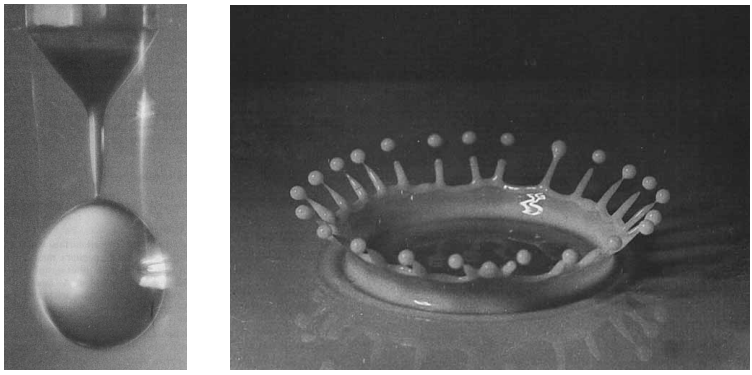

(a) (b)

Figure 2.5: Similarity of breakup profiles in free-surface flows: (a) formation of a water drop from a nozzle and (b) splashing of milk droplet falling into a thin layer of milk [67].

thus determining the final size of the emerged drops. Accordingly, the time scale on which perturbations grow and eventually break the inviscid jet into droplets is called the Rayleigh time t_R and is given by a balance of surface tension and inertia

$$t_R = \sqrt{\frac{\rho R_0^3}{\gamma}}, \tag{2.9}$$

where ρ is the fluid density, γ is the surface tension and R_0 is the initial radius of the fluid column. The description of the non-linear fluid motion in the vicinity of the pinch point proved to be even more challenging. At the pinch point, the radius of curvature approaches zero and the small amount of fluid left in the pinch region is driven by increasingly strong forces. Hence, the velocity goes to infinity and the separation of a drop corresponds to a singularity of the equations of motion, in which the velocity and capillary pressure diverge [5]. The study of the breakup dynamics of Newtonian fluids has gained momentum after the characterisation of a pendant water drop using high-speed photography by Peregrine et al. [67]. In the instances preceding breakup, the drop is connected to the nozzle with a slender liquid filament that ultimately ruptures near the surface of the forming drop rather than in the centre of the filament (see Figure 2.5a). Moreover, this strong up-down asymmetry at the breakup point is independent of the employed setup as can be seen from the comparison of both

pictures in Figure 2.5. This observation suggests the existence of a universal solution for these free-surface flows. Since the flow is without a typical length scale near breakup, the concept of self-similarity was successfully applied to this problem to retrieve an analytical solution. Different self-similar solutions were established depending on the relative importance of inertial and viscous stresses [17].

The breakup behaviour of viscoelastic fluids is very distinct from that of Newtonian liquids. Adding a small amount of flexible polymers to the liquid drastically alters the thinning dynamics of the jet. As the local radius of the instabilities decreases, elastic stresses are growing and the jet consists of a series of small droplets joined by small threads, that become increasingly thinner with distance [68]. The breakup length of the jet is considerably enhanced and this effect can thus be considered as strain-hardening of the polymer solution in an extensional flow field. These viscoelastic effects can be used to alter the atomisation characteristics and to suppress the formation of unwanted satellite drops [15, 16].

In the following sections, we will give a short overview of the dynamics of free-surface flows. The next section discusses how dimensional analysis can help identifying the dominant stresses resisting breakup. An overview of the typical experimental configurations is given in Section 2.2.3. The main concepts of the linear analysis of the early stages of the jet are considered in Section 2.2.4 and the use of similarity solutions to describe the dynamics near pinching is explained in Section 2.2.5. The final three sections give an overview of the scaling laws for different material classes. More information about the fluid dynamics in free-surface flows can be found in two reviews on the subject by Eggers [5, 17], whereas the review by McKinley [3] provides more insight into capillary-driven flows of non-Newtonian fluids.

2.2.2 Dimensional analysis

The thinning dynamics during free-surface flows are determined by the balance of surface tension with the dominant resisting force. The latter depends on the relative magnitudes of the relevant fluid properties, i.e. density, viscosity and elasticity. Dimensional analysis provides a pragmatic strategy to establish which thinning mechanism is dominating at a certain filament radius. Recently, Clasen et al. [4] presented a set of dimensionless groups that are used to predict the dispensing of complex fluids. These dimensionless groups for free-surface

flows compare the characteristic velocities and have been derived from the fundamental governing equations in the seminal work of Middleman [69, 70]. We will highlight the groups that are relevant for the fluids that are studied in this work. The relative importance of the different resisting forces is primarily given via two material-property-based dimensionless parameters. The former is the Ohnesorge number, which compares the viscous and the inertial effects resisting breakup:

$$Oh = \frac{\eta}{\sqrt{\rho\gamma R}}. \tag{2.10}$$

The Ohnesorge number can be considered as the ratio between the viscous time scale $t_\eta = \eta R/\gamma$ and the the Rayleigh time t_R. The latter is the Deborah number, which represents the ratio of the characteristic elastic relaxation time λ of the fluid to the characteristic process time. Depending on whether viscous or inertial forces are dominant, the characteristic process time is either t_η or t_R [71]. Since low viscous elastic liquids are mainly used throughout this work, we will employ the Rayleigh time as reference time, giving following expression for the Deborah number

$$De = \sqrt{\frac{\lambda^2\gamma}{\rho R^3}}. \tag{2.11}$$

This number is often labelled the intrinsic Deborah number, as it compares thinning velocities that are based solely on material properties and does not take the detailed geometry of the filament into account [3]. Moreover, it should be noted that these dimensionless numbers can be determined in two different ways [4]. If the initial filament radius R_0 is the characteristic length scale that enters the number, the overall or global dimensionless number is obtained. This is often used to make an initial estimate of the overall thinning dynamics. Conversely, a local number can be calculated with the radius $R(t)$ to determine at which radius a transition from one thinning regime to another is to be expected.

Once the initial thinning mechanism is established, the relevant thinning velocity is compared to the jet velocity v_0 indicating the transition between dripping and jetting dispersion. The time needed for the jet to breakup is compared to the characteristic time associated with the convective jetting velocity, which is taken as the time for the jet to travel a distance equal to R_0. For low viscous fluids, the dimensionless Weber number is defined as the square ratio of the Rayleigh time t_R to the convective time R_0/v_0:

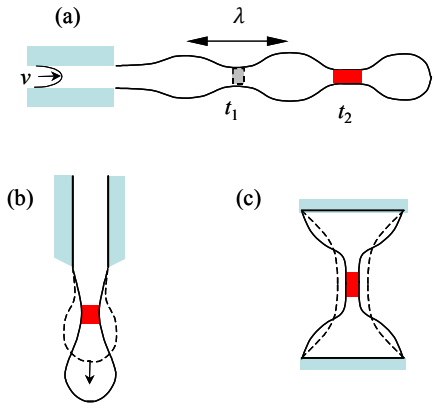

Figure 2.6: Three prototypical geometries for studying breakup of complex fluids: (a) continuous jetting instability, (b) dripping from a nozzle, (c) necking and breakup of an unstable liquid bridge [3].

$$We = \frac{\rho v_0^2 R_0}{\gamma}. \tag{2.12}$$

The last important dimensionless group is the Bond number that expresses the ratio of gravitational forces to the surface tension forces:

$$Bo = \frac{\rho g R^2}{\gamma}, \tag{2.13}$$

where g is the gravitational constant. Generally, the effect of gravity is ignored in the analysis of free-surface flows. This assumption is justified for small threads since they correspond to small Bond numbers. However, for jets with a larger nozzle radius R_n gravitational stretching has to be taken into account and can have unexpected effects on the stability of the jet [72, 73].

2.2.3 Experimental geometries

Free-surface flows have been generally studied using three experimental setups, which are shown in Figure 2.6: (a) jets produced when a fluid leaves a nozzle at

high speeds, (b) slow dripping under gravity and (c) the unstable liquid bridge [5]. These setups can be easily distinguished from each other by the Weber number. Although each geometry demonstrates a specific initial evolution, the last stages of capillary breakup are solely dominated by the internal properties of the fluid. Hence, all setups capture the same phenomenon and the different results are readily compared.

A continuous jet is formed when the flow rate is sufficiently high, so the time scale for breakup is considerably larger than that of the fluid motion ($We > 1$). Capillary instabilities start emerging at a certain distance from the nozzle and will progressively thin as the jet flows downstream. Historically, jetting flow has been by far the most widely used experimental setup for the study of drop formation with documented experiments dating back to the 19th century [1, 74]. Since ambient noise will always create some variation on the wavelength of the instability λ_w in an undisturbed jet, one often forces a specific wavelength to the jet. Mostly, a piezo-electric transducer produces pressure oscillations at the nozzle, which translate into controlled sinusoidal disturbances of the jet profile. As a result, the jet breaks into drops in a perfectly periodic fashion. The wavelength can be controlled by the frequency of the piezo and the jet velocity. Unfortunately for experimentalists, jets tend to get quite long even at moderate Weber numbers, especially for highly viscous and viscoelastic liquids. The combination of large jet lengths and small filament radii makes tracking the complete thinning dynamics experimentally challenging. Hence, jet dynamics are often quantified with breakup lengths and droplet size distributions [15]. Moreover, the evolution of the jet are less reproducible compared to the other two setups because the driving signal is never purely sinusoidal as it is influenced by noise and higher order harmonics [5].

The second setup is a dripping experiment, in which the fluid exits the nozzle at a far lower velocity ($We < 1$), allowing the formation of a hemispherical droplet at the end of the nozzle. Due to the slow fluid release, capillary forces are at first in balance with gravitational forces. The profile of a static pendant drop of fixed volume is solely determined by the Bond number [75]. As the drop becomes heavier, gravity overcomes surface tension and a capillary instability is formed between the nozzle and the drop. After the initial instability, the fluid begins to fall, creating a slender liquid filament before a drop separates. At a filament radius where the Bond number is sufficiently small, the capillary pressure in the thread is solely driving the breakup. At this point, the thinning of the filament is insensitive to the flow rate and the nozzle dimension [5], so it can be used to study the universal breakup of viscous liquids [67, 75, 76] and viscoelastic liquids [77–79].

Finally, the third geometry consists of an unstable liquid bridge that is generated by rapidly pulling two rigid cylindrical plate apart. After the initial step strain, there is no imposed velocity ($We = 0$) and the interplay of inertial, viscous, elastic and capillary forces governs the thinning rate of the bridge. The main advantage of this configuration is that the thinnest part of the filament, which characterises the thinning rate, remains approximately at a fixed Eulerian location. Providing the setup with a laser micrometer or a high-speed camera suffices to quantify the complete thinning dynamics. Consequently, the liquid bridge is at present the most popular configuration to measure rheological properties of liquids during breakup (see Section 2.1.3) and it will be employed for most free-surface flow experiments in this work.

2.2.4 Small perturbations and linear stability

In this section, we will explain the physical mechanism of the transition of a circular jet into a series of small droplets as well as the associated characteristic time and length scales. This breakup is driven by the surface tension of the liquid because a lower energy state is reached by minimising the surface area (i.e the formation of spherical drops). Surface tension can be physically understood as an energy per unit of area, so if the surface area increases with δS, the surface energy E_s changes with

$$\delta E_s = \gamma \delta S. \tag{2.14}$$

The Belgian physicist Joseph Plateau [1] was the first to realise that a jet is rendered unstable by any perturbation that reduces the surface area. A periodic perturbation can be decomposed in a superposition of independent Fourier modes and such a sinusoidal disturbance is presented as

$$R = R_0 + \varepsilon \cos(kz) \tag{2.15}$$

where ε is a small number and $k = 2\pi/\lambda_w$ is the wavenumber of the instability. Figure 2.7 shows a water jet with forced sinusoidal disturbances at different wave numbers [80]. The change in surface energy caused by a sinusoidal disturbance is evaluated by integrating the surface tension over the perturbed surface of the jet. The surface energy is only reduced for dimensionless wave numbers $kR_0 < 1$, indicating that any perturbation with a wavelength larger than the perimeter of the jet is potentially unstable.

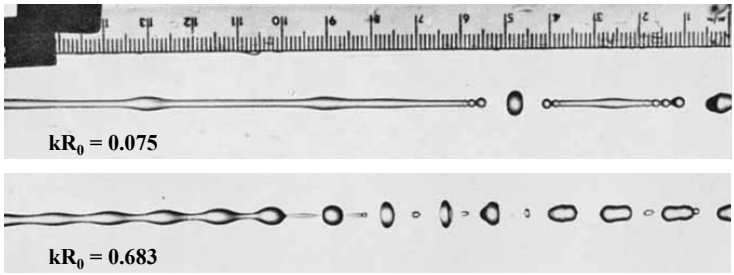

Figure 2.7: Photographs of water jets with unstable disturbances at two distinct wave numbers [80].

However, this thermodynamical description only reveals an unstable range of modes, but does not provide an optimal wavelength, which had been previously deduced from experiments by Savart [74, 81] as $\lambda_w = 8.76R_0$. Lord Rayleigh [2] was the first to realise that the existence of the most unstable wavelength could be identified by considering the fluid dynamics in the jet. An instability causes differences in the Laplace pressure between constricted and the expanded regions, driving the fluid out of constricted regions and thus reducing the radius even more. Starting from an undisturbed jet, the disturbance amplitude will be dominated by the mode corresponding to the fastest growth rate. This wavelength determines the final size of the emerged droplets and the growth rate of the instability is crucial to detect at which speed the instability develops. Rayleigh performed a linear stability analysis on the Navier-Stokes equations, assuming an inviscid liquid with $\eta = 0$. The perturbation has the form $\varepsilon(t) = \varepsilon_0 e^{\omega t}$, where $\varepsilon_0 \ll 1$. The perturbation is unstable if the real part of the growth rate ω is positive, indicating that the amplitude of the surface waves grows exponentially. The growth rate is expressed as

$$\omega^2 = -t_R^{-2} kR_0 \left(1 - (kR_0)^2\right) \frac{I_1(kR_0)}{I_0(kR_0)}, \tag{2.16}$$

where I_0 and I_1 are the modified Bessel Functions. Figure 2.8a shows the dispersion curve of the dimensionless growth rate $\omega\, t_R$ versus the dimensionless wavenumber. The most amplified wavenumber is found at $k_m R_0 = 0.697$ - or expressed as a wavelength $\lambda_w = 9.01R_0$ - and the cut-off wavenumber of $kR_0 = 1$ is in agreement with Plateau's theory.

Viscous stresses considerably alter the dynamics of the jet instabilities. As the viscosity increases, inertia becomes less important and the viscous stresses become dominant in resisting the formation of the capillary instabilities. This

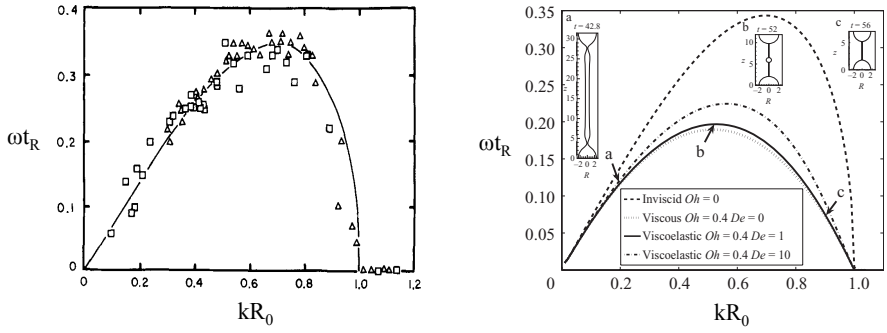

(a) (b)

Figure 2.8: Dimensionless growth rate of sinusoidal perturbations on a cylinder as a function of the dimensionless wave number kR_0: (a) according to inviscid Rayleigh theory [82] and (b) with the effects of viscosity and elasticity [83].

results in a reduction of the growth rate and an increase of the most unstable wavelength [13, 14], which is shown in the viscous dispersion curve in Figure 2.8b. The linear stability analysis on the full Navier-Stokes equations in the long wave limit [84] provides a growth rate

$$\omega = t_R^{-1}\left(\sqrt{\frac{1}{2}\left(\left(kR_0\right)^2-\left(kR_0\right)^4\right)+\frac{9}{4}Oh^2\left(kR_0\right)^4}-\frac{3}{2}Oh\left(kR_0\right)^2\right) \tag{2.17}$$

and a most unstable wavenumber

$$k_m R_0 = \frac{1}{\sqrt{2+\sqrt{18}Oh}}. \tag{2.18}$$

Finally, the effect of viscoelasticity on the initial stages has been investigated [68,83,85]. In general, adding a small amount of flexible polymers to a Newtonian liquid suffices to induce dramatic changes in the jet breakup [77]. However, performing a linear stability analysis on a viscoelastic jet shows that the instabilities grow faster compared to a Newtonian fluid with the same Ohnesorge number [83] (see Figure 2.8b). The importance of this observation appears to be rather small, since non-linear effects quickly start dominating the breakup in these fluids.

2.2.5 Non-linear effects and similarity solutions

Linear theory is successful in describing the initial stages of breakup. Nevertheless, perturbation theory cannot be extended to the regime close to breakup. The growth of sinusoidal modes can for instance not explain basic features such as satellite drops, so the inclusion of non-linear effects is essential. The three-dimensional Navier-Stokes equations are too complicated to obtain an analytical solution describing the non-linear motion in the free-surface flow. It is, however, possible to simplify these equations using a slenderness assumption. When the fluid thread is long and thin, the flow is predominantly oriented in the axial direction, so the velocity field is essentially one-dimensional. The slenderness assumption is closely related to the lubrication approximation that is traditionally applied to flows in a narrow channel [86]. The Navier-Stokes equations are simplified by stating that the typical radial length scale of the problem is much smaller than the longitudinal scale $\ell_r \ll \ell_z$. The situation of free-surface flows is, however, much more complicated. In a classic lubrication flow, viscous stresses are balanced by a pressure difference, while inertia does not matter. The relative importance of inertia, viscosity and surface tension during free-surface flows depends on the physical properties of the fluid and the filament size. Moreover, the ratio of the radial and longitudinal length scale depends on the solution of the free-surface problem and is time dependent.

A one-dimensional approximation is obtained by expanding the velocity field in the radial direction and assuming that the lowest-order terms should suffice to describe the radial motion. Independently, Eggers and Dupont [87] and Garcia and Castellanos [88] gave essentially the same leading-order equations. The procedure to derive the leading-order equation is described in detail in Appendix C and results in the following continuity and momentum equation respectively

$$\frac{\partial R}{\partial t} + v\frac{\partial R}{\partial z} = -\frac{R}{2}\frac{\partial v}{\partial z} \tag{2.19}$$

$$\rho\left(\frac{\partial v}{\partial t} + v\frac{\partial v}{\partial z}\right) = -\gamma\frac{\partial \kappa}{\partial z} + \frac{3\eta}{R^2}\frac{\partial}{\partial z}\left(R^2\frac{\partial v}{\partial z}\right) - \rho g, \tag{2.20}$$

where the mean curvature of the axisymmetric surface κ is defined as

$$\kappa = \frac{1}{R\sqrt{1+(\partial R/\partial z)^2}} - \frac{\partial^2 R/\partial z^2}{(1+(\partial R/\partial z)^2)^{3/2}}. \tag{2.21}$$

Although the leading-order contribution to the mean curvature is $\kappa = 1/R$, the higher order terms are generally incorporated in simulations, because these terms result in equilibrium surface shapes that are in better agreement with experimental observations [5, 89].

Free-surface shapes are remarkably similar near the pinch point, independent of initial conditions. A drop of water falling from a faucet and the water jet, respectively shown in Figure 2.5a and 2.7, both form a slender filament that ultimately ruptures near the surface of the forming drop rather than in the centre of the filament. On the other hand, a dripping experiment with glycerine forms a very long symmetrical thread. So while the initial dimension of the experimental setup (i.e. the nozzle radius) hardly seems to affect the shape, there is a strong dependence on viscosity. As the motion near a point of breakup gets faster, only fluid very close to that point is able to follow, making the breakup localised both in space and time. Thus one expects the motion to become independent of initial conditions and the flow only depends on an internal length scale ℓ_v, which is solely based on the physical properties of the liquid [67, 90]

$$\ell_v = \frac{\eta^2}{\rho\gamma}. \tag{2.22}$$

Note that this length scale is closely related to the Ohnesorge number as $\ell_v = Oh^2 R_0$. By using the the capillary velocity $v_c = \gamma/\eta$, the corresponding internal time scale t_v is found as

$$t_v = \frac{\eta^3}{\rho\gamma^2}. \tag{2.23}$$

The absence of a characteristic length scale near the pinch point suggests that a similarity transformation must exist for this problem. In the case of self-similarity, the solution of a flow problem is a function of some dimensionless combination of dimensional independent variables and parameters of the problem, rather than a function of z and t separately [91]. We call this dimensionless combination a similarity variable and denote it as ξ. The basic idea of self-similarity is that the series of profiles $R(z,t)$ and $v(z,t)$ for various fixed times t will collapse into a single universal form when plotted as a function of ξ rather than as a function of z. To rescale the one-dimensional flow equations (Eqs. 2.19 and 2.20), the intrinsic scales (Eqs. 2.22 and 2.23) are chosen as units of length and time, and the point (z_0, t_0) where the singularity occurs as the origin of the coordinate system. The dimensionless coordinates are thus

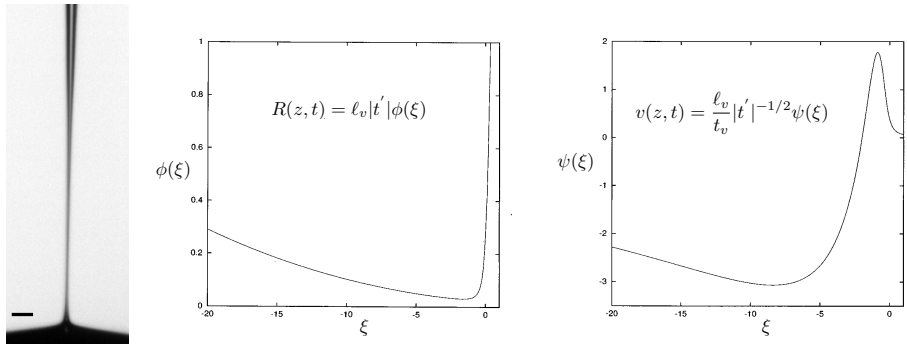

(a) (b)

Figure 2.9: (a) Asymmetric pinching of glycerol-water mixture with $Oh = 0.36$. The scale bar represents 50 μm. (b) The similarity functions ϕ and ψ of the universal inertia-viscous scaling before breakup [5].

$z' = (z - z_0)/\ell_v$ and $t' = (t_0 - t)/t_v$. The filament radius and the velocity are expressed with the similarity description [90]

$$R(z,t) = \ell_v |t'|^{\alpha_1} \phi(\xi), \tag{2.24}$$

$$v(z,t) = \frac{\ell_v}{t_v} |t'|^{\alpha_2} \psi(\xi) \tag{2.25}$$

where $\phi(\xi)$ and $\psi(\xi)$ are the similarity functions that solely depend on the similarity variable ξ, defined as

$$\xi = \frac{z'}{|t'|^{\beta}}. \tag{2.26}$$

The values of the exponents α_1, α_2 and β are retrieved by balancing the terms in the equation of motion. When all terms of the Navier-Stokes equations are used, the balance of surface tension, viscous and inertial stresses results in the universal scaling first described by Eggers [90]. In this case, the exponents are $\alpha_1 = 1$, $\alpha_2 = -1/2$ and $\beta = 1/2$. These scales for the pinching problem are in fact already implicitly present in the slenderness assumption used for the derivation of the one-dimensional Navier-Stokes equations (see Eq. C.15). This inertia-viscous (IV) scaling is called universal, because it provides an asymptotical solution for all Newtonian liquids when breakup is approached or

$t^{'} \to 0$. The similarity description allows transforming the equation of motion into a set of coupled, ordinary differential equation for the similarity functions $\phi(\xi)$ and $\psi(\xi)$. The solutions are presented in Figure 2.9b and indicate the extreme asymmetry of the solution. On the steep right side of $\phi(\xi)$, the solution merges onto the drop and on the left side it forms a thin thread. The solution thus predicts that the minimal radius of the filament is located close to the droplet, which agrees with experimental observations [67, 76]. The minimum of the similarity function $\phi(\xi)$ equals 0.0304 and is used to predict the evolution of the minimal radius of near pinch-off

$$R_m(t) = \min\left[\phi(\xi)\right] \ell_v |t^{'}| = 0.0304 \, \frac{\gamma}{\eta} \, (t_p - t) \tag{2.27}$$

with t_p the pinching time. Despite the tremendous theoretical importance of this inertia-viscous (IV) scaling, this scaling is not commonly observed in practice. Only fluids with moderate Ohnesorge numbers display a perceivable transition to this scaling at very small filament radii [92–95]. Figure 2.9a shows an example of a filament of a glycerol-water mixture with $Oh = 0.36$ where the asymmetric shape of the Eggers similarity solution can be recognised. For more viscous fluids, inertia mainly causes a vertical shift of the necking point along the filament towards the drop when approaching the breaking point [4]. This rapid shift of the neck explains the formation of satellite drops at each breakup event, which might result in an unwanted bimodal droplet size distribution [17].

2.2.6 Scaling laws for Newtonian fluids

Away from breakup, filament thinning is captured by other self-similar scalings. The dynamics of a Newtonian liquid are at this point governed by either inertia or viscosity, giving different thinning laws. For very viscous liquids corresponding to large Ohnesorge numbers, inertia may be neglected whereas viscosity is omitted for water-like fluids. A boundary between these two thinning regimes was defined by Campo-Deaño and Clasen [95] with a critical Ohnesorge number $Oh^* = 0.2077$. Hence, for fluids with $Oh < Oh^*$, the behaviour is initially captured by an inertia-capillary (IC) balance, whereas the thinning is described by a viscous (V) scaling for fluids with $Oh > Oh^*$. Ultimately, the thinning adopts the universal Eggers' scaling (see Eq. 2.27), but the critical radius at which this transition occurs may not be within observable limits. Since the former scaling laws dominate for a longer period, they are more relevant from an experimental rheological perspective.

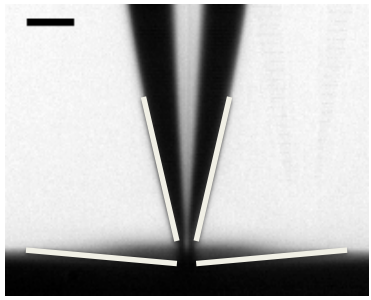

Figure 2.10: Closeup of the pinching of a water drop taken at $t_p - t = 0.01$ ms. The white lines indicate the edges in the focus plane, showing double-cone shape near pinch-off. The scale bar represents 50 μm.

As indicated by the Rayleigh timescale t_R, breakup happens very fast for liquids with a small Ohnesorge number, where the capillary pressure is solely resisted by the inertia of the accelerating fluid elements. Figure 2.10 shows a water filament in the final instances before pinch-off. The filament is very asymmetrically shaped as a double-cone, with one shallow angle and the other larger than 90°. This overturning of the profile impedes a one-dimensional parametrisation of the filament radius $R(z,t)$ close to pinching [96]. Similarity solutions for water-like liquids were thus discovered by solving the full inviscid equations of motion [97, 98]. Nevertheless, the profile shape can still be captured with the similarity description of Eqs. 2.24-2.26 using the exponents $\alpha_1 = 2/3$, $\alpha_2 = -1/3$ and $\beta = 2/3$, resulting in an evolution of the minimal radius

$$R_m = 0.64 \left(\frac{\gamma}{\rho}\right)^{1/3} (t_p - t)^{2/3}. \tag{2.28}$$

This 2/3-power scaling of the time until the pinch time t_p was already apparent in the expression of the Rayleigh timescale (see Eq. 2.9) and the front factor was numerically determined [94] and later experimentally confirmed [79]. The self-similar profile adopts a unique shape with two cones of angles 18.1° and 112.8°, independent of the initial conditions [98].

More viscous fluids have a significantly longer filament lifetime. Above the critical Ohnesorge number, the filament thins and breaks in the middle between the droplets (see Figure 2.11a). This different scaling is found by dropping the inertial term in the momentum equation and thereby reducing it to the linear Stokes form. A symmetric self-similar solution to this equation was derived by Papageorgiou [99] with similarity exponents $\alpha_1 = 1$, $\alpha_2 = -0.825$ and $\beta = 0.175$.

(a)

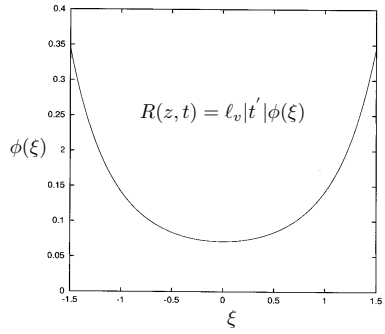

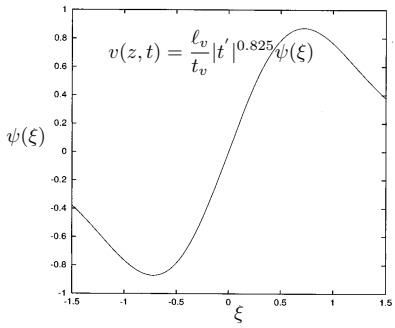

(b)

Figure 2.11: Viscosity dominated thinning: (a) filament of a Newtonian silicon oil with $Oh = 2.6$ (the scale bar shows 100 μm) and (b) the symmetric similarity functions ϕ_{St} and ψ_{St} of the Stokes similarity solution [5].

The similarity variable ξ can, however, only be computed using an arbitrary normalisation length, which depends on the initial conditions. This implies that the Stokes solution is universal, up to a single parameter which sets the width of the solution. The Stokes similarity functions ϕ_{St} and ψ_{St} are shown in Figure 2.11b. The minimal radius behaves like

$$R_m(t) = 0.0709 \, \frac{\gamma}{\eta} \, (t_p - t) \, , \tag{2.29}$$

so with the same linear time dependancy as the Eggers scaling, but with a different numerical prefactor.

2.2.7 Scaling laws for generalised Newtonian fluids

The self-similar scaling laws for pinching have been extended to non-Newtonian fluids [3]. A first important category are the generalised Newtonian fluids, which are not elastic and for which the viscosity is a function of the deformation rate. The strain thinning of these fluids is generally described by a power law dependence on the second invariant of the rate of deformation tensor $\mathrm{II}_{\mathbf{2D}}$

$$\eta = K_n |\mathrm{II}_{\mathbf{2D}}|^{(n-1)/2}, \tag{2.30}$$

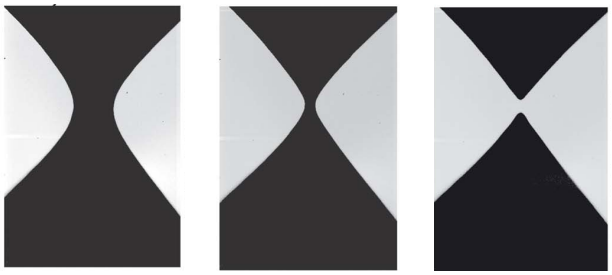

Figure 2.12: Very localised pinching of mayonnaise, which behaves as a power law with $n = 0.35$ [102].

where n is the power law exponent and K_n is the consistency index. This expression is used to find a similarity solution in the form of Eqs. 2.24-2.26 with exponents $\alpha_1 = n$, $\alpha_2 = -n/2$ and $\beta = 1 - n/2$ [100, 101]. The minimal filament radius varies as

$$R_m = \Phi \frac{\gamma}{K_n} (t_p - t)^n \,, \tag{2.31}$$

where the prefactor Φ is a numerical factor depending on the power law exponent n [100]. This scaling has been successfully used on concentrated emulsions and other consumer products that exhibit inelastic shear thinning behaviour [102, 103]. Not surprisingly, the breakup is accelerated for shear thinning liquids ($n < 1$) compared to Newtonian liquids. The strain rate has the highest value in the thinnest region of the filament and consequently the viscosity of the liquid decreases at the necking point. This local decrease in the effective viscosity leads to a positive feedback effect and the strain rate accelerates continuously. Hence, the fluid column displays enhanced axial gradients with a very localised pinch region (see Figure 2.12). In fact, a detailed analysis for the power-law fluid shows that the slenderness assumption is violated for a power law fluid with exponent $n \leq 2/3$ [100]. So, even if the base viscosity is high, thread-like features close to breakup disappear and the breakup is less likely to produce satellite droplets. This might be a desirable effect for filling and dispensing operations from an engineering point of view.

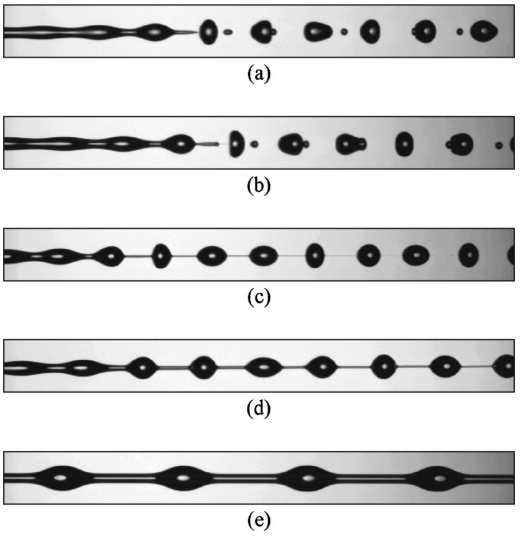

Figure 2.13: Effect of viscoelasticity on jet breakup of aqueous solutions: (a) 50% glycerol, (b) 0.3% 100k PEO, (c) 0.1% 300k PEO, (d) 0.05% 1000k PEO and (e) 0.043% 5000k PEO [104].

2.2.8 Breakup of viscoelastic fluids

The thinning of viscoelastic fluid jets may differ substantially from Newtonian jets. Whereas the linear instabilities are still quite similar (see Section 2.2.4), the presence of high molecular weight, flexible polymers completely alters non-linear dynamics of the jet [68]. The uniaxial extensional flow that is present in the filament is very efficient in unraveling the polymer chains. This deformation leads to large elastic stresses that stabilise the breakup process by forming cylindrical threads between the droplets. Figure 2.13 shows a series of aqueous jets with the same Ohnesorge number, but with increasing elasticity [104]. The first image shows as a reference a 50% glycerol-water jet for which thinning is controlled by an inertia-capillary balance. By adding polymers to the solution, the jet morphology changes completely. As the molecular weight of the polymer increases and elastic stresses in the fluid become increasingly important, the jet breakup evolves from the inviscid asymmetric shape towards the typical beads-on-a-string (BOAS) morphology with cylindrical filaments. Consequently, the breakup length increases and the formation of small satellite drops is suppressed.

The non-linear dynamics of a viscoelastic jet were for the first time successfully

simulated by Bousfield et al. [105] using the Oldroyd-B model. It was shown that the elastic stresses grow exponentially in the neck as a result of the uniaxial deformation induced by the ever-increasing capillary pressure. This unbound growth of the axial elastic stresses occurs for extensional flows with a Weissenberg number $Wi = \lambda\dot{\epsilon} > 1/2$, which corresponds to strain rates where the macromolecules unravel from the coiled to the stretched state. The necking of the filament is at this point governed by an elasto-capillary balance, resulting in an exponential decrease of the minimal filament radius

$$R_m \sim e^{-t/3\lambda}, \tag{2.32}$$

where λ is the relaxation time of the fluid. This evolution of the filament implies that the fluid selects a constant extension rate of $\dot{\epsilon} = 2/(3\lambda)$ (see Eq. B.9) in the elasto-capillary balance, corresponding to a Weissenberg number $Wi = 2/3$.

The expressions for elasto-capillary thinning were generalised by Entov and Hinch [106] to a dilute polymer solution with an arbitrary spectrum of relaxation times, $\lambda_i \{i = 1, \ldots, n\}$. Using a simple zero-dimensional stress balance with a multimode finite extensible non-linear elastic (FENE) dumbbell model, they showed that after a short transition period, the filament selects a necking rate so that only the mode with the longest time constant is in fact being stretched. Anna and McKinley [61] examined the same problem with a Zimm spectrum of relaxation times, $\lambda_i = \lambda_z/i^{3/2}$, where λ_z is the Zimm relaxation time or the longest relaxation time of the entire polymer chain. Since the longest mode λ_z attains an elasto-capillary balance in which the Weissenberg number $Wi = \lambda_z\dot{\epsilon} = 2/3$, all other modes experience a weak stretching flow with $Wi = \lambda_i\dot{\epsilon} = 2/(3\,i^{3/2})$ for $i \geq 2$. This value is below the critical value of $Wi = 1/2$ required for a coil-stretch transition in a uniaxial extensional flow, so these modes only augment the negligible viscous response of the solvent.

Since it was established that there is only one dominant relaxation time during the elasto-capillary balance, an analytical solution for the thinning of a viscoelastic fluid can be evaluated using the one-dimensional description of the equations of motion with an FENE dumbbell model with a single relaxation time [17, 107]. This description is similar to the Newtonian case (Eqs. 2.19 and 2.20), but there is an additional polymeric normal stress component $\Delta\sigma_p$ in the momentum balance. The polymeric stresses are related to the corresponding components of the conformation tensor $\mathbf{A}$ that provides a measure for the shape and orientation of the polymer [25, 108]. The non-linearity of the dumbbell is taken into account by a maximum extension, expressed with the finite extensibility parameter L. Two additional microstructural evolution equations

relate the dumbbell conformation to the flow field and thus provide a rheological equation of state to evaluate the elastic stress. If the polymers are still far from full extension, the elasto-capillary balance is retrieved where the elastic stress increases at the same rate as the radius decreases. By demonstrating that the profile in the corner region connecting the filament to the drop is self-similar with a typical length scale that is set by the thread radius, Clasen et al. [107] achieved a modified expression for minimal radius:

$$R_m = \left(\frac{GR_0^4}{2\gamma}\right)^{1/3} e^{-t/3\lambda}, \tag{2.33}$$

where G is the elastic modulus. The elasto-capillary regime continuous until the polymer chains reach their finite extensibility limit and the elastic stresses cease to grow and balance the increasing capillary pressure. The necking dynamics deviates from the exponential decay and the filament radius decreases linearly corresponding to a viscous liquid with a very high and anisotropic elongational viscosity resulting from the fully extended polymer chains [109, 110]. The filament diameter evolves according to

$$R_m = \frac{\gamma}{2\,\eta_E}\,(t_p - t)\,, \tag{2.34}$$

where η_E is the steady state uniaxial elongation viscosity. This limiting viscosity can be described by molecular parameters from the dumbbell model [61, 106]

$$\eta_E = 3\,\eta_s + 2\,G\lambda L^2\left(1 - \frac{1}{2\,\lambda\dot{\epsilon}}\right), \tag{2.35}$$

where η_s is the solvent viscosity, which is often negligible.

2.3 Conclusions

In this chapter, we have explained the importance of extensional rheology and the difficulties in measuring the extensional rheological properties of a liquid. Since extensional deformations generate a strong irrotational flow field that can induce large deformations in the microstructure of a complex fluid, the extensional rheology cannot be predicted from the shear response. However, directly measuring extensional properties is difficult as it is rather complicated to generate a pure extensional flow field. Some experimental methods have been

developed to determine a transient extensional viscosity by actively stretching a liquid sample and measuring the stress during the deformation. Unfortunately, for low viscous fluids, surface tension destabilises the liquid filament so that force measurements are impossible.

An alternative measurement technique for these low viscous fluids is provided by capillary breakup rheometry. This technique exploits surface tension to create a uniaxial extensional flow field in a filament and material parameters are determined by monitoring the breakup dynamics of this free-surface flow. Since there is no external forcing in this measurement, the fluid column selects its own time scales and the interpretation of the filament thinning data is not so straightforward.

Hence, a thorough understanding of the dynamics in free-surface flows of complex fluids is required. The theory is quite mature for Newtonian liquids owing to the use of linear stability analysis and similarity solutions to predict the initial and final stages of the thinning, respectively. In general, the thinning dynamics depend on the relative importance of inertial and viscous stresses, which can be expressed with an internal length scale ℓ_v or with the dimensionless Ohnesorge number. The breakup behaviour of complex fluids is very different from that of Newtonian liquids and various (de)stabilising phenomena are observed. Viscoelasticity, for instance, creates long stable threads, whereas locally destabilised filaments are formed for generalised Newtonian liquids. Non-Newtonian constitutive laws are usually not well tested in the non-linear regime of various free-surface flows and this thesis aims to provide new experimental observations on the breakup of complex fluids. For that reason, we study the thinning dynamics of two model systems, i.e. dilute polymer solutions and suspensions of non-colloidal spheres in a Newtonian medium.

Chapter 3

Materials and methods

In this chapter, we introduce the materials and experimental methods that are used in this work. Section 3.1 presents the polymer solutions and suspensions that are studied in Chapters 5 and 6, respectively. Some basic physical properties of the fluids are included, however more advanced characterisation can be found in the following chapters. The different experimental techniques are presented in Section 3.2, where we mainly review two free-surface flow setups, i.e. the capillary breakup rheometer and the jetting setup. The modifications that were made to the optical components of these setups as well as the image processing routines are discussed in Chapter 4.

3.1 Materials

3.1.1 Polymer solutions

The model polymer solutions that are studied in Chapter 5 consist of a series of dilute polyethylene oxide (PEO) solutions in water. Similar solutions have been used in other jetting and capillary breakup studies [15, 79, 95, 104, 111] allowing comparison of our results to literature data. Moreover, PEO is used as a water-soluble industrial additive to enhance the rheological product performance. It is for instance added in very low concentrations to water-based agricultural sprays to reduce turbulent frictional drag and to prevent misting [112]. Two types of PEO were used to prepare the solutions, both with an approximate molecular weight of 10^6 g/mol: PEO_1 (PolyOx Resin WSR N-12K, Dow, USA)

	c ($wt\%$)	η ($mPa.s$)	ρ (kg/m^3)	γ (mN/m)
PEO_1	0.10	1.68	998	62.2
PEO_2	0.05	1.31	998	62.4
	0.075	1.51	998	62.4
	0.10	1.72	998	62.4

Table 3.1: Characteristics of the model polymer solutions at 22°C.

and PEO_2 (Sigma Aldrich, Bornem, Belgium). PEO_2 was used for most jetting experiments after the observation that PEO_1-solutions were rather susceptible to UV-degradation. Solutions with three different concentrations were prepared by allowing the polymer to dissolve in distilled water on a rolling bench for 24 hours. The samples were shielded from light and all experiments were performed within 72 hours after preparation to minimise the effect of degradation of the polymer molecules. Some important physical properties of the solutions are listed in Table 3.1. Although we expected the same rheological behaviour of the solutions of both polymers at the same concentration, we detected significant differences, especially in extensional flows. We will elaborate on these differences in Chapter 5.

3.1.2 Suspensions

The model suspensions that are studied in Chapter 6 consist of non-Brownian spherical particles dispersed in Newtonian silicone oils with volume fractions ϕ between 0.02 and 0.40. The key physical properties of the poly(dimethylsiloxane) (PDMS) oils at a temperature of 22°C are summarised in Table 3.2. Three different-sized particles are used: polystyrene spheres with a radius $R_p = 10$ μm (PS10) and $R_p = 20$ μm (PS20), and poly(methyl methacrylate) spheres with $R_p = 3$ μm (PMMA3) (Dynoseeds, Norway). The roughness of the PS spheres has been determined by AFM measurements to be of 100 nm by Deboeuf et al. [113]. The particles are initially dispersed in the continuous phase using a vortex mixing device (Vortex Genie 2, Scientific Industries) and the suspensions are subsequently placed on a rolling bench for 30 minutes to homogenise the samples. The PS spheres have a density $\rho = 1050$ kg/m^3 and for the PMMA spheres $\rho = 1180$ kg/m^3. To judge the stability of the dispersions, the sedimentation velocity $v_{s,0}$ for dilute suspensions is calculated using Stokes' law:

	γ (mN/m)	ρ (kg/m^3)	η_m $(Pa.s)$
$PDMS_1$	21.0	1070	0.180
$PDMS_2$	21.0	970	0.360

Table 3.2: Characteristics of the silicone oils at 22°C.

$$v_{s,0} = \frac{2R_p^2 \Delta\rho g}{9\eta_m}, \tag{3.1}$$

where $\Delta\rho$ is the difference between the densities of particle and fluid, η_m is the medium viscosity and g is the gravitational constant. This formula is based on the assumption that particle inertia can be neglected, which can be verified with the particle Reynolds number $Re_p = \rho\dot{\gamma}R_p^2\eta_m^{-1} \ll 1$. For more concentrated suspensions, the settling is slowed down because the required back flow of the liquid in the upward direction is hindered by the presence of the neighbouring particles. The settling velocity v_s is calculated by the empirical Richardson-Zaki expression [114]

$$\frac{v_s}{v_{s,0}} = (1-\phi)^{6.55}, \tag{3.2}$$

where the exponent is chosen to match the prediction for dilute particle concentrations by Batchelor [115]. The maximal sedimentation velocity is determined for the dilute samples of PS20 to be of $v_s \approx 10$ μm/min. Therefore, each capillary breakup experiment is performed within 15 minutes after (re)dispersing the particles using the vortex mixer.

Because micron-size particles are investigated in a relatively high-viscosity medium, Brownian motion is unable to re-distribute the particles and eliminate particle density gradients within the timescale of the experiment. This can be verified by the Péclet number Pe, which is the ratio of the rate of advection by the flow to the rate of diffusion by Brownian motion in a dilute dispersion:

$$Pe = \frac{6\pi\eta_m\dot{\epsilon}R_p^3}{k_BT}, \tag{3.3}$$

where k_B is the Boltzmann constant and T is the absolute temperature. The strain rate has the lowest value during capillary breakup experiments of the most viscous samples and a characteristic value $\dot{\epsilon} \sim 10$ s^{-1} can be estimated by the

Figure 3.1: Picture of the CaBER with the top (1) and bottom (2) plate in detail. The linear motor (3) and the sliding covers for the laser micrometer (4) are also highlighted.

inverse viscous time scale $\dot{\epsilon} \sim t_\eta^{-1} = \gamma / (\eta R_0)$. Even for the smallest particles, the Péclet number is of the order $Pe = O(10^4)$, which justifies neglecting Brownian motion in our study.

3.2 Methods

3.2.1 Capillary breakup rheometer (CaBER)

Capillary breakup rheometry is a rheological technique, in which a fluid droplet is rapidly stretched between two plates to create an unstable liquid bridge. The necking subsequently monitored in order to extract information on the extensional flow properties of a low viscous fluid. The technique was introduced in Section 2.1.3 and the physical principles of surface-tension-driven flows of different materials were discussed in Section 2.2. The experiments are performed with the CaBER-1 extensional rheometer (Thermo Haake GmbH, Karlsruhe, Germany), shown in Figure 3.1. The central column contains a linear motor that is connected to the upper plate. The position of the lower plate can be

changed with a micrometer screw to vary the final gap size L_1. Both plates are made of stainless steel. Two sliding covers contain the laser micrometer, which tracks the temporal evolution of the mid-filament diameter with a resolution of 10 μm.

The experiments are executed at an ambient temperature of 22°C with circular disks with a radius $R_0 = 2$ mm. These small disks are chosen to reduce gravitational sagging. Gravitational effects lead to a weak axial flow, such that more than half of the initial sample volume is found below the mid-plane. Since the analysis of the filament thinning always presumes an axial symmetry, this drainage should be minimised. The Bond number, which expresses the ratio of gravitational to capillary forces, has an initial value of $Bo \approx 1$ with these plates. During the thinning process, the Bond number will decrease, so the filament is only drained by capillary forces [116]. The initial gap is kept fixed at $L_0 = R_0 = 2$ mm, leading to sample volumes of 0.03 ml. The fluid samples are carefully loaded between the plates with a syringe to avoid air bubbles in the fluid. The syringe is generally connected to a nozzle with an inner diameter of 0.25 mm to precisely control the sample loading, but nozzles with a larger diameter of 1.36 mm are employed for the suspensions to avoid changes in the volume fraction.

The unstable liquid bridge is created by stretching in a linear motion over a timespan of 50 ms. The final gap L_1 depends on the investigated sample. The suspensions are stretched to separations of 6 and 8 mm to create nice slender filaments. However, the low viscous polymer solution already break during the initial stretching phase with these final distances. The final gap is therefore reduced to $L_1 = 5$ mm, which is only slightly above the upper stability limit $L_1 = 2.25R_0$ of a liquid cylinder [117]. This small stretch step creates very short filaments with an inherently high axial curvature. These filaments can hardly pass for slender filaments and the self-similar scaling laws do not apply, because these laws are founded on the slenderness approximation [95]. As the filament gets thinner, it evolves to a slender shape and the extracted radii can be used to determine the extensional flow properties.

In the experiments that are presented in this study, the evolution of the minimal filament radius R_m is not monitored with the laser micrometer of the CaBER. The laser micrometer only captures the mid-point radius, which is not necessarily the minimal radius for complex fluid threads [111]. Instead the thinning dynamics are determined with a high-speed camera (Fastcam SA2, Photron, USA) to better capture the heterogeneous nature of the filament near breakup. The camera is connected to a tube lens system equipped with 5x and 10x

microscopic objectives (Olympus, Japan) that is described in Section 4.1. Images are generally taken at a rate of 3000 fps with a shutter time of 10 μs, but rates can be increased to 9000 fps for examining the final pinch-off dynamics. The image series are analysed with the Matlab-based, self-written image processing routines that are discussed in Section 4.2.2. The code determines the shape of the edges of the filament (which can for instance be used to calculate the curvature) and allows following the evolution of the minimal radius in time $R_m(t)$. The extracted radius data can be used to calculate the evolution of the Hencky strain $\epsilon_H(t)$ and the strain rate $\dot{\epsilon}(t)$

$$\epsilon_H(t) = 2 \ln\left(\frac{R_0}{R_m(t)}\right) \tag{3.4}$$

$$\dot{\epsilon}(t) = -\frac{2}{R_m(t)}\frac{dR_m(t)}{dt}. \tag{3.5}$$

These formula's are based on a uniaxial extensional flow field of a cylinder (see Appendix B) and are therefore approximate values. The strain rate generally varies with time, except for an elastic sample, where the exponentially decreasing radius is consistent with a uniaxial extensional flow with a strain rate of $\dot{\epsilon} = 2/(3\lambda)$ (see Eq. B.9).

There are two methods of extracting quantitative material information from the instrument based on the temporal evolution of the minimal filament radius. The former consists of fitting the data with the appropriate scaling law for capillary breakup in order to extract rheological parameters (e.g. viscosity η or the relaxation time λ). The fluid properties control whether inertia, viscosity or elasticity is dominantly resisting surface tension and determine which of the scaling laws presented in Section 2.2 is valid. This strategy is mostly used throughout this study. The latter method consists of converting the radius data into an apparent extensional viscosity $\eta_{E,app}$ by assuming that the stress equals the capillary pressure of a cylindrical filament γ/R_m [61, 118]. Combining this stress with the expression for the strain rate in Eq. 3.5, the apparent extensional viscosity is defined as

$$\eta_{E,app}(t) = -\frac{\gamma}{2\, dR_m/dt}. \tag{3.6}$$

Since the radius of a Newtonian liquid decreases linearly in time during capillary breakup, the apparent extensional viscosity is constant for a Newtonian liquid. However, the curvature effects during the thinning of a viscous filament, as

Figure 3.2: Experimental setup for the jetting tests with the Photron SA2 high-speed camera with tube lens and the Harvard syringe pump to control the flow rate.

expressed by the coefficient in the viscous similarity solution (Eq. 2.29), are neglected in the definition of $\eta_{E,app}$. Hence, Eq. 3.6 overestimates the apparent Trouton ratio of Newtonian liquids, giving $Tr = \eta_{E,app}/\eta = 7.05$ instead of the standard Trouton ratio $Tr = 3$. In contrast, a viscoelastic sample shows significant strain hardening with $\eta_{E,app} \sim \lambda \exp(t/3\lambda)$ during the elasto-capillary regime.

3.2.2 Jetting setup

Figure 3.2 shows the experimental setup used to study jet breakup of a polymer solution. A syringe containing 50 ml of the sample fluids, is placed in a syringe pump (Harvard Apparatus, Holliston, MA, USA) to deliver fluid at a constant flow rate and is connected with a flexible tube to a nozzle (Nordson EFD precision tips). Two different nozzles with diameters of 0.15 mm and 0.25 mm are used throughout the experiments. The thinning dynamics of the jet are visualised with a high-speed camera (Fastcam SA-2, Photron, San Diego, CA, USA) connected to one of two employed lens systems. The former consists of a tube lens system (see Section 4.1) equipped with a 5x Olympus microscopic objective to obtain high resolution images (1.9 μm/pixel) in order to detect variations in the filament shape. Consequently, the field of view of this lens is limited to 1.46 x 2.37 mm and the jet was captured with multiple images. Hence, the nozzle is mounted on a two-dimensional linear stage driven by a micrometer screw allowing a precise motion of 50 mm in the vertical direction.

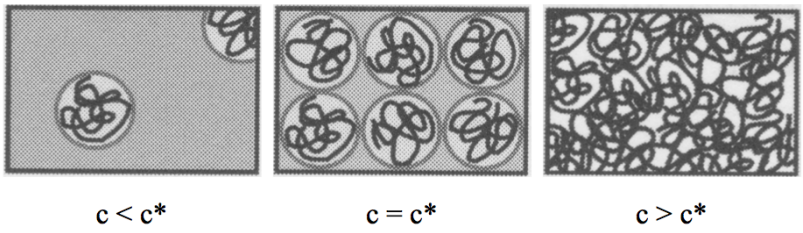

Figure 3.3: Schematic drawing of the critical overlap concentration c^* of a polymer solution.

The latter is a lower magnification 55 mm focal length telecentric lens (TEC-M55 Computar, CBC, Tokyo, Japan) with a spatial resolution of 9.5 μm/pixel to capture the breakup mechanism of jets with a higher velocity. Illumination is provided with a fiber optic illuminator Fiber-Lite DC-950 (Dolan-Jenner Industries, Boxborough, MA, USA) and a 50 mm condenser lens.

All experiments are executed according to the same protocol: first a stable flow is ensured by waiting 90 s and the jet is subsequently captured by taking a series of pictures of its different sections. The images are taken at a rate ranging from 3000 to 3600 frames/s with a shutter time of 2.7 μs. The image processing is carried out with a self-written algorithm based on the robust Canny edge detector [119] that is discussed in more detail in Section 4.2.4. The different minima of the jet radius are linked in the subsequent images based on their location to obtain the temporal evolution of each instabilities. The presented data is averaged by following the thinning of at least 10 instabilities for each flow rate.

3.2.3 Intrinsic viscosity measurements

The rheological response of a polymer solution changes tremendously as the concentration increases above the critical overlap concentration c^*. At this critical concentration, the solution is completely filled with polymer coils and the coils start to interpenetrate as shown in Figure 3.3. The critical overlap concentration marks the transition from a dilute regime to a semi-dilute solution. The flow properties of dilute solutions ($c < c^*$) are determined by interactions between the polymer coil and the solvent, whereas intermolecular interactions of the polymer coils dominate the flow behaviour of semi-dilute solutions ($c > c^*$).

In order to calculate the concentration c^* where the solution is completely filled with non-overlapping coils, we need to obtain information about the dimensions of a single polymer coil.

A straightforward estimate of the coil size in a specific solvent is provided by the intrinsic viscosity $[\eta]$, which should not be confused with the dynamic viscosity η that is frequently encountered throughout this work. It is actually a measure for the capacity of a polymer to increase the viscosity of a solution. The viscosity of a polymer solution can be conceived as the sum of the solvent viscosity η_s and the polymeric contribution η_p:

$$\eta = \eta_s + \eta_p = \eta_s \left(1 + \eta_{sp}\right), \tag{3.7}$$

where $\eta_{sp} = \eta_p/\eta_s$ is the specific viscosity that expresses the incremental viscosity due to the presence of the polymer coils. To determine the interactions between a single polymer molecule and the solvent, viscosity measurements are performed for dilute polymer solutions. Although the polymers are isolated from each other in dilute solutions, there are still occasional coil overlaps during flow [120]. These interaction are only prevented in an ideal dilute solution when the polymer concentration $c \to 0$. The intrinsic viscosity $[\eta]$ is determined by extrapolating the reduced viscosity $\eta_{red} = \eta_{sp}/c$ to zero polymer concentration:

$$[\eta] = \lim_{c \to 0} \eta_{red}. \tag{3.8}$$

The intrinsic viscosity is thus the incremental viscosity per unit concentration of the polymer extrapolated to zero concentration. The value of the intrinsic viscosity is affected by many parameters, such as molecular weight, polymer architecture (branching), temperature and solvent. The intrinsic viscosity can be related to the dimensions of the polymer coil by assuming that each coil in the dilute solution contributes to the viscosity as would a hard sphere of radius equal to the radius of gyration R_g of the coil [108]. The specific viscosity is then described by Einstein's formula for the viscosity of dilute suspensions [114]:

$$\eta_{sp} = 2.5\,\phi. \tag{3.9}$$

The specific viscosity solely depends on the polymer volume fraction ϕ that can be described with the polymer concentration c and the density of the dissolved polymer ρ_c, giving

$$\phi = \frac{c}{\rho_c} = \frac{cN_A V_h}{M_w}, \tag{3.10}$$

where N_A is Avogadro's constant, M_w the molecular weight and V_h the hydrodynamic volume of the coil. By combining Eqs. 3.8 - 3.10, it is clear that the intrinsic viscosity can be considered as a measure for the volume demand of the single polymer coil in ideally diluted solution and is thus inversely proportional to the density of the polymer coil [120]:

$$[\eta] = \frac{2.5}{\rho_c}. \tag{3.11}$$

Hence, the product of the polymer concentration and the intrinsic viscosity $c[\eta]$ is often used as measure for the polymer volume fraction. Moreover, knowledge of the intrinsic viscosity allows for the determination of the size of a single polymer coil in a dilute solution. Since a dissolved polymer molecule has density variations within the coil, the hydrodynamic volume cannot be calculated as if the polymer were a hard sphere. We can, however, assume that the hydrodynamic volume is proportional to the radius of gyration to the third power $V_h \sim R_g^3$ and with this understanding, we can combine Eqs. 3.10 and 3.11 to the so-called Fox-Flory equation:

$$[\eta] = \frac{\Phi_0 R_g^3}{M_w}. \tag{3.12}$$

In this equation, the constants are combined in a single Flory constant $\Phi_0 = 3.67 \times 10^{24}$ mol^{-1}, which is the same for all polymers regardless of the solvent and temperature [121,122]. The knowledge of the dimensions of a single polymer coil allows for the calculation of the critical overlap concentration c^*, where the solution volume is completely filled with polymer coils. We choose to work with the criterium from Greassley [122], where the overlap concentration c^* is defined as the concentration where the average chain spacing is $2R_g$, giving

$$c^* = \frac{M_w}{8\, R_g^3 N_A} = \frac{\Phi_0}{8\, N_A [\eta]} = \frac{0.77}{[\eta]}. \tag{3.13}$$

As the intrinsic viscosity depends on the coil dimensions, it is often employed to determine the molecular weight of an unknown polymer. This relation is easily deduced for a polymer dissolved in a theta solvent, in which the polymer behaves like an ideal chain. For these systems, the radius of gyration squared is

proportional to the molecular weight of the polymer $R_g^2 \sim M_w$, which allows to rewrite Eq. 3.12 as

$$[\eta]_\theta = K_{[\eta],\theta} M_w^{1/2}. \tag{3.14}$$

For non-theta systems, this equation can be corrected with a polymer expansion factor $\alpha = [\eta]/[\eta]_\theta$ that is dependent on the molecular weight and has to be determined experimentally. This results in the Mark-Houwink-Sakurada relationship

$$[\eta] = K_{[\eta]} M_w^a, \tag{3.15}$$

where $K_{[\eta]}$ and a are constants for a given polymer-solvent system at a given temperature. The exponent a is a measure for the solvent quality and hence describes the solution structure of the dissolved polymer [123].

In this study, the intrinsic viscosity was determined by measuring a series of dilute polymer solutions. The viscosity is accurately measured with an Ubbelohde viscometer equipped with a capillary with a diameter of 0.53 mm (Schott Instruments). Although these solutions are very dilute, they are not ideal and there are still interactions between single polymer coils taking effect during the flow. Hence, the specific viscosity is described with a quadratic dependence on the polymer volume fraction $c[\eta]$, also known as the Huggins equation. The reduced viscosities of the dilution series are then fitted with a linear dependancy from the concentration c to determine $[\eta]$:

$$\eta_{red} = \frac{\eta_{sp}}{c} = [\eta] + K_H [\eta]^2 \, c. \tag{3.16}$$

In this equation, the second term captures interactions between single polymer coils in a non-ideal solution using the Huggins constant K_H, which is constant for a given polymer-solvent system [120]. We have selected 6 solutions with a relative viscosity η_r between 1.2 and 2.5 to guarantee an exact analysis. The data points below the critical value $\eta_r = 1.2$ can deviate from the linear fit, because measurement errors are amplified in the calculation of the reduced viscosity [120]. Dilutions with a relative viscosity above the upper critical limit might not satisfy the linear relationship of Eq. 3.16 due to increasing intermolecular interactions.

3.2.4 Other methods

Shear rheometry

Shear rheological measurements on the suspensions are performed with a strain controlled rheometer (ARES-G2, TA Instruments) equipped with a double wall Couette geometry. This geometry is less sensitive to sedimentation of the particles than a parallel disk system, where the top plate would rotate in pure medium fluid with even minor settling. The gap of the double wall Couette measures 1.7 mm, which is significantly larger than the maximum particle diameter.

Because the viscosity of the polymer solutions is near the lower detection limit of the rotational rheometer, we have determined the viscosity of these samples with the more sensitive Ubbelohde viscometer, that was introduced in the previous section.

Surface tension measurements

The surface tension γ is measured with a platinum Wilhelmy plate with a wetted length of 20 mm that is attached to an electrobalance (KSV Nina). The measurement is repeated three times and the average value is taken.

Chapter 4

Capillary breakup with high resolution imaging

Prior to discussing the experimental results, we introduce some modifications to the capillary breakup setup that are made during this work. The free-surface flows are consistently recorded with high-speed photography and improvements were made to the image resolution as well as to the post-processing of these images. Section 4.1 discusses the tube lens that was specifically built for the CaBER setup. This lens was also employed during some jetting experiments requiring a higher spacial resolution. Section 4.2 introduces the different image processing routines that are used extract information from the images. The code to process the images of a static capillary breakup experiment is illustrated in Section 4.2.3 where the software is applied to a set of tests that were performed on the Cambridge Trimaster.

4.1 Lens systems

The Capillary Breakup Extensional Rheometer (CaBER) that was introduced in Section 3.2.1, is designed to function as a stand-alone setup. After a fast stretching step, the mid-point radius of an unstable filament is followed with laser micrometer. By carefully selecting the final stretch distance, the extensional flow properties of model viscous samples with a viscosity $\eta > 70$ mPa.s can be determined using the laser micrometer as well as relaxation times $\lambda > 1$ ms for elastic liquids [111].

However, in many fluids, the minimal filament radius is not found at the mid-point between the two end droplets. This is observed for instance in low viscous liquids [76, 95, 111] and in several two-phase systems such as emulsions and suspensions [102, 103]. A single point measurement is thus insufficient to determine the minimal filament radius of these fluids and the entire filament is recorded with a high-speed camera to follow the pinch-off dynamics.

Additionally, high resolution imaging of the filament can provide improved or complementary information on the breakup behaviour. For very low viscous liquids, high curvature effects will dominate the initial thinning process. The slender filament approximation, which is used in all theoretical predictions of capillary thinning, is not valid for these curved filaments. Hence, material parameters like viscosity or relaxation time can only be extracted at the later thinning stages [95]. At this point, the filament is very thin so reliable data is only obtained with a high resolution lenses. High resolution imaging has furthermore been used to distinguish individual micron-sized particles in a sample and to track their positions under extensional flow [124].

Since we are interested in phenomena close to breakup within this study, the lens system of our CaBER setup must have an adequate resolution. This is especially important for the experiments on non-colloidal suspensions, which are described in Chapter 6, where we want to visualise the flow of individual particles during the breakup process. In order to fulfil this resolution requirement, the high-speed camera is coupled with a microscopic objective (Olympus, Japan).

4.1.1 Microscopic lenses and infinity optics

As we are using a high resolution lens, it is crucial to understand the concept of optical resolution. The resolution of a lens is defined as the minimum distance between two objects that can still be distinguished as two separate entities. The ability of a lens to resolve detail is not only determined by the quality of the lens, but it essentially limited by diffraction. Light coming from a point in the object diffracts through the circular lens aperture and appears as a diffraction pattern in the image. This pattern is known as an Airy pattern (see Figure 4.1a) and consists of a central bright spot -the Airy disk - and surrounding bright rings separated by dark zones. The Airy disk contains 84 percent of the luminous energy and is perceived as the image point. Based on the knowledge of this diffraction pattern, different standards have been developed to determine whether or not points can be distinguished (see Figure 4.1b and 4.1c). The

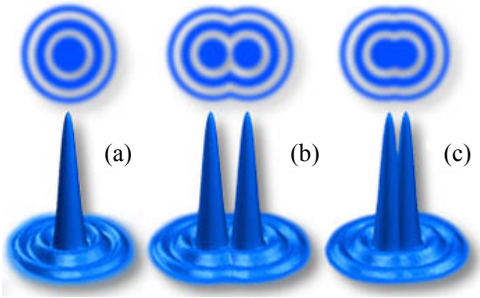

Figure 4.1: Illustration of the Airy disk with the intensity distribution: (a) a single Airy pattern, (b) two disks that are just far enough to be resolved and (c) two disks that are not individually resolvable by the Rayleigh criterion.

most common standard is the Rayleigh criterion that specifies that two points are discernible if the Airy disk of the first point overlaps with the first dark ring of the second point. This criterion gives the following expression for the resolution of a lens:

$$r_{lens} = \frac{0.61\lambda_w}{\mathrm{NA}}, \tag{4.1}$$

where λ_w is the wavelength of the light and NA is the numerical aperture of the lens. The numerical aperture is a measure for the ability of the lens to gather light and describes the acceptance cone of an objective. It is defined by

$$\mathrm{NA} = n \sin \alpha \tag{4.2}$$

where n is the refractive index of the medium in which the lens is operated and α is the half-angle of the maximum cone of light that can enter or exit the lens. It can be seen that a larger numerical aperture corresponds to a larger aperture which decreases the size of the Airy disk according to Fraunhofer diffraction theory [125]. It is important to remark that resolution should not be confused with magnification. Increasing the magnification without changing the resolution results in empty magnification without further detail. Since the numerical aperture of microscopic objectives is considerably higher than other (zoom) lenses with the same magnification, their resolution is superior.

Nearly all microscopic objectives that are currently sold are from the infinity-corrected type. As their name suggests, these objectives direct light into parallel

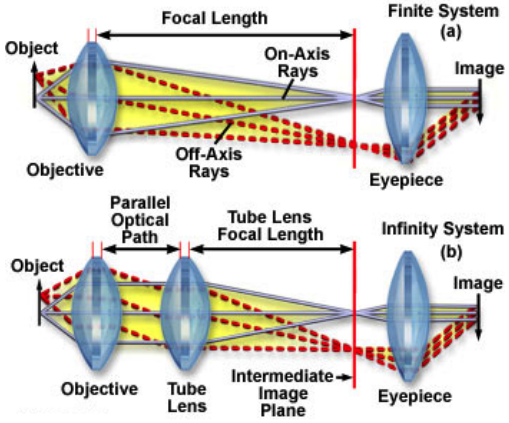

Figure 4.2: Comparison of the light path of (a) a standard and (b) an infinity-corrected microscopic objective [126].

rays focused at infinity. An infinity-corrected system focuses light rays exiting the objective to the real image plane with the help of a secondary tube lens (see Figure 4.2b), this in contrary to a classic finite system (see Figure 4.2a), where no second lens is required to form a intermediate image near the back focal point of the objective lens. Infinity-corrected lenses offer two advantages: longer working distances and the ability to add in-line components (e.g. filters, beamsplitters, etc.) to the system. The parallel optical path between the two lenses ensures no additional aberrations will be generated when supplementary components are added to the path.

The term infinity optics does not imply that the tube lens can be positioned at an infinite distance from the objective lens. Figure 4.2b shows that light from an object on the optical axis moves parallel to this axis along the optical path after passing the objective lens. On the other hand, light coming from the periphery of the object forms a flux of parallel rays which advances at a diagonal angle to the optical axis. Because of this, there is a maximum distance between the two lenses: if the distance would be too large, there will be rays of light that cannot be captured by the tube lens. This causes the image around the edges of the field of view to become dark or blurred, preventing the microscope to perform at its full potential. Although this technique is used by all major microscope manufacturers, there are some subtle differences between their systems. For instance, Nikon and Olympus systems correct for aberrations in their objective

Figure 4.3: Design of the tube lens.

lenses, whereas the correction in Zeiss and Leica systems occurs in the tube lens. Since the light rays are not one hundred percent parallel to the optical axis after the objective, each manufacturer has a different tube lens (see Table 4.1), which is optimised for their objectives.

Manufacturer	Tube lens focal length (mm)
Olympus	180
Nikon	200
Zeiss	164.5
Leica	200

Table 4.1: Common infinity-corrected tube lengths.

4.1.2 Tube lens design

Since our lab has a collection of Olympus microscopic objectives, we have chosen to design a lens that mimics the tube lens inside an Olympus microscope. Figure 4.3 shows an illustration of the lens design. The key component is a bi-convex lens with a focal length of 175 mm, which roughly equals the standard focal length of an Olympus tube lens (see Table 4.1). This lens is placed in a lens tube with zoom housing that provides 4 mm of linear travel for the lens with high precision (0.5 mm per revolution), which is used for fine tuning of the lens position. The microscopic objective is positioned at a distance of 50 mm from the bi-convex lens. Although the design has been tested for 5x, 10x, 20x and 50x objectives, only the two objectives with the lowest magnification are useful for CaBER experiments. A higher magnification lens has a smaller depth of field, making it more difficult to obtain sharp images of the thinning filament. The resolution of the different objectives is listed in Table 4.2. The design

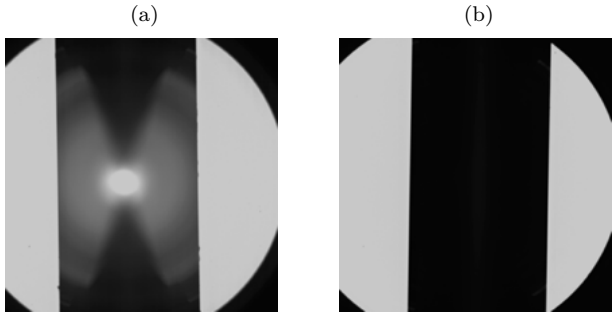

Figure 4.4: Image of a calibration cylinder ($R = 1$ mm) with a 5x objective mounted on (a) an earlier tube lens design without diaphragms and (b) the current tube lens.

can be slightly altered to include a special objective lens turret, allowing the attachment of four different microscopic objectives to the tube lens. However, the lens turret hinders positioning the tube lens near the CaBER, because of space limitations caused by the side covers of the instrument. Contrary to a regular microscope, the objectives are not perfectly parfocal in our design. The focal plane can shift up to 150 μm by switching objectives, which is more than 3 times larger than the depth of field of the 10x objective.

Magnification	r_{lens} (μm)
5x	6
10x	3
20x	2

Table 4.2: Resolution of the different objectives in combination with the tube lens.

On the other side of the zoom housing, a tube system is placed to position the camera sensor at the focal length of the bi-convex lens. Two diaphragms are added to the design to better guide the light inside the tube. The former is positioned near the camera and the latter is placed near the lens. The importance of these diaphragms is illustrated in Figure 4.4, where two images of a metal calibration cylinder are shown. The first picture is taken with the initial version of the tube lens without diaphragms. The image is distorted due to internal reflections of the light in the tubing, causing the appearance of two

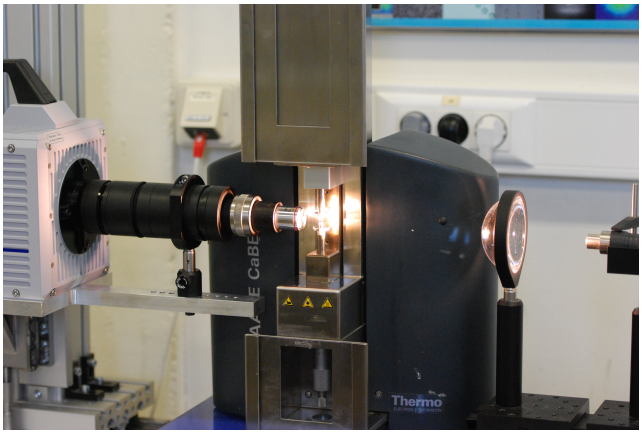

Figure 4.5: The new Caber setup with the high-speed camera equipped with the tube lens and microscopic objective.

triangles and concentric circles within the image of the cylinder. In contrast, the second picture is taken with the current design and displays none of the former distortions.

High-speed imaging moreover requires sufficient light intensity. The maximal shutter time of the camera is given by the inverse of the frame rate. Due to the fast flow phenomena near breakup, shutter times are often considerably lower than this maximum value, typically between 8 and 30 μs. Light is provided by a 150 W quartz halogen light source (Fiber-Lite DC-950, Dolan Jenner, Boxborough, USA) with an intensity control knob and is guided towards the instrument through a flexible fiber optic cable. The light exiting the cable is focused with a condenser lens to provide sufficient light intensity. Figure 4.5 shows the optical setup around the CaBER, with the tube lens mounted on the high-speed camera on the left side and the fiber-optic illumination on the right side. To prevent the tube lens from bending under its own weight, a support system with a tube slip ring is included. This slip ring is attached to a bottom plate which also supports the camera. The plate is connected to a Newport linear stage allowing accurate positioning of the camera. Additional information on the design is given in Appendix D including a technical drawing and a components list.

4.2 Image processing software

The free-surface flow experiments that are performed in this study are recorded with high-speed imaging. The next step is the extraction of relevant information from these images. When this surface tension-driven thinning of a fluid filament is used as a rheological measurement, the determination of the minimal filament radius R_m is required to extract quantitative material information (see Sections 2.2 and 3.2.1). Consequently, it is necessary to accurately determine the edges of the filament to locate this origin of the draining flow. To this end, a set of image processing routines was written in Matlab to obtain the evolution of the minimal radius $R_m(t)$ during static capillary breakup and jetting experiments. Before discussing these specific routines, we start with a basic introduction on edge detection, explaining some important concepts that are encountered in the code.

4.2.1 Edge Detection

Throughout this work we have generated a large amount of 8-bit grayscale images with the high-speed camera setup. Each pixel of these images only carries intensity information, resulting in 256 shades of grey varying from black at the weakest intensity to white at the strongest. Edge detection is an image segmentation technique that is based on the discontinuity of the intensity values. Edge pixels are thus pixels where the intensity value suddenly changes and edges are sets of connected edge pixels. The transition between two intensity levels ideally occurs over the distance of one pixel. However, that kind of intensity step profile is only found in computer-generated animation. In reality, digital images contain noisy and blurred edges. The noise level is principally determined by the electronic components of the camera (e.g. the CMOS sensor) and the degree of blurring is dictated by the focussing mechanism and the resolution of the employed lens system. Real edges are more appropriately represented by an intensity ramp profile, where the slope of the ramp is inversely proportional to the degree of blurring in the edge.

The first column of Figure 4.6 shows a segment of an ideal vertical edge with a horizontal intensity ramp profile. The third and fourth row of figure also show the first and second order derivative. Moving from left to right along the intensity profile, the first order derivative becomes positive at the onset of the ramp, stays positive at the ramp points and returns to zero in the white constant intensity zone. The magnitude of the first order derivative is thus a

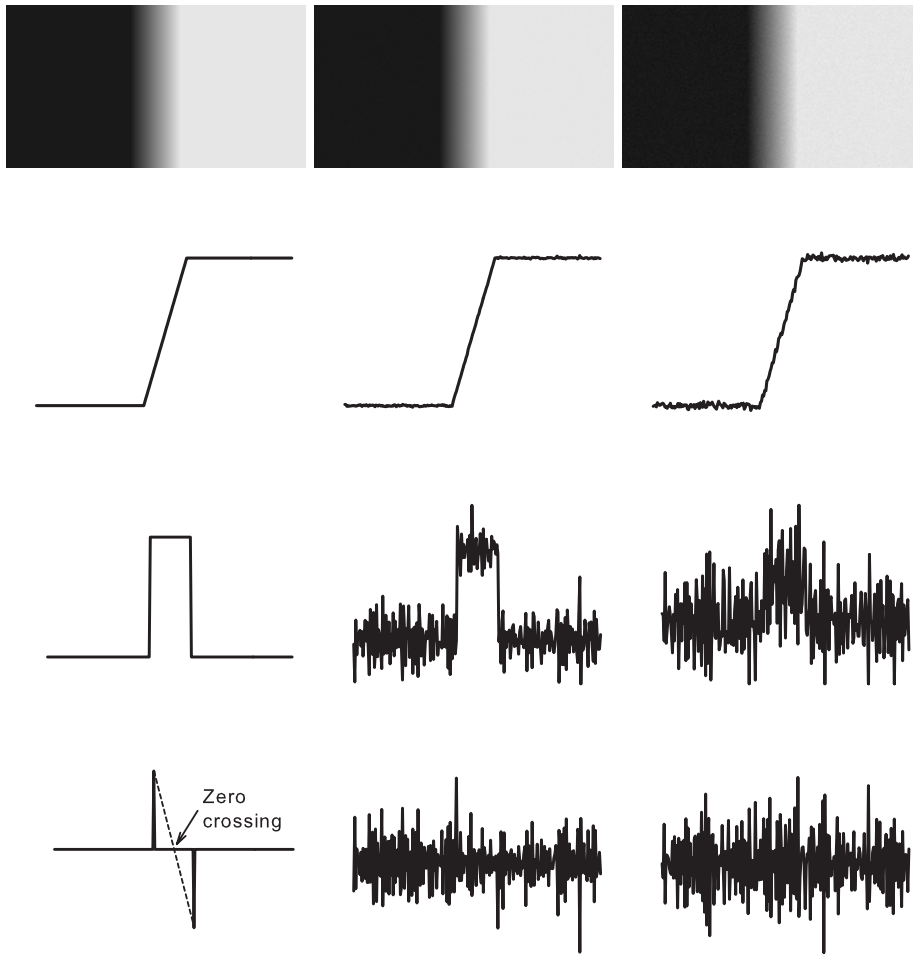

Figure 4.6: Detail of an ideal vertical edge is shown in the first column. The intensity profile and the first and second order derivative of the intensity profile are shown on the second, third and forth row respectively. The second and third column depict the same edge that are corrupted with additive Gaussian noise with zero mean and a standard deviation of 10^{-4} and 10^{-5}.

measure for the abruptness of the intensity level change and can be used to detect the presence of an edge at an image point. The second order derivative is zero for the entire profile except for a positive peak at the onset of ramp and a negative peak at the end of the ramp. The sign of the second order derivative marks whether an edge pixel lies on the light or dark side of the edge. The intersection between a line connecting the two extrema of the second order derivative and the zero intensity axis indicates a point called the zero crossing of the second order derivative. These zero crossings can be used to locate the centres of thick edges, as shown later in this section.

As previously mentioned, real images are unlike the ideal edge of in the first column of Figure 4.6 not free of background noise. The images in in the second and third column of Figure 4.6 are corrupted with additive Gaussian noise with zero mean and a standard deviation of 10^{-4} and 10^{-5}. The horizontal intensity profile passing through the centre of the image is shown for each image together with the first and second order derivative. Differentiating is a numerically unstable process and is very sensitive to high frequency noise. By adding noise to the image, the first order derivatives become increasingly different from the noiseless case. The original step profile is even barely noticeable for the image with the highest noise. The second order derivative is naturally even more susceptible to noise. The original peaks are completely overshadowed by the enlarged high frequency noise. This is even the case for the image with the lowest noise level, where the noise is hardly visible in the image and the intensity profile. Since the distinct positive and negative peak components are crucial features for edge detection based on the second order derivative, these profiles are impossible to process directly.

Because the images that are obtained with the high-speed camera comprise similar noise levels to those shown in Figure 4.6, image smoothing should be considered prior to using of derivatives for edge detection. Image smoothing is accomplished by filtering in frequency domain with a lowpass filter. This filter type modifies the Fourier transform of the image by weakening high frequencies while passing low frequencies. The inverse Fourier transform renders a filtered image where edges are blurred and the background noise is attenuated. The most common lowpass filter to realise this smoothing is a Gaussian lowpass filter, which is given in two dimensions by

$$G(x, y) = e^{-\frac{x^2+y^2}{2\sigma^2}} \tag{4.3}$$

This filter reduces the intensity of structure at scales smaller than the Gaussian standard deviation σ. It is crucial to use the appropriate value for σ because a

too small σ does not sufficiently remove the background noise, whereas a very high value blurs the edges so much that the edge location is slightly shifted.

As illustrated in Figure 4.6, edges can be located by detecting intensity changes with first or second order derivatives. The use of second order derivatives will be discussed in Section 4.2.2. First order derivatives can quantify the edge strength and direction at a location (x, y) of an image f using the gradient vector ∇f:

$$\nabla f \equiv \begin{bmatrix} g_x \\ g_y \end{bmatrix} = \begin{bmatrix} \partial f/\partial x \\ \partial f/\partial y \end{bmatrix}. \tag{4.4}$$

This gradient vector has the important geometrical property that it is oriented in the direction of the greatest rate of change of f at location (x, y). The edge is thus locally perpendicular to gradient direction $\alpha(x, y)$, which is measured as

$$\alpha(x, y) = \arctan\left(\frac{g_y}{g_x}\right) \tag{4.5}$$

with respect to the x-axis. The edge strength is expressed with the magnitude of ∇f

$$M(x, y) = \sqrt{g_x^2 + g_y^2}, \tag{4.6}$$

which is the value of the rate of change in the direction of the gradient vector. The gradients are generally calculated using gradient masks, which are digital approximations of the partial derivatives in the neighbourhood of a point. Prewitt and Sobel operators are typical examples of such masks. When the possible edge points are located, the final operation is selecting the stronger edges. A common approach to achieve this objective is thresholding the gradient image. Edge points are only chosen when the edge strength $M(x, y)$ is sufficiently large. Combining thresholding with image smoothing will reduce the number of broken edges.

In conclusion, three fundamental steps are performed in edge detection [127].

1. Image smoothing for noise reduction, usually with a lowpass filter.
2. Detection of edge points: local operation that extracts all points from an image that are potential candidates to become edge points.

3. Edge localisation: eliminate false edge points and select only the points that are true members of the set of points comprising the edge.

In the following sections, two different techniques will be introduced that follow these steps to determine the edges of capillary breakup filaments and the contours of a liquid jet.

4.2.2 Minimal diameter detection in CaBER filaments

A more sophisticated technique using the second order derivative is employed to determine the profile edges of the thinning filament during a CaBER experiment. The processing routines are based on the Marr-Hildreth edge detector [128] that localises edge points with a Laplacian of Gaussian filter $\nabla^2 G$. The expression for the Laplacian of Gaussian (LoG) is found by performing the following differentiations:

$$\nabla^2 G(x,y) = \frac{\partial^2 G(x,y)}{\partial x^2} + \frac{\partial^2 G(x,y)}{\partial y^2} \tag{4.7}$$

$$= \left(\frac{x^2 + y^2 - 2\sigma^2}{\sigma^4} \right) e^{-\frac{x^2+y^2}{2\sigma^2}}. \tag{4.8}$$

The Marr-Hildreth algorithm consists of convolving the LoG filter with an input image $f(x,y)$ and then locating the zero crossings of $g(x,y)$ to determine the edge points. The convolution operation can be rewritten as

$$g(x,y) = \left[\nabla^2 G(x,y)\right] * f(x,y) \tag{4.9}$$

$$= \nabla^2 \left[G(x,y) * f(x,y)\right]. \tag{4.10}$$

This expression indicates that the filter meets two essential requirements for an edge detector. First, the image is blurred with the Gaussian filter, hereby reducing the background noise. The size of the Gaussian filter can be adjusted to the desired scale by choosing an appropriate standard deviation σ. Large values are required to process blurry edges, whereas small values suffice for sharp focussed edges. The size of the filter is chosen such that it is slightly larger than 6σ, as 99.7% of the volume under a 2D Gaussian surface lies between $\pm 3\sigma$

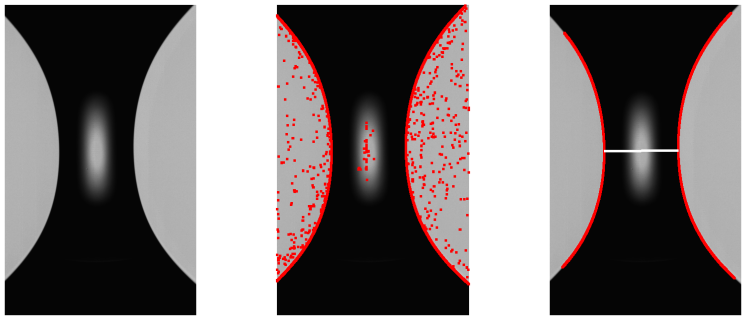

(a) (b) (c)

Figure 4.7: Example of the image processing for CaBER filaments with (a) the original picture, (b) the edge points detected with an LoG filter with $\sigma = 1$ and (c) the selected points with connectivity labelling and the location of the minimal diameter.

around the mean. The Laplacian subsequently calculates the second derivative of this corrected image to detect the edge points. The Laplacian has the additional advantage of being isotropic, so it responds equally to intensity changes in any direction and thereby avoids the use of multiple masks to determine the strongest response at every image point [127].

This method was chosen for processing the CaBER images owing to its high accuracy in finding the zero-crossing locations [129]. Hence, the edge points can be located with sub-pixel accuracy with this technique. A similar technique was employed by Crocker and Grier [130] to obtain sub-pixel locations of colloidal particles with digital microscopy. In the final step of the algorithm the filament edge points are selected by utilising connectivity labelling to find the longest edge in the image. Figure 4.7 illustrates the edge detection of a typical filament that was captured during a capillary breakup experiment. As a result of the low value of σ, the LoG filter detects a large number of edge points, including a large amount of false ones in the background. These false edge points are however eliminated in the final step and the correct filament edges are recovered in Figure 4.7c. The edges are used to determine the filament profile $R(z)$ - that is for instance essential to calculate the curvature of the filament - and to establish the minimal filament radius R_m with sub-pixel accuracy.

The determination of the minimal radius in consecutive images is required to

process CaBER experiments. To this end, a commercially available program was written in Matlab that we have named Edgehog. The user interface of the software is depicted in Figure 4.8. As discussed in Section 3.2.1 , the temporal evolution of the minimal radius $R_m(t)$ is used to deduce other experimental parameters. For the calculation of strain rate $\dot{\epsilon}$ and the apparent extensional viscosity $\eta_{E,app}$ with Eqs. 3.5 and 3.6, numerical differentiation of the minimal radius is required. Since this operation is highly susceptible to noise, the filament diameter data is smoothed with a Savitzky-Golay filter. This technique has been preferred to a weighted adjacent averaging as it tends to better preserve features of the data [131]. Furthermore, the software allows fitting of the minimal radius with two models, one for viscous (Eq. 2.29) and one for viscoelastic samples (Eq. 2.33), to respectively extract the viscosity η and the dominant relaxation time λ.

4.2.3 Case: Cambridge Trimaster

As an illustration of the image processing code, a set of capillary breakup experiments are processed that were performed by Damien Vadillo at Cambridge University [132]. Four solutions of monodisperse polystyrene (PS) with different molecular weights in diethyl phthalate (DEP) are examined. The polymer concentration is varied to obtain approximately the same Ohnesorge number (Eq. 2.10) for all samples. As a consequence, differences observed on the experimental filament thinning profiles are directly associated with the non-linear response of the polymer chains. The fluid properties are shown in Table 4.3, where the critical overlap concentration c^* indicates that all samples are in the dilute region.

	M_w (kg/mol)	c^* $(wt\%)$	c $(wt\%)$	Oh $(-)$	λ (μs)
PS110	110	3.74	0.5	0.079	197
PS210	210	2.80	0.4	0.079	92
PS306	306	2.49	0.2	0.074	≈ 30
PS488	488	1.53	0.1	0.070	83

Table 4.3: Characteristics of the PS solutions in DEP.

Capillary breakup experiments on these fluids were performed with the Cambridge Trimaster [133]. This apparatus is similar to the CaBER, but the fluid is symmetrically stretched at a higher velocity of 150 mm/s to reduce the stretching time and prevent breakup during the stretching step. The overall

(a)

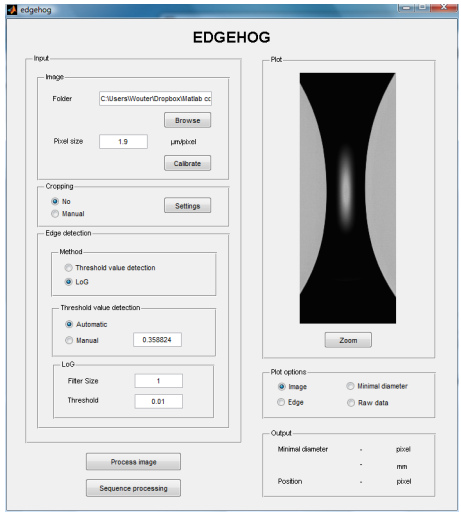

(b)

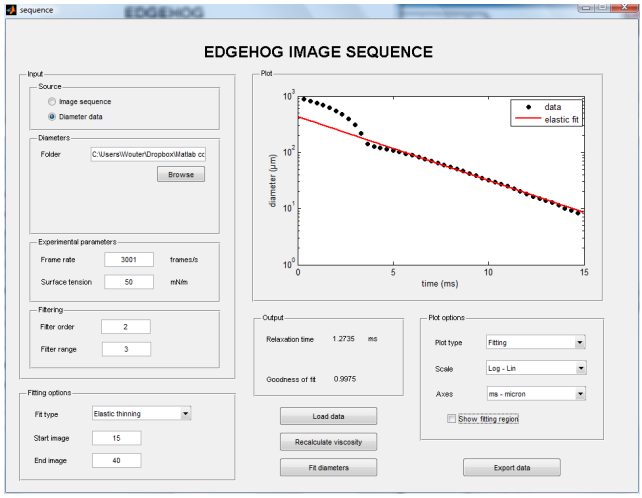

Figure 4.8: Image of the user interface of the Edgehog software with (a) the processing window of a single filament image and (b) the processing window for an image sequence.

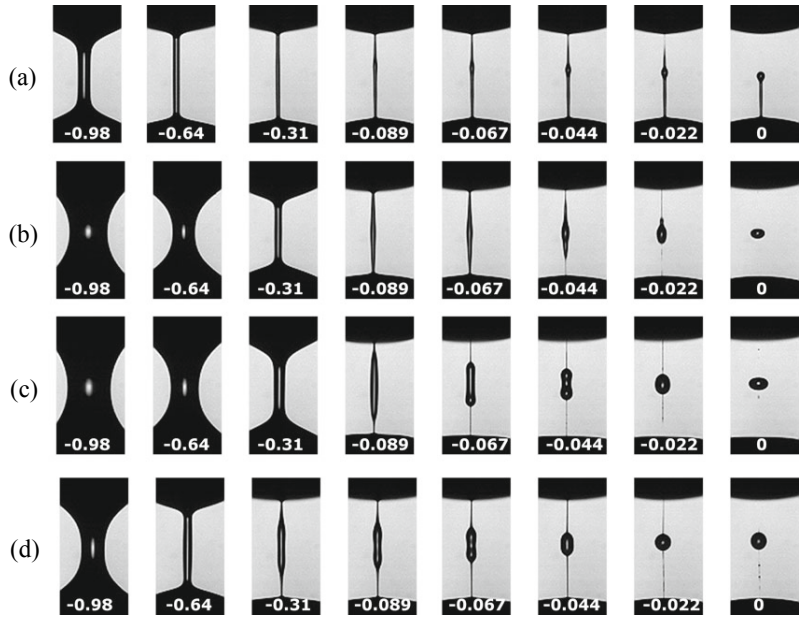

Figure 4.9: Images from the last instances of the capillary breakup of different solutions of PS in DEP: (a) 0.5 wt% PS110, (b) 0.4 wt% PS210, (c) 0.2 wt% PS306 and (d) 0.1 wt% PS488. The number in the bottom of the images indicates the time to pinch-off $t_p - t$ in ms.

breakup time for all samples was approximately 9.5 ms, which is longer than the stretching time of 5.3 ms. The fluid is loaded between two cylindrical pistons with a radius $R_0 = 0.6$ mm and it is stretched from an initial distance $L_0 = 0.6$ mm to a final distance $L_1 = 1.4$ mm. The evolution the filament is recorded with a high-speed camera (Photron Fastcam 1024 PCI) at 45 000 frames per second with a spatial resolution of 5.6 μm/pixel.

Figure 4.9 shows the capillary-driven thinning and breakup of the different fluids. The filaments display a non-uniform shape near pinch-off, where the filament at the top and bottom ends thins faster than in the middle, resulting in the formation of a single central droplet. This shape is characteristic for inertia-controlled breakup, which is in agreement with the small Ohnesorge number of the solutions. The necking points evolve in long slender threads connecting the central droplet to the top and bottom drop. This observation suggests that elastic stresses originating from the stretched polymer molecules

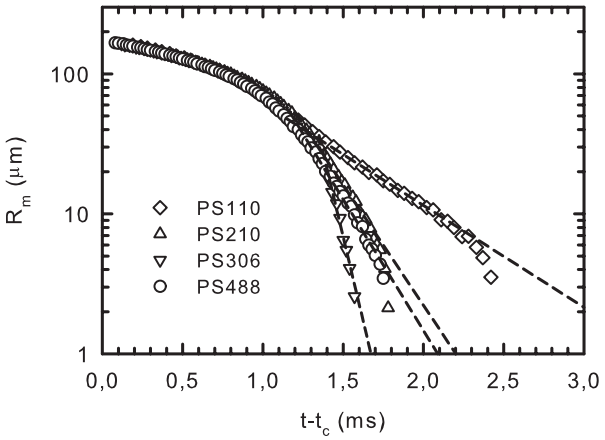

Figure 4.10: Evolution of the minimal filament radius as a function of time. The dashed lines represent fits of the elasto-capillary balance with Eq. 2.33.

have become sufficiently large to resist the diverging capillary pressure. However, the relaxation time of the fluid must be very small because the elastic stresses are unable to create a uniform cylindrical filament [133]. This breakup behaviour where a central droplet is accompanied with a short living tail indicates that these fluids are desirable for inkjet printing, because the limited amount of elasticity tends to suppress the formation of unwanted satellite droplets [9, 133, 134].

The minimal filament radii $R_m(t)$ are acquired from the high-speed image series with the Edgehog image processing software. Figure 4.10 exhibits the extracted radii that are shifted along the time axis with a reference time t_c to show that the data points of the different samples overlap during the inertia-controlled thinning until $R_m \approx 35$ μm. This regime is followed by an elasto-capillary balance where the radius decreases exponentially in time. The characteristic relaxation times λ are obtained by fitting this exponential regime with Eq. 2.33 and the extracted values are listed in Table 4.3. The relaxation time of the PS306 solution has a large uncertainty, because only 6 frames were used to fit the exponential decay. Nevertheless, the relaxation times of the PS210 and PS488 solutions are $O(100\ \mu\text{s})$, making them the lowest values that have been reliably obtained in capillary breakup experiments. Moreover, these values are only slightly higher than the lowest relaxation times reported in uniaxial extensional flows, which were measured with jetting rheometers [135, 136].

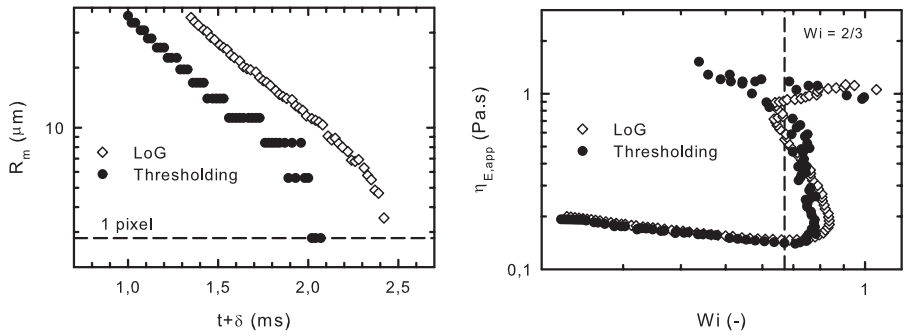

(a) minimal radius (b) apparent extensional viscosity

Figure 4.11: Comparison of (a) the filament minimal radius and (b) the apparent extensional viscosity retrieved from the images of the PS110 solution with the LoG filter and with thresholding.

The accurate detection of the relaxation is made possible by processing the images with the LoG filter. Despite the limited spatial resolution of the camera setup at Cambridge University, reasonably smooth radius data is obtained due to the sub-pixel localisation of the edges. Figure 4.11a compares two methods of extracting the minimal filament radius during the capillary breakup of the PS110 solution. The first data series is obtained with the LoG filter and these radii were already presented in Figure 4.10. The second method converts each image into a binary image, based on an intensity level threshold, before determining the minimal radius. This data set is horizontally shifted with a factor $\delta = 0.4$ in Figure 4.11a for a better comparison between the graphs. Since each radius consists of a discrete number of pixels, this method generates a step function for $R_m(t)$, which is clearly visible for the data near pinch-off. Similar step functions are frequently encountered as a description of the thinning dynamics of dilute polymer solutions during capillary breakup [95, 111, 137, 138]. However, it is challenging to extract reliable small relaxation times $\lambda = O(1 \text{ ms})$ from these measurements. Considering that the elasto-capillary balance only manifests at small radii for fluids with limited elasticity, the relaxation time is retrieved by fitting an exponential decay through a pronounced step function, inducing significant uncertainties on the extracted parameter. On the contrary, small relaxation times are determined with more accuracy from the smooth curves that are acquired with the sub-pixel edge detection of the LoG filter.

Additionally, the calculation of the apparent extensional viscosity is more

straightforward starting from smooth evolution of the radius. The required numerical differentiation of $R_m(t)$ (see Eq. 3.6) is very sensitive to noise, so the use of discrete values induces more errors. This effect is illustrated in Figure 4.11b where the apparent extensional viscosity $\eta_{E,app}$ is plotted as a function of the dimensionless Weissenberg number $Wi = \lambda\dot{\epsilon}$. The elastic stresses generate a strong increase in the apparent extensional viscosity during the elasto-capilary balance, which is revealed by a constant Weissenberg number $Wi = 2/3$. Both extensional viscosity and strain rate are calculated using a Savitzky-Golay filter of second order polynomial and a fitting window of 15 points. Despite the application of this smoothing filter, the extensional viscosities $\eta_{E,app}$ that are derived from the radii determined with simple thresholding, are clearly scattered in the strain hardening region.

4.2.4 Jet radius detector

Different image processing routines are required to extract the evolution of the radius from the images of the jetting flow. Contrary to the single static liquid bridge geometry that is studied in the CaBER, a jet contains a series of Rayleigh instabilities that each thin and eventually break up to form a stream of droplets. The analysis is further complicated by the fact that the position of these minima changes in time as the instability is translated along the jet, as illustrated in Figure 4.12a. Additionally, the shape of the jet does not allow reusing the edge detection code for CaBER filaments, introduced in Section 4.2.2. This code is specifically written to detect vertical edges and it frequently overlooks edge points when the edge approaches an angle of 45°. This inability to locate tilted edges can be viewed in Figure 4.7c where the top and bottom edge of the filament is not completely captured. As a result, the former code is incapable of precisely describing the jet edges in the late stages of thinning, where the connection of the thin filament and the drop generally exhibits edges with angles well above 45° (see Figure 5.1).

Accordingly, the edges of the jet are localised with the robust Canny edge detector [119]. This detector has a more complex algorithm, but its performance is superior to the previously discussed methods. In summary, the Canny algorithm consists of the following four basic steps.

1. Smooth the input image with a Gaussian filter.
2. Compute the angle image $\alpha(x, y)$ and gradient magnitude image $M(x, y)$ (see Eqs. 4.5 and 4.6).

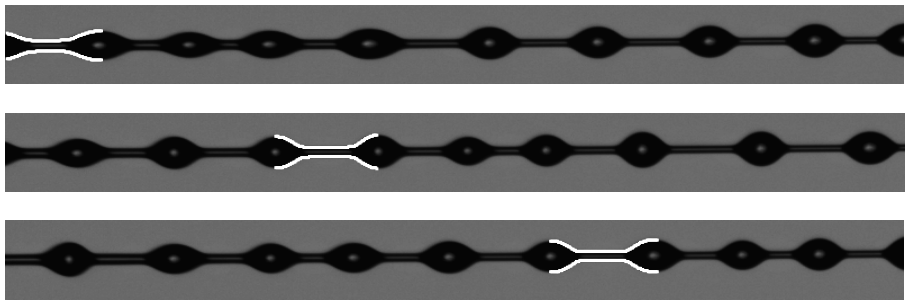

(a)

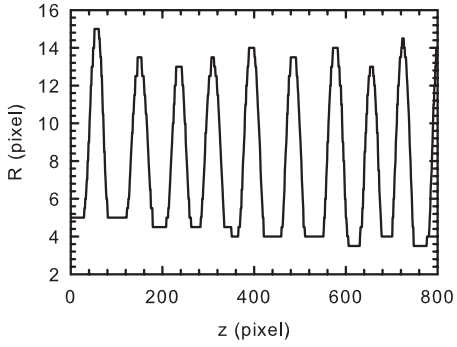

(b)

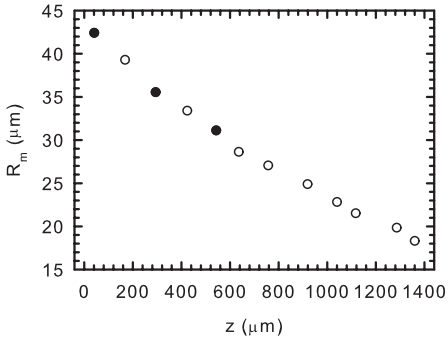

(c)

Figure 4.12: Detection of the jet radius. (a) Images of a viscoelastic jet at $We = 25$ with a time difference of 0.6 ms where the evolution of a single instability is highlighted. (b) Local radius of the jet of the third image as a function of the axial position. (c) The minimal radius R_m of the single instability is followed in consecutive images and shown as a function of the axial position. The filled symbols correspond to the images.

3. Apply non-maxima suppression to the gradient magnitude image.
4. Use double thresholding and connectivity analysis to detect and link the edges.

The first two steps have been discussed in Section 4.2.1. In the third step, the wide ridges that are typically encountered around local maxima in the gradient magnitude image, are thinned using non-maxima suppression based on the local orientation of the edge, which is given by $\alpha(x, y)$. The final operation reduces the false edge points by hysteresis thresholding, which uses two threshold values with a ratio of the high to low threshold of 3:1. The edge points that are found with the high threshold are considered 'strong' edge pixels, whereas the additional edge points detected with the low threshold are viewed as 'weak' edge pixels. After the thresholding operations, all strong pixels are assumed to be valid edge points. Longer edges are created by filling the gaps in these strong edges with some of the weak edge pixels using connectivity analysis. A more detailed explanation of Canny detector is found in the book by Gonzalez and Woods [127].

Figure 4.12b shows the local radius of the jet of the third image in Figure 4.12a, which was determined with the Canny detector, as a function of the axial position. The sequence of instabilities and droplets is captured in the graph and generally, the minimal radius of the instability R_m gets lower as the jet moves further away from the nozzle. Unlike the Marr-Hilldreth detector, the Canny detector is unable to determine the position of the edges with sub-pixel accuracy. Hence, a more accurate value of R_m is determined for each minimum using a LoG filter with a standard deviation of 1.0. To process the jetting experiments, we follow the dynamics of a single instability in consecutive frames. The temporal evolution of the instability, expressed with $R_m(t)$, is then used to acquire extensional rheological information of the fluid. Since the jet velocity is known, the minimal radii in the subsequent images are linked based on their location. Figure 4.12c shows the decrease of minimal radius R_m of the single instability in consecutive images and shown as a function of the axial position. The filled symbols correspond to the instabilities that are accentuated in the images of Figure 4.12a.

4.3 Conclusion

In this chapter, we have discussed some important modifications to the experimental setup that is used to study free-surface flows in the following

chapters. First, a new tube lens is introduced that allows the use of microscopic objectives to visualise the filament breakup during a CaBER experiment. In combination with an improved illumination path, this lens system significantly enhances the spatial and temporal resolution of the setup.

The second part of the chapter considers several image processing routines that are employed to extract the minimal filament radius R_m from the breakup images. A modified version of the Marr-Hildreth edge detector is introduced that locates the filament edge with sub-pixel accuracy. This detector is incorporated into the Matlab-based Edgehog software that automatically processes images of a CaBER experiment and calculates the extensional flow parameters. The strength of the processing code is illustrated with a series of capillary breakup experiments on model inkjet printing fluids. We are able to reliably determine relaxation times $\lambda = O(100\ \mu\text{s})$, which are the lowest values obtained in similar experiments. Furthermore, the procedure to follow a single Rayleigh instability during a jetting experiment is explained in the final section.

Chapter 5

Breakup of weak viscoelastic jets

As a first model system, we study the capillary breakup of dilute aqueous solutions of high molecular weight polymers. The presence of macromolecules introduces some elasticity to the fluid, which dramatically changes the droplet formation. Generally, the pinching of these fluids is examined with static capillary breakup experiments, but we will also study the flow of a continuous jet and show some remarkable differences between these two free-surface flows. Moreover, we will assess the use of jetting flow as a rheological technique to detect very low relaxation times.

5.1 Introduction

When a liquid is sent through a nozzle at sufficiently high velocity, a liquid jet is formed that spontaneously disintegrated into a series of small droplets under the influence of surface tension. Sinusoidal instabilities emerge on the jet surface and progressively thin as the jet flows downstream. Adding a small amount of flexible polymers to the liquid stabilises the jet and significantly delays breakup. As the local radius of the instabilities decreases, elastic stresses rapidly grow and the jet consists of a series of small droplets joined by small threads, that become increasingly thinner with distance [68]. This typical 'beads-on-a-string' morphology is displayed in Figure 5.1 for an aqueous polyethylene oxide (PEO) solution. Since such viscoelastic behaviour is very useful to

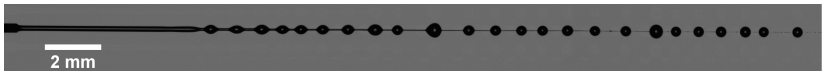

Figure 5.1: Example of a jet of 0.1 wt% PEO solution from a nozzle with an inner radius $R_n = 75$ μm at $We = 4.0$. Breakup occurs at a distance of approximately 30 mm from the nozzle.

inhibit misting and suppress the formation of unwanted satellite droplet, high-molecular weight polymers are often used as additives in spraying and printing operations [4, 15, 16, 133].

Throughout the jetting process, the fluid is subjected to a complex extensional deformation with rapidly varying strain rates. The breakup dynamics depend on the magnitude of the inertial, viscous and elastic stresses, which can all act to resist the capillary pressure within the filament. As discussed in Section 2.2.2, the relative importance of these resisting stress is described using two dimensionless numbers [3–5]. The Ohnesorge number $Oh = \eta/\sqrt{\rho\gamma R}$ compares the viscous and the inertial effects and the Deborah number $De = \lambda\sqrt{\gamma/\rho R^3}$ is the ratio of the characteristic elastic relaxation time λ of the fluid and the inertia-capillary Rayleigh time of an inviscid jet. In these expressions, R represents the radius of the jet.

Within this chapter, we study weak viscoelastic jets with Deborah numbers that are of order unity and small Ohnesorge numbers $Oh \ll 1$, so that viscous stresses are negligible. The temporal evolution of a single instability of the jet is shown in Figure 5.2, where a characteristic picture is included for each of the four thinning regimes that govern the thinning of the jet. After exiting the nozzle, the jet initially remains almost cylindrical and instabilities slowly arise at the wavenumber k_m associated with the highest growth as predicted by linear stability analysis (see Section 2.2.4). The amplitude of this instability grows exponentially, resulting in high strain rates in the filament. The capillary pressure is dominantly resisted by the inertia of the accelerating fluid elements, resulting in an evolution of the minimal radius R_m near breakup described by the inviscid similarity solution (see Section 2.2.6):

$$R_m = 0.64 \left(\frac{\gamma}{\rho}\right)^{1/3} (t_p - t)^{2/3}. \tag{2.28}$$

The rapid decrease of the filament radius locally induces large strain rates that stretch the polymer molecules in the thread. As a result, the elastic stresses

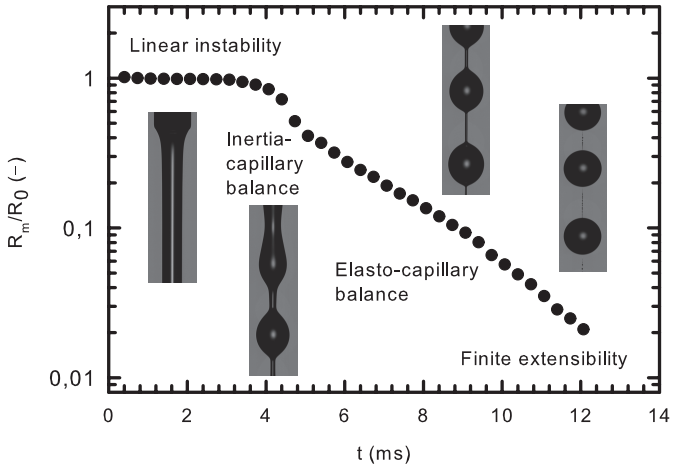

Figure 5.2: Thinning of a viscoelastic PEO jet with the different scaling regimes. The growth of the instabilities is illustrated with a representative picture for each of the regimes.

balances the increasing capillary pressure in the thread and the third regime, the elasto-capillary balance, starts during which the filament radius decreases exponentially in time (see Section 2.2.8) as

$$R_m = \left(\frac{GR_0^4}{2\gamma}\right)^{1/3} e^{-t/3\lambda}. \tag{2.33}$$

The temporal evolution of the filament radius can be expressed as an apparent extensional viscosity [61] and exponential decrease is equivalent to a significant strain hardening. This elasto-capillary regime continues until the polymer chains reach their finite extensibility limit and the elastic forces cease to grow, which results in a fast breakup [110].

Monitoring the elasto-capillary balance in a continuous jet offers a promising method for measuring sub-micron relaxation times in extension. As discussed in Chapter 1, recent modelling of the drop-on-demand inkjet printing has shown that unwanted satellite droplets can be suppressed with polymer solutions with small relaxation times $\lambda < 100$ μs [9]. Considering that such a limited amount of viscoelasticity has a profound impact on the process, it is crucial to have a

reliable methods to measure such low relaxation times.

The most popular device to measure these extensional properties in polymer solutions is currently the CaBER that was introduced in Section 3.2.1, but its detection limit is only 1 ms for low viscous fluids [111]. This restriction is induced by the initial stretching step that shifts the position of the narrowest part of the filament away from the position of the laser micrometer. Different studies [95, 132, 133] have worked on improving the detection limit of these capillary thinning experiments by monitoring the breakup with a high-speed camera and by optimising the initial stretching distance and velocity. The most optimised version of this device is presented in Section 4.2.3 and is capable of measuring relaxation times $\lambda = O(100\ \mu\text{s})$.

Unlike the filament thinning setup, a continuous jet does not require an initial axial deformation and it should therefore be a more appropriate experimental configuration for measuring relaxation times in the microsecond range. A jetting rheometer was originally proposed by Schummer and Tebel [118] who perturbed the jet at set frequencies and captured the thinning behaviour with high-speed photography. Although the theory on the non-linear behaviour of viscoelastic jets was in its infancy, the extensional behaviour of polymer solutions could be compared by determining the evolution of the apparent extensional viscosity. In the following decades, the characteristic 'beads-on-a-string' structure was simulated and the exponential necking of the ligament connecting the beads was linked to material parameters with various non-linear constitutive models [105, 106]. These results were first applied to extract a relaxation time with a free jetting rheometer by Christanti and Walker [104].

Recently, McKinley and co-workers [135, 136, 139, 140] introduced the Rayleigh Ohnesorge Jetting Extensional Rheometer (ROJER) as a new technique to specifically probe the extensional behaviour of weak viscoelastic liquids. In this setup, the cylindrical jet is excited by a piezo-actuator to create a controlled disturbance and the thinning dynamics are visualised with stroboscopic imaging. By selecting a wavenumber k that is larger than the most unstable one ($k_m R_0 \leq kR_0 \leq 1$), the formation of secondary beads between the large droplets is suppressed, resulting in a more precise measurement of the filament radius [83, 139]. Moreover, a temporal resolution of $O(1\ \mu\text{s})$ is achieved by changing the phase difference between the strobe and the perturbation frequency [136, 139]. Relaxation times down to values as small as 60 μs have been determined with this setup by fitting the 3λ timescale of Eq. 2.33 to the exponential decrease of the radius in the elasto-capillary regime [136].

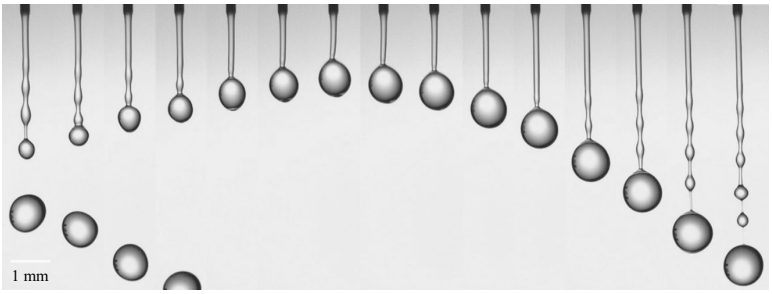

Figure 5.3: Illustration of the gobbling phenomenon where a large terminal drop periodically develops at the end of a thin jet a viscoelastic fluid. The time interval between the consecutive images is 6 ms. [141]

However, the use of this expression to extract the relaxation time is arguable in light of the findings of the gobbling phenomenon [141]. This effect appears in a capillary jet of a dilute high molecular weight polymer solution near the dripping-jetting transition ($We = \rho v_0^2 R_0/\gamma \approx 1$). As shown in Figure 5.3, the jet develops a beads-on-a-string morphology at this low imposed velocity, but the beads are swallowed by a large terminal drop, which periodically grows and pinches off. Under these conditions, the thread between the beads should theoretically thin at a different rate, $R_m \sim \exp(-t/2\lambda)$, and the experimentally observed radii appear to follow this new scaling [141].

Naturally, the question arises whether this new time scale of 2λ is also valid for other jetting experiments or if the generally employed time scale of 3λ [83,104,136] remains correct at higher jet velocities. Quantitative experiments of viscoelastic fluids are scarce [17] and at present, no direct comparison of relaxation times obtained with jetting and static capillary thinning experiments on the same fluid has been reported, because both experiments are probing different time scales. Despite the fact that jetting rheometry is a suitable measurement technique for weakly viscoelastic liquids, the jet quickly becomes too long for resolving the filament radius during the complete elasto-capillary regime. The selected model fluids should therefore exhibit relaxation times that are located near the lower detection boundary of the capillary thinning device. The set of model polymer solutions was introduced in Section 3.1 and some additional characterisation of the polymers is discussed in Section 5.2. The employed experimental techniques were described in Section 3.2 and the protocol for the detection of the dynamics of the Rayleigh instabilities is discussed in Section 4.2.4. We clarify the experimental observations, which are respectively presented for the CaBER and jetting setup in Sections 5.3 and 5.4, using a

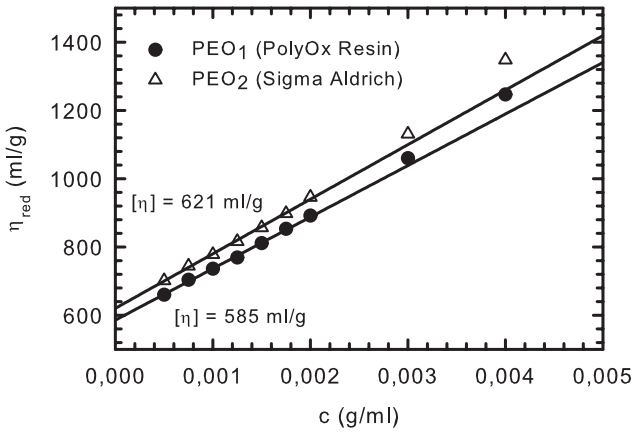

Figure 5.4: Reduced viscosity as a function of concentration, allowing the determination of the intrinsic viscosity $[\eta]$ of both polymer molecules in water at a temperature 22°C.

numerical and analytical analysis of the filament thinning in Section 5.5.

5.2 Polymer characterisation

The model polymer solutions that are studied in this chapter consist of dilute aqueous solutions of two types of PEO with approximately the same molecular weight. To verify that the solutions are actually in the dilute regime, the critical overlap concentration c^* of the polymer coils is evaluated. This concentration marks the transition from a dilute regime to a semi-dilute solution that is accompanied by great changes in the rheological response of the polymer solution. The first step is the determination of the single coil size based on intrinsic viscosity measurements of both polymers according to the procedure described in Section 3.2.3. Figure 5.4 shows the reduced viscosity η_{red} for a concentration series of both polymers at 22°C. By extrapolating these values to zero polymer concentration, it is demonstrated that PEO_1 has a slightly lower intrinsic viscosity than PEO_2. The overlap concentration c^* is then calculated with the criterium from Greassley [122] as

	$[\eta]$ (ml/g)	c^* (g/l)	M_w (kg/mol)	L $(-)$	λ_z (ms)
PEO_1	585	1.32	1035	116	0.112
PEO_2	621	1.24	1135	121	0.131

Table 5.1: Properties of the two PEO molecules in dilute aqueous solutions at a temperature of 22°C.

$$c^* = \frac{0.77}{[\eta]}. \tag{3.13}$$

The intrinsic viscosity is also used to calculate a more precise value for the molecular weight M_w of both polymers using the Mark-Houwink-Sakurada (MHS) equation for PEO solutions [79]

$$[\eta] = 0.072 M_w^{0.65}. \tag{5.1}$$

Additionally, the MHS-exponent $a = 0.65$ provides information on the solvent quality by employing the Zimm theory for dilute polymer solutions. The Zimm model expands the Rouse model for the diffusion of an unentangled chain by including hydrodynamic interactions with the solvent. For long flexible polymer chains, the intrinsic viscosity scales as $[\eta] \sim M_w^{3\nu-1}$ where ν is the excluded volume exponent that scales the equilibrium radius of gyration of the chain with molecular weight, $R_g \sim M_w^{\nu}$. The limiting values of $\nu = 0.5$ and $\nu = 0.6$ correspond to a theta solvent and a good solvent respectively. The exponent $\nu = (a+1)/3 = 0.55$ therefore indicates that water is a relatively good solvent for PEO.

Another important polymer property is the finite extensibility parameter L representing the ratio of a fully extended polymer dumbbell to its equilibrium length. The extensibility can be described in terms of molecular parameters as

$$L = \sqrt{3} \left(\frac{j \sin^2(\theta_b/2)\, M_w}{C_\infty M_u} \right)^{1-\nu}, \tag{5.2}$$

where θ_b is the average bond angle in the monomer, j is the number of bonds of a monomer of molar mass M_u and C_∞ is the characteristic ratio for a given polymer-solvent system. The values for PEO are $\theta_b = 109.4°$ (for which the C-C bond angle was taken), $j = 3$, $M_u = 44$ g/mol and $C_\infty = 4.1$ [142]. The

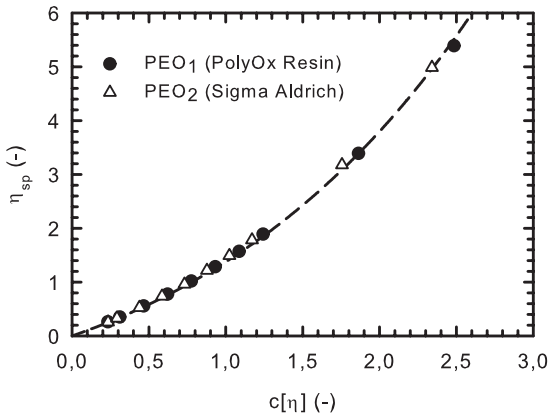

Figure 5.5: Specific viscosity as a function of the polymer volume fraction $c[\eta]$ to verify that the polymeric contribution to the viscosity η_p is described by the Martin equation (Eq. 5.3) with $K_M = 0.32$.

different polymer properties are summarised in Table 5.1.

Finally, we return to the shear viscosity measurements that are presented in Table 3.1. The small differences that are observed for the 0.1% solutions of both polymers is explained by the difference in the intrinsic viscosity. Figure 5.5 shows the specific viscosity $\eta_{sp} = \eta_p/\eta_s$ of different concentrations of both polymers as a function of the polymer volume fraction $c[\eta]$. The viscosity measurements of both polymers form a single master curve for PEO. To include data points with concentrations above the linear range of the Huggins equation (see Eq. 3.16), we employ the empirical Martin equation that assumes an exponential increase of the specific viscosity with the polymer volume fraction $c[\eta]$:

$$\eta_{sp} = c\,[\eta]\,e^{K_M c[\eta]} \tag{5.3}$$

where K_M is the Martin coefficient. A Taylor series expansion of this equation shows that the Huggins equation is satisfied for small concentrations.

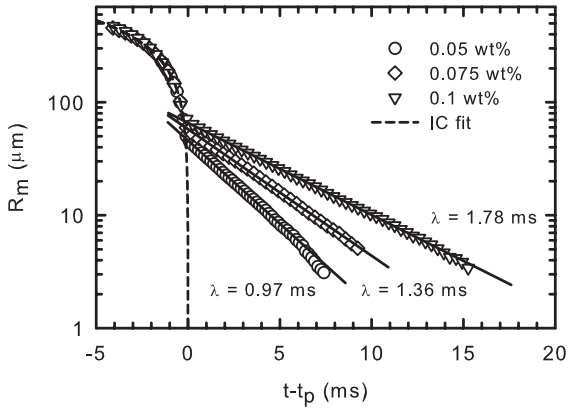

Figure 5.6: Temporal evolution of the minimal filament radius during capillary breakup experiments of three polymer solutions. The dashed line indicates a power law fit of the inertia-capillary regime (Eq. 2.28) and the straight lines represent an exponential fit used to extract the dominant relaxation time λ (Eq. 2.33).

5.3 CaBER experiments

The extensional flow properties of the model fluids are first characterised with CaBER experiments. The large spatial and temporal resolution of the setup allows an accurate determination of the characteristic relaxation time of the fluids, which is used in the next section to evaluate the time scales during the jet breakup. Figure 5.6 shows the evolution of the minimal radius of the filament during the experiment for the three solutions of PEO_2. The initial decrease of the filament radius is predicted by the global Ohnesorge number, which is calculated using the estimated radius at the cessation of stretching that was determined by a lubrication solution for a Newtonian fluid

$$R = R_0 \left(\frac{L_1}{L_0} \right)^{-3/4}, \tag{5.4}$$

with L_0 and L_1 the initial and the final gap respectively [56]. By comparing the characteristic thinning velocities of the viscosity and inertia dominated regimes, the boundary between the two regimes is located at a critical value $Oh^* = 0.2077$ [95]. The values for the model solutions are far below the critical value (see Table 5.2), so the capillary pressure is initially only resisted by fluid

	c	c/c^*	Oh	G	λ	De
	$wt\%$	$(-)$	$(-)$	(Pa)	(ms)	$(-)$
PEO_1	0.10	0.758	0.0068	2.37	1.38 ± 0.10	0.35
PEO_2	0.05	0.402	0.0052	1.08	0.97 ± 0.03	0.24
	0.075	0.603	0.0061	1.62	1.36 ± 0.05	0.34
	0.10	0.804	0.0069	2.16	1.78 ± 0.11	0.45

Table 5.2: Characteristics of the model fluids at a temperature of 22°C.

inertia. The fluid continues to accelerate and appears to approach a finite-time singularity at the pinching time t_p, as described by Eq. 2.28 and represented by the dashed line in Figure 5.6. The high strain rates in the fluid neck generate a build-up of elastic stresses in the polymer molecules that start to dominate the fluid inertia and suppress the singularity. This transition marks the onset of the elasto-capillary (EC) regime where the filament radius decreases exponentially in time resulting in a constant strain rate, which is inversely proportional to the longest relaxation time λ. In order to better distinguish the differences in elasto-capillary regime, the curves in Figure 5.6 are shifted by t_p along the time axis, so that the initial inertia-capillary regimes collapse for the three fluids. For lower polymer concentrations, the transition occurs at smaller radii, suggesting that a higher strain is necessary to reach sufficiently high elastic stresses. The characteristic relaxation time λ of each solution is extracted from the thinning rate in the elasto-capillary regime using the 3λ time scale of Eq. 2.33. The relaxation time increases with polymer concentration and the values are listed with the standard deviation in Table 5.2.

The onset of the EC regime is also recognised from the shape of the filament in Figure 5.7. The asymmetric shape that characterises inertia resisted thinning, disappears at the start of the start of the EC regime and a cylindrically shaped filament emerges. The shape remains axially uniform for the two highest concentrations, whereas the 0.05 % solution shows significant necking at both the top and the bottom droplet, generating a large bead in the middle of the filament. Small differences in radius and hence in capillary pressure between the short filaments above and below this central bead impel the bead to coalesce with one of the two fluid reservoirs. The formation of a central bead was also observed by Tirtaatmadja et al. [79] during dripping experiments on a series of dilute solutions of PEO with varying molecular weight in glycerol-water mixtures. The bead disappeared for the higher molecular weight samples, which exhibited higher relaxation times λ and thus higher Deborah numbers. Bhat et al. [71] found a comparable trend in simulations of the breakup of viscoelastic filaments. Satellite beads only appeared in the case of sufficient inertia (Oh $<$

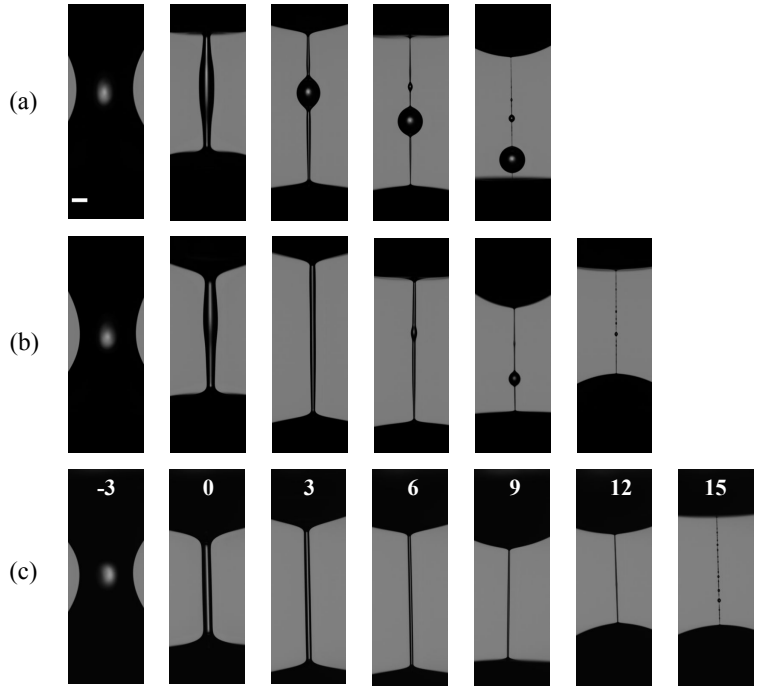

Figure 5.7: Static thinning and breakup of a filament for aqueous PEO_2 solutions of (a) 0.05 %, (b) 0.075 % and (c) 0.1 %. The shifted time $t - t_p$ is displayed and the scale bar represents a distance of 200 μm.

1) and moderate elasticity (De < 0.3). In fluids with a comparable Ohnesorge number as our model fluids, bead formation is more pronounced for lower Deborah numbers, which agrees with our observations. Moreover, the presence of the bead does not appear to affect the thinning dynamics, as no deviations from the exponential decay are observed in Figure 5.6. The minimal radius can be tracked for all solutions until a value of 5 μm. At this point the filament morphology changes dramatically forming a characteristic beads-on-a-string structure before pinching off.

Although most of the jetting experiments are carried out with solutions of PEO_2, we have also performed some tests with PEO_1 solutions. Figure 5.8 compares the thinning dynamics of 0.1 % solutions of the two types of PEO. Despite the fact that both polymer have similar molecular weights, a significant difference in relaxation time is observed between two samples with the same concentration. This distinction can be explained by kinetic theory using the small difference

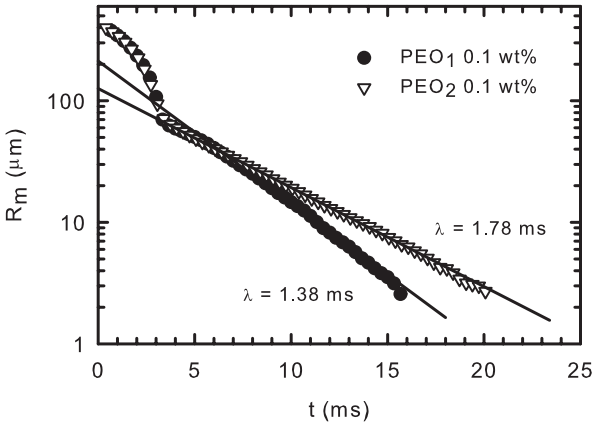

Figure 5.8: Temporal evolution of the minimal filament radius during capillary breakup of 0.1 % solutions of the two types of PEO, displaying different characteristic relaxation times.

between the intrinsic viscosity of both polymers that was detected in Section 5.2. The characteristic relaxation time of a polymer solution in the dilute regime can be predicted by Rouse-Zimm theory. The longest Zimm relaxation time λ_z of an isolated polymer coil in a dilute solution is given by

$$\lambda_z = \frac{1}{U_{\eta\tau}} \frac{\eta_p}{G}, \tag{5.5}$$

where $U_{\eta\tau} = \lambda_\eta / \lambda_z$ is the universal ratio of the characteristic relaxation time λ_η of a dilute polymer solution system and the longest relaxation time λ_z. The numerical value of the universal ratio $U_{\eta\tau}$ depends on the solvent quality [143] and can be approximated for good solvents from the excluded volume exponent ν by $U_{\eta\tau} = \zeta(3\nu)$ with ζ as the Riemann zeta function. This leads to a numerical value of the the front factor $1/U_{\eta\tau} = 0.463$ [79]. The polymer contribution to the viscosity η_p is determined from the measurement of the specific viscosity η_{sp}. In the limit of low concentrations - which is assumed in the Zimm theory - η_p is described by the Huggins equation (Eq. 3.16) as

$$\eta_p = \eta_s c\,[\eta]. \tag{5.6}$$

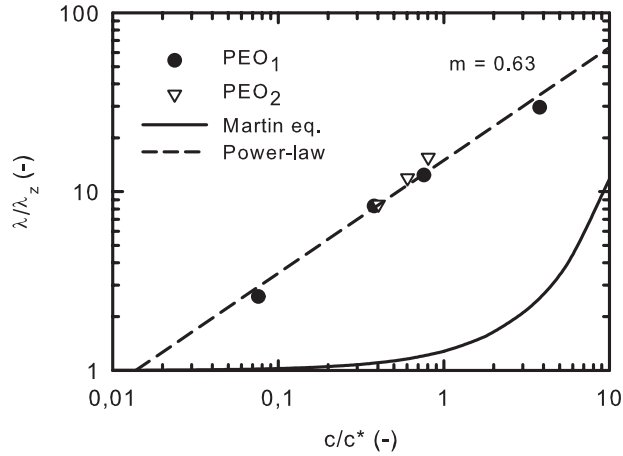

Figure 5.9: Reduced relaxation times λ/λ_z as a function of the reduced concentration c/c^* for a concentration series of both PEO polymers. The correction to the Zimm time with the Martin equation (Eq. 5.9) is shown and the power-law dependence (Eq. 5.10) is fitted to the data with an exponent $m = 0.63$.

The elastic modulus G is invariant with mode number in the Rouse-Zimm theory and is only a function of the number density of the polymer chains in solution $n_p = c\,N_A/M_w$:

$$G = n_p k_B T = \frac{c\,N_A k_B T}{M_w}, \tag{5.7}$$

where c is the weight concentration of the polymer [108]. Combining Eqs. 5.5 - 5.7, an expression for the Zimm relaxation time λ_z is given by

$$\lambda_z = \frac{1}{U_{\eta\tau}} \frac{\eta_s[\eta] M_w}{N_A k_B T}. \tag{5.8}$$

The Zimm time is concentration independent, but depends on the solvent quality as $\lambda_z \sim M_w^{3\nu}$. The values of λ_z are computed for both polymers from the intrinsic viscosity measurements and are listed in Table 5.1. The relaxation times that are extracted from the CaBER experiments are compared to λ_z in Figure 5.9. Some additional solutions of PEO_1, which are not used in the jetting experiments, are included to display a wider concentration range. Although the

solutions are in the dilute regime ($c/c^* < 1$), the characteristic relaxation time is up to an order of magnitude larger than the Zimm time. This discrepancy is consistent with observations by several authors who have also noticed an increase in relaxation time with concentration for various polymer systems in the dilute regime [16, 79, 95, 110, 144, 145]. The overlap concentration c^* is determined in shear flow where the polymer chains are in quiescent conditions with a random coil configuration. However, the extensional flow during capillary breakup experiments is sufficiently strong to induce large conformational changes in the polymer coil. Entov and Hinch [106] established that the Weissenberg number $Wi = \lambda\,\dot{\epsilon} = 2/3$ is constant during the elasto-capillary regime and exceeds the critical value of 1/2 for coil-stretch transition of a dilute polymer solution in extensional flow [32]. As a result of this unraveling of the polymer coils from the equilibrium coiled configuration, the polymer chains extend over a larger volume and will feel the presence of the surrounding macromolecules. These long-range interactions between unraveling polymer coils lead to an increase in the effective relaxation time of the solution.

As these polymer interactions will be enhanced with an increasing concentration, the solution exhibits semi-dilute behaviour with a concentration dependence of the relaxation time. In the stretched state, the transition from dilute to semi-dilute concentration regimes will occur at a much lower value than indicated by the value of c^*. Birefringence measurements for a planar extensional flow in a four-roll mill setup by Harrison et al. [146, 147] have shown that fully extended polystyrene molecules are observed at $c/c^* < 0.01$, whereas at $c/c^* < 0.1$ chain-chain interactions inhibit the polymer molecules from reaching full extension. Relaxation times approaching the Zimm time λ_z were observed at similar concentrations during capillary breakup experiments [79, 110]. However, a truly concentration independent relaxation has not been found, due to limits in temporal and spatial resolution. Additionally, it is not possible to determine a relaxation time below a lower concentration limit as polymer chains will be fully stretched before their elastic stresses can balance the capillary pressure [95, 132].

A first correction to the Zimm relaxation time is added to Figure 5.9 by replacing the solvent viscosity in Eq. 5.8 by the shear viscosity of the solution. Clasen et al. [110] suggested to estimate the increase of the polymer contribution to the viscosity η_p with the Martin equation (Eq 5.3), giving a dependence of the longest relaxation time λ with the reduced concentration c/c^*

$$\lambda = \lambda_z \exp\left(0.77\, K_M \frac{c}{c^*}\right). \tag{5.9}$$

The Martin coefficient $K_M = 0.32$ was obtained from regressing the specific viscosity in Figure 5.5. This approach is quite accurate for relaxation times that are determined during small amplitude oscillatory shear experiments, but it fails for extensional relaxation times [110, 132]. Figure 5.9 clearly shows that the relaxation times determined from capillary thinning start to exceed the dilute limit at much smaller concentrations than theoretically expected from Eq. 5.9. A second correlation was proposed by Tirtaatmadja et al. [79] who observed a power-law dependence of the extensional relaxation time with the reduced concentration

$$\frac{\lambda}{\lambda_z} \sim \left(\frac{c}{c^*}\right)^m, \tag{5.10}$$

where the exponent m depends on the solvent quality. We retrieved an exponent $m = 0.63$ for the data presented in Figure 5.9, which is similar to the exponent $m = 0.65$ determined by Tirtaatmadja et al. [79] for PEO in glycerol/water mixtures. Clasen et al. [110] explain this power-law dependence with scaling theory for unentangled semi-dilute polymer solutions [148–150]. Although such scaling theories are generally used for concentrations $c > c^*$ in weak shear flows, the unraveling of the polymer coils in the strong extensional flow field causes interactions with neighbouring chains at much lower concentrations.

The solution is described with semi-dilute blob theory where the polymer is considered as a group of spheres or blobs with radius ξ_h, where the motion of each blob is uncorrelated to that of the others [151]. This correlation length ξ_h may be conceived as the distance between entanglement points of the polymer chains and thus decreases with increasing concentration. Intramolecular hydrodynamic interactions dominate on length scales shorter than the correlation length, but these interactions are screened out on larger scales. Inside the blob, the dominating single chain hydrodynamics are thus captured by Zimm theory and a longest relaxation time λ_ξ of a blob can be determined. Since hydrodynamic interactions are negligible on distances larger than ξ_h, the intermolecular interactions between expanded and overlapping chains are described by Rouse dynamics. The longest relaxation time of the whole chain λ is found by applying Rouse relaxation spectrum with λ_ξ as the smallest relaxation time, giving the following concentration dependence:

$$\frac{\lambda}{\lambda_z} \sim \left(\frac{c}{c^*}\right)^{\frac{2-3\nu}{3\nu-1}}. \tag{5.11}$$

Although the theoretical exponent $(2 - 3\nu)/(3\nu - 1) = 0.54$ differs from the experimentally observed value, this correlation explains the power-law dependence of the extensional relaxation time on the reduced concentration.

5.4 Jetting experiments

After identifying extensional properties with CaBER experiments, the breakup behaviour of the model fluids is studied during jetting flows. The viscoelastic jet breaks up into a series of droplets as described in Section 5.1. The initial stable zone with a constant radius is followed by the development of capillary instabilities and a filament emerges between two beads. The filament appears to be a Lagrangian equivalent to the capillary bridge in the CaBER experiment, draining its fluid into the adjacent beads. After its formation, the filament thins very rapidly to a radius $R_m \approx 50$ μm during a short inertia-capillary (IC) regime. Elastic stresses start dominating at these dimensions and the growth of the instability is arrested during the elasto-capillary (EC) regime. The jet exhibits a long beads-on-a-string structure (see Figure 5.1), where the beads are connected by stable, nearly cylindrical filaments. These filaments continue to drain at a constant strain rate, resulting in an exponential thinning with distance from the nozzle. When the filament radius becomes smaller than 5 μm, the cylindrical shape is lost and two necking points originate at the contact points with the beads. The flow towards the beads is obstructed and second and third generation beads appear [152]. Finally, the polymer molecules reach their finite extensibility limit and the filament breaks. Most of the higher generation beads are swallowed by one of the main droplets, but some small satellite drops remain flying between the main drops. In the following section, we first discuss some observations during the initial linear stability regime of the jet. Next, we focus on the elasto-capillary regime and compare the time scales with the static capillary tests from the CaBER experiments.

5.4.1 Linear stability regime

In order to determine the jet velocity and the Weber number, it is crucial to obtain an accurate value of the initial jet radius R_0. The initial radius is larger than the nozzle radius for all our jetting experiments and this expansion after exiting the nozzle is explained by the presence of the polymer molecules in the solution. The polymer chains are partially stretched due to the shear flow in the nozzle, especially near the walls where the highest shear rates are

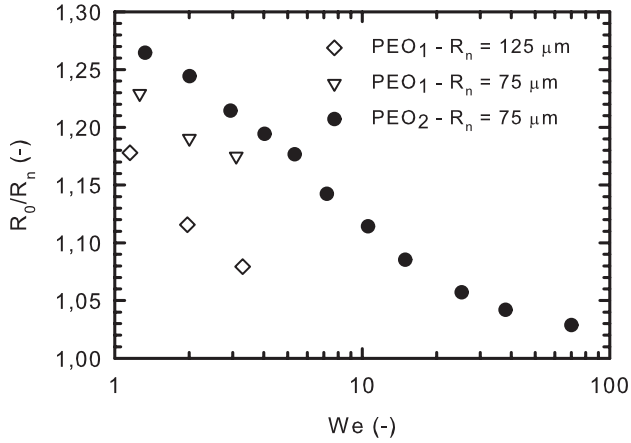

Figure 5.10: Dimensionless radius of the initial straight section R_0 as a function of the Weber number for different 0.1 % PEO solutions with varying nozzle radius.

encountered [153]. Near the exit of the nozzle, the flow rearranges from a parabolic Poiseuille flow to a uniform velocity profile without a radial velocity gradient in the straight section of the jet. Due to the changing flow type, the chains start to relax to a coiled configuration and the associated radial normal stresses cause a swelling of the jet beyond the nozzle radius [23]. Figure 5.10 shows that the increase of the radius after the nozzle is quite subtle in comparison to more elastic samples, such as polymer melts or concentrated polymer solutions, where the extrudate swell is even visible to the naked eye. The expansion at the nozzle is stronger for the PEO_2 solution since it has a higher relaxation time and thus displays more pronounced elastic behaviour. The swelling further depends on the needle size because the shear rate near the needle wall rapidly increases as the needle radius decreases:

$$\dot{\gamma} = \frac{4\dot{Q}}{\pi R_n^3}. \tag{5.12}$$

The higher shear rate causes a larger deformation of the polymer chains that generates a larger first normal stress difference. From this perspective, the decrease of the ratio R_0/R_n with the Weber number is somewhat counterintuitive. However, this trend is in agreement with the behaviour of Newtonian jets with varying flow rates [17]. The jet radius of a Newtonian

jet only equals the nozzle radius at a Reynolds number $Re = 8$, where Re is based on the tube radius $Re = \rho v_n R_n/\eta$ with v_n as the average velocity in the nozzle [154, 155]. The jet expands for low velocities ($Re < 8$), whereas it contracts at high jet velocity ($Re > 8$). The jet contraction originates from the change from a parabolic flow profile at the nozzle exit to a uniform velocity in the straight jet [156]. By taking a simple macroscopic momentum balance under the assumption that the pressure at the nozzle exit can be approximated by the atmospheric pressure, Harmon [157] found a constant ratio $R_0/R_n = \sqrt{3}/2$ and this ratio is also experimentally observed for high jet velocities ($Re > 200$) [154, 155]. However, for lower jet velocities, the changing axial velocity gradient $\partial v/\partial z$ induces a decrease in the pressure at the tube exit resulting in a velocity dependent contraction [155]. All our experiments are performed in the velocity region where this velocity dependent contraction is observed for Newtonian liquids and the levelling of R_0 at high Weber numbers is also similar to the Newtonian case. Consequently, the evolution of R_0/R_n in Figure 5.10 is explained by the superposition of viscoelastic extrudate swelling and the velocity dependent contraction of the jet.

After the fluid has emerged through the nozzle, capillary instabilities arise in the linear stability regime. Although these instabilities form a clear barrier between two droplets when the fluid motion becomes non-linear in the IC regime, Figure 5.11a shows that they are hardly visible in the initial straight section. The wavelength of the instabilities is an important parameter in characterising the jetting flow as it determines the final droplet size. Since we have restricted our experiments to unforced jets, the instability should exhibit a wavelength λ_w corresponding to the largest growth rate. To retrieve the wavelength of the jets, the profile $R(z)$ for the initial part of the jet is extracted from the image (see Figure 5.11b). The instabilities are very prominent in the non-linear regime, but subtle oscillations in $R(z)$ are also detected at the end of the linear regime.

Figure 5.11c focuses on the first recognisable instabilities and the wavelength is evaluated from the distance between the first two local minima of $R(z)$. In this case, the wavelength is similar to the most unstable wavelength $\lambda_w = 9.01R_0$ for an inviscid liquid according to Rayleigh theory. This procedure is repeated ten times for each Weber number and the average values are presented as dimensionless wavenumbers kR_0 in Figure 5.11d. The error bars indicate that substantial variations in the wavenumbers in our measurements of an unforced jet. However, it is clear that the average wavenumbers are smaller than the inviscid Rayleigh limit of $kR_0 = 0.697$. The fact that viscoelasticity shifts the most unstable wavenumber towards lower values has been theoretically demonstrated using linear stability analysis [68, 83, 158]. In comparison to the

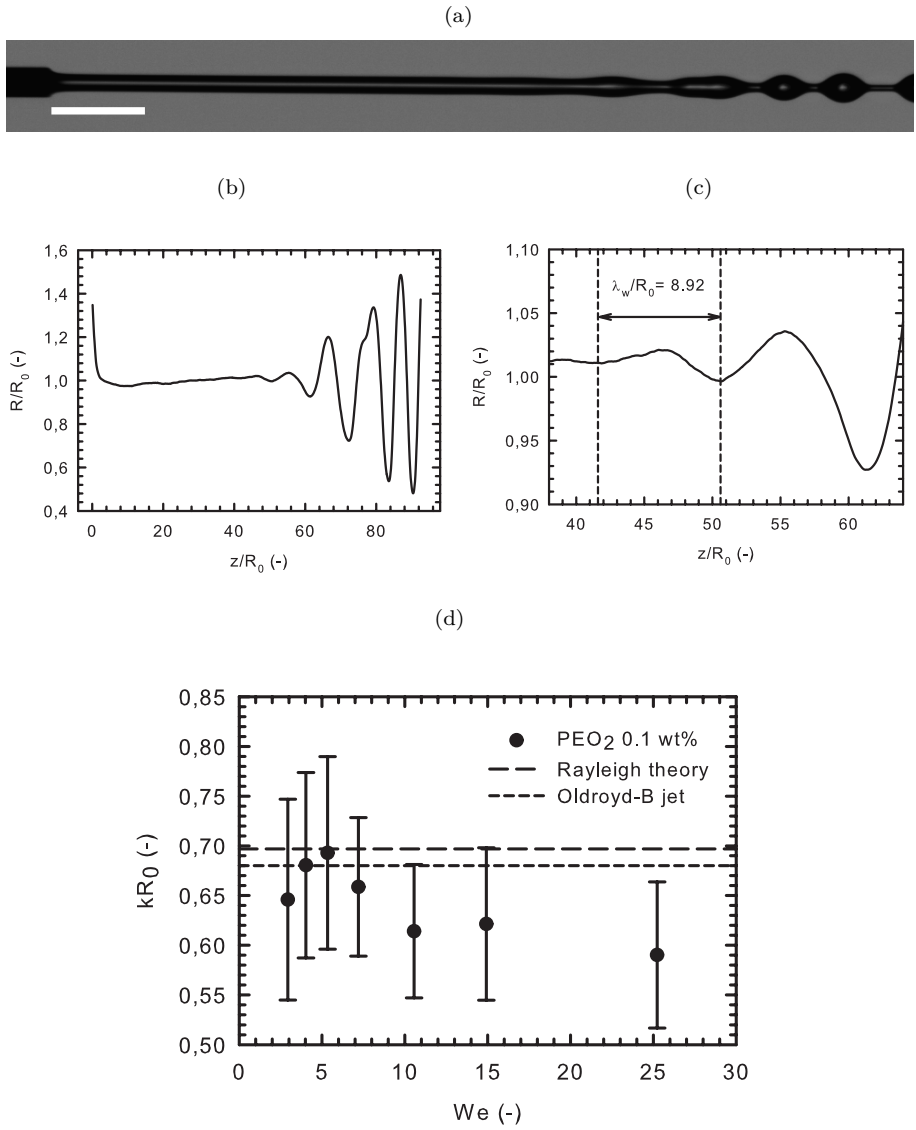

Figure 5.11: Determining the dimensionless wavenumber kR_0 of a 0.1 % PEO_2 jet. (a) Image of the initial part of jet at $We = 4$ (the scale bar represents 1 mm) and (b) the local jet radius as a function of the axial position. (c) Focussing on the initial straight section allows the identification of the wavelength λ_w. (d) The dimensionless wave number for different Weber numbers are compared with the predictions of most unstable wavenumber for an inviscid jet and an Oldroyd-B jet [83].

prediction of Ardekani et al. [83] for an Oldroyd-B liquid with similar Ohnesorge and Deborah number as the model fluid (short dashed line), the experimental wavenumbers are relatively small.

5.4.2 Elasto-capillary balance

To study the elasto-capillary balance, jetting experiments are performed with three PEO_2 solutions at approximately the same jet velocity (We ≈ 8). Despite the fact that same flow rate is chosen for all solutions, small differences in the initial radius R_0 cause slight variations in the jet velocity. A higher polymer concentration increases the initial jet radius and hence lowers the actual jet velocity expressed by the Weber number (see Table 5.3). As shown in Figure 5.12a, all fluids exhibit a similar thinning behaviour as in the static capillary experiments. Only the initial radius of the filament is notably smaller, because the jet originates from a nozzle with an inner radius $R_n = 75$ μm. Similar to the CaBER experiments, more concentrated solutions thin at a lower constant strain rate, revealing an increase of the time scale θ in the EC regime. However, it is striking that the minimal jet radius R_m decreases faster for the same sample in comparison to the CaBER experiments. The different thinning rate in the EC regime of both experiments is emphasised in Figure 5.12b by rescaling the time with the relaxation time λ that was obtained during the CaBER experiments. Since Eq. 2.33 has proven to describe all static capillary experiments, the three solutions exhibit the same slope of $-1/3\log(e)$ in this graph.

In contrast, the jetting experiments display a steeper slope, which is roughly the same for all samples. This observation demonstrates that the time scale θ in the EC regime of the jetting experiments is proportional to the relaxation time λ. To accurately determine this scale, at least ten instabilities are followed in time for each sample to obtain an average value of θ, which is listed with the standard deviation in Table 5.3. The time scale is determined with a reduced accuracy of only two significant digits because the fits of the exponential decay are less precise than for the CaBER experiments. This lower precision is caused by the lower resolution of the telecentric lens that is used for the jetting experiments. The ratio of the time scale with the relaxation time θ/λ is determined for each sample and an approximation of the standard deviation of the ratio of two normally distributed variables is included in Table 5.3 [159, 160]. A time scale $\theta \approx 2\lambda$ is observed during the jetting of all samples. As a result, the reference slope of $-1/2\log(e)$ appears to correctly describe the thinning.

(a)

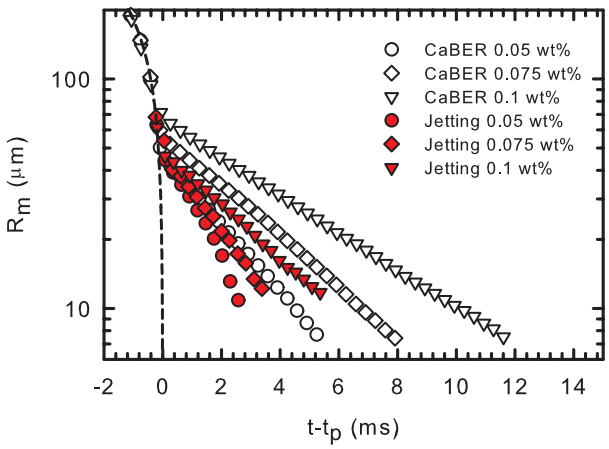

(b)

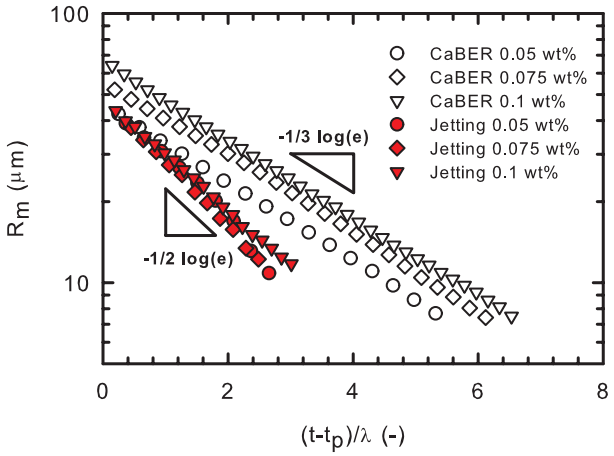

Figure 5.12: Development of the minimal filament radius during the elasto-capillary regime in static capillary experiments and in jetting experiments at We ≈ 8 for three PEO_2 solutions. (a) The evolution of the radius is presented in the same way as Figure 5.6 and the increase of relaxation time with polymer concentration is also visible during the jetting experiments. (b) The time is rescaled with the relaxation time λ obtained with the CaBER, emphasizing the different time scales in both experiments.

(a)

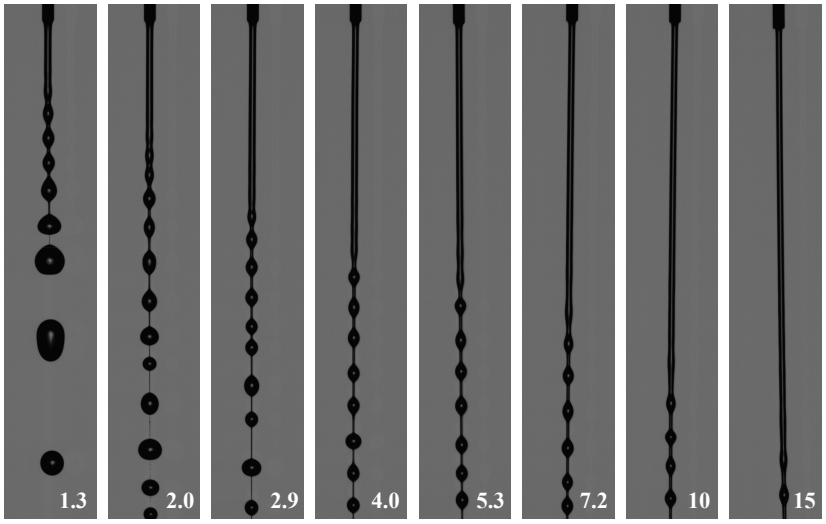

(b)

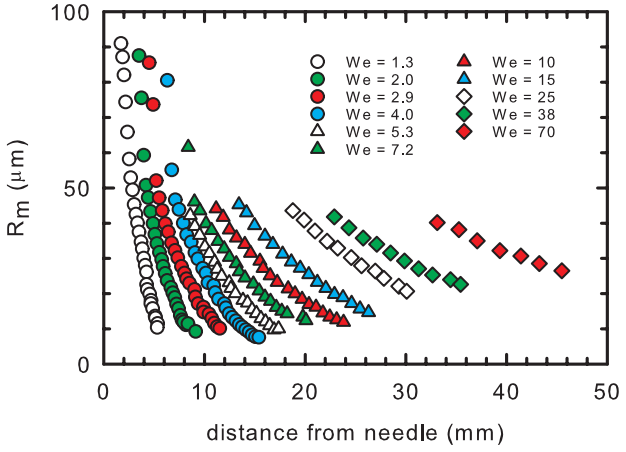

Figure 5.13: Thinning dynamics of the 0.1 % PEO_2 solution for different Weber numbers. (a) Images of the different jets with the Weber number in the bottom corner. (b) The development of the filament instability is represented as a function of the distance from the needle with a focus on the elasto-capillary regime.

c (wt%)	$\dot{Q}$ (ml/min)	R_0 (μm)	We (–)	θ (ms)	θ/λ (–)
0.05	3.17	80	8.9	2.0 ± 0.1	2.1 ± 0.1
0.075	3.17	82	8.3	2.7 ± 0.1	2.0 ± 0.1
0.10	3.17	85	7.2	3.7 ± 0.1	2.1 ± 0.2

Table 5.3: Overview of the parameters of the jetting experiments with the three PEO_2 solutions.

In the previous experiments, the validity of the new time scale is shown for a single Weber number that is one order higher than the dripping-jetting transition (We $\approx$ 1). The next series of jetting experiments explores whether this new time scale is valid for a wide range of jet velocities. The 0.1% PEO_2 solution is examined for a range of Weber numbers and the evolution of the minimal filament radius R_m is shown as a function of the distance from the needle in Figure 5.13b. The lowest flow rate (We = 1.3) was chosen close to the dripping-jetting transition and some of the beads still appear to coalesce just before breakup at this flow rate (see Figure 5.13a). This experiment is thus performed at the boundary of the gobbling regime [141].

The evolution of the minimal radius R_m is followed during the EC regime for all flow rates using the optical setup that is able to capture a section of the jet with a length of roughly 15 mm. However, for small Weber numbers, this field of view is sufficient to monitor the complete non-linear thinning dynamics of the jet, including the inertia resisted regime. A single frame can capture a segment of the jet from origin of the capillary instability until the late stages of the EC regime. As the Weber number increases, the initial straight segment lengthens, which is shown in the images as well as in the position of the onset of the EC regime in Figure 5.13b. Additionally, the length of the EC regime increases due to the higher jet velocity and the jet becomes too long to track the complete thinning of an instability for intermediate flow rates ($We > 5$). Further increasing the flow rate results in the acquisition of even fewer data points and eventually the EC regime can only be partially captured in a single image for high flow rates ($We > 15$). Since the diameter of larger filaments can be determined more accurately, we focus on the beginning of the EC regime for these flow rates. Jetting experiments could be carried out until the Weber number reaches a value of 70. At this highest jet velocity, the instability can only be followed for seven consecutive frames, which is a minimum to reliably fit the EC regime.

(a)

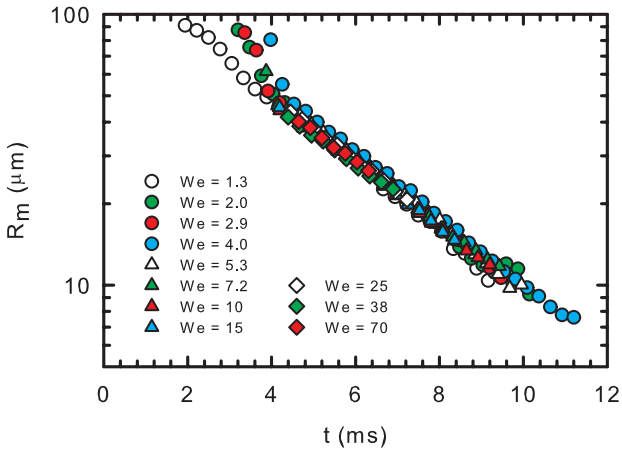

(b)

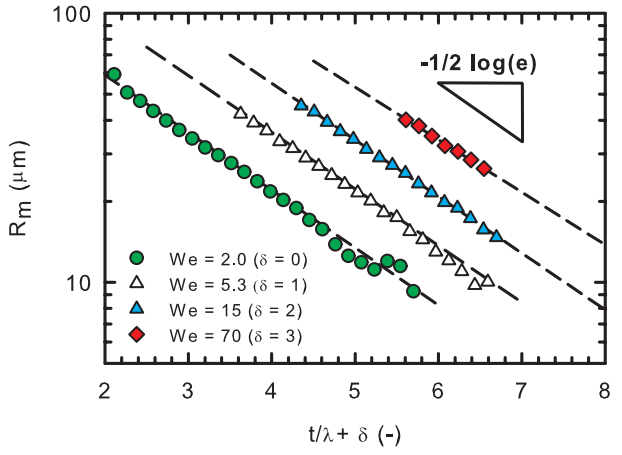

Figure 5.14: Thinning dynamics of the 0.1 % PEO_2 solution for different Weber numbers. (a) The data points in Figure 5.13b are shown as a function of time and appear to collapse in the EC regime for different Weber numbers. (b) Four experiments of are rescaled with the relaxation time λ obtained with the CaBER and the curves are shifted with a factor δ. The fit of the EC regime (dashed lines) corresponds to the reference slope, representing a thinning with a time scale of 2λ.

$\dot{Q}$ (ml/min)	R_0 (μm)	We (–)	θ (ms)	θ/λ (–)	L_p (mm)
1.60	95	1.3	1.8 ± 0.1	2.0 ± 0.2	6.8 ± 0.4
1.90	93	2.0	1.8 ± 0.1	2.0 ± 0.2	14.5 ± 1.9
2.22	91	2.9	1.9 ± 0.2	2.2 ± 0.2	23.2 ± 3.4
2.54	89	4.0	1.8 ± 0.1	2.1 ± 0.2	29.2 ± 2.6
2.85	88	5.3	1.8 ± 0.1	2.1 ± 0.2	33.8 ± 4.0
3.17	85	7.2	1.8 ± 0.1	2.1 ± 0.2	39.8 ± 4.5
3.70	83	10	1.9 ± 0.1	2.1 ± 0.2	47.9 ± 5.9
4.23	81	15	1.8 ± 0.1	2.1 ± 0.2	59.5 ± 5.0
5.29	79	25	1.9 ± 0.1	2.1 ± 0.2	74.3 ± 5.0
6.34	78	38	2.0 ± 0.2	2.3 ± 0.3	–
8.46	77	70	2.0 ± 0.2	2.2 ± 0.3	–

Table 5.4: Overview of the jetting experiments with the 0.1 % aqueous PEO_2 solution. The jet velocity is varied from a value near the dripping-jetting transition (We = 1.3) to the experimental limit of the setup (We = 70).

The same data set of jetting experiments is presented in Figure 5.14a as a function of time after exiting the nozzle. The time until the first detection of an instability is calculated using the jet velocity v_0 and the distance of this instability from the nozzle. All experiments exhibit unmistakably the same thinning behaviour in the EC regime. Whereas the experiments with a higher Weber number show a less steep slope in the EC regime in Figure 5.13b, the thinning of the filament between two beads appears to be unaffected by the jet velocity in the temporal domain. In order to assess the thinning rates at different Weber numbers, four experiments are featured in the Figure 5.14b. The time axis is rescaled with the relaxation time λ from the CaBER measurements and then shifted with a factor δ for a better comparison of the slopes of the curves. The slope of the exponential fit through the EC regime of each experiment resembles the reference slope of $-1/2\log(e)$. Hence, the time scale in the EC regime $\theta \approx 2\lambda$ seems unaffected by changes in the jet velocity. A detailed list of the values of θ/λ with approximate standard deviations for all experiments is given in Table 5.4. These values are quite close to 2 for most flow rates, however the values for the two highest flow rates are slightly higher. As mentioned before, only a part of the EC regime is observed for these high flow rates, so there is a larger uncertainty on the slope of the fitted curve.

All previous jetting experiments are performed with a constant nozzle radius $R_n = 75$ μm. To examine the potential dependence of the thinning dynamics on the nozzle size, Figure 5.15 compares the evolution of the minimal filament

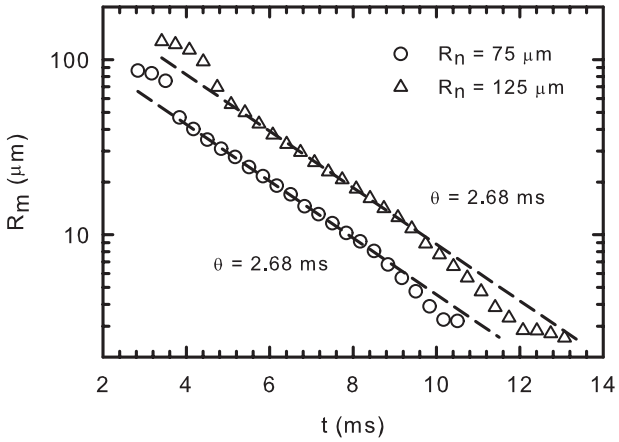

Figure 5.15: Comparison of the thinning dynamics of a 0.1 % PEO_1 jet with two different nozzles at $We \approx 3$.

radius R_m for jets of the same 0.1 % PEO_1 solution exiting from two different needles. The initial jet radius R_0 is clearly different for both experiments and appears to scale with the nozzle radius R_n. In both cases, the initial radius slightly exceeds the nozzle radius as discussed in Section 5.4.1. Additionally, the larger nozzle causes the IC regime as well as the EC balance to start at a larger radius. The time scale θ of the exponential decrease is identical for both experiments and exhibits the same relationship with the relaxation time, i.e. $\theta \approx 2\lambda$. Nevertheless, the breakup time slightly increases with the nozzle size, because the EC balance starts at a larger radius.

5.5 Analysis of the filament thinning

We have detected different thinning rates during the elasto-capillary regime in static capillary breakup and jetting experiments. To determine the origin of this difference, an analytical and numerical analysis of the thinning filament is conducted for both setups. We start our analysis from a simple zero-dimensional force balance balance that is introduced in the following section. Contrary to some other studies on the rupture of viscoelastic filaments [107, 161, 162], we do not consider the full expression for the mean curvature in the capillary pressure term. Since we are mainly interested in the elasto-capillary balance, it is more

straightforward to approximate the filament as a uniform cylindrical column with a constant radius R.

5.5.1 Stress balance for a viscoelastic filament

As a first step, we formulate a general expression for the tensile force F_z in the thinning ligament. The total axial force in the ligament is composed of bulk stresses applied to the cross-sectional area of the thread and the line force in the axial direction:

$$F_z = \pi R^2 \left(-P + 2\eta_s \frac{\partial v_z}{\partial z} + \sigma_{p,zz} \right) + 2\pi R\gamma. \tag{5.13}$$

The bulk stresses are composed of an isotropic pressure $-P$ and the extra stress, which consists of a viscous contribution from the solvent and an elastic term σ_p from the dissolved polymer. The pressure can be eliminated in favour of radial components with the stress boundary condition [79]:

$$-P + 2\eta_s \frac{\partial v_r}{\partial r} + \sigma_{p,rr} = -\frac{\gamma}{R} + \frac{1}{2}\rho v_r^2, \tag{5.14}$$

where the last term includes the inertia from the moving boundary. By assuming a time-varying uniaxial extensional flow field (see Appendix B), the axial and radial velocity gradient are linked via the strain rate $\dot{\epsilon}(t)$ (see Eq. B.1), which is given by

$$\dot{\epsilon}(t) = -\frac{2}{R}\frac{dR}{dt}. \tag{5.15}$$

Combining the force balances in the axial and radial direction yields a general stress balance for a slender viscoelastic filament:

$$\frac{F_z}{\pi R^2} = \frac{\rho}{2}\left(\frac{dR}{dt}\right)^2 + \frac{\gamma}{R} + 3\eta_s\dot{\epsilon} + \Delta\sigma_p. \tag{5.16}$$

The tensile stress in the filament is balanced by an inertial term, the capillary pressure from the axial curvature, a viscous stress of the solvent, where the characteristic Trouton ratio $Tr = 3$ appears, and the polymeric normal stress

difference $\Delta\sigma_p = \sigma_{p,zz} - \sigma_{p,rr}$. The elastic nature of the dilute polymer solution can be expressed by employing an elastic dumbbell constitutive model (FENE-P) [163]. The FENE model assumes that the polymer solution consists of a Newtonian solvent containing a dilute suspension of polymer chains that are modelled as non-linear elastic springs with a maximum extensibility L^2. Entov and Hinch [106] have used this model to demonstrate the slowest relaxation mechanism, that of the entire molecule, is the only relevant relaxation timescale for capillary breakup. The elastic deformation of the polymer coils is described with the conformation tensor $\mathbf{A}$ that is related to the connector vector between the two ends of the dumbbell $\mathbf{Q}$ as

$$\mathbf{A} = \frac{\langle \mathbf{QQ} \rangle}{Q_{eq}^2}. \tag{5.17}$$

In this definition, the ensemble average of the dyadic product of the dumbbell connector vector is scaled with the equilibrium size of the freely jointed chain Q_{eq}^2 [25]. Deforming these dumbbells generates a polymeric stress that is expressed as

$$\sigma_{\mathbf{p}} = G\left(Z\mathbf{A} - \mathbf{I}\right), \tag{5.18}$$

where the parameter Z is the correction term accounting the non-linearity and the finite extensibility of the dumbbell as

$$Z = \frac{L^2}{L^2 - \mathrm{tr}(\mathbf{A})} \tag{5.19}$$

with $\mathrm{tr}(\mathbf{A})$ the trace of the conformation tensor. The elastic deformation of the polymer coils under flow is correlated to the creation of polymeric stress by the microstructural evolution equation:

$$\frac{D\mathbf{A}}{Dt} - \mathbf{A}\nabla\mathbf{v} - \nabla\mathbf{v}^T\mathbf{A} = -\frac{1}{\lambda}\left(Z\mathbf{A} - \mathbf{I}\right), \tag{5.20}$$

where the upper-convective derivative of the tensor describes the confirmation changes in the dumbbell. In the limit of $L \to \infty$, finite extensibility effects are absent and the solution behaves as an elastic Oldroyd-B solution. Due to the radial symmetry and the uniaxial extensional flow field, the tensorial evolution equation reduces to a set of two differential equations, one for the axial (A_{zz}) and one for the radial (A_{rr}) components:

$$\dot{A}_{zz} = -4\frac{\dot{R}}{R}A_{zz} - \frac{1}{\lambda}(ZA_{zz} - 1) \tag{5.21}$$

$$\dot{A}_{rr} = 2\frac{\dot{R}}{R}A_{rr} - \frac{1}{\lambda}(ZA_{rr} - 1). \tag{5.22}$$

In these equations, the dotted symbols $\dot{R}$, $\dot{A}_{zz}$ and $\dot{A}_{rr}$ represent the time derivative of the respective variable. These equations form a closed set of equations in combination with the stress balance of the filament (Eq. 5.16), in which the polymeric stress is determined with Eq. 5.18. To identify the relative importance of the different terms in the stress balance, the stress balance and the evolution equations are non-dimensionalised by introducing the dimensionless radius $h = R/R_0$, the dimensionless time $\tau = t/t_R$ and the dimensionless axial force $\bar{F_z} = F_z/(\gamma R_0)$, giving

$$\frac{\dot{h}^2}{2} = \frac{\bar{F_z}}{\pi h^2} - \frac{1}{h} + 6\,Oh_s\frac{\dot{h}}{h} - Ec\,Z(A_{zz} - A_{rr}). \tag{5.23}$$

$$\dot{A}_{zz} = -4\frac{\dot{h}}{h}A_{zz} - \frac{1}{De}(ZA_{zz} - 1) \tag{5.24}$$

$$\dot{A}_{rr} = 2\frac{\dot{h}}{h}A_{rr} - \frac{1}{De}(ZA_{rr} - 1). \tag{5.25}$$

The scaling introduces a new dimensionless group in the equations, the elastocapillary number, $Ec = GR_0/\gamma$, which is the ratio between the elastic modulus of the dilute solution and the initial capillary pressure. The Ohnesorge number Oh_s is based on the solvent viscosity and is related to the other dimensionless groups as

$$Oh_s = \frac{Ec\,De}{\eta_{sp}} \tag{5.26}$$

using the specific viscosity η_{sp} that compares the polymeric and the solvent contribution to the viscosity, $\eta_{sp} = \eta_p/\eta_s = G\lambda/\eta_s$ [164]. The dimensionless numbers for the 0.1% PEO_2 model solution are listed in Table 5.5 for both CaBER and jetting experiments, where the latter values are calculated with $R = 85$ μm.

	Oh_s	De	Ec
CaBER	0.0040	0.445	0.0029
Jetting	0.0137	18.0	0.0346

Table 5.5: Dimensionless numbers of the CaBER and jetting experiments for the 0.1 % PEO_2 solution.

5.5.2 Tensile force difference

In order to evaluate the stress balance in the filament, the tensile force F_z should be determined for both experimental setups. For the CaBER experiments, the filament is connected to two fluid drops on the stationary end plates. These drops act as quasi-static reservoirs that soak up the fluid drained into them from the thinning filament. They also diminish the no-slip boundary condition at the end plates, which would otherwise induce a radial shear flow near the ends of the radially-contracting fluid thread [3]. The line tension acting at the junction of the cylindrical surface and spherical drop results in an axial force $F_z(t) = 2\pi\gamma R(t)$ [116]. Accordingly, a stress balance for the static CaBER experiment is constructed, where the viscous stress contribution is neglected because of the small solvent Ohnesorge number (see Table 5.5), giving

$$\frac{\dot{h}^2}{2} = \frac{1}{h} - Ec\, Z(A_{zz} - A_{rr}). \tag{5.27}$$

This stress balance was proposed by Tirtaatmadja et al. [79] similar to the seminal analysis of Entov and Hinch [106], who considered the viscous stress of the solvent instead the inertial contribution. The theory of Entov and Hinch was expanded by Clasen et al. [107] by regarding the filament as a slender axisymmetric volume taking the full description of the curvature into account (see Eq. 2.21). In this case, the stress balance is solved with an asymptotical analysis in the centre of the thread and on the end drops. To obtain a complete expression for the tensile force, a similarity analysis in the corner region is performed using the full leading order momentum balance (see Eq. 2.20) including a polymeric stress contribution. This analysis shows that the tensile force evolves as $F_z(t) \approx 3\gamma R(t)$, revealing that the approximated force in Eq. 5.27 is quite reasonable.

The theoretical analysis by Clasen et al. [107] does not distinguish between a static liquid bridge and a continuous jet, although the simulation results are only compared with experimental results of static capillary tests. However, we

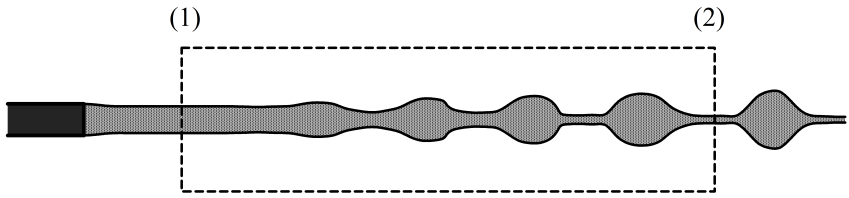

Figure 5.16: Control volume of the viscoelastic jet.

have clearly shown the difference between these two experimental setups in the EC regime in Section 5.4. A different approach for acquiring an expression for the tensile force in a jet was suggested in the research on the gobbling phenomenon [141]. The evaluation of the tensile force is not solely based on a single Lagrangian element, but we take a step back and look at the entire jet. The axial force can be estimated by integrating the one-dimensional momentum equation over a control volume that is shown in Figure 5.16. The control volume is located between two cross sections of the jet. The former is located at a stationary location right below the nozzle in the stable section where the jet is still uniform. The latter is positioned in the centre of a thinning filament between two adjacent beads. The one-dimensional momentum equation is deduced for a Newtonian liquid in Appendix C. An elastic contribution from the polymer molecules is added to Eq. C.30 to describe a viscoelastic jet, giving the following integrated equation

$$\frac{\partial}{\partial \tau}\left(\int_{\bar{z}_1}^{\bar{z}_2}\left(h^2\bar{v}\right)d\bar{z}\right)+h^2\bar{v}^2\Big|_{\bar{z}_1}^{\bar{z}_2}=h^2\left(K+3Oh_s\frac{\partial \bar{v}}{\partial \bar{z}}+\Delta\sigma_p\right)\Big|_{\bar{z}_1}^{\bar{z}_2}=\frac{\bar{F}_z}{\pi}\Big|_{\bar{z}_1}^{\bar{z}_2}, \tag{5.28}$$

where $\bar{v}$ and $\bar{z}$ are respectively the dimensionless velocity and the dimensionless axial coordinate and K is the curvature term. By averaging this equation over a time interval that is substantially longer than the time between two beads passing across any given cross-section of the jet, the first term on the left-hand side can be dropped. Moreover, the time averaging implies that the convective term can be rewritten in function of the flow rate as

$$h^2\bar{v}^2=\frac{\bar{\dot{Q}}\bar{v}}{\pi}. \tag{5.29}$$

Since the flow rate and the jet velocity remain constant on both ends of the

control volume, the convective term is constant and therefore Eq. 5.28 implies that the tensile force exerted on any cross-section remains constant. The value of this force is estimated by applying Eq. 5.23 to the first cross-section close to the nozzle. In this uniform section of the jet, the inertial, viscous and elastic contribution can be neglected, resulting in a simple expression for the tensile force $F_z = \pi R_0 \gamma$. Inserting this constant force into Eq. 5.23 generates a general stress balance for the viscoelastic jet:

$$\frac{\dot{h}^2}{2} = \frac{1}{h^2} - \frac{1}{h} - Ec\, Z(A_{zz} - A_{rr}), \tag{5.30}$$

where the solvent viscosity term is disregarded due to the small value of Oh_s. This stress balance is different from the balance for the gobbling phenomenon [141], since the inertial term is taken into account instead of the viscous solvent dissipation. Unlike the capillary breakup of a static bridge of Eq. 5.27, an additional term appears in the stress balance originating from the creation of new surface near the nozzle of the jet. This constant force will grow increasingly important close to breakup as the area of the liquid column rapidly reduces.

5.5.3 Elasto-capillary balance

To verify the importance of the different tensile forces for the two free-surface flow geometries, both stress balances should be evaluated during the elasto-capllary regime, where the inertial terms can be neglected. To this end, we will derive an expression for the polymeric stress $\Delta\sigma_p$, which is closely connected to the microstructural evolution equations (Eqs. 5.24 - 5.25). Entov and Hinch [106] presented an elegant analytical solution for the evolution equation assuming that the axial stretch of the polymer chain is large ($A_{zz} \gg 1$ & $A_{zz} \gg A_{rr}$). This assumption implies that only Eq. 5.24 should be solved to describe the increase of elastic stresses. During the EC balance, the deformation is still small compared to the maximal extension ($A_{zz} \ll L^2$), so the finite extensibility does not play a role and $Z \approx 1$. Under the assumption that the initial value of the axial stretch equals one ($A^0_{zz} = 1$), the following solution for the polymeric stress is derived as

$$\Delta\sigma_p = \frac{G}{h^4} \exp\left(-\frac{\tau}{De}\right). \tag{5.31}$$

Inserting this expression into Eq. 5.27 for the CaBER experiment and ignoring the inertial term results in an exponentially decreasing filament radius:

$$h = Ec^{1/3} \exp\left(-\frac{\tau}{3De}\right). \tag{5.32}$$

Apart from the prefactor of $2^{-1/3}$ that was found by the similarity analysis of the corner region, this expression is equivalent to Eq. 2.33 that was used to process the CaBER experiments. According to this expression, the ligament radius will only reach zero at an infinite time, since the finite extensibility of the polymer molecules is not taken into account. Entering Eq. 5.32 into Eq. 5.31, the elastic stretch as well as the polymeric stress appear to be growing unrestrictedly. However, when the axial stretch A_{zz} approaches the finite extensibility parameter L^2, the non-linear correction term Z will lead to an upper bound of the polymeric stress and the finite extension will determine the final breakup of the filament.

To assess the thinning rate of the jet in the EC regime, the expression for the polymeric stress is inserted into the stress balance of the inertia-viscoelastic jet (Eq. 5.30). As the radius approaches zero, the inertial term and the capillary pressure term can be neglected and the dominant balance is established between the axial stress and the elastic stress. At this time, the radius is described by

$$h = \sqrt{Ec} \exp\left(-\frac{\tau}{2De}\right). \tag{5.33}$$

This is the same expression that was found for the gobbling phenomenon, where the viscous term was neglected in the stress balance instead of the inertial term [141]. Like in the previous analysis for the CaBER, the radius decreases exponentially in the EC regime, however the time scale is different. The creation of new surface near the nozzle generates a tensile force in the jet which changes the thinning dynamics. Introducing this constant force into the stress balance changes the dimensionless time scale from $3De$ to $2De$, which is the value that was observed throughout all jetting experiments. Consequently, the difference in tensile force is key to explain the different thinning rates in the EC regime between static capillary breakup and jet breakup of viscoelastic liquids.

This concept of the different tensile forces cannot be directly experimentally verified in the two setups, because the force in the thread is too small to measure. However, the shape of the corner region, where a filament is attached to the neighbouring drops, might give an indication on the evolution of the force.

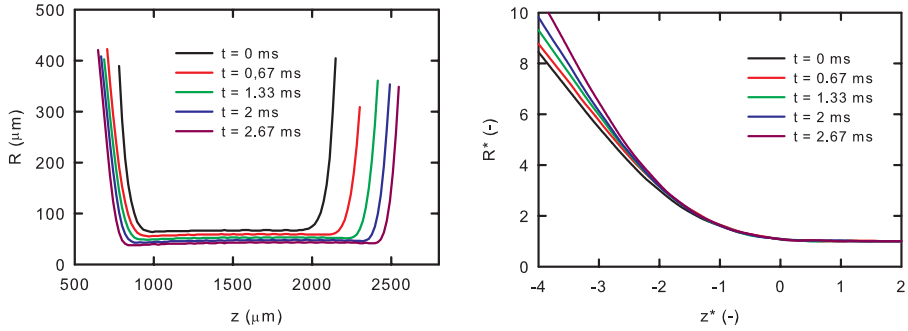

(a) regular profiles (b) scaled profiles

Figure 5.17: Filament profiles of the 0.1 % PEO_1 solution during a CaBER experiment, for which time until breakup is indicated. (a) The profiles R are shown as a function of the axial coordinate z. (b) The rescaled edge profiles of the corner region exhibit a similar shape in agreement with previous simulations and observations [107].

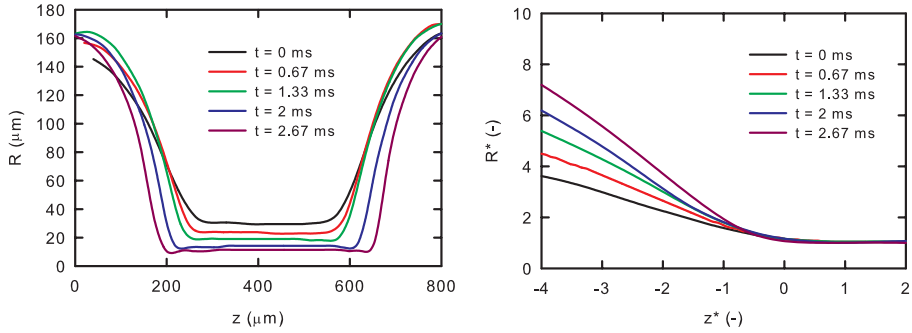

(a) regular profiles (b) scaled profiles

Figure 5.18: Experimental filament profiles of a jet of the 0.1 % PEO_1 solution with We = 2.9. The time until breakup is indicated for each profile. (a) The selected profiles R are shown as a function of the axial coordinate z. (b) The edge profiles are rescaled with the minimal thread radius and do not show the same self-similarity as the CaBER profiles.

When the tensile force decreases exponentially in time, as it does for a static liquid bridge since $F_z(t) \sim R(t)$, simulations and experiments have shown that this corner should reveal a self-similar structure of the corner region [107, 165]. To examine the existence of this similarity region, all lengths need to be scaled with a characteristic length scale being the minimal radius R_m, giving

$$R^* = \frac{R}{R_m} \tag{5.34}$$

$$z^* = \frac{z - z_0}{R_m}. \tag{5.35}$$

The axial origin z_0 is asymptotically located in the corner region. These rescaled edge profiles are shown next to the original profiles in Figure 5.17 for a static capillary breakup experiment of the 0.1 % PEO_1 solution. The experimental profiles converge properly onto a master curve, proving the self-similar structure of the corner. Hence, it can be inferred that the tensile force is exponentially decreasing as expected for the CaBER experiment. Additionally, jetting profiles are redrawn with the same scale. To obtain sufficient resolution in the corner region, the thinning jet was visualised with the same microscopic objective that was used for the CaBER experiments. Due to the limited field of view of this setup, a rather low Weber number of 2.9 was chosen to view a sufficient amount of subsequent instabilities. Figure 5.18 shows a sequence of edge profiles. The consecutive rescaled corner regions cease to coincide when the drop is approached. Consequently, the absence of a similarity region for the jetting experiments suggests a different tensile force in the thread that does not decrease exponentially in time as in the CaBER experiments, which explains the different thinning rates in both experiments.

5.5.4 Numerical simulations

The combination of the simplified force balance in the filament (Eq. 5.27 or 5.30) and the evolution equation (Eqs. 5.24 - 5.25) makes an initial value problem that can be used to describe the complete thinning of the inertia-elastic filament. This simple model is used to explore the transitions between different thinning regimes in both CaBER and jetting flows. By solving the microstructural evolution equation, the growth of the axial stretch A_{zz} provides insight in the polymer deformation in the uniaxial extensional flow field. The equations are solved in Matlab with an implicit BDF-solver (routine ode15s) to cope with the stiffness of the system. The transition from the inertia dominated to

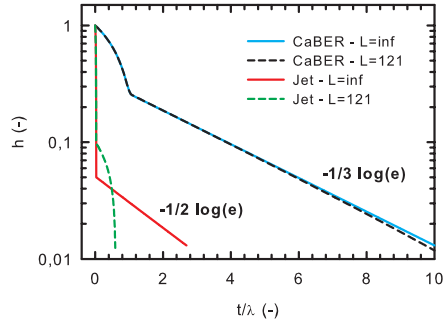

(a) Radius

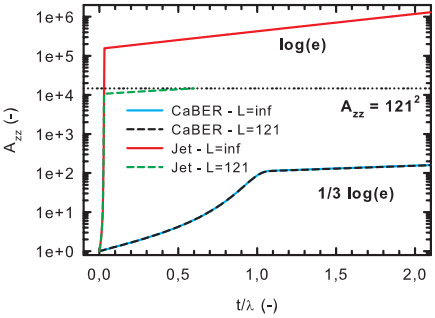

(b) Axial stretch

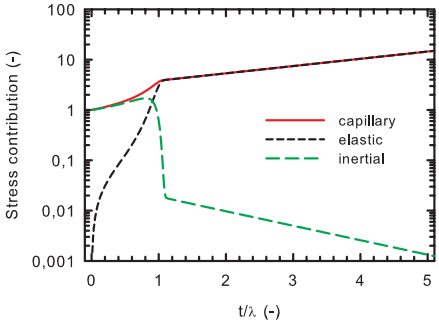

(c) Stress CaBER

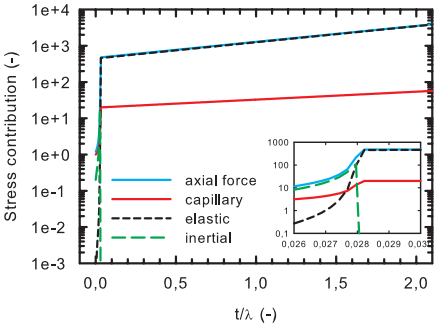

(d) Stress Jet

Figure 5.19: Numerical simulation of capillary breakup in the jetting and CaBER setup with the dimensionless parameters listed in Table 5.5. (a) The evolution of the filament radius, (b) the axial stretch of the polymer chains and the evolution of the stresses for $L = \infty$ in (c) the CaBER and (d) the jetting setup, in which the insert focusses on the transition from the IC to the EC regime.

elasto-capillary regime causes an abrupt change in the polymeric deformation, so the absolute and relative tolerances are chosen at a low value of 10^{-10}.

A general comparison of the numerical simulation for both setups is presented in Figure 5.19. The reference radius R_0 is chosen to resemble the experimental observation and therefore the dimensionless groups in Table 5.5 are used for the calculations. The initial value of the three dimensionless variables are all equal

to one for these first simulations: $h^0 = 1$, $A^0_{zz} = 1$ and $A^0_{rr} = 1$. Figure 5.19a compares the evolution the dimensionless filament radius h as function of time, which has been scaled with the relaxation time to emphasise the different time scales in the EC regime. When finite extensibility effects are neglected ($L = \infty$), the time scales of 3λ and 2λ are recovered over a long period for the CaBER and jetting case respectively, conforming with the experimental observations and the analytical derivation in Section 5.5.3.

For the CaBER simulations, the transition for the IC to the EC regime is explained by the temporal evolution of the stress contributions in Eq. 5.27 that is shown in Figure 5.19c. Initially, the polymer chains are close to the equilibrium confirmation and the inertial acceleration balances the capillary pressure in the fluid column. This balance results in a fast decay of the radius inducing strong stretching of the polymer, as shown in Figure 5.19b. The elastic stress in the column rises quickly to balance the capillary pressure and the inertial contribution drops to a negligible value. As a result of this elasto-capillary balance, the growth of the axial deformation of the chains suddenly slows down to an exponential increase with a time constant corresponding to three times the relaxation time of the fluid: $A_{zz} \sim \exp(t/3\lambda)$.

The respective elastic and capillary stresses in Figure 5.19c match this exponential increase. If the finite extensibility effects are included in the analysis, a deviation from the exponential decrease of the filament radius is observed in Figure 5.19a at $h \approx 0.02$, which corresponds to an axial stretch $A_{zz} \approx 0.1L^2$. As the axial deformation approaches the finite extensibility parameter, the non-linear correction term Z increases considerably, resulting in a sudden breakup.

In the jetting simulations in Figure 5.19a, the filament radius drops initially much faster in comparison to the CaBER case before reaching an EC balance. This fast decay originates from the different stress balance of which the evolution of the different terms is shown in Figure 5.19d. The term driving the filament breakup is the stress from the constant axial force. This term scales with the inverse square radius and therefore increases more quickly than the capillary stress in the CaBER case. This larger driving stress induces a higher initial acceleration, generating sufficient inertial stress to obtain an equilibrium, as can be seen in the inserted graph. Moreover, the polymer chains have to be stretched much further to produce sufficient elastic stress to balance this axial stress. Eventually, the elastic stresses reach the axial stress level, at which point the inertial stress drops. However, the following balance is then not an EC, but rather a balance of axial and elastic stresses.

Figure 5.19b shows that the axial deformation of the chains at the onset of this regime is 3 orders of magnitude larger than at the onset of the EC balance in the CaBER case for $L = \infty$. Hence, the transition to the axial-elastic (AE) stress balance occurs at dimensionless stresses that are several orders of magnitude larger than in the former case. Once this balance is reached, the axial stretch and the elastic stress also increase exponentially, but with a smaller time constant: $A_{zz} \sim \exp(t/\lambda)$. Contrary to the CaBER simulations, an exponential decrease of the filament radius is not observed when finite extensibility effects are considered. The initial polymer deformation is so large that the inertial regime is immediately followed by a non-linear elastic stress build-up, leading to a very fast breakup of the filament.

These numerical simulations are compared with experimentally obtained filament radii in Figure 5.20. The model solution for the CaBER case using $R_0 = 1$ mm displays a very similar shape as the experimental curve, however the onset of the EC regime occurs at a higher radius. This inconsistency in the transition radius was also encountered in previous studies [79, 166]. Since the IC regime typically demonstrates necking near the end droplets, it is highly improbable to accurately capture this regime with a zero-dimensional model. A better correspondence to the experimental EC balance is found by choosing a lower value for the reference radius R_0. Decreasing the reference radius however results in a poor description of the inertia-capillary regime. Nevertheless, the EC balance is correctly described by the model and the breakup time is well predicted by including finite extensibility effects.

The jetting simulations also show good qualitative agreement with the experimental data, but display the opposite shift of the onset of the AE balance. Due to the large initial stretching that is required to reach an AE balance, the simulated transition radius is too low. An improved consistency is obtained by increasing the initial deformation of the polymer molecules A^0_{zz} [141, 153]. It is probable that the polymer chains are partially oriented and elongated after exiting the nozzle. At this point, the velocity field in the jet undergoes an abrupt change from a Poiseuille flow inside the tube to a plug flow in the initial straight section of the jet. This stick-slip singularity at the nozzle exit results in potentially large initial elastic stresses in the jet [167]. Since the Deborah number in Table 5.5 is sufficiently large ($De \gg 1$), effects of this initial configuration can propagate along the jet while the fluid column begins to exhibit the linear instabilities [141]. The pre-stretch at the nozzle exit is included in the jetting model by changing the initial chain confirmation ($A^0_{zz} > 1$,

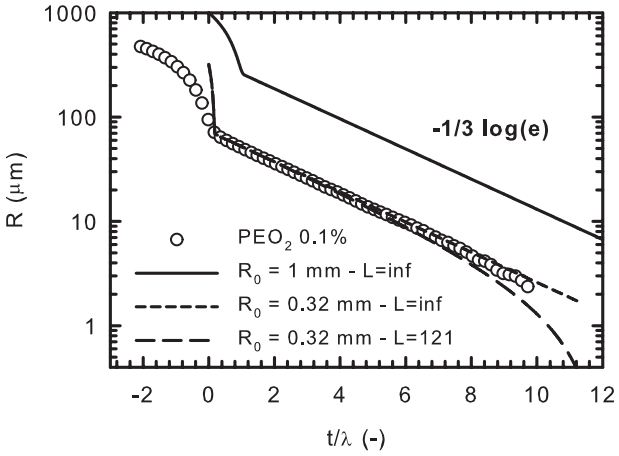

(a) CaBER

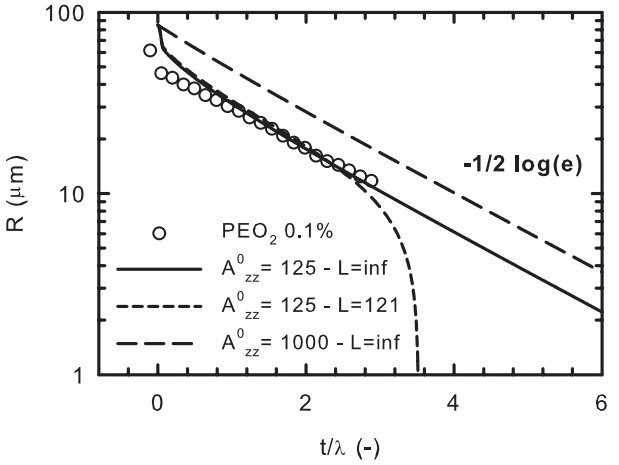

(b) Jet

Figure 5.20: Comparison of the experimental evolution of the minimal radii with numerical simulation. (a) For the CaBER setup, an agreement between experiment and model is found by lowering the initial radius R_0. (b) The jetting simulations are matched to the experimental observations by changing the initial axial stretch A^0_{zz} of the polymer molecules.

$A^0_{rr} = A^{0\,-1/2}_{zz}$) and by incorporating this additional elastic contribution, the initial axial stress in the jet is

$$\frac{F_z}{\pi R_0^2} = \frac{\gamma}{R_0} + Ec\,Z\left(A^0_{zz} - A^{0\,-1/2}_{zz}\right). \tag{5.36}$$

The initial confirmation A^0_{zz} and the associated initial stress are new initial values for the numerical simulations of the coupled differential equations for the jet (Eqs. 5.24, 5.25 and 5.30). A^0_{zz} becomes an extra parameter to fit the experimental observations and the results for two different values of pre-strech are presented in Figure 5.20b. By employing the larger pre-stretch $A^0_{zz} = 1000$, an axial-elastic balance is immediately established at the initial radius and the appearance of an initial inertia-capillary thinning is suppressed. The modelled breakup exhibits an extensional decrease of the filament radius with a time scale of two times the relaxation time matching the experimental radius decay. A more consistent description is acquired by reducing the initial axial stretch to $A^0_{zz} = 125$. The modelled radius shows a more gradual drop from the initial value and subsequently approaches the experimental data points. The driving axial stress is not solely balanced by the elastic stress for times $t < 2\lambda$, leading to a fairly long transition zone where the capillary term still affects the thinning. The elastic stress only matches the driving stress after this period and then an exponential decrease of the filament radius with the correct time scale is retrieved.

During the AE balance, the polymer chains are still stretched at a faster rate than in the CaBER case (see Figure 5.19b). Hence, breakup occurs slightly sooner than in the experiments, when finite extensibility effects are included in the model. However, in both the CaBER and the jetting case, the finite extensibility of the polymer chains affects the thinning dynamics sooner in the simulations than in the experiments. A comparable difference between the modelled and experimental finite extensibility effects is also encountered in other studies on capillary breakup of similar polymer solutions [61,168]. Two possible explanations have been proposed for the earlier onset of these finite extensibility effects. The former assumes a difference between a theoretical parameter L that was calculated based on molecular parameters (see Eq. 5.2) and the experimentally observed L [53]. The latter states that pre-averaging of the connector vector $\mathbf{Q}$ in the Peterlin approximation of the FENE model overpredicts the elastic stresses in a uniaxial extensional flow compared to the full FENE model [169].

5.5.5 Breakup length

The breakup length L_p is an important parameter to quantify the breakup of a free jet [15, 16]. It is generally defined as the minimum distance from the nozzle over which the liquid jet is still connected. The correlations presented in this section are only valid for the relatively moderate Weber numbers that are examined in this study. For very large Weber numbers, the velocity difference between the jet and the surrounding air generates shear at the jet interface, leading to waves on the jet surface of due to the Kelvin-Helmholtz instability [17, 84, 136]. The breakup length L_p is expressed with the jet velocity v_0 and the pinching time t_p as

$$L_p = v_0 t_p. \tag{5.37}$$

The pinching time can be approximated by the characteristic time scale for the growth of instability [17]. For an inviscid Newtonian fluid, the Rayleigh time t_R (Eq. 2.9) is used as the characteristic time giving

$$\frac{L_p}{R_0} \sim We^{1/2}. \tag{5.38}$$

For a low viscous elastic samples, the Rayleigh time remains a good time scale for the linear stability and the IC regime. However, the EC regime is generally the longest regime in breakup of a viscoelastic liquid and the duration of this regime scales with the relaxation time λ of the fluid. A time span of the EC regime is found by rewriting the jet radius evolution (Eq. 5.33) and solving the time at two transition radii: the filament radius h_{EC} where the EC balance starts and the radius h_{FE} where the finite extensibility of the polymer chains induces breakup. The combined pinching time for a low viscous elastic liquid is therefore given by

$$t_p \approx t_R + 2\lambda \ln\left(\frac{h_{EC}}{h_{FE}}\right). \tag{5.39}$$

The first transition radius h_{EC} can be determined from the jetting experiments, but the second transition radius h_{FE} cannot be experimentally resolved due to the limited resolution of the lens. However, the onset of finite extensibility effects can be estimated with the evolution of the axial stretch of the polymer chains. As shown in Figure 5.19b, the axial stretch A_{zz} increases exponentially during the EC regime as $A_{zz} \sim \exp(t/\lambda)$. Hence, the time span of the EC regime is also retrieved by evaluating A_{zz} at the onset and the end of this

regime. The axial stretch at the onset A_{zz}^{EC} is estimated with the stress balance in the jet (Eq. 5.30), where the inertial contribution and the capillary pressure term are neglected. The axial tension is then balanced by the elastic stress and by assuming that $A_{rr} \ll A_{zz}$, the axial stretch at the transition to EC regime is found as

$$A_{zz}^{EC} = \frac{1}{Ec\, h_{EC}^2}. \tag{5.40}$$

The polymer stretch close to the finite extensibility limit A_{zz}^{FE} is evaluated with the axial evolution equation (Eq. 5.24), where we expect a negligible temporal change of the polymer stretch [106, 110]. This gives an expression for the finite extensibility parameter $Z = 2\lambda\dot{\epsilon}$ that is inserted into Eq. 5.19 to find a solution for the polymer stretch:

$$A_{zz}^{FE} = L^2 \left(1 - \frac{1}{2\lambda\dot{\epsilon}}\right). \tag{5.41}$$

As the filament radius approaches zero, the strain rate diverges and the final term becomes negligible. A more conservative estimation is retrieved by taking the constant stain rate during the EC regime $\dot{\epsilon} = 1/\lambda$, giving $A_{zz}^{FE} = L^2/2$. The combined pinching time is thus estimated by

$$t_p \approx t_R + \lambda \ln\left(\frac{A_{zz}^{FE}}{A_{zz}^{EC}}\right) = t_R + \lambda \ln\left(\frac{L^2 Ec\, h_{EC}^2}{2}\right). \tag{5.42}$$

This time scale is inserted in Eq. 5.37 to get an expression for the breakup length. Taking a value of $h_{EC} = 0.5$, which is typical for the polymer solutions that are used in this study, gives

$$\frac{L_p}{R_0} \sim We^{1/2} \left(1 + De \ln\left(\frac{L^2 Ec}{8}\right)\right). \tag{5.43}$$

Figure 5.21 shows the jet breakup length of different PEO_2 solutions as a function of the Weber number. Experiments with $We > 4$ appear to follow the scaling with the square root of the Weber number, as illustrated by the reference slope of 1/2. Additionally, more concentrated solutions exhibit larger breakup lengths for the same Weber number. Seeing that the relaxation time λ increases with concentration, this observation is in agreement with the proportionality of the breakup length to the Deborah number.

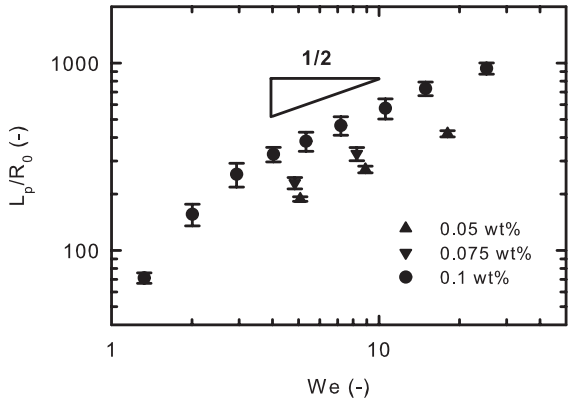

Figure 5.21: Breakup distance of jets of PEO_2 solutions as a function of the Weber number. The breakup length shows a dependancy to square root of the Weber number.

5.6 Conclusion

In this chapter, we have investigated the instability growth and the resulting breakup of weak viscoelastic jets with low Ohnesorge numbers. Jetting experiments were executed for three model solutions over a range of Weber numbers from the dripping-jetting transition at $We = O(1)$ to long stable jets at $We = 80$, which corresponds to the experimental limit of our setup. Due to flow rearrangement when the fluid exits the nozzle, the polymer molecules cause a limited extrudate swell that increases with polymer concentration and decreases with the jet velocity. Capillary instabilities start to form in the initial linear stability zone and the wavenumber of the disturbances are in line with theoretical predictions. The stable zone is followed by a sudden decrease of the filament radius in a non-linear inertia-capillary regime. The high strain rates in the filament stretch the polymer molecules and the generated elastic stresses stabilise the filament resulting in a characteristic beads-on-a-string morphology.

We have mainly focused on this important elasto-capillary regime where the minimal radius of the instability decreases exponentially in time. The thinning dynamics during this regime are compared with static capillary breakup experiments and a different time scale for the exponential decay is identified for both free-surface flows. Whereas the generally employed time scale $\theta = 3\lambda$ is observed for the CaBER experiments, the jetting experiments exhibit a time

scale $\theta = 2\lambda$, which was previously only suggested for jets in the vicinity of the dripping to jetting transition. This new scaling remains valid for all examined Weber numbers. Both time scales are explained with a stress balance over the viscoelastic filament. The different scaling in the jet is attributed to a constant axial force in the jet, which is caused by the creation of new surface under the nozzle. Numerical simulations of the jet breakup with the FENE model are in agreement with the experimental observation by selecting a proper value for the initial deformation of the polymer molecules A^0_{zz}. Additionally, the experimental profiles of the corner region where the filament is connected to the droplet are rescaled according to the scales proposed by Clasen et al. [107]. The self-similar structure present in the CaBER experiments is not observed during the jetting experiments, indicating that the axial force is not decaying with the filament radius. The existence of a different scaling in the elasto-capillary regime in a continuous jet is not only of fundamental interest, but it also affects the interpretation of the new jetting rheometer [136], resulting in a 50 percent increase of the extracted relaxation time.

Chapter 6

Capillary breakup of suspensions of non-colloidal particles

In this chapter, we present our study on the capillary breakup of a second complex fluid, that is suspensions of spherical particles. Depending on the concentration and the particle size, the presence of particles alters the rheology of the fluid inducing effects ranging from strain thinning to the manifestation of yield stresses. We have limited this study to large, non-colloidal spheres in a Newtonian matrix and attempted to develop a framework for the extensional rheology of these systems.

6.1 Introduction

The capillary-driven breakup of Newtonian liquids has been studied intensively and the non-linear dynamics preceding droplet formation are fairly well understood [5]. The description of non-Newtonian fluids however remains a challenge in this strong extensional flow as the constitutive laws are usually not well tested in this regime [17]. Adding particles to a Newtonian matrix generates a complex fluid with a divergent flow behaviour under extensional deformation. Such fluids are for instance encountered as inks in graphic and other conventional printing operations, where the solid particles can disturb

the normal jetting process [170, 171]. Furthermore, inkjet printing is used as a fabrication tool for ceramic components and printed electronics, where the functional components of the ink are solid particles [10, 172]. Despite the practical importance of particle-laden drops, the knowledge on the effects of particles on the stability and breakup of liquid jets is rather limited compared to Newtonian fluids.

The breakup of Newtonian liquids was thoroughly discussed in Section 2.2, but we will briefly repeat the most important concepts that are employed in this chapter. The thinning dynamics of an unstable liquid thread are determined by the balance of surface tension with the dominant resisting force, which is either inertia or viscosity for a Newtonian liquid. The dominant thinning mechanism is revealed by the Ohnesorge number $Oh = \eta/\sqrt{\rho\gamma R}$, which compares the time scales of viscosity controlled breakup and inertia controlled breakup. Once a filament is sufficiently slender, the fluid motion is described by different self-similar solutions depending on the value of this dimensionless group. For moderate Ohnesorge numbers, a universal solution considering all terms of the one-dimensional Navier-Stokes equation was developed by Eggers [90]. In this case, the minimal radius R_m obeys the thinning law

$$R_m = 0.0304\frac{\gamma}{\eta}(t_p - t) \tag{2.27}$$

where t_p is the pinching time. Although the universality of the solution implies a validity for all fluids, in practice, this inertia-viscous (IV) scaling is merely observed in close proximity to breakup for fluids in a narrow viscosity range [95]. Nevertheless, Newtonian fluids with these viscosities are employed to generate stable droplets in inkjet printing applications [10]. More viscous fluids with larger Ohnesorge numbers tend to follow a different viscous (V) scaling. A symmetric self-similar solution to this equation was derived by Papageorgiou [99], giving the following expression for the minimal radius:

$$R_m = 0.0709\frac{\gamma}{\eta}(t_p - t)\,. \tag{2.29}$$

Recently, the extensional properties of suspensions have been investigated with free-surface flows by various research groups. Different thinning dynamics have been observed for suspensions with different particles sizes and volume fractions. Dispersions that exhibit shear thickening can show viscoelastic pinch-off or dilatancy effects depending on the strain rate [173–176]. However, other non-Brownian suspensions display a faster thinning rate close to pinch-off than that predicted by the viscous scaling law for the bulk viscosity [18–21, 177,

178]. This flow behaviour is not necessarily a strain thinning effect and can rarely be captured by a power-law model [20]. The shear response of these systems is dominated by hydrodynamic interactions and can be described by a single viscosity up to moderate particle concentrations [114]. This viscosity is proportional to the viscosity of the suspending medium and has a strong dependence on the particle volume fraction ϕ. Careful experiments on the shear rate dependence of these suspensions were performed by Zarraga et al. [179] who found no shear thinning for $\phi < 0.45$. Many semi-empirical correlations have been proposed to describe the relative shear viscosity η_r of the suspension. Throughout this chapter, we will use the Maron-Pierce model [180]

$$\eta_r(\phi) = \left(1 - \frac{\phi}{\phi_m}\right)^{-2}, \tag{6.1}$$

where $\eta_r = \eta/\eta_m$ is the relative viscosity compared to the medium viscosity η_m. The highest volume fraction is estimated by the random close packing limit of $\phi_m = 0.64$ [181]. This equation has the same form as the commonly used Krieger-Dougherty expression [182], which employs a different power law exponent $-[\eta]\rho\phi_m = -1.6$. It is found that the exponent of the Maron-Pierce model describes the suspension viscosity of the most concentrated suspension more accurately, as will be shown in Section 6.3.2.

The acceleration that is observed during the late stages of capillary breakup of these suspensions is in fact caused by the finite-size effects of the particles, rendering the continuum approximation invalid for small filaments. Furbank and Morris [18, 19] demonstrate this in an extensive experimental study on dripping and jetting flows of granular suspensions (with particle radius $R_p = 53$ - 103 μm) and describe the thinning as a two stage process. The necking is initially dominated by the suspension viscosity, followed by a second stage in which the suspending fluid properties appear to be critical. Lindner and co-workers continued this work by performing dripping experiments of granular suspensions with a wide range of particle sizes and concentrations. They claim that the second stage is split into a short regime where the thinning rate is independent of the volume fraction, matching that of the medium fluid and an accelerated regime where the suspension clearly thins faster than the medium fluid [21]. This acceleration is observed at very low particle concentrations, even when there is only a single particle in the thinning filament [177].

In this chapter, we will further quantify this acceleration of suspensions near pinch-off with capillary breakup tests of an unstable liquid bridge. Contrary to previous studies where the breakup dynamics are examined by comparison to

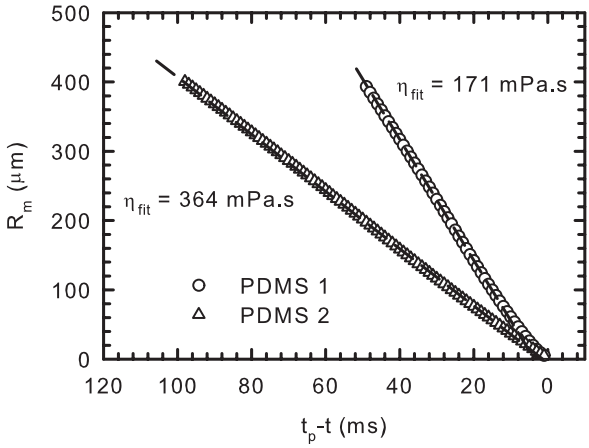

Figure 6.1: Thinning dynamics of the two viscous silicone oils. Both oils follow the viscous scaling for the most part of breakup process.

viscous oils with approximately the same viscosity, we will apply the self-similar scaling laws to extract material parameters. Furthermore, we will focus on the final thinning stage and use high resolution optics to distinguish the motion of individual particles. The model suspensions that are used in this chapter have been introduced in Section 3.1 and the CaBER setup has been thoroughly discussed in various sections of Chapters 2 to 4. Reference capillary breakup experiments on the Newtonian suspending media are presented in Section 6.2. The different stages in the pinching of the suspensions are described in Section 6.3, where a clear distinction is made between the thinning of the suspension and that of the interstitial fluid. A comparison to modelled capillary breakup is presented in Section 6.4, followed by the conclusions in Section 6.5.

6.2 Newtonian oils

As reference cases, capillary breakup experiments are performed on the two silicone oils without particles. For these inelastic fluids, the dominant material parameter resisting the breakup is indicated by the Ohnesorge number [4]. The global Ohnesorge number for this experiment, given in Table 6.1, uses the radius predicted at the cessation of stretching, determined by a lubrication solution

for a Newtonian viscous fluid (see Eq. 5.4). By comparing the characteristic thinning velocities of the viscosity and inertia dominated regimes, the boundary between the two regimes is located at a critical value $Oh^* = 0.2077$ [95]. Since the values in Table 6.1 are sufficiently above Oh^*, both oils initially display viscosity-dominated thinning.

	η_m $(Pa.s)$	Oh $(-)$	η_{fit} $(Pa.s)$
PDMS 1	0.180	1.20	0.171
PDMS 2	0.360	2.52	0.364

Table 6.1: Rheological properties of the silicone oils at a temperature of 22°C.

Figure 6.1 shows the evolution of the minimal radius during capillary breakup of the two silicone oils, in which the pinching time t_p is used as a temporal reference. As expected from the large Ohnesorge number, both fluids thin linearly in time consistent with the viscous scaling (Eq. 2.29), allowing the extraction of viscosities from the thinning data. The quality of the fits over a radius range from 250 to 50 μm is demonstrated in Figure 6.1 and the extracted viscosities $\eta_{fit} = 364$ mPa.s and $\eta_{fit} = 171$ mPa.s, respectively, are in agreement with the shear-viscosity values (see Table 6.1).

However, deviations from this viscous scaling occur close to breakup. This observation is highlighted in Figure 6.2, where, in order to simplify the comparison between samples, we eliminate viscosity from Eq. 2.27 and Eq. 2.29 by rescaling time and radius as follows. The time is rescaled with the viscous time scale [4],

$$t_\eta = \frac{14.1\,\eta_m R_0}{\gamma}. \tag{6.2}$$

so that both curves initially exhibit the same slope. The time axis is further shifted with t_c, the time at which the filament radius equals the reference radius, so both curves initially collapse. By rescaling the minimum filament radius with R_0, the viscous (V) scaling (Eq. 2.29) reduces to

$$\frac{R_m}{R_0} = \frac{t_p - t}{t_\eta} \tag{6.3}$$

and the inertia-viscous (IV) scaling (Eq. 2.27) becomes

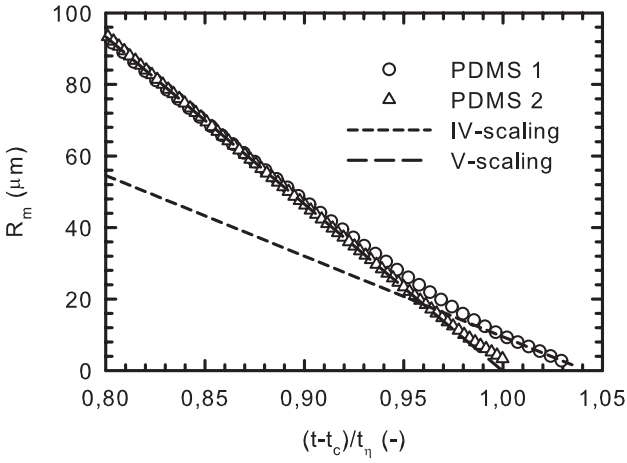

Figure 6.2: Enlargement of the final thinning dynamics of both silicone oils. The time is rescaled with t_η to allow a better comparison of both samples. The low viscous PDMS 1 clearly exhibits a transition from the viscous (V) scaling to the inertia-viscous (IV) scaling during the final breakup stages.

$$\frac{R_m}{R_0} = 0.429\,\frac{t_p - t}{t_\eta}. \tag{6.4}$$

In this representation shown in Figure 6.2, the thinning curves of both samples coincide, following the viscous scaling (Eq. 6.3) until a radius $R_m = 50$ μm. Although the filament thinning of PDMS 2 follows the viscous scaling until breakup, the thinning of the less viscous PDMS 1 under goes a transition and decelerates prior to breakup.

This transition in scaling has been explained by Eggers [5, 90]. He showed that the decaying filament radius gives rise to a strongly increasing capillary pressure close to pinch-off, resulting in a diverging strain rate (see Eq. 3.5). Hence, the inertial term grows more quickly than the other terms and can no longer be neglected in dominant balance. Thus, the pinching of the filament is controlled by an inertia-viscous-capillary balance (IV-scaling) and follows the similarity solution described by Eq. 6.4 prior to breakup, rather than the V-scaling. This deceleration of the breakup dynamics is accompanied by a shift of the location of the minimum radius in the axial direction from the centre of the filament towards the end drops, turning the initial symmetric viscous pinching into an

asymmetric pinching. Theoretically, the transition radius from viscous scaling to inertia-viscous scaling is approximated by equating the estimates of the inertial and capillary term as

$$R = R_0 Oh^{2/(2\beta-1)}, \tag{6.5}$$

with $\beta = 0.175$ [17]. However, this value is an order of magnitude larger than our experimental transition radius, which is comparable to other experimental observations [93]. The reason for this discrepancy is presently not understood, although it might be related to breaking of the symmetry which could delay the transition [4, 183].

Since the thinning of Newtonian fluids are generally used as a benchmark for more complex suspension dynamics, recognising this transition in crucial. Moreover, the transition radius we observe is comparable to the particle size in the current investigation and therefore comparable to the reported length scale at which changes in the break-up process occur due to finite-size effects [18, 21]. Thus, in order to decouple the transition of V- to IV-scaling from the suspension dynamics, most suspension experiments in this chapter are performed with PDMS 2 as a continuous phase.

6.3 Suspensions

6.3.1 Thinning stages

In order to quantify the particulate effects on the pinching dynamics, we have examined the filament evolution for suspensions with varying volume fraction and particle size. As an example of the general thinning dynamics we observe, Figure 6.3b shows the experimental breakup curve for 10% of PS20 in PDMS2. We also include a series of experimental images in Figure 6.3a to illustrate how the unstable filament approaches breakup. In general, we observe four thinning distinct thinning regimes, which we now describe: a suspension regime, a concentration fluctuation regime, an accelerated regime and a final deceleration regime governed by the properties of the medium fluid only.

In the initial suspension regime - illustrated by the first two images in Figure 6.3a - the filament initially appears entirely black, because the particles render the sample opaque. The suspension can be considered as a homogeneous fluid

(a)

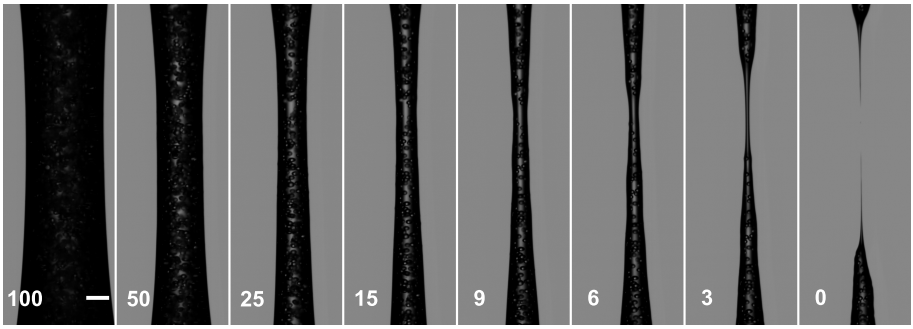

(b)

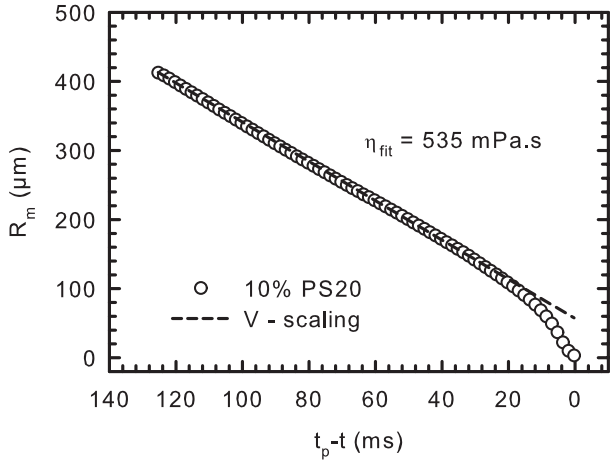

Figure 6.3: Evolution of the minimal radius during capillary breakup of suspension with $\phi = 0.10$ of PS20 in PDMS 2. Initially, the dynamics are solely determined by the effective viscosity of the suspension. Subsequently, the thinning velocity accelerates causing a faster rupture of the filament. The number in the bottom left of the images indicates the time to pinch-off $t_p - t$ in ms and the scale bar represents 200 μm. In the last three frames, localised thinning of the continuous phase between two particles is observed.

and the thinning dynamics are fully determined by the effective viscosity of the suspension. The viscosity that is recovered by fitting the viscous scaling (Eq. 2.29) to the minimal radius data, corresponds to the prediction of the Maron-Pierce correlation (see Eq. 6.1) for a particle fraction $\phi = 0.10$. In previous dripping studies, a clear linear decrease of the minimal radius R_m with time - as predicted by the similarity solutions - is not observed. The breakup dynamics are instead interpreted by comparing experimentally the suspension breakup dynamics with the thinning of a Newtonian oil with the same viscosity as the suspension [21, 177].

We recognise two reasons why the study of the breakup starting from an unstable filament has a more straightforward interpretation than a dripping experiment. First, the self-similar solutions are only applicable if the slenderness assumption is valid [95]. The instant creation of a slender, unstable filament in the CaBER allows the viscous scaling to remain suitable for most of the breakup process. In the dripping setup, the filament only gradually achieves the required slenderness to observe the self-similar shapes. This formation exhibits different dynamics, which are until now only empirically captured for suspensions [19]. Secondly, once this filament of the dripping experiment is slender enough, the diameter is often of the same magnitude as the particle size, particularly for larger granular particles. Hence, the fluid can no longer be treated as a continuum.

As the filament becomes thinner, transparent zones emerge and individual particles are clearly distinguished. The suspension appears heterogeneous revealing lighter oil-rich regions and darker zones with clusters of particles. We call this phase the concentration fluctuation regime. Regions of the filament with a lower particle density locally exhibit a smaller effective viscosity and will therefore thin faster. As the model of McIlroy & Harlen [22] predicts, these fluctuations in the local concentration of particles are amplified as the volume of the filament region is reduced, inducing an accelerated thinning rate compared to the suspension regime. Consequently, we observe a deviation from the viscous scaling law once the filament radii has reduced to 100 μm, as shown in Figure 6.3b.

The particle density fluctuations also manifest in the shape of the filaments shown in Figure 6.3a, starting from the fourth image (with time stamp 15). Unlike previous images where the surface is almost as smooth as that of a pure oil bridge, we now detect local curvature differences in the filament. This observation indicates the onset of localised thinning because gradients in the capillary pressure generate flow away from the point of highest curvature. Figure 6.4 displays the local curvature of the thinning filament at different times. The

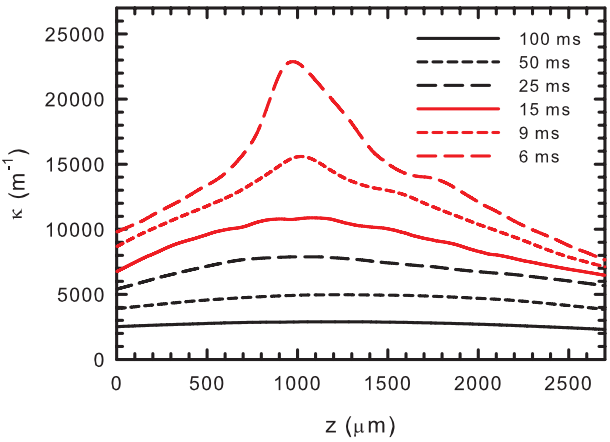

Figure 6.4: Local curvature of filaments of 10% PS20 in PDMS 2 that were shown in Figure 6.3a. The local pronounced maxima arising near breakup reveal a very localised thinning, caused by particle density fluctuations.

curvature κ is determined with the formula for an axisymmetric volume (Eq. 2.21). In the first three filaments, the curvature changes very gently, which is in agreement with an homogeneous fluid. However, the smoothness disappears in the last three filaments and a local maximum in the curvature emerges, indicating heterogeneous thinning of the thread. These particle density fluctuations in the suspension during capillary breakup are also observed by Roché et al. [174] during extensional experiments on concentrated cornstarch dispersions. However, the nearly periodic surface fluctuations between solvent-rich and jammed regions that are present in their work, are not detected in our samples, which are significantly less concentrated. Furthermore, similar concentration fluctuation effects are observed for concentrated suspensions of colloidal particles in a complex flow field with a strong extensional contribution [184].

After the concentration fluctuation regime, where a certain amount of particles are still present in the thinnest region of the filament, particle-density fluctuations in the thinning filament eventually lead to particle-free sections, which are clearly observed in the last three images of Figure 6.3a. In this particle-free zone, the radial velocity is locally accelerated, resulting in confined thinning with the filament resembling the shape of a power law fluid [185]. This continuous-phase thinning begins at roughly 7 ms before pinch-off for this particular suspension and the evolution of the minimum radius in this phase

(a)

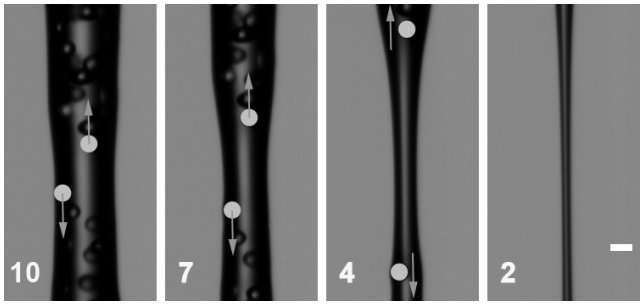

(b)

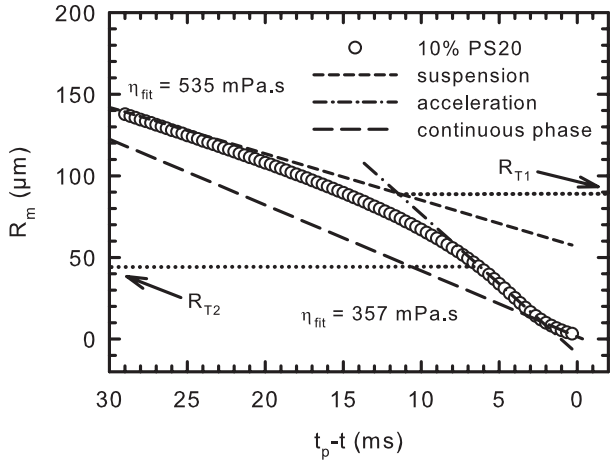

Figure 6.5: The final stages of the capillary breakup of 10% PS20 in PDMS 2. (a) The magnified images show that the final thinning takes place between two particles which are highlighted by the grey circles. Their movement reveals the large extension rates before pinch-off. The numbers in the bottom left indicate the time to pinch-off $t_p - t$ in ms and the scale bar represents 50 μm. (b) The evolution of the filament diameter shows that the accelerated regime is followed by a deceleration where the dynamics appear to return to the self-similar scaling of the continuous phase, demonstrated by the fitted viscosity. The onset of the particle density fluctuations is indicated with the transition radius R_{T1} as well as the onset of continuous phase thinning with R_{T2}.

is highlighted in Figure 6.5b. We split this continuous phase into two distinct regimes.

First, there is an accelerated thinning [21, 177] where the radius decays linearly with time and radial velocity $v_r = -dR_m/dt$ reaches a maximum. For this short period, the thinning is approximately twice as fast as that of the pure medium fluid. Enlarged pictures of this accelerated pinching stage are shown in Figure 6.5a, in which the two nearest particles are accentuated with a grey circle. The displacement of these particles in the consecutive frames demonstrates the acceleration in this zone. In these pictures, two particle clusters appear to form a barrier for the continuous phase, isolating roughly 2 nl of the medium fluid from the rest of the filament. Due to the slower or even arrested thinning in the clusters, the continuous phase in between is forced to resemble an hour glass shape similar to a small-scale filament stretching with the clusters as boundaries, resulting in a faster pinching of the thread.

Second, the radial velocity reduces and the thinning decelerates prior to breakup. This deceleration was not detected in previous studies on similar systems [18, 19, 21, 177, 178] because these small filament radii were below the resolution limit of the employed camera setup. By fitting these last radii with the viscous scaling (Eq. 2.29), the viscosity of the interstitial viscous oil is recovered. The thinning appears to return to the self-similar scaling of a Newtonian liquid bridge, indicating that the thinning is no longer affected by the presence of the particles. This final stage is also detected by the 1D-simulations of McIlroy and Harlen [22] and it is examined in more detail in Section 6.3.3.

Reviewing the breakup dynamics of this suspension, we have not encountered the interstitial fluid regime as described by Bonnoit et al. [21], where thinning dynamics observed between the suspension regime and the accelerated regime are governed only by the medium fluid. Figure 6.5b indicates that part of the concentration fluctuation stage has approximately the same thinning rate as the the final stage, so this region was probably labeled the interstitial fluid regime. However, we presume this zone is merely a transition state in the self-dilution of the sample, because there is no distinct physical ground why the suspension would thin at this rate. In the following sections the different thinning stages are separately regarded and the effect of changing different suspension properties is investigated. We first consider the first two stages, where there are still particles present in the neck, before continuing to the thinning of the interstitial fluid in the final two stages.

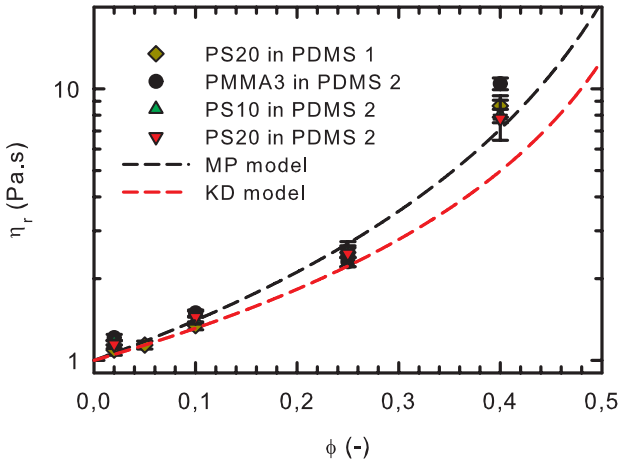

Figure 6.6: Extracted relative viscosity during the effective fluid stage of the examined suspensions. The values correspond better with the prediction from the Maron-Pierce model (Eq. 6.1) than from the Krieger-Dougherty model.

6.3.2 Suspension thinning and concentration fluctuations

To obtain a better understanding of the mechanisms causing this accelerated breakup, we have performed a series of CaBER experiments for different particle concentrations and sizes. Qualitatively, all samples follow the thinning curve of Figure 6.5b with the four thinning stages that are described in the previous section. Initially, the examined suspensions behave as effective Newtonian fluids. The initial linear section of the thinning curve is fitted with the viscous scaling law (Eq. 2.29) for each sample to acquire the characteristic viscosity. Figure 6.6 shows the extracted values as a function of concentration, displaying the relative viscosity η_r to allow the comparison of samples with different medium viscosities. The model prediction for the suspension viscosity (Eq. 6.1) is included and describes the data points fairly well. The characteristic viscosity is independent of particle size and altering the medium does not affect the relative viscosity. Only for $\phi = 0.40$, some minor differences between the samples are observed. This illustrates the difficulty of determining perfectly reproducible viscosities for more concentrated suspensions, because small variations in the particle volume fraction generate relatively large viscosity differences.

As the filament becomes thinner, particle density fluctuations are amplified

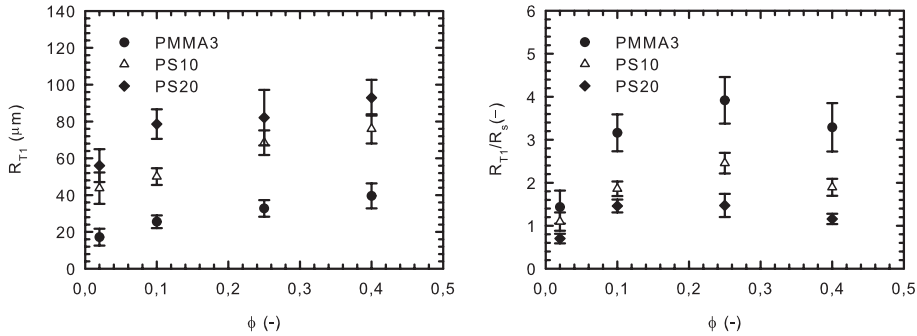

Figure 6.7: (a) Overview of the transition radius R_{T1} at which the particle density fluctuations start for the suspensions with PDMS 2 as medium. (b) The radii are rescaled with the length scale of Eq. 6.12.

for all examined samples. Local heterogeneities consequently emerge and the fastest thinning occurs in a locally diluted region. Although each sample demonstrates the four thinning regimes, we observe differences in the thinning rate of the accelerated regime and the transitions between the consecutive thinning stages occur at different filament radii. By examining the local slopes of the thinning curves, we explore the effects of changing suspension properties on the concentration fluctuation regime. We have chosen to quantify the onset of the dilution with a transition radius R_{T1}, which is defined as the intersection between fitting lines of the suspension regime and the accelerated regime (see Figure 6.5b). The precise value of the transition radius depends upon the initial particle distribution and so varies in consecutive experiments of the same suspension. The average transition radius is presented in Figure 6.7a as a function of volume fraction for the suspensions with PDMS 2 as medium. In general, the radius increases with volume fraction and particle size.

In order to understand this evolution, we define a structural length scale for the variation in the particle density. The distribution of non-interacting, identical spherical particles in a second medium is statistically characterised with a particle nearest-neighbour probability density function $H_p(r)$ [186]. This function describes the probability associated with finding the nearest neighbour particle at some given distance r from a reference particle. An evaluation of this function was first considered by Hertz [187] for an ideal system of non-interacting

point particles. This analysis assumes that the mixing process produces a random distribution of the particles so that the system has thermodynamical structure of an ideal gas in which the particles are Poisson distributed in the surrounding medium [188] and ignores the effects of excluded volume. These assumptions result in a probability density function

$$H_p(r) = 4\pi\rho_N r^2 \exp\left(-\frac{4}{3}\pi\rho_N r^3\right), \tag{6.6}$$

where ρ_N is the particle number density. The number density can be rewritten in terms of the volume fraction and the particle radius as $\rho_N = 3\phi/(4\pi R_p^3)$. Inserting this definition into the probability density function gives

$$H_p(r) = \frac{3\phi\, r^2}{R_p^3} \exp\left[-\phi\left(\frac{r}{R_p}\right)^3\right]. \tag{6.7}$$

Thus, the mean nearest-neighbour distance between the particles is defined as the first moment of r, where r is distributed according to $H_p(r)$:

$$\langle r\rangle = \frac{R_p}{\phi^{1/3}}\,\Gamma\left(\frac{4}{3}\right), \tag{6.8}$$

where Γ is the gamma function. However, since variations in the inter-particle distance will induce local density variations, it is more relevant to examine the variance of the nearest-neighbour distance. The variance is defined as the second central moment of the distribution $H_p(r)$,

$$\langle r^2\rangle = \int_0^\infty \left[r - \langle r\rangle\right]^2 H_p(r)dr, \tag{6.9}$$

so the standard deviation is used as a length scale of concentration fluctuations:

$$\sqrt{\langle r^2\rangle} = 0.325\,\frac{R_p}{\phi^{1/3}}. \tag{6.10}$$

The structural length scale is proportional to the particle radius in a similar way to that observed in the experiments (see Figure 6.7a). Despite this correct trend, using the standard deviation does not capture the increase of the transition radius R_{T1} with increasing particle volume fraction. The transition radius is experimentally determined with a reduction in the local

viscosity indicating particle density gradients in the filament. However, these concentration variations are only recognised when the associated viscosity change is significant in comparison to the suspension viscosity. This effect also needs to be taken into account as a weight factor in the definition of the structural length scale. A simple way to incorporate this effect is to multiply by the ratio of the derivative of the suspension viscosity with respect to volume fraction relative to the viscosity. Using the Maron-Pierce model (Eq. 6.1), this derivative is evaluated as

$$\frac{\partial \eta}{\partial \phi} = \frac{2\eta_s}{\phi_m}\left(1 - \frac{\phi}{\phi_m}\right)^{-3} = \frac{2\eta}{\phi_m - \phi}. \tag{6.11}$$

Thus, combining the weight factor with the standard deviation gives the length scale R_s for the transition radius:

$$R_s = \frac{\sqrt{\langle r^2 \rangle}}{\eta}\frac{\partial \eta}{\partial \phi} = \frac{0.65 R_p}{\phi^{1/3}\left(\phi_m - \phi\right)}. \tag{6.12}$$

This length scale is employed to rescale the transition radii of various suspensions in Figure 6.7b. Compared to the experimental data, the length scale R_s does not capture the lower transition radii at low volume fractions and overestimates the transition radii at high concentrations ($\phi = 0.40$). Moreover, the effect of the particle size on the transition radius is overestimated by the linear dependence on R_p. Nevertheless, the scaling works well for the simulated transition radii, which we will discuss in Section 6.4.

In the our analysis, we have assumed that deviations from the effective fluid regime are caused by local dilution of the suspension. However, in concentrated samples of small particles, a change in the local viscosity could arise from extensional thinning effect due to colloidal interactions or changes to the particle distributions. For the PMMA3 suspensions, it is impossible to distinguish from the filament images or the minimal radius evolution which of the two mechanisms causes the accelerated thinning. Although we have previously considered the suspension viscosity to be shear rate independent, this assumption was based on the observations for suspension with significantly larger particles than PMMA3 [179]. For these inelastic suspensions, extension thinning can be identified through the flow behaviour under shear deformation [4, 102, 103]. The strain thinning is characterised for both flow types by a power law dependence $\eta = K|\mathrm{II}_{2D}|^{(n-1)/2}$, where n is the power law exponent and K is the consistency index. The power law model is universally defined by using the second invariant of the rate of deformation tensor $2D$ as a measure of the flow strength:

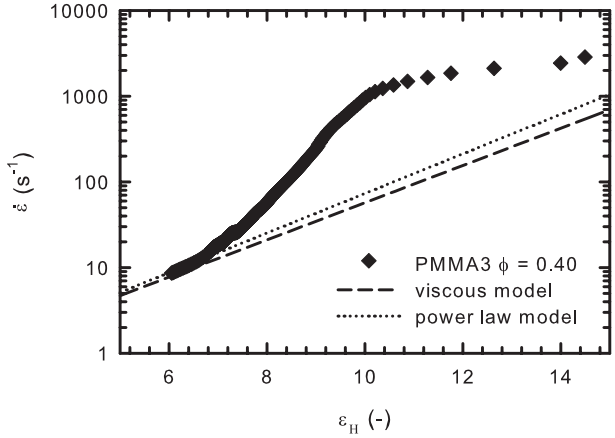

Figure 6.8: Evolution of the extension rate during a capillary breakup experiment as a function of the local Hencky strain. The rates observed during the thinning of 40% PMMA suspensions are significantly higher than those of a reference viscous liquid with the same viscosity (Eq. 6.14) and a shear-thinning fluid with a power law of $n = 0.94$ obtained from fitting to the shear viscosity of the suspension (Eq. 6.15).

$$\mathrm{II}_{2D} = \frac{1}{2}\left[(\mathrm{tr}2D)^2 - \mathrm{tr}\,(2D)^2\right]. \tag{6.13}$$

The magnitude of the second invariant equals $3\dot{\epsilon}^2$ for uniaxial extension, while the value for pure shear flow is $\dot{\gamma}^2$, with $\dot{\gamma}$ the shear rate. The strain rate during the effective fluid regime is derived by combining the definition of the strain rate (Eq. 3.5) with the expression for viscosity dominated thinning (Eq. 2.29):

$$\dot{\epsilon} = 0.142\frac{\gamma}{R\eta}. \tag{6.14}$$

Figure 6.8 demonstrates how the extension rate diverges from the normal viscous behaviour described by Eq. 6.14 after the linear viscous thinning stage. The local viscosity decrease gives rise to a sudden growth of the extension rate for strain rates $\dot{\epsilon} > 15\ \mathrm{s}^{-1}$. Assuming that extension thinning is responsible for this viscosity decrease, a similar shear thinning should be observed at comparable flow strengths. A relationship between shear and extension rate of $\dot{\gamma} = \sqrt{3}\dot{\epsilon}$ is obtained by equating the second invariant for both flow types.

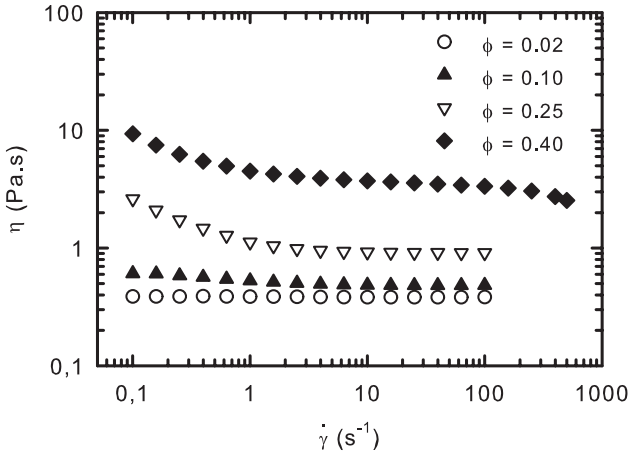

Figure 6.9: Flow curves of suspensions of PMMA3 in PDMS 2 of various concentrations. The dilute samples behave completely Newtonian over the entire range of shear rates. In contrast, minor shear thinning behaviour is observed for the most concentrated sample.

Figure 6.9 shows the flow curves of all PMMA3 suspensions. The applied shear rates are quite low compared the equivalent extension rates during capillary thinning, but a comparison is certainly possible for the two highest concentrations. For volume fractions $\phi \leq 0.10$, the suspension behaviour is Newtonian over the entire measuring range. The two highest concentrations display a larger zero-shear viscosity. This viscosity increase at low shear rates does not manifest during filament thinning because the equivalent extension rates are an order of magnitude higher. Contrary to the 25% suspension, that exhibits a constant viscosity for $\dot{\gamma} > 5$ s^{-1}, the 40% sample is slightly shear thinning over the entire measuring range. The thinning effect even strengthens for shear rates $\dot{\gamma} > 200$ s^{-1}, although this could be a measurement error. The maximum shear rate is limited due to inertia of the device and potential particle migration to the wall. These last data points are not included in the power law fit and an exponent $n = 0.94$ is obtained. Together with the consistency index $K_n = 4.2$ Pa.s^n, this value is used to calculate the minimal radius evolution of power law fluid [3, 4, 100]:

$$R_m = \Phi \frac{\gamma}{K_n} (t_p - t)^n \,, \tag{2.31}$$

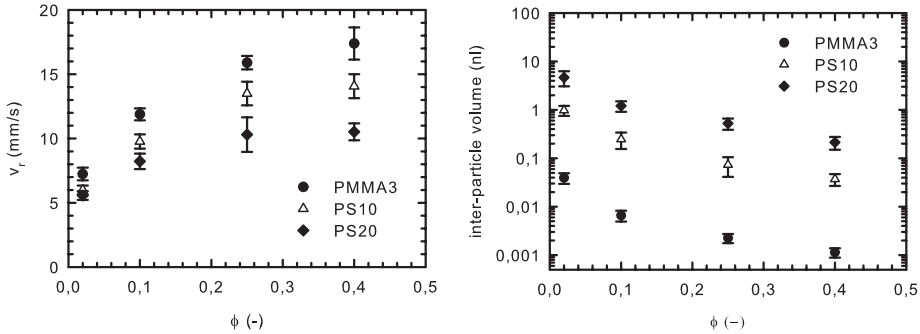

(a) radial velocity

(b) inter-particle volume

Figure 6.10: Characteristic properties of the acceleration of the continuous phase for all PDMS 2-based suspensions: (a) the maximum radial velocity during the acceleration stage as a function of volume fraction and (b) the volume of medium fluid that is trapped between the particle clusters.

where the prefactor Φ is a numerical factor depending on the power law exponent n. However, this model does not coincide with the experimentally observed thinning dynamics. An expression for the strain rate is established by inserting the expression for the filament radius of a power law fluid (Eq. 2.31) into the definition of the strain rate (Eq. 3.5):

$$\dot{\epsilon} = \frac{2n}{t_p - t}. \tag{6.15}$$

The evolution of this model strain rate is depicted as the dotted line in Figure 6.8. Since the power law exponent n is quite close to 1, the thinning is not particularly different at the Hencky strain where the transition takes place. The strain rate is only 20% higher and remains of the same order of magnitude as that of the viscous model in later thinning stages. The limited shear thinning is thus insufficient to solely explain the transition to a locally lower viscosity at a larger filament radius R_{T1} for the 40% PMMA3 suspension.

6.3.3 Continuous phase acceleration

The concentration fluctuations eventually lead to particle-free sections in the filament. As discussed in Section 6.3.1, we split this final continuous phase into two regimes: the acceleration regime and the deceleration regime. In the accelerated regime, the filament radius generally thins linearly with time for a short period and the thinning rate reaches a maximum. In the case of 10% PS20 in PDMS 2, the maximum thinning rate is observed between 7 and 3 ms before breakup, indicated by dash-dot line in Figure 6.5b. Since the profiles are no longer self-similar, a fitted viscosity can no longer be used to compare the behaviour of the different samples. Therefore, we quantify the acceleration regime for each sample using the maximum radial velocity $v_r = -dR_m/dt$.

The average maximum radial velocity v_r is plotted in Figure 6.10a for all samples with PDMS 2 as the medium fluid. The error bars indicate the variation between consecutive experiments due to differences in the local particle distribution. We observe that v_r increases for smaller particles and higher particle concentrations. This velocity increase appears to be related to the volume of medium fluid trapped between the particle clusters. The inter-particle volume is determined with image analysis at the start of the continuous phase thinning and remains constant until breakup. The latter observation proves that a small quantity of medium fluid is isolated from the rest of the suspension during this thinning stage. The inter-particle volume is presented in Figure 6.10b for all PDMS 2-based suspensions. The volume increases for larger particles and lower concentrations, thus exhibiting the opposite trends compared to the radial velocity.

An additional feature to describe the continuous phase thinning is the starting point of this zone which is expressed with a second transition radius R_{T2}. Figure 6.11 represents the observed transition radii relative to the particle size in order to detect similar behaviour for different particles. We expect the transition radii to scale with the particle diameter, since this part of the breakup process resembles a filament stretching between two particles or two particle clusters for higher concentrations. The relative diameters for PS10 and PS20 are in fact quite similar whereas the values for the PMMA3 particles are slightly higher. Since the number of particles scales with R_p^{-3} for a fixed volume fraction, suspensions with these smallest particles contain a considerably larger amount of particles for the same volume fraction. Moreover, these small particles start exhibiting colloidal attractions, which can be deduced from the increase of the shear viscosity at low rates for $\phi > 0.10$ (see Figure 6.9). These colloidal interactions tend to facilitate the formation of particle clusters, as illustrated in Figure 6.12b. This figure shows magnified filament images of suspensions with

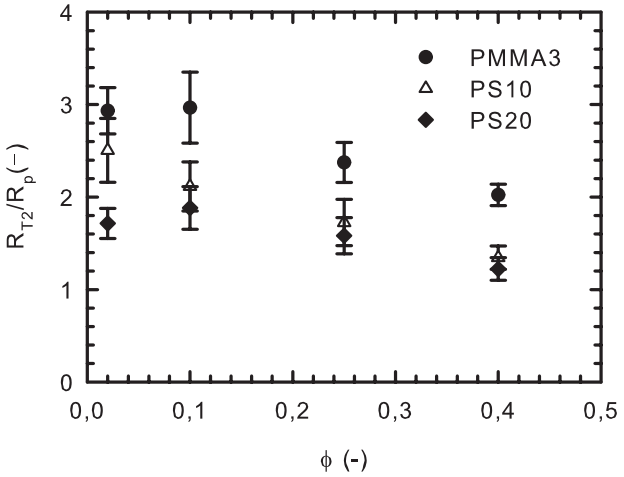

Figure 6.11: Overview of the filament radius at the onset of the accelerated continuous phases thinning for the suspension with PDMS 2 as medium. The transition radii are rescaled with the particle size.

different particle sizes and a fixed volume fraction $\phi = 0.25$ at the onset of the accelerated thinning of the interstitial fluid. For the smallest spheres, the zone of interstitial fluid is confined on both sides by two or three PMMA3 particles positioned radially next to each other. In contrast, the interstitial fluid is only confined between two single particles for the suspensions with larger spheres, explaining the similar relative values for R_{T2} for these samples.

Furthermore, the onset of the accelerated thinning depends on the volume fraction in a similar way for all particle sizes. The transition radius R_{T2} is comparable for volume fractions $\phi \leq 0.10$, but decreases for the higher particle concentrations. This trend can be explained by examining images of filaments at different particle volume fractions (see Figure 6.12a). At the start of the thinning of the interstitial fluid, the filament shape is rather different for each dispersion of PS20. The volume of medium fluid that is stretched between the particles is evidently reducing as the particle concentration grows, as was already shown in Figure 6.10b. While the zone of medium fluid almost takes in the entire image for the 2% sample, the approximate 0.1 nl interstitial fluid is hardly visible in the image of the 40% sample. The thinning filaments of the more concentrated samples moreover exhibit a double triangular form resembling the shape of an unstable filament of a power-law fluid. Due to the highly non-linear

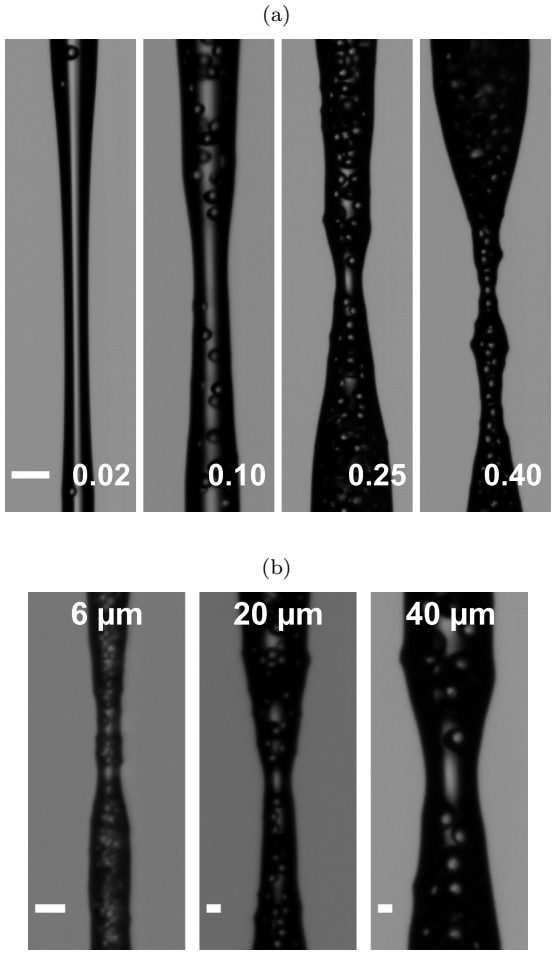

Figure 6.12: Images of filaments of PDMS 2-based suspensions at the onset of the accelerated thinning of the interstitial fluid at which a zone with medium fluid appears between two (clusters of) particles. (a) Suspensions of PS20 with different volume fractions, indicated at the bottom of each picture. The inclosed volume and the transition radius R_{T2} significantly decrease with particle volume fraction. The scale bar represents 100 μm. (b) Suspensions with different particle sizes and a fixed volume fraction $\phi = 0.25$. Contrary to the larger particles, the zone with medium fluid is surrounded by a cluster of multiple 6 μm particles, which explains the larger relative value of the transition diameter R_{T2}. The scale bars represent 20 μm.

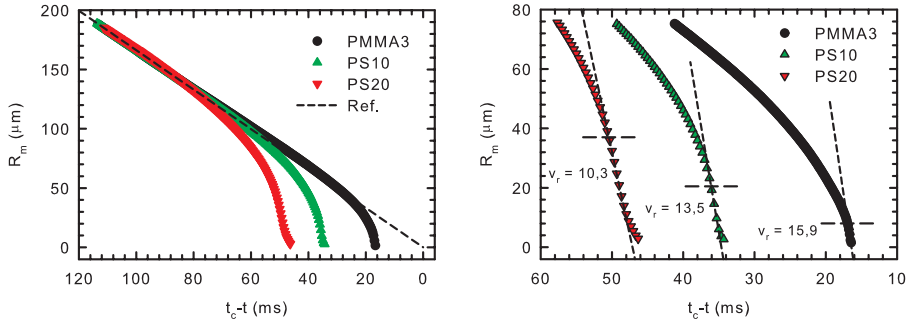

Figure 6.13: Breakup dynamics of suspensions of different particle sizes in PDMS 2 with a fixed volume fraction $\phi = 0.25$. (a) Whereas the initial effective viscosity regime is independent of particle size, breakup occurs considerably sooner for the suspensions with the larger particles. As reference, the radius evolution of a viscous fluid with the same viscosity is included. (b) Differences in the final thinning stages are illustrated by shifting the time axis so that the graphs coincide at a diameter of 150 μm. The onset of the continuous phase thinning (R_{T2}) is indicated with a dashed line.

relationship between the suspension viscosity and particle volume fraction ϕ (see Eq. 6.1), concentration fluctuations have a more pronounced effect on the local viscosity for these samples. The thinnest zone with a low local particle fraction will therefore pinch much faster than its surroundings, creating a very heterogeneous filament with thick triangular zones above and below the pinching point. This specific filament shape ensures that the interstitial fluid is trapped between 2 individual particles and lowers the value of the transition radius R_{T2}.

However, the trends of the radial velocity v_r and the second transition radius R_{T2} do not capture the effect that particle size has on the ultimate breakup time of the suspensions. Although the smallest-particle (PMMA3) suspension has the largest value of v_r, this suspension takes the longest time to breakup, as demonstrated in Figure 6.13a. This figure shows the evolution of the minimal filament radius for three suspensions of different particles with a fixed volume fraction $\phi = 0.25$. Initially, the thinning trajectories of the three samples overlap in the suspension stage as the suspension viscosity solely depends on the volume fraction. However, the suspension with largest particles (PS20) deviates from this linear thinning already much earlier, so that while the smallest particle

(PMMA3) suspension is still in the first thinning stage, the PS20 sample has already pinched due to a combination of the particle density fluctuations and the accelerated thinning of the interstitial fluid. Since smaller-particle suspensions demonstrate a smaller R_{T1}, the acceleration regime is limited and large v_r cannot affect the dynamics. Consequently, the reduction in breakup time is less than that observed for larger particle sizes. Evidently, it is the concentration fluctuation regime, characterised by the transition radius R_{T1}, that is key to understanding particulate effects on breakup time, rather than the accelerated regime itself.

Figure 6.13b focusses on the final pinch-off dynamics of the three samples. The short linear decay where the highest thinning rate is achieved, i.e. the accelerated regime, is demonstrated by a linear fit with a slightly different slope for each sample. The maximum rate of the PMMA3 dispersion is accurately determined with a increased sampling rate of 9000 s^{-1}. For each case, the horizontal dashed line indicates the second transition radius R_{T2}, which corresponds to the visible onset of continuous-phase thinning between two particle clusters.

Since the breakup of the PDMS 1-based suspensions was also examined by Lindner and co-workers [21,177], a comparison of the overall acceleration during the dripping and CaBER experiments can be executed for these samples. In their studies, the acceleration was quantified by comparing the breakup of each suspension with that of a purely viscous silicon oil matching the shear viscosity of the suspension. The average difference in rupture time Δt_p between both fluids was taken as an estimate for the acceleration. This time difference is a pragmatic criterion combining the effects of concentration fluctuations and interstitial fluid acceleration. Although we have not physically tested any reference fluid, the viscous thinning dynamics can be estimated with the proper scaling law (Eq. 2.29), which gives the following pinching time starting from a filament with diameter R_{T1}:

$$t_{p,v} = \frac{14.1\,\eta\,R_{T1}}{\gamma}. \tag{6.16}$$

Before the transition radius R_{T1} is reached, the suspensions are in the effective fluid stage, so the thinning dynamics are identical to those of the reference liquid. The dashed reference line in Figure 6.13a illustrates this similarity for large filament diameters. As discussed in Section 6.2, PDMS 1 undergoes a transition from the viscous to the inertia-viscous scaling at small filament diameters. The reference liquids for the low concentrations ($\phi \leq 0.10$) have a viscosity that is only slightly higher than that of PDMS 1, so the same transition will probably

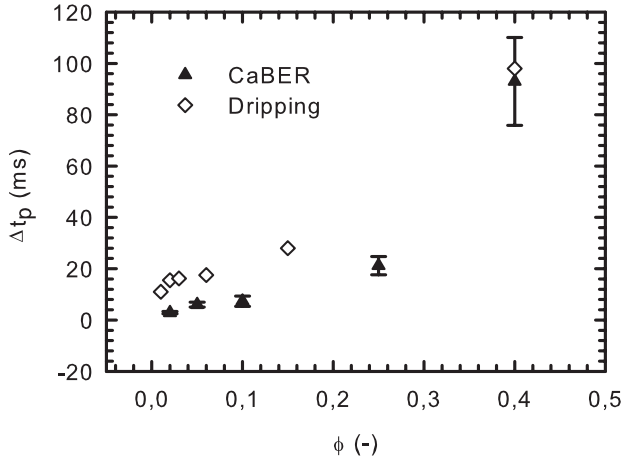

Figure 6.14: Average difference in rupture time Δt_p between the PS20 suspensions in PDMS 1 and the pure viscous fluid as a function of the volume fractions. Our CaBER experiments are compared with dripping experiments from literature [21, 177].

occur for these liquids. Hence, the actual pinching time $t_{p,v}$ of these reference fluids will somewhat higher than the viscous prediction of Eq. 6.16. The extra time is estimated from the diameter evolution of the pure PDMS 1 (see Figure 6.2) and should be around 3 ms. Figure 6.14 compares the average difference in rupture time Δt_p of our CaBER experiments to the literature values from the dripping experiments. The time difference in the CaBER experiments is strikingly lower than those of the dripping tests for all measured concentrations. An explanation for this discrepancy is currently unavailable, because additional quantitative data on the acceleration during the dripping experiments is not presented in both studies [21, 177]. Due to the limited resolution of the optical setup capturing the pendant drop, the data points in the accelerated regime are very limited for the PS20 dispersions. Moreover, no comparison to the self-similar scaling laws was made, so an insufficient slenderness of the thinning filament might make the interpretation even more complex.

6.3.4 Deceleration

As discussed in Section 6.3.1, the acceleration is succeeded by a deceleration which has not been detected in previous experimental studies. The transition into this final regime, and therefore the extent of the deceleration, also depends on the suspension properties in a similar way as previously discussed. For example, in Figure 6.13b the larger particle cases have a more pronounced deceleration regime, owing to a larger transition radius R_{T2}. In the PMMA3 case, the final transition is below the spatial and temporal resolution of our setup.

The deceleration regime also exhibits linear decay (see Figure 6.5b) characterised by a balance between surface tension and the viscosity of the medium fluid. This indicates a return to self-similar scaling of a viscous Newtonian fluid. This hypothesis is confirmed by scaling the filament profiles near breakup to verify the convergence to the universal Stokes similarity solution ϕ_{St} [5, 17, 99], which was introduced in Section 2.2.6. The Stokes similarity solution solely depends on the similarity variable ξ as

$$\phi_{St}(\xi) = \frac{R}{\ell_v |t'|}, \tag{6.17}$$

$$\xi = \frac{z'}{|t'|^{\beta}}, \tag{2.26}$$

where $\beta = 0.175$ is the scaling exponent for the Stokes similarity solution. The dimensionless position z' and time t' are respectively scaled with the internal length scale ℓ_v (Eq. 2.22) and the internal time scale t_v (Eq. 2.23) of the fluid as discussed in Section 2.2.5. These definitions imply that minimal filament radius can be used to rescale the experimental filament profiles, since the viscous (V) scaling (Eq. 2.29) can be rewritten as

$$R_m = 0.0709\, \ell_v |t'|. \tag{6.18}$$

Combining Eqs. 6.17 - 6.18, the proper definitions for the scaled profile radius R^* and the scaled axial coordinate z^* are determined:

$$R^* = \frac{R}{R_m}, \tag{6.19}$$

$$z^* = \frac{z - z_0}{R_m} (t_p - t)^{1-\beta}, \tag{6.20}$$

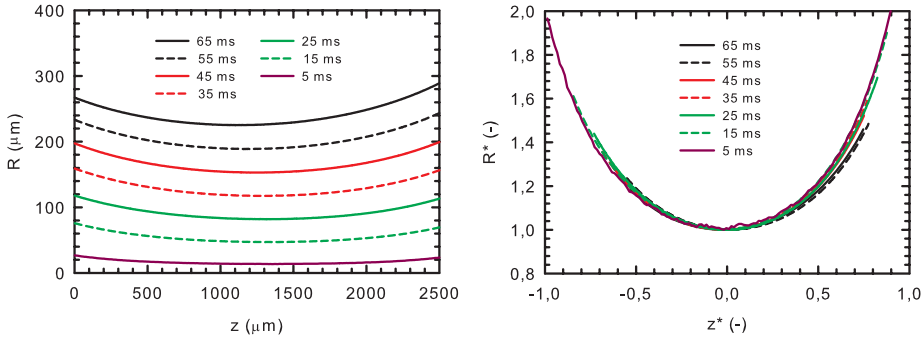

(a) regular profiles (b) scaled profiles

Figure 6.15: Experimental filament profiles of the Newtonian PDMS 2, for which time until breakup is indicated. (a) The profile radius R is shown as a function of the axial coordinate z. (b) The profiles are rescaled according to the viscous similarity solution.

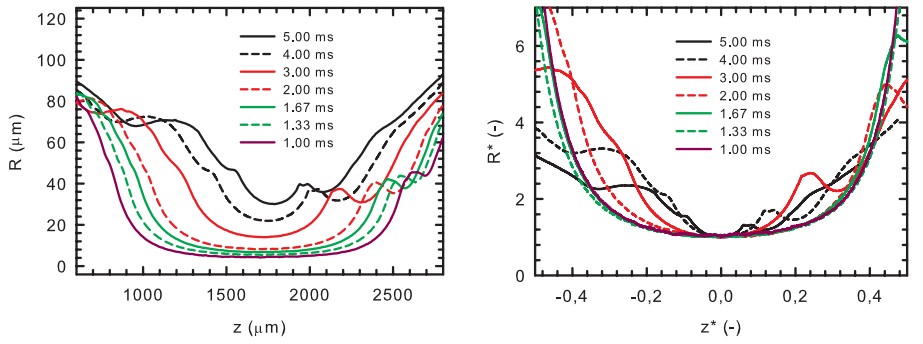

(a) regular profiles (b) scaled profiles

Figure 6.16: Filament profiles of a PDMS 2-based suspension of PS20 particles with $\phi = 0.10$ near pinch-off. The time until breakup is indicated for each profile. (a) The experimental profiles are shown where the first three are situated during the accelerated thinning of the continuous phase and the other four are observed in the deceleration stage. (b) The profiles are rescaled and the profiles in the deceleration stage are clearly overlapping and exhibit the same shape as the viscous self-similar solution.

where z_0 is axial coordinate corresponding to the minimal radius. This rescaling is first evaluated on filament profiles of a capillary breakup experiment of pure PDMS 2 oil, which already demonstrated to follow the viscous scaling. Figure 6.15 shows that the selected profiles that are initially considerably different, all coincide after rescaling. These profiles thus exhibit self-similarity and approach the symmetric shape of ϕ_{St}, proving the validity of the viscous scaling for this system. A similar rescaling was also used by Kowalewski [92] on a jet of a glycerol-water mixture with a comparable viscosity ($\eta = 400$ mPa.s).

The rescaling of the axes is subsequently employed on filament profiles of a suspension of PS20 in PDMS 2 with $\phi = 0.10$ near pinch-off in Figure 6.16. Seven profiles are selected in the final 5 ms before breakup, during which the continuous phase is thinning between particle clusters. The first three profiles at times $5, 4$ and 3 ms before breakup, occur during the accelerated thinning regime and do not exhibit self-similarity. In this regime, a small region around $z^* = 0$ is observed to be particle-free and surrounded by clusters of particles. On the other hand, the last four profiles at times $2, 1.67, 1.33$ and 1 ms before breakup, clearly demonstrate the self-similar nature of the final deceleration regime, approaching the symmetric shape of ϕ_{St}. The rescaled profiles of the oil and the suspension are however not completely identical, since the Stokes solution ϕ_{St} is universal, up to a single parameter which sets the width of the solution [5, 99].

Although the interstitial fluid continues to thin between two particle clusters in this regime, finite-size effects cease to alter the thinning dynamics so that the thinning rate can be solely described by the viscosity of the medium fluid. Consequently, we are able to recover the Newtonian thinning transitions described in Section 6.2. In Figure 6.17, we plot the deceleration regime for the PS20 suspension with a range of volume fractions for both medium fluids PDMS 1 and PDMS 2. The deceleration is more prominent for suspensions with a lower particle volume fraction. To allow comparison of samples with a different medium viscosity, the time is rescaled with the viscous time scale t_η (Eq. 6.2), where we have chosen the particle radius as the reference radius: $R_0 = R_p$. The time axis is further shifted with t_c, the time at which filament radius equals the reference radius.

The slopes of the two possible self-similar solutions for a viscous liquid are shown in Figure 6.17. For the suspensions with PDMS 1 as medium fluid, there is the appearance of a transition from the V-scaling to the IV-scaling close to breakup, whereas the PDMS 2-based dispersions persist in following the V-scaling. The switch to the IV-scaling results in a relatively longer deceleration zone for the

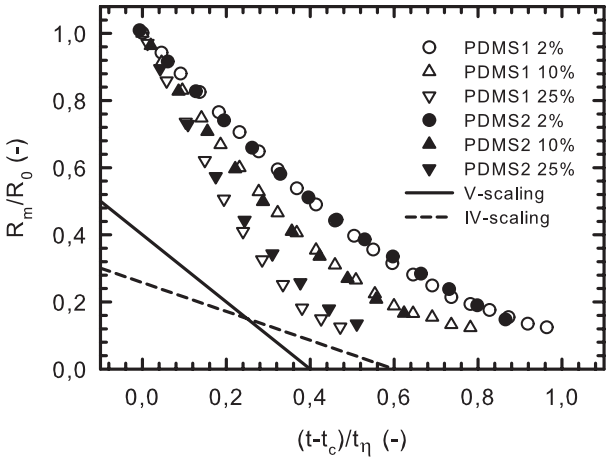

Figure 6.17: Deceleration of the filament thinning near pinch-off for a series of suspensions of PS20 with both medium fluids. The time is rescaled with t_η and minimum filament radius is depicted relative to the particle radius. The deceleration is more pronounced for lower particle volume fractions and for lower medium viscosity, where the thinning dynamics tend to the slower inertia-viscous (IV) scaling before breakup.

PDMS 1-based suspensions. Moreover, the final shape of a Newtonian filament is controlled by the preferred scaling law prior to breakup [4]. This is illustrated in Figure 6.18 for two suspensions with a volume fraction $\phi = 0.10$. The PDMS 2-based suspensions exhibit a symmetrical pinching, where the breakup occurs in the centre of the filament. In contrast, the symmetry in the filament of the PDMS 1-based suspensions is broken under the influence of inertia, generating a vertical shift of the necking point along the filament towards the particle clusters. This asymmetrical pinch-off results in the formation of a small satellite droplet, which is not observed with PDMS 2-based suspensions. This contrast between the two medium fluids was already observed during the capillary thinning experiments on the pure liquids in Section 6.2. However, during the deceleration regime of these PDMS 1 suspensions, the transition to IV-thinning occurs at significantly smaller radii, agreeing with the prediction of Eq. 6.5 due to the smaller reference radius R_0.

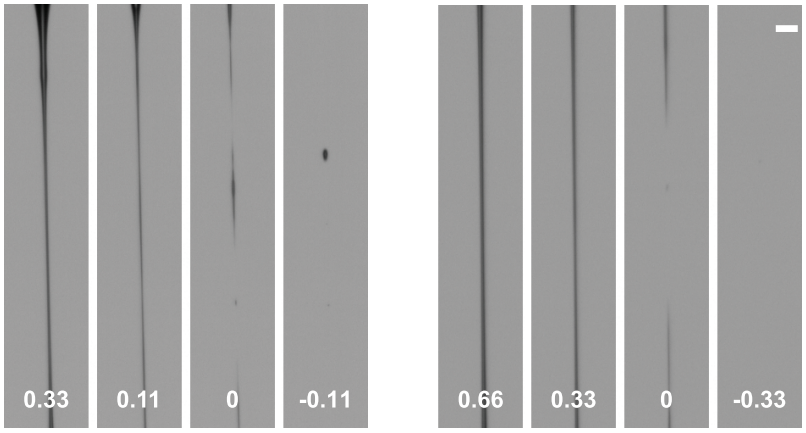

(a) PDMS 1 (b) PDMS 2

Figure 6.18: Comparison of the filament shape near pinch-off of two suspensions of PS20 with $\phi = 0.10$ with (a) PDMS 1 and (b) PDMS 2 as medium liquid. The loss of axial symmetry causes the formation of a satellite droplet for the fluid with the lowest viscosity. The time before breakup (in ms) is shown for each image and the scale bar represents 50 μm.

6.4 Simulations

6.4.1 One-dimensional particle model

In order to obtain a better understanding of the correlation between changes in the thinning dynamics and the particle distribution in the filament, the experiments are compared with modelled filament thinning. These simulations were performed by Claire McIlroy of the University of Leeds to mirror some of the previously presented experiments. The simulations are executed with the method developed by McIlroy and Harlen [22] that solely examines the effects of axial variations in particle concentration in accordance with the study of Crosby and Lister [189], which demonstrated that the effects of particle variations in the r and θ directions may be neglected. The model assumes that the filament generated by the CaBER is sufficiently long and thin that it can treated as an axisymmetric slender jet. Thus, as governing equations for the dimensionless filament radius $h(\bar{z}, \tau)$ and the velocity $\bar{v}(\bar{z}, \tau)$, we use the one-dimensional form that is thoroughly discussed in Appendix C, being

$$\frac{\partial h^2}{\partial \tau} + \frac{\partial}{\partial \bar{z}}(h^2 \bar{v}) = 0, \tag{6.21}$$

$$\frac{\partial}{\partial \tau}(h^2 \bar{v}) + \frac{\partial}{\partial \bar{z}}(h^2 \bar{v}^2) = \frac{\partial}{\partial \bar{z}}\left(h^2\left(K + 3Oh\frac{\partial \bar{v}}{\partial \bar{z}}\right)\right), \tag{6.22}$$

for conservation of mass and momentum, respectively. Here the curvature term is defined as

$$K = \frac{h_{zz}}{(1+h_z^2)^{3/2}} + \frac{1}{h(1+h_z^2)^{1/2}}, \tag{6.23}$$

with the z-subscript denoting differentiation with respect to $\bar{z}$. These governing equations (Eqs. 6.21-6.23) have been non-dimensionalised with respect to the initial radius R_0 and the Rayleigh time $t_R = \sqrt{\rho R_0^3/\gamma}$. The initial shape of the free surface is modelled as an arc of a circle to simulate a liquid bridge held between two end plates, as in the CaBER technique. For each realisation, the particles are initially uniformly distributed at random axial positions z_p, for $p = 1, \ldots, N_p$, throughout the liquid bridge. The average volume fraction is given by

$$\phi_{av} = \frac{N_p}{V_{tot}} V_p, \tag{6.24}$$

where V_p is the particle volume, which for spherical particles is

$$V_p = \frac{4}{3}\pi R_p^3. \tag{6.25}$$

Thus, the effective particle radius R_p is controlled by varying the number of particles N_p. The particles are assumed to be sufficiently large that Brownian motion is negligible. In addition, we assume that the overall effects of particle-particle and particle-surface interactions can be neglected so that each particle moves with the axial velocity $v(z_p, t)$ of the fluid, obtained by linear interpolation. The local volume fraction ϕ is then determined from the number of particles within a segment of the filament. This concentration discretisation is larger than the mesh size used in the solution of Eqs. 6.21-6.22 and, within limits, does not affect the ultimate thinning dynamics [22].

The effects of particle concentration on the dynamics are incorporated by assigning a local viscosity from the Maron-Pierce relation (see Eq. 6.1), which introduces a local Ohnesorge number in Eq. 6.22, given by

$$Oh_i = Oh_s \left(1 - \frac{\phi_i}{\phi_{max}}\right)^{-2}, \quad i = 1, \dots N_b, \tag{6.26}$$

where Oh_s denotes the Ohnesorge number of the solvent and N_b is the number of bins used in the concentration discretisation. In this way, the particles contribute only to the local viscosity of the fluid and the direct effects of individual particles on the free surface are neglected. The governing equations (Eqs. 6.21-6.23) are then solved via a semi-implicit numerical scheme, where the velocity terms are treated explicitly. Simulations are executed to mimic the particles used in the experiments for various concentrations $\phi < 0.25$. In general, ten realisation are performed for a single suspension to account for the statistical variation arising from the initial particle distribution. Suspensions with $R_p = 3$ μm are not included in the comparison, due to computational time constraints.

6.4.2 Comparison to experiments

We first evaluate the quality of the model predictions by comparing a single breakup curve. Figure 6.19a compares the experimental evolution of the minimal filament radius (points) for 10% of PS20 in PDMS 2, which is also displayed in Figure 6.3b, with the results of the numerical simulation (solid line). Despite the simplicity of the model, the corresponding simulation captures the qualitative features of the experiments, including a transition to an accelerated thinning of the filament due to fluctuations in the local particle density and a final deceleration. Moreover, it quantitatively captures both the radius of onset and the thinning velocity during this phase of thinning. The small difference in the slope of the initial linear regime is caused by a small difference between the experimentally observed suspension viscosity and the predictions of Maron-Pierce model used in the simulations. The degree of agreement between the simulations and experiments strongly suggests that the acceleration is a consequence of the amplification of particle-density fluctuations in the thinning filament. These fluctuations result in local regions of lower than average viscosity that are able to thin more easily, producing a more rapid thinning in these regions.

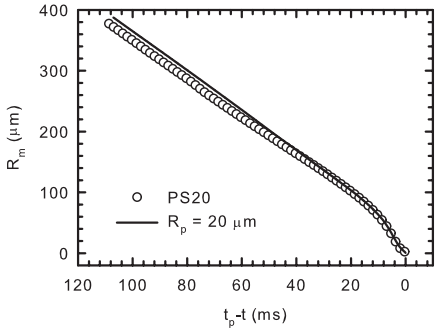

(a) 10% PS20

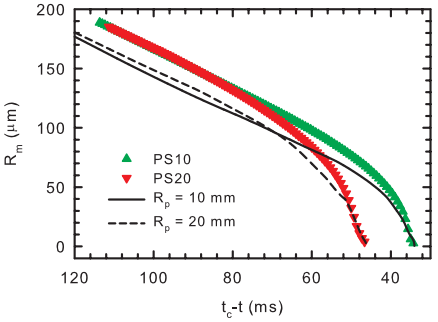

(b) particle size

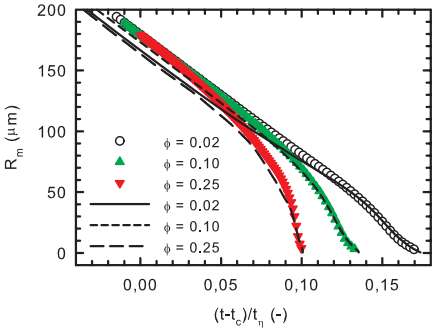

(c) volume fraction

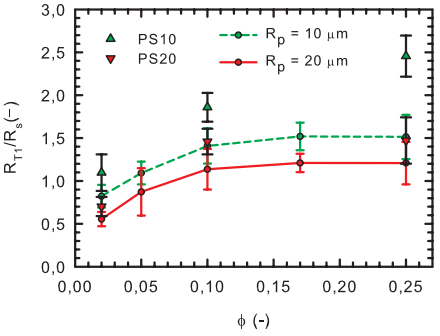

(d) transition radius

Figure 6.19: Comparison of the modelled capillary breakup with the experiments for PDMS 2 -based suspensions. (a) The evolution of the minimal radius during capillary breakup of a suspension with 10% of PS20 (dots) and simulation results (solid line) with the same concentration and particle size. (b) Breakup curves for dispersions with varying particle size at $\phi = 0.25$ and (c) varying concentration for $R_p = 20$ μm. (d) Overview of the scaled tradition radius R_{T1}/R_s for the experiments (triangles) and simulations (dots and line).

Similar to the experimental section, we explore the effects that changing suspensions properties has on the thinning dynamics. Figure 6.19b shows two experimental thinning curves for PS10 and PS20 with a fixed volume fraction $\phi = 0.25$ that are also shown in Figure 6.13a. The results of the one-dimensional model are shown by the two lines, which are shifted so that the experimental and modelled curve have the same pinching time. The model results agree qualitatively with the experimental data, as the larger particle deviates earlier from the linear thinning of suspension thinning stage and the final thinning dynamics are well represented. Despite the similarity, we observe differences in the transition radius R_{T1} that indicates the onset of concentration fluctuations. Compared to the experimental data, the model underpredicts R_{T1}, resulting in a larger breakup time.

In a similar fashion, Figure 6.19c shows the evolution of the minimal filament radius for three suspensions of PS20 having volume fractions $\phi = 0.02, 0.10$ and 0.25. Again, the model results are given by the lines that have the same pinching time as the experimental points. In this case, the time axis is rescaled by t_η (Eq. 6.2) so that, as in Figure 6.19b, the initial thinning trajectory of the three samples overlap. A deviation from the linear suspension regime is observed at larger filament radii for the more concentrated experimental samples and the model results are again in qualitative agreement. Once more, we observe small differences in the transition radius R_{T1} predicted by the model compared to the experimental data.

A comparison of the simulated and experimental transition radius R_{T1} is shown in Figure 6.19d, where the radii are rescaled with R_s. Also in the simulations, the precise value of the transition radius depends upon the initial particle distribution and so varies in consecutive experiments and numerical realisations of the same suspension. As mentioned in Section 6.3.2, the scaling works well for the simulated transition radii, particularly in the range $\phi = 0.10 - 0.25$. For smaller concentrations, the transition between the suspension regime and the accelerated regime is not as pronounced, as the slopes of the respective regimes are similar. It is to be expected that this scaling should work better for the simulated thinning profiles than the experiments as both neglect the effects of the excluded volume in the particle distributions, whereas the experimental systems contain impenetrable hard spheres. Expressions for H_p in a system of impenetrable hard spheres have been established by Torquato and co-workers [190, 191], but the moments of this function cannot be obtained analytically. Moreover, the scaled transition radius has the highest value for the concentrated samples of the smallest particles PMMA3, which may be the result of colloidal forces.

6.5 Conclusion

We have studied the drop formation of non-colloidal suspensions in a Newtonian medium by examining the pinch-off dynamics of an unstable liquid bridge. This geometry instantly creates a slender filament enabling the use of self-similar scaling to explain the thinning dynamics. This strategy results in a more straightforward interpretation of the capillary breakup than in previous dripping studies on similar fluids [18, 21], identifying four distinct thinning regimes. The suspension initially behaves as homogeneous viscous fluid and the filament radius decreases linearly in time following the viscous scaling for the effective viscosity of the suspension, which is accurately described by the Maron-Pierce model. As the filament thins, local particle density fluctuations are amplified resulting in a heterogeneous suspension with diluted zones that exhibit faster thinning rates due to the local decrease in viscosity. By examining the shear response of the suspensions, we have excluded that strain thinning causes this acceleration. The onset of this concentration fluctuation regime is defined with a transition radius R_{T1} that increases with particle radius and volume fraction. A scaling for this radius was proposed based on the standard deviation of the mean inter-particle distance and the relative dependence of the viscosity to small changes in the volume fraction. The value of the transition radius is crucial in estimating the reduction in breakup time compared to a viscous fluid with matching shear viscosity.

The local dilution eventually develops a particle-free section, where a small volume of medium fluid is caught between two particle clusters. At this point, the breakup resembles a small-scale filament stretching experiment and the thinning rate reaches a maximum. The onset of this third regime has been quantified by a second transition radius R_{T2} that decreases for large particle volume fractions. Subsequently, we observe a transition from the accelerated regime to a last deceleration regime, which has not been detected in previous experimental studies. The thinning of the continuous phase appears unaffected by the presence of the particles and follows the viscous scaling of the medium fluid. This scaling has been verified by rescaling the filament profiles to retrieve the symmetric Stokes similarity solution. In the final section, we have demonstrated excellent agreement between capillary breakup experiments and the model for capillary breakup of particulate suspensions developed by McIlroy and Harlen [22] for a range of suspensions with different particle size and concentration.

Chapter 7

Conclusions and outlook

Main conclusions

In this work, we have investigated the capillary-driven breakup of liquid filaments in different experimental geometries. For low and moderately viscous liquids, surface tension can destabilise a sufficiently slender filament, leading to the formation of two droplets. The thinning dynamics during this free-surface flow are determined by the balance of surface tension with the dominant resisting stress, which depends on the relative magnitudes of relevant fluid properties, such as density, viscosity and elasticity. Due to the absence of a no-slip boundary condition at the free surface, a uniaxial extensional flow field is created in the filament that is capable of inducing strong deformations in the microstructure of complex fluids. The rheological behaviour in extension can therefore not be predicted from the shear response, since shear flows are inherently weaker due to the rotational component. Depending on the type of non-Newtonian fluid, the non-linear deformation can either have stabilising or destabilising effect on the fluid column.

Detection of fast extensional relaxation processes

Measuring the extensional rheology of low viscous liquids is very challenging, primarily due to the complexity of generating a homogeneous flow field. For this reason, free-surface flows are used as a characterisation method for the extensional flow properties of such liquids. Generally, an unstable liquid

column is created by rapidly stretching a fluid droplet between two plates and monitoring the breakup dynamics to extract rheological material parameters. The commercially available CaBER device, which follows the minimal filament radius with a laser micrometer, can detect viscosities down to $\eta = 70$ mPa.s and measures relaxation times until a lower limit of $\lambda = 1$ ms [111]. In order to extend the measuring range to fast relaxation processes near pinch-off, we have improved the CaBER setup in our lab in two ways.

- The spatial and temporal resolution of the setup is enhanced by following the thinning filament with a high-speed camera equipped with new lens system. This lens consists of a custom-made tube lens combined with a microscopic objective that provides a resolution of 3 μm. Additionally, the illumination is optimised to allow shutter times down to 3 μs. This improved setup enables us to visualise very small structures in the filament with great detail. The enhanced resolution is most clearly demonstrated during final pinching of non-colloidal suspensions, where it is possible to track the movement of individual particles with particle radii as low as $R_p = 3$ μm.
- Image processing routines are substantially improved by employing a modified version of the Marr-Hilldreth edge detector to locate the position of the filament edges with sub-pixel accuracy. A commercially available program was written to easily process consecutive images of a CaBER experiment and determine the relevant material parameters from the evolution of the minimal filament radius $R_m(t)$. The code was employed to characterise a set of capillary breakup experiments on inkjet printing model fluids performed with a custom-built extensional rheometer at Cambridge University that can stretch with higher velocities. The software is able to quantify relaxation times in these fluids of $\lambda = O(100$ ms), which are the smallest relaxation times that have been reliably obtain in capillary breakup experiments.

With the improved capillary breakup rheometer, we are now able quantify very fast relaxation processes in complex fluids that are used in commercial spraying and printing applications. The presence of such very small viscoelasticity can be beneficial to tune spraying patterns or to suppress the formation of satellite droplets that reduce the printing quality. Knowledge of the extensional rheological properties of these weak viscoelastic fluids is an important element in understanding the performance of these fluids during their application.

Viscoelastic jets exhibit different breakup dynamics than other free-surface flows

The viscoelastic nature of polymer solutions delays the breakup process of free-surface flows. The strong extensional flow field in the filament unravels the polymer chains, resulting in strong non-linear elastic stresses and a corresponding increase of the transient extensional viscosity. Capillary instabilities are stabilised during the important elasto-capillary regime, where the surface tension is balanced by the elastic polymeric stresses and the characteristic beads-on-a-string morphology appears. We have investigated experimentally the instability growth and the resulting breakup of inviscid, weak elastic jets. Unforced jets of different dilute polymer solutions are captured for a series of Weber numbers, ranging from the dripping-jetting transition at $We = 1$ to long stable jets at $We = 80$. The different thinning stages of the weak elastic jet are thoroughly described for different material and process parameters.

- The jet radius initially expands beyond the dimensions of the nozzle radius due to flow rearrangement when the fluid exits the nozzle. This extrudate swell increases with polymer concentration and decreases with the Weber number in a similar way as an inviscid Newtonian jet. The straight section of the jet is characterised by the onset of Plateau-Rayleigh instabilities that grow according to the predictions by linear stability analysis. The average wavelength of the instabilities is larger than in the case of a inviscid Newtonian liquid.

- The non-linear thinning is dominated by the elasto-capillary regime where the minimal filament radius decreases exponentially in time. By comparing the thinning dynamics of the jet with static capillary breakup experiments, a different time scale for the exponential decay is identified in both free-surface flows. A new time scale of $\theta = 2\lambda$ is observed during the jetting experiments, which implies that jets break up faster than static liquid bridges of the same elastic fluid. The smaller time scale in the EC regime of the jet is explained by a constant axial force, which is caused by the constant creation of new surface under the nozzle.

- The corner region where the filament is connected to the droplet displays a similarity structure in the static capillary breakup tests. On the contrary, the jetting profiles are not self-similar, indicating that the axial force is not decaying with the filament radius. Moreover, numerical simulations of the jet breakup with the FENE dumbbell model agree with the experimental observation when a proper value for the initial deformation of the polymer molecule is selected.

- The elasto-capillary regime ends when the polymer chains reach their finite extensibility limit resulting in the breakup of the jet. The breakup length is quantified for different solutions at various Weber numbers. An expression for the breakup length is proposed that shows a correlation with the square root of the Weber number, the Deborah number and the finite extensibility parameter.

The different time scale in the EC regime of a continuous jet is not only of fundamental interest as these jets are encountered in various spraying and dispensing applications. Since the extensional relaxation times of weak viscoelastic fluids are usually measured in a static capillary breakup experiment, the use of the wrong time scales results in an overproduction of the breakup time. Moreover, for the interpretation of the rheological data determined with the new jetting rheometers, it is important to use the correct time scales.

Suspensions are destabilised by the amplification of particle density fluctuations

As a second model system, we have studied the drop formation of non-colloidal suspensions in a Newtonian matrix. The breakup process is examined with the CaBER setup, where the instant creation of a slender filament results in a more straightforward interpretation of the capillary breakup than during previous dripping experiments. Experiments are performed on suspensions with varying particle radius and volume fraction and the results are in excellent agreement with simulations by Claire McIlroy and Oliver G. Harlen from Leeds University. The thinning dynamics are explained by dividing the breakup process into four distinct stages.

- The suspension initially behaves as a homogeneous viscous fluid and the filament radius decreases linearly in time following the viscous similarity scaling for the effective viscosity of the suspension. This viscosity is accurately predicted by the Maron-Pierce model.
- As the filament becomes thinner, it is destabilised by the amplification of local particle density fluctuations. These fluctuations generate a heterogeneous filament with diluted zones that exhibit a smaller viscosity and hence faster thinning rates. The onset of this concentration fluctuation regime is captured by a transition radius R_{T1} and a scaling for this radius is proposed based on the standard deviation of the mean inter-particle distance and the relative dependence of the viscosity to small changes in the volume fraction.

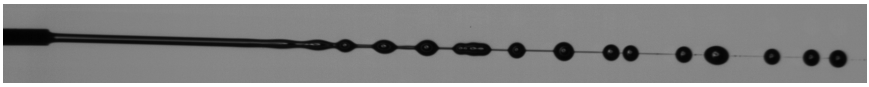

(a) Unforced instabilities

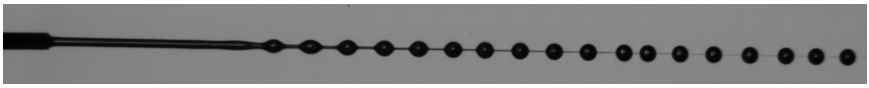

(b) Forced instabilities

Figure 7.1: Comparison of two viscoelastic jets (0.1% PEO_2 solution, $We = 3.8$): (a) an unforced jet that was studied in Chapter 5 and (b) a jet with periodic instabilities originating from a piezo-electric actuator that is attached to the nozzle ($kR_0 = 0.68$).

- The third regime starts when a particle-free section appears in the filament, where a small volume of medium fluid is caught between two particle clusters. At this point, the breakup process resembles a small-scale filament stretching experiment and the thinning rate reaches a maximum value.
- Just before breakup, a final deceleration regime is observed during which the depleted filament approaches the thinning rate of the pure medium fluid. The viscous self-similar scaling is verified by rescaling the filament profiles to retrieve the symmetric Stokes similarity solution.

Outlook for future research

Some suggestions for further research can be made based on the present thesis:

- All jetting experiments that are presented in this work start from unforced jets where the wavelength of the instability corresponds to the largest growth rate. Although such natural jets are encountered in most spraying and dispensing applications, the inevitable variation in the wavelength (see Figure 5.11d) makes the experimental procedure quite burdensome. Only a small fraction of the filaments can be analysed, because small changes in the wavelength can cause random coalescence of the beads before breakup. This coalescence along the thread is illustrated in Figure 7.1a, in which two adjacent droplets are joining and the larger drops further along the thread are a result of earlier coalescence. The natural

variation can be eliminated by imposing periodic perturbations to the fluid via a piezo-electric actuator that positioned close to the nozzle. The drive frequency of the piezo element f_p is taken over by the jet and if the corresponding wavenumber $k = 2\pi f_p/v$ lies in the unstable region, sinusoidal capillary instabilities with a single wavelength arise at the jet surface and are convected downstream. As shown in Figure 7.1b, this setup generates a periodic stream of equally sized beads, which simplifies the image processing of the experiment. Moreover, the periodic nature of the perturbation enables the use of stroboscopic imaging in order to increase the temporal resolution of the setup.

- The simulations in Section 5.5.4 show that the finite extensibility of the polymer chains has a large influence on the breakup of a viscoelastic jet. Throughout our jetting study, we have only investigated polymer solutions with approximately the same molecular weight and thus the same extensibility. Hence, it should be interesting to examine the thinning dynamics of a series of low viscous polymer solutions with the same relaxation time λ, but with different finite extensibility parameters L.

- In Section 6.3.3, we have stated that the final breakup stages of a non-colloidal suspension resemble a small-scale filament stretching experiment. Different thinning rates are found when changing the particle size and concentration, but an explanation for these trends is missing. Since the model suspensions consist of a Newtonian matrix, it is possible to model the liquid trapped between two end particles of finite diameter as a stretching Newtonian liquid bridge with a non-uniform prescribed movement of the end plates. A model, based on the one-dimensional mass and momentum conservation equations (Eqs. C.22 & C.24), was developed by Mariano Rubio and Alejandro Sevilla of University Carlos III in Madrid. By comparing the experimental data with these simulations, we hope to acquire a better understanding of this accelerated thinning regime.

- A large disadvantage of extensional rheometry is that a single rheometer can only probe a limited viscosity range. In our lab, polymer melts can be measured with the EVF setup and low viscous samples are characterised with the CaBER. However, many samples have an intermediate viscosity, which eliminates the use of the former devices. A filament stretching setup (see Section 2.1.3) would therefore be an excellent addition to the rheometry lab.

Appendix A

Rheological definitions

Basic concepts

In rheology, the deformation and flow of various materials is examined. This study involves the intimate relation between the flow and deformation on the one hand and stress on the other hand. The stress in a material is generally expressed using the three-dimensional symmetric stress tensor $\mathbf{T}$:

$$\mathbf{T} = \begin{bmatrix} T_{xx} & T_{xy} & T_{xz} \\ T_{yx} & T_{yy} & T_{yz} \\ T_{zx} & T_{zy} & T_{zz} \end{bmatrix}. \tag{A.1}$$

where T_{ij} are the stress components. The stress tensor completely describes the the stress condition around a point in the material. The first index refers to the direction of the stress component and the second to the normal to the plane the stress acts on. The diagonal elements represent the normal stresses that are oriented normal to the plain on which they act. The off-diagonal elements provide the shear stresses that are oriented within the plane under consideration. In absence of flow, there is still a hydrostatic pressure present in the fluid. The pressure causes an identical normal stress in all direction giving

$$\mathbf{T} = -P\mathbf{I} \tag{A.2}$$

where the sign convention is adopted that pressure is negative and tensile stress is positive. The application of flow induces additional stresses in the material that are captured with the extra stress tensor $\boldsymbol{\sigma}$ giving

$$\mathbf{T} = -P\mathbf{I} + \boldsymbol{\sigma}. \tag{A.3}$$

Since the pressure does not affect the flow in incompressible fluids, the extra stress tensor is the relevant rheological term. These extra stresses are only generated when adjacent fluid elements are in relative motion. This implies that rigid body rotations do not contribute to the stress. Hence, a distinction must be made between the stretching and the rotational part of the flow. A three-dimensional flow field is characterised with the velocity gradient tensor $\nabla\mathbf{v}$:

$$\nabla\mathbf{v} = \begin{bmatrix} \frac{\partial v_x}{\partial x} & \frac{\partial v_x}{\partial y} & \frac{\partial v_x}{\partial z} \\ \frac{\partial v_y}{\partial x} & \frac{\partial v_y}{\partial y} & \frac{\partial v_y}{\partial z} \\ \frac{\partial v_z}{\partial x} & \frac{\partial v_z}{\partial y} & \frac{\partial v_z}{\partial z} \end{bmatrix} \tag{A.4}$$

in which v_x, v_y and v_z are the velocity components in the three Cartesian directions. The rotational component can be removed by using the so-called symmetric part of the velocity gradient. The result is the rate of strain tensor $2\mathbf{D}$ that is defined as

$$2\mathbf{D} = \nabla\mathbf{v} + (\nabla\mathbf{v})^{\mathbf{T}}. \tag{A.5}$$

The rotational part of the flow is captured by the vorticity tensor $\boldsymbol{\Omega}$, which is defined as

$$\boldsymbol{\Omega} = \nabla\mathbf{v} - (\nabla\mathbf{v})^{\mathbf{T}}. \tag{A.6}$$

Constitutive equations

The intrinsic relation between the stress and the deformation of a fluid is provided by a rheological constitutive equation. The most simple example is the constitutive equation of a Newtonian liquid that states that the extra stress in the liquid is proportional to the rate of strain tensor

$$\boldsymbol{\sigma} = 2\eta\mathbf{D} \tag{A.7}$$

where η is the shear viscosity of the fluid. This three-dimensional version of Newton's law also predicts an extensional viscosity $\eta_E = 3\eta$ for a uniaxial extensional deformation (see Section 2.1).

However, many fluids do not satisfy the linear proportionality between stress and strain rate and are considered non-Newtonian. A first class of non-Newtonian fluids are the generalised Newtonian liquids, for which the stress is still completely determined by the instantaneous value of the strain rate, but is not proportional to it anymore. In order words, the viscosity of the fluid is not a constant but becomes a function of the flow strength, which is expressed by the second invariant of the rate of strain tensor, giving

$$\boldsymbol{\sigma} = 2\eta(\mathrm{II}_{\mathbf{2D}})\mathbf{D}. \tag{A.8}$$

For simple steady shear, the second invariant equals $\dot{\gamma}^2$, so the viscosity of the generalised Newtonian liquid is a function of the instantaneous value of the shear rate. In general, there are several common expression for $\eta(\mathrm{II}_{\mathbf{2D}})$. The most widely used form of the general viscous constitutive model is the power-law model:

$$\eta = K_n|\mathrm{II}_{\mathbf{2D}}|^{(n-1)/2}, \tag{A.9}$$

where n is the power law exponent and K_n is the consistency index. Alternatives like the Ellis model, the Cross model and the Carreau model use additional parameters to describe the viscosity.

A second class of rheological constitutive equations considers the fact the many materials exhibit an intermediate behaviour between a viscous fluid and an elastic solid. For an ideal elastic solid, the stress proportional to the deformation instead of the rate of deformation in a liquid. Materials with a rheological behaviour in between a solid and a liquid are called viscoelastic fluids. The most simple constitutive equation for these fluids is the Maxwell model

$$\lambda\dot{\boldsymbol{\sigma}} + \boldsymbol{\sigma} = 2\eta\mathbf{D} \tag{A.10}$$

where λ is the characteristic relaxation time of the material. The material exhibits solid-like behaviour for time scales smaller than λ, whereas it exhibits liquid-like behaviour for larger time scales. Since the Maxwell model is a linear equation, it is only valid for small deformations. For larger strains, the material response also depends on the applied strain and it can display non-linear viscoelastic behaviour, such as normal stresses in shear deformation or extensional strain hardening. Several non-linear constitutive equations have been developed to predict these phenomena. A general time-dependent non-linear model is obtained by incorporating rheological non-linearity into the

Maxwell equation. This is achieved by replacing the substantial time derivative $\dot{\boldsymbol{\sigma}}$ in Eq. A.10 with the upper-convected time derivate $\boldsymbol{\sigma}^{\nabla}$, generating the upper-convected Maxwell (UCM) model:

$$\lambda \boldsymbol{\sigma}^{\nabla} + \boldsymbol{\sigma} = 2\eta \mathbf{D}. \tag{A.11}$$

The upper-convected time derivative is a time derivative in a special coordinate system whose base coordinate vectors stretch and rotate with material lines. It is defined as:

$$\boldsymbol{\sigma}^{\nabla} = \frac{d\boldsymbol{\sigma}}{dt} + \mathbf{v} \cdot \nabla \boldsymbol{\sigma} - \boldsymbol{\sigma} \nabla \mathbf{v} - \nabla \mathbf{v}^{T} \boldsymbol{\sigma}. \tag{A.12}$$

This definition implies that stresses are only produced when material elements are deformed [23]. The UCM model is non-linear because $\boldsymbol{\sigma}^{\nabla}$ contains products of the velocity gradient and the stress tensor. For small deformations, the non-linear terms disappear and the upper-convected time derivative reduces to the substantial time derivative, giving the linear Maxwell model. For large deformations, the UCM model can predict non-linear phenomena, such as an unbounded growth of the extensional viscosity in a uniaxial extensional deformation for a Weissenberg number $Wi = \lambda \dot{\epsilon} > 1/2$.

Appendix B

Uniaxial extensional deformation

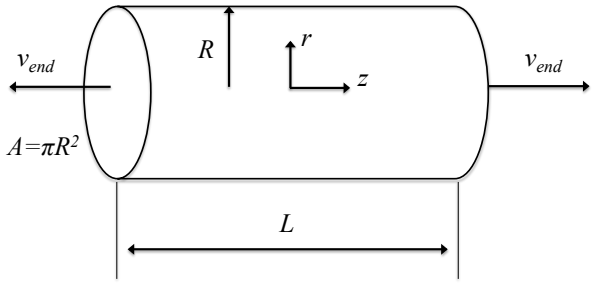

Figure B.1: Cylindrical sample undergoing uniaxial extension.

A uniaxial extensional deformation is characterised by a positive extensional deformation in just one coordinate and a contraction in the two other directions. This is shown in the rate of deformation tensor (see Eq. 2.2), which consists of one positive and two negative diagonal components. As illustrated in Figure B.1, the easiest way to imagine the generation of a uniaxial extension is to pull on both ends of a rod of fluid. In order to generate a steady uniaxial extensional deformation the flow field should be:

$$v_z = \dot{\epsilon}\, z \qquad \text{and} \qquad v_r = -\frac{\dot{\epsilon}\, r}{2} \tag{B.1}$$

where $\dot{\epsilon}$ is the constant extension rate. In order to achieve this velocity field in symmetric way, the sample ends should move with the velocity

$$v_{end} = \frac{\dot{\epsilon}\, L}{2}. \tag{B.2}$$

where L is the length of the rod. This end plate velocity can be rewritten as a simple first order differential equation

$$\frac{dL}{dt} = \dot{\epsilon}\, L, \tag{B.3}$$

which can be solved by integrating from the initial length L_0 to L

$$L = L_0\, e^{\dot{\epsilon} t}. \tag{B.4}$$

Hence, the length of the sample increases exponentially and the sample ends must move with an exponentially increasing velocity

$$v_{end} = \frac{1}{2}\dot{\epsilon}\, L_0\, e^{\dot{\epsilon} t}. \tag{B.5}$$

The strain in the sample is defined as

$$\epsilon = \dot{\epsilon}\, t = \ln\left(\frac{L}{L_0}\right). \tag{B.6}$$

This logarithmic strain measure is characteristic for extensional deformation of a fluid and is generally called the Hencky strain.

During filament stretching and capillary breakup experiments, the effective strain rate is calculated using observations of the filament radius. An expression for the strain rate is derived from Eq. B.4

$$\dot{\epsilon} = \frac{1}{L}\frac{dL}{dt}. \tag{B.7}$$

Because of the conservation of volume for an incompressible material, $R^2 L = R_0^2 L_0$, this expression can be rewritten as

$$\dot{\epsilon} = -\frac{2}{R}\frac{dR}{dt} \tag{B.8}$$

and the evolution of the radius is found as

$$R(t) = R_0 \exp\left(-\frac{\dot{\epsilon}t}{2}\right). \tag{B.9}$$

This expression indicates that the radius of a cylindrical filament should decrease exponentially under a constant strain rate.

The stress causing the sample to elongate is the normal stress difference $T_{zz} - T_{rr}$. Ignoring surface tension and other factors like gravity for simplicity, this stress is the tensile force per unit area acting on the end of the sample

$$T_{11} - T_{22} = \frac{F_T}{A}. \tag{B.10}$$

The area A and the force F_T are obviously time dependent. Because of the conservation of volume, the evolution of the area $A(t) = \pi R^2$ can be predicted using Eq. B.9

$$A(t) = \pi R_0^2 \exp(-\dot{\epsilon}t). \tag{B.11}$$

Thus the stress difference becomes

$$T_{11} - T_{22} = \frac{F_T \exp(\dot{\epsilon}t)}{\pi R_0^2}. \tag{B.12}$$

Appendix C

One-dimensional Navier-Stokes equation for thin filaments

This appendix provides an overview of the mass and momentum equations that are required to accurately describe the dynamics in a free-surface flows. We start by introducing the full three-dimensional Navier-Stokes equations that are subsequently simplified to a one-dimensional approximation under the assumption that the flow is predominantly located in the axial direction. Assuming the fluid column is sufficiently slender, the internal length and time scales (Eqs. 2.22 and 2.23) naturally appear by selecting the proper scales for the terms in these equations. The leading order equations are obtained with a radial expansion of the three-dimensional equations that was introduced by Eggers and Dupont [87]. These simplified equations are encountered in most papers on capillary breakup and are used for the simulations in Chapter 6. The equations are also employed in the research of viscoelastic fluids by replacing Newton's law with an appropriate constitutive equation [83, 107, 161, 168, 192]. As an illustration of the predictive strength of this simplified description, we simulate the static capillary breakup of Newtonian liquids with different viscosities, similar to the experiments that are presented in Section 6.2.

Full Navier-Stokes equations

We start by defining the set of partial differential equations that are used to study free-surface flows in a time dependent fluid domain. The main challenge for describing these flows is to find an accurate description for the fluid boundary. The driving force for filament breakup is proportional to the mean curvature, which goes to infinity as the jet radius goes to zero, making jet breakup a very singular phenomenon [17]. The momentum conservation is represented by the Navier-Stokes equation for an axisymmetric column of an incompressible fluid. These equations are expresses in cylindrical coordinates [86] as

$$\begin{aligned}
&\rho\big(\partial_t v_r + v_r\partial_r v_r + v_z\partial_z v_r\big) \\
&\qquad = -\partial_r P + \eta\left(\partial_r^2 v_r + \partial_z^2 v_r + \partial_r v_r/r - v_r/r^2\right), \qquad \text{(C.1)} \\
&\rho\big(\partial_t v_z + v_r\partial_r v_z + v_z\partial_z v_z\big) \\
&\qquad = -\partial_z P + \eta\left(\partial_r^2 v_z + \partial_z^2 v_z + \partial_r v_z/r\right) - \rho g. \qquad \text{(C.2)}
\end{aligned}$$

The gravitational acceleration points in negative axial direction. The continuity equation reads

$$\partial_r v_r + \partial_z v_z + v_r/r = 0. \qquad \text{(C.3)}$$

The previous equations hold for $0 \le r < R(z,t)$. On the free boundary, a stress boundary condition is defined, where the pressure and the viscous forces are balanced by the capillary forces:

$$\mathbf{n^T}\,\mathbf{T}\,\mathbf{n} = -\gamma\kappa, \qquad \text{(C.4)}$$

$$\mathbf{n^T}\,\mathbf{T}\,\mathbf{t} = 0. \qquad \text{(C.5)}$$

In these equations, $\mathbf{n}$ and $\mathbf{t}$ are unit vectors normal and the tangent the surface, respectively. Both vectors can be expressed in function of R' where the prime refers to a differentiation with respect to z. Since there are no gradients in the surface tension, the tangential stress at the interface is zero. Explicitly, this gives

$$P - \frac{2\eta}{1+R'^2}\left(\partial_r v_r + (\partial_z v_z)R'^2 - (\partial_r v_z + \partial_z v_r)R'\right) = \gamma\kappa\,|_{r=R} \qquad \text{(C.6)}$$

for the normal stress and

$$\frac{\eta}{1+R'^2}\left(2(\partial_r v_r)R' - 2(\partial_z v_z)R' + (\partial_r v_z + \partial_z v_r)(1-R'^2)\right) = 0\,|_{r=R} \qquad \text{(C.7)}$$

for the tangential stress. The expression for the mean curvature κ of an axisymmetric volume was introduced in Chapter 2. Finally, the surface has to move with the velocity field at the boundary:

$$\partial_t R + v_z R' = v_r\,|_{r=R}. \qquad \text{(C.8)}$$

This set of six coupled partial differential equation provides a full solution for the free-surface flow. Once the velocity known, the interface is moved according to Eq. C.7. The shape of the interface then couples back into the flow via the boundary conditions (Eqs. C.6 - C.7). In the next sections we show how these equations can be simplified to a set of two coupled partial differential equations.

Scaling

We want to find approximate solutions to the equations of motion in a thin filament where the typical thickness ℓ_r of the fluid neck is small compared with a typical axial scale ℓ_z . This means the problem contains a small parameter ε which relates the two scales

$$\ell_r = \varepsilon \ell_z. \qquad \text{(C.9)}$$

This assumption is similar to the classic lubrication theory to describe the flow in very narrow channels [86]. Additionally, the problem is characterised by a time scale τ. These three scales are now used to estimate the order of magnitude of the different terms in the Navier-Stokes equation. The axial velocity component is approximated by $v_z \approx \ell_z/\tau$, which can be seen as a definition for τ. From the continuity equation (Eq. C.3), we have $\partial_z v_z \approx \partial_r v_r$ and therefore $v_r \approx \varepsilon \ell_z/\tau$. The momentum equation consists of three terms, i.e inertial and viscous stresses and the pressure, that should have the same order of magnitude to get a balanced equation. The main contribution from the pressure comes from the mean curvature κ that is dominated by the radius of curvature perpendicular to the axis, $\kappa \approx 1/\ell_r$. The scales for the three important terms in the axial momentum balance are

$$\rho \partial_t v \approx \rho \frac{\ell_z}{\tau^2}, \tag{C.10}$$

$$\partial_z P \approx \frac{\gamma}{\ell_r \ell_z}, \tag{C.11}$$

$$\eta \partial_z^2 v_z \approx \frac{\eta}{\ell_z \tau}. \tag{C.12}$$

By equating the inertial and the pressure term, we get

$$\frac{\gamma}{\rho} = \frac{\ell_r \ell_z^2}{\tau^2} = \frac{\varepsilon \ell_z^3}{\tau^2}, \tag{C.13}$$

and balancing the inertial and the viscous term gives

$$\frac{\eta}{\rho} = \frac{\ell_z^2}{\tau}. \tag{C.14}$$

By combining Eq. C.9 with Eqs. C.13 - C.14, an expression for the three scales is obtained:

$$\ell_z = \varepsilon \frac{\eta^2}{\gamma \rho}\,, \qquad \ell_r = \varepsilon^2 \frac{\eta^2}{\gamma \rho}\,, \qquad \tau = \varepsilon^2 \frac{\eta^3}{\rho \gamma^2}, \tag{C.15}$$

where the typical internal length ℓ_v and time scale t_v appear as defined Chapter 2 (Eqs. 2.22 and 2.23). As expected, these scales are solely based on the physical properties of the liquid and the flow becomes independent of the initial conditions.

Radial expansion

A crucial simplification was introduced by Eggers and Dupont [87] by keeping only the lowest order radial dependence in the set of equations. The velocity and the pressure are expanded in a Taylor series with respect r

$$v_z(r,z,t) = v_0 + v_2 r^2 + \ldots, \tag{C.16}$$

$$v_r(r,z,t) = -\frac{v_0' r}{2} - \frac{v_2' r^3}{4} - \ldots, \tag{C.17}$$

$$P(r,z,t) = P_0 + P_2 r^2 + \ldots. \tag{C.18}$$

The pressure and axial velocity are symmetrically expanded and the coefficients for radial velocity are chosen in accordance with the continuity equation (Eq. C.3). These expansions are inserted in the full Navier Stokes description (Eq. C.1- C.3 and C.6 - C.8) and the equations are simplified by taking only the lowest order terms into account. The axial momentum balance (Eq. C.2) reduces to

$$\rho\left(\partial_t v_0 + v_0 v_0'\right) = -P_0' + \eta\left(4v_2 + v_0''\right) - \rho g. \tag{C.19}$$

In this equation, P_0 and v_2 can be eliminated using the simplified boundary conditions in the normal

$$P_0 + \eta v_0' = \gamma\kappa, \tag{C.20}$$

and the tangential direction

$$-v_0' R' + 2v_2 R - \frac{1}{2} v_0'' R - 2v_0' R' = 0. \tag{C.21}$$

This elimination results in the leading order approximation of the momentum balance and by dropping the index in v_0, we obtain

$$\rho\left(\partial_t v + v v'\right) = -\gamma\kappa' + 3\eta\frac{\left(R^2 v'\right)'}{R^2} - \rho g. \tag{C.22}$$

The typical Trouton ratio of 3 appears as a coefficient for the viscous term in this one-dimensional approximation of the Navier-Stokes equation.

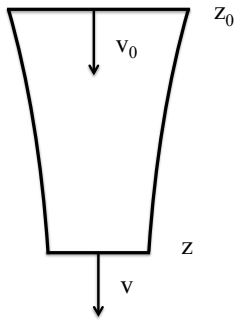

Figure C.1: Section of a rotationally symmetric fluid jet.

Continuity equation

The continuity equation can be derived by introducing the radial expansion into the kinetic boundary condition (Eq. C.8). However, it is more intuitive to simply take a macroscopic mass balance over the slender filament. Figure C.1 displays an axisymmetric control volume between two cross sections a slender jet. The circular cross sections are perpendicular to the axial velocity v, so only this component is considered in the mass balance, giving

$$\int_{z_0}^{z} \frac{\partial(\rho\pi R^2)}{\partial t} dz = \rho\pi R_0^2 v_0 - \rho\pi R^2 v. \tag{C.23}$$

Assuming the fluid is incompressible, the fluid density can be eliminated and the differentiation of this equation to z gives

$$\frac{\partial R^2}{\partial t} + \frac{\partial(R^2 v)}{\partial z} = 0. \tag{C.24}$$

Dimensionless governing equations

The capillary thinning of a Newtonian fluid can thus be described by the continuity equation (Eq. C.24) and the momentum balance (Eq. C.22). Generally, these equations are presented in dimensionless version using the

reference radius R_0 as length scale and the Rayleigh time t_R (Eq. 2.9) as time scale, giving

$$\frac{\partial h^2}{\partial \tau} + \frac{\partial}{\partial \bar{z}}(h^2 \bar{v}) = 0, \tag{C.25}$$

$$\frac{\partial \bar{v}}{\partial \tau} + \bar{v}\frac{\partial \bar{v}}{\partial \bar{z}} = -\frac{\partial \bar{\kappa}}{\partial \bar{z}} + \frac{3\,Oh}{h^2}\frac{\partial}{\partial \bar{z}}\left(h^2\left(\frac{\partial \bar{v}}{\partial \bar{z}}\right)\right), \tag{C.26}$$

where the global Ohnesorge number appears as a coefficient indicating the importance of the viscous contribution. The curvature term (Eq. 2.21) is defined as

$$\bar{\kappa} = \frac{1}{h\sqrt{1+(\partial h/\partial \bar{z})^2}} - \frac{\partial^2 h/\partial \bar{z}^2}{(1+(\partial h/\partial \bar{z})^2)^{3/2}}. \tag{C.27}$$

It is convenient to write all terms on the right-hand side of Eq. C.26 in the same from by rewriting the gradient of the mean curvature $\bar{\kappa}$ as [107]:

$$\frac{\partial \bar{\kappa}}{\partial \bar{z}} = -\frac{1}{h^2}\frac{\partial}{\partial \bar{z}}\left(h^2 K\right) \tag{C.28}$$

where K is defined as

$$K = \frac{1}{h\sqrt{1+(\partial h/\partial \bar{z})^2}} + \frac{\partial^2 h/\partial \bar{z}^2}{(1+(\partial h/\partial \bar{z})^2)^{3/2}}. \tag{C.29}$$

The curvature term K has almost the same form as $\bar{\kappa}$, but the sign in front of the first term is reversed. Eq. C.28 is used to rewrite the dimensionless momentum balance such that the inertial terms on the left are balanced by a single gradient in the right-hand side. Additionally, the left-hand side of Eq. C.26 is simplified with the Eq. C.25, giving

$$\frac{\partial}{\partial \tau}\left(h^2 \bar{v}\right) + \frac{\partial}{\partial \bar{z}}\left(h^2 \bar{v}^2\right) = \frac{\partial}{\partial \bar{z}}\left(h^2\left(K + 3Oh\frac{\partial \bar{v}}{\partial \bar{z}}\right)\right) = \frac{1}{\pi}\frac{\partial \bar{F}_z}{\partial \bar{z}}. \tag{C.30}$$

The right-hand side of the equation consists of the gradient of the dimensionless tensile force $\bar{F}_z$ in the filament. The total axial force in the filament is composed of bulk stresses applied to the cross-sectional area of the thread and the projection of the line force in the axial direction

$$\bar{F}_z = \pi h^2 \left(-\bar{P} + 2Oh \frac{\partial \bar{v}}{\partial \bar{z}} \right) + \frac{2\pi h}{\sqrt{1 + (\partial h / \partial \bar{z})^2}}. \tag{C.31}$$

The dimensionless pressure $\bar{P}$ can be eliminated with the stress boundary condition in the normal direction (Eq. C.20), which explains in the different sign of the surface tension contribution to the force.

Numerical scheme

To illustrate the predictive power of this set of simplified equations, we simulate a CaBER experiment with fixed boundaries $h = 1$ and $\bar{v} = 0$ at the top and bottom plate for all time steps. The equations are solved with Matlab with a numerical procedure that is based on the finite difference scheme proposed by Eggers and Dupont [87]. The spatial mesh is a fixed grid consisting of N homogeneously distributed grid points $\{z_i\}_{i=0}^{N}$ between the two end plates, at which the value of the approximate radius h_i is defined. The value of the approximate velocity v_i is defined at the position $z_{i+\frac{1}{2}}$, located halfway between two grid points:

$$z_{i+\frac{1}{2}} = \frac{1}{2} \left(z_i + z_{i+1} \right). \tag{C.32}$$

The solution at each time level is thus defined by two arrays $\{h_i\}_{i=0}^{N}$ and $\{v_i\}_{i=0}^{N-1}$. Difference analogues of Eq. C.25 are defined for each z_i point and analogues of Eq. C.27 are set at each intermediate point $z_{i+\frac{1}{2}}$. The partial differential equations are solved with a θ-method. In this type of solver, the time derivative is replaced by a forward difference discretisation where k denotes the present time-level and $k+1$ the next time-level. The value of the parameter θ determines the weight of the spatial terms that are evaluated at the present or the next time level:

$$\frac{\boldsymbol{c}^{k+1} - \boldsymbol{c}^{k}}{\Delta t} = \theta \boldsymbol{F}(\boldsymbol{c}^{k+1}) + (1 - \theta) \boldsymbol{F}(\boldsymbol{c}^{k}) \tag{C.33}$$

where $\boldsymbol{c}$ represents an array of the variables (h and v) and $\boldsymbol{F}$ is an array of difference analogues of the spatial terms of the continuity and momentum equation for all mesh nodes. Since first order derivatives were employed in the discretisation of the PDE's, the solver becomes an explicit Euler method

for $\theta = 0$ and an implicit Euler method for $\theta = 1$. An explicit method is computationally cheap, but has the clear disadvantage that the time step Δt must be restricted in order to to fulfil the Courant stability condition. Moreover, the time step Δt should be smaller than the diffusion time h^2/Oh, restricting the assessment of higher viscosities [22, 107]. A purely implicit method has the advantage of being unconditionally stable, so the only reason to restrict the time-step is because of accuracy requirements. An implicit Euler has an accuracy of $O(\Delta t)$ which is the same as the explicit Euler. In our simulations, θ is set to 1/2, which is in fact a more accurate Crank-Nicholson method. One can show that this scheme is also unconditionally stable and its accuracy is one order higher than the implicit Euler method, i.e. $O(\Delta t^2)$. The discretisation results in a system of 2N-5 non-linear equations for each time step that arise from the N-2 continuity equations at each non-boundary z_i node and the N-3 momentum equations at each non-boundary $z_{i+\frac{1}{2}}$ node. This system is solved with the Newton-Raphson method, which generally requires only two iterations to reach convergence.

We have simulated a CaBER experiment with plate radius $R_0 = 2$ mm and the final gap $L_1 = 8$ mm. The initial shape of the free surface is modelled as an arc of a circle to mimic a liquid bridge held between two end plates. The initial middle radius $R_m(0) = 0.4$ mm was chosen to create some slenderness in the initial column. Figure C.2 displays the evolution of three liquid bridges with $Oh = 0.1$, $Oh = 0.4$ and $Oh = 1.8$. These Ohnesorge numbers correspond to silicon oils with a viscosity of 20, 80 and 360 mPa.s, respectively. This latter value matches PDMS 2 that was used as medium for the suspensions in Chapter 6. The dimensionless time to breakup $(t_p - t)/t_R$ is specified for each filament, suggesting larger breakup times for the more viscous fluids.

The fluid shown in Figure C.2a has an Ohnesorge number below the critical value $Oh^* = 0.2077$ [95], indicating that breakup is dominated by an inertia-capillary balance. The effect of inertia is clear from the shape of the filaments as the inertial stress shifts the pinching point in the axial direction from the centre towards the stagnant drops. The location of the pinching point guarantees that a large satellite drop is formed in the centre after breakup. The one-dimensional approximation however does not capture the overturning of the profile that is generally observed during inertia dominated pinching (see Figure 2.10) [89, 96]. The most viscous fluid, presented in Figure C.2c, displays symmetric pinching that agrees with visco-capillary balance where the filament thinning is unaffected by inertia. The shape of the thread resembles the image of a viscous silicon oil filament shown in Figure 2.11a. The filament breaks in the middle between the droplets suggesting that no satellite droplet is formed.

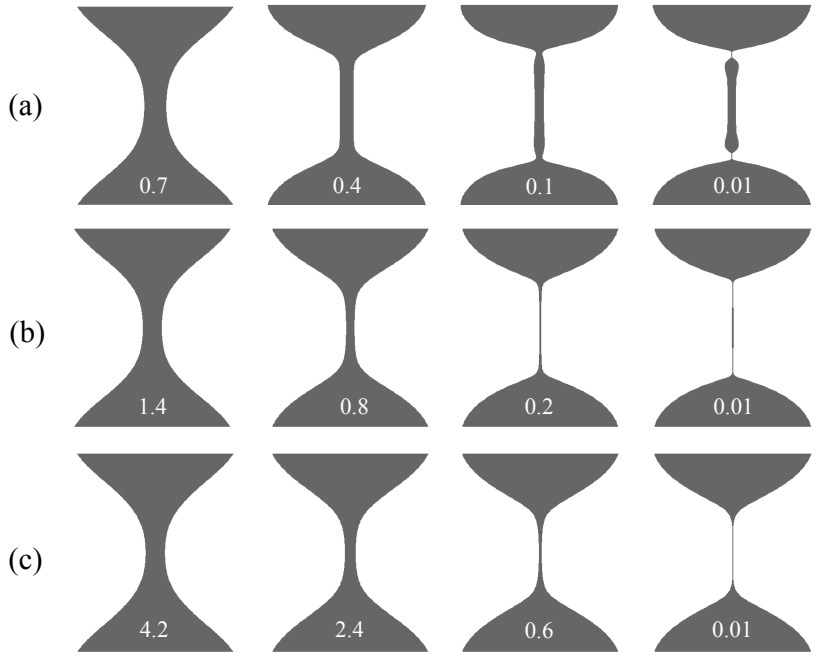

Figure C.2: Simulations of capillary breakup of Newtonian filaments with varying viscosity indicated with a global Ohnesorge number of (a) $Oh = 0.1$, (b) $Oh = 0.4$ and (c) $Oh = 1.8$. The dimensionless time to breakup is indicated in each figure.

The formation of a satellite droplet can also be deduced from the velocity profile that is shown in Figure C.3. The more viscous filament exhibits a symmetric velocity curve that reveals flow from the centre towards the droplets. The maximum velocity is found halfway between the centre and the intersection of the filament with the static droplets, in which the velocity returns to zero. In contrast, the low viscous fluid has two pinching points close to the static droplets. The velocity of this fluid is clearly higher than for the former fluid, which suggests that the filament thins significantly faster. The fluid near the pinching points is not solely draining into the large fluid reservoirs, but there is also a strong flow from these pinching points back to the centre of the filament. Hence, a large amount of fluid is trapped in the filament and will form a large droplet after pinch-off.

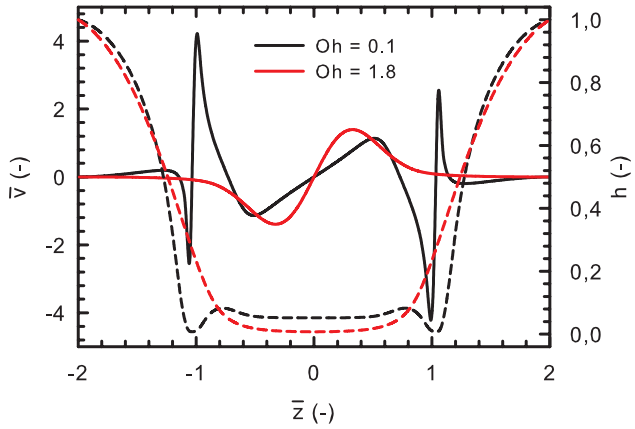

Figure C.3: The velocity (full lines) and radius profiles (dashed lines) of two thin filament with different viscosity just before pinch-off at the same minimal radius $h_m = 0.007$.

Figure C.2b shows the evolution of thin filaments of a third liquid with an intermediate viscosity. The shape of the threads initially resembles that of the more viscous fluid. However the symmetrical shape disappears near pinch-off as minimal radius shifts towards the static drops, indicating an inertial effect. This fluid has a similar Ohnesorge number as the experimental thread in Figure 2.9a and exhibits the universal inertia-viscous scaling before breakup [90]. This vertical shift of the necking point generates a satellite drop with a much smaller volume than in the case of inertia-capillary thinning.

Appendix D

Technical drawings of the tube lens

This appendix provides some additional technical information on the design of the tube lens that is discussed in Section 4.1.2. The tube lens was constructed with optical components from Thorlabs. Figure D.1 shows an exploded view of the lens design, so the individual parts can be distinguished. A summary of these parts is presented in Table D.1 and a technical drawing is displayed in Figure D.2.

Some practical remarks on the lens assembly:

- The internal threads of the lens tube differs from the C-mount thread of the camera and the RMS thread of the Olympus objective. The necessary adapters are included in the design, but must be removed when attaching the end caps for dust-free storage of the lens.
- In order to position the bi-convex lens at a distance of 175 mm of the camera sensor, two basic lens tubes are combined with an adjustable focussing tube. The latter component allows a length variation of nearly one inch to obtain the proper tube length. The fine tuning of the tube length is illustrated in Figure D.2, where the adjustable focusing element is positioned for the case that the CMOS sensor is located 9 mm inside the camera.

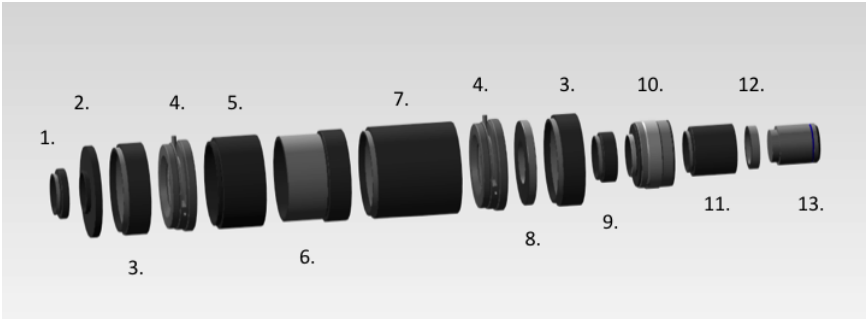

Figure D.1: Exploded view of the tube lens. The components are numbered and listed in Table D.1.

Number	Part Number	Description
1	SM1A9	C-mount adapter
2	SM1A2	Adapter with external SM1 and internal SM2 threads
3	SM2L05	Lens tube ($d = 2$”), thread depth = 0.5”
4	SM2D25	Iris diaphragm ($d = 2$”), lever-actuated
5	SM2L10	Lens tube ($d = 2$”), thread depth = 1”
6	SM2V10	Rotatable adjustable focussing element ($d = 2$”)
7	SM2L20	Lens tube ($d = 2$”), thread depth = 2”
8	SM2A6	Adapter with external SM2 and internal SM1 threads
9	SM1L03	Lens tube ($d = 1$”), thread depth = 0.3”
10	SM1ZM	Zoom housing ($d = 1$”) with inside
	LB1294	Bi-convex lens, 1", $f = 175$ mm
11	SM1L10	Lens tube ($d = 1$”), thread depth = 1”
12	SM1A3	Adapter with RMS threads
13	RMS4X	Olympus microscopic objective
14	SM1CP1	Internally SM1-threaded end cap
15	SM1CP2	Externally SM1-threaded end cap

Table D.1: Components of the tube lens system.

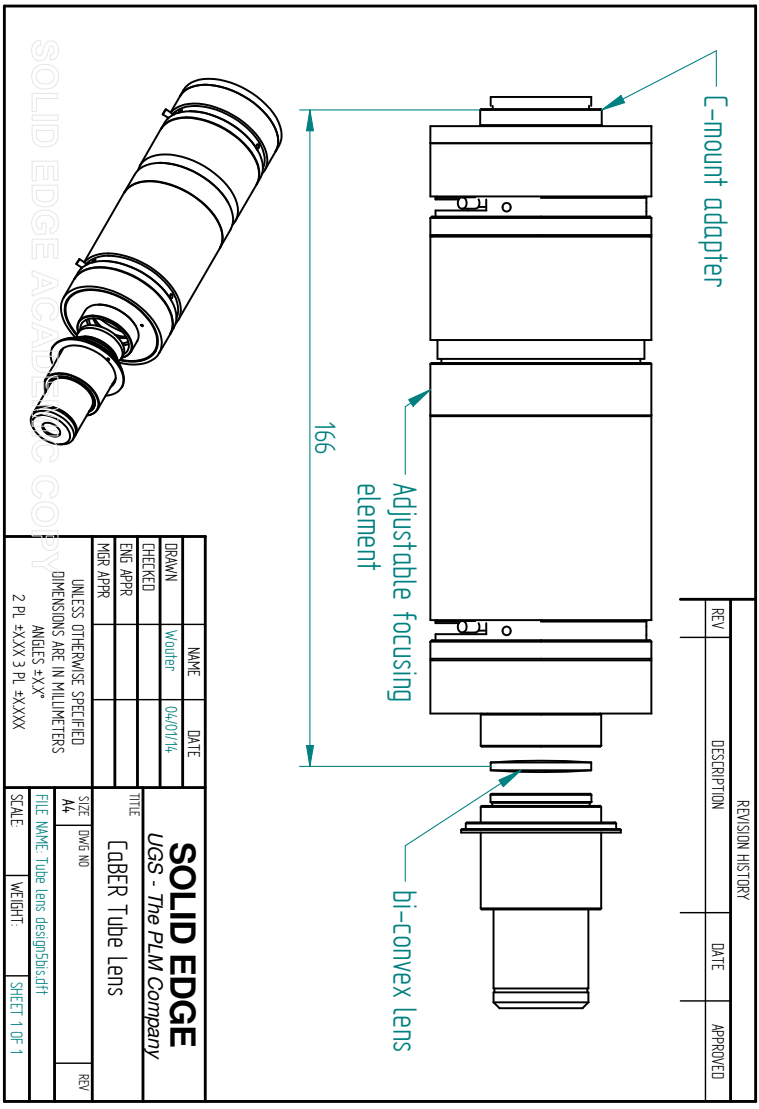

Figure D.2: Technical drawing of the tube lens where the zoom lens housing is hidden to show the bi-convex lens. The distance between the C-mount adapter and the lens can be varied with the adjustable focusing element in order to get the required distance of 175 mm between the lens and the camera sensor.

Bibliography

[1] Plateau, J. *Statique éxperimentale et théorique des liquides soumis aux seules forces moléculaires* (1873).

[2] Rayleigh, L. On the instability of jets. *Proceedings of the London Mathematical Society* **10**, 4–13 (1878).

[3] McKinley, G. H. Visco-elasto-capillary thinning and break-up of complex fluids. *Rheology reviews* **3**, 1–48 (2005).

[4] Clasen, C., Phillips, P. M., Palangetic, L. & Vermant, J. Dispensing of rheologically complex fluids: The map of misery. *AIChE Journal* **58**, 3242–3255 (2012).

[5] Eggers, J. Nonlinear dynamics and breakup of free-surface flows. *Reviews of Modern Physics* **69**, 865–929 (1997).

[6] Akesson, N. B., Steinke, W. E. & Yates, W. E. Spray atomization characteristics as a function of pesticide formulations and atomizer design. *Journal of Environmental Science and Health Part B-pesticides Food Contaminants and Agricultural Wastes* **29**, 785–814 (1994).

[7] Smolinski, J. M., Gulari, E. & Manke, C. W. Atomization of dilute polyisobutylene mineral oil solutions. *Aiche Journal* **42**, 1201–1212 (1996).

[8] Chao, K. K., Child, C. A., Grens, E. A. & Williams, M. C. Antimisting action of polymeric additives in jet fuels. *Aiche Journal* **30**, 111–120 (1984).

[9] Morrison, N. F. & Harlen, O. G. Viscoelasticity in inkjet printing. *Rheologica Acta* **49**, 619–632 (2010).

[10] Derby, B. Inkjet printing of functional and structural materials: Fluid property requirements, feature stability, and resolution. *Annual Review of Materials Research* **40**, 395–414 (2010).

[11] Hoath, S. D., Harlen, O. G. & Hutchings, I. M. Jetting behavior of polymer solutions in drop-on-demand inkjet printing. *Journal of Rheology* **56**, 1109–1127 (2012).

[12] Hoath, S. D. *et al.* Inkjet printing of weakly elastic polymer solutions. *Journal of Non-Newtonian Fluid Mechanics* **205**, 1–10 (2014).

[13] Donnelly, R. J. & Glaberson, W. Experiments on capillary instability of a liquid jet. *Proceedings of the Royal Society of London Series A-mathematical and Physical Sciences* **290**, 547–556 (1966).

[14] Goedde, E. F. & Yuen, M. C. Experiments on liquid jet instability. *Journal of Fluid Mechanics* **40**, 495–511 (1970).

[15] Mun, R. P., Byars, J. A. & Boger, D. V. The effects of polymer concentration and molecular weight on the breakup of laminar capillary jets. *Journal of Non-Newtonian Fluid Mechanics* **74**, 285–297 (1998).

[16] Christanti, Y. & Walker, L. M. Surface tension driven jet break up of strain-hardening polymer solutions. *Journal of Non-Newtonian Fluid Mechanics* **100**, 9–26 (2001).

[17] Eggers, J. & Villermaux, E. Physics of liquid jets. *Reports On Progress In Physics* **71**, 036601 (2008).

[18] Furbank, R. J. & Morris, J. F. An experimental study of particle effects on drop formation. *Physics of Fluids* **16**, 1777–1790 (2004).

[19] Furbank, R. J. & Morris, J. F. Pendant drop thread dynamics of particle-laden liquids. *International Journal of Multiphase Flow* **33**, 448–468 (2007).

[20] Miskin, M. Z. & Jaeger, H. M. Droplet formation and scaling in dense suspensions. *Proceedings of the National Academy of Sciences of the United States of America* **109**, 4389–4394 (2012).

[21] Bonnoit, C., Bertrand, T., Clement, E. & Lindner, A. Accelerated drop detachment in granular suspensions. *Physics of Fluids* **24**, 043304 (2012).

[22] McIlroy, C. & Harlen, O. G. Modelling capillary breakup of particulate suspensions. *Physics of Fluids* **26**, 033101 (2014).

[23] Macosko, C. W. *Rheology - Principles, Measurements and Applications* (Wiley, 1994).

[24] Barnes, H. A. *An introduction to rheology* (Elsevier Science Ltd, 1989).

[25] McKinley, G. H. & Sridhar, T. Filament-stretching rheometry of complex fluids. *Annual Review of Fluid Mechanics* **34**, 375–415 (2002).

[26] Peng, S. T. J. & Landel, R. F. Rheological behavior of fm-9 solutions and correlation with flammability test-results and interpretations. *Journal of Non-newtonian Fluid Mechanics* **12**, 95–111 (1983).

[27] Fano, G. Contributo allo studio dei corpi filanti. *Archivio di Fisiologia* **5**, 365–370 (1908).

[28] Petrie, C. J. S. One hundred years of extensional flow. *Journal of Non-Newtonian Fluid Mechanics* **137**, 1–14 (2006).

[29] Padmanabhan, R. Measurement of extensional viscosity of viscoelastic liquid foods. *Journal of Food Engineering* **25**, 311–327 (1995).

[30] Funami, T. Next target for food hydrocolloid studies: Texture design of foods using hydrocolloid technology. *Food Hydrocolloids* **25**, 1904–1914 (2011).

[31] Petrie, C. J. S. & Denn, M. M. Instabilities in polymer processing. *Aiche Journal* **22**, 209–236 (1976).

[32] de Gennes, P. G. Coil-stretch transition of dilute flexible polymers under ultrahigh velocity-gradients. *Journal of Chemical Physics* **60**, 5030–5042 (1974).

[33] Perkins, T. T., Smith, D. E. & Chu, S. Single polymer dynamics in an elongational flow. *Science* **276**, 2016–2021 (1997).

[34] Smith, D. E. & Chu, S. Response of flexible polymers to a sudden elongational flow. *Science* **281**, 1335–1340 (1998).

[35] Smith, D. E., Babcock, H. P. & Chu, S. Single-polymer dynamics in steady shear flow. *Science* **283**, 1724–1727 (1999).

[36] Meissner, J. Experimental aspects in polymer melt elongational rheometry. *Chemical Engineering Communications* **33**, 159–180 (1985).

[37] Trouton, F. T. On the coefficient of viscous traction and its relation to that of viscosity. *Proceedings of the Royal Society London A* **77**, 426–440 (1906).

[38] Petrie, C. J. S. Extensional viscosity: A critical discussion. *Journal of Non-Newtonian Fluid Mechanics* **137**, 15–23 (2006).

[39] Chatraei, S., Macosko, C. W. & Winter, H. H. Lubricated squeezing flow - a new biaxial extensional rheometer. *Journal of Rheology* **25**, 433–443 (1981).

[40] Meissner, J., Stephenson, S. E., Demarmels, A. & Portmann, P. Multiaxial elongational flows of polymer melts - classification and experimental realization. *Journal of Non-Newtonian Fluid Mechanics* **11**, 221–237 (1982).

[41] Laun, H. M. & Schuch, H. Transient elongational viscosities and drawability of polymer melts. *Journal of Rheology* **33**, 119–175 (1989).

[42] Taylor, G. The formation of emulsions in definable fields of flow. *Proceedings of the Royal Society of London A* **146**, 501–523 (1934).

[43] Scrivener, O. *et al.* Dynamical behavior of drag-reducing polymer-solutions. *Journal of Non-newtonian Fluid Mechanics* **5**, 475–495 (1979).

[44] Fuller, G. G. & Leal, L. G. Flow birefringence of concentrated polymer-solutions in two-dimensional flows. *Journal of Polymer Science Part B-polymer Physics* **19**, 557–587 (1981).

[45] Galindo-Rosales, F. J., Alves, M. A. & Oliveira, M. S. N. Microdevices for extensional rheometry of low viscosity elastic liquids: a review. *Microfluidics and Nanofluidics* **14**, 1–19 (2013).

[46] Meissner, J., Raible, T. & Stephenson, S. E. Rotary clamp in uniaxial and biaxial extensional rheometry of polymer melts. *Journal of Rheology* **25**, 1–28 (1981).

[47] Meissner, J. Development of a universal extensional rheometer for uniaxial extension of polymer melts. *Transactions of the Society of Rheology* **16**, 405–420 (1972).

[48] Meissner, J. & Hostettler, J. A new elongational rheometer for polymer melts and other highly viscoelastic liquids. *Rheologica Acta* **33**, 1–21 (1994).

[49] Sentmanat, M., Wang, B. N. & McKinley, G. H. Measuring the transient extensional rheology of polyethylene melts using the ser universal testing platform. *Journal of Rheology* **49**, 585–606 (2005).

[50] Macosko, C. & Lorntson, J. The rheology of two blow-molding polyethylenes. In *Annual Technical Conference Society of Plastic Engineering* (1973).

[51] Anna, S. L., Rogers, C. & McKinley, G. H. On controlling the kinematics of a filament stretching rheometer using a real-time active control mechanism. *Journal of Non-newtonian Fluid Mechanics* **87**, 307–335 (1999).

[52] Matta, J. E. & Tytus, R. P. Liquid stretching using a falling cylinder. *Journal of Non-newtonian Fluid Mechanics* **35**, 215–229 (1990).

[53] Szabo, P., McKinley, G. H. & Clasen, C. Constant force extensional rheometry of polymer solutions. *Journal of Non-newtonian Fluid Mechanics* **169**, 26–41 (2012).

[54] Sridhar, T., Tirtaatmadja, V., Nguyen, D. A. & Gupta, R. K. Measurement of extensional viscosity of polymer-solutions. *Journal of Non-newtonian Fluid Mechanics* **40**, 271–280 (1991).

[55] Tirtaatmadja, V. & Sridhar, T. A filament stretching device for measurement of extensional viscosity. *Journal of Rheology* **37**, 1081–1102 (1993).

[56] Spiegelberg, S. H., Ables, D. C. & McKinley, G. H. The role of end-effects on measurements of extensional viscosity in filament stretching rheometers. *Journal of Non-newtonian Fluid Mechanics* **64**, 229–267 (1996).

[57] Kolte, M. I., Rasmussen, H. K. & Hassager, O. Transient filament stretching rheometer .2. numerical simulation. *Rheologica Acta* **36**, 285–302 (1997).

[58] Orr, N. V. & Sridhar, T. Probing the dynamics of polymer solutions in extensional flow using step strain rate experiments. *Journal of Non-newtonian Fluid Mechanics* **82**, 203–232 (1999).

[59] Rothstein, J. P. & McKinley, G. H. Inhomogeneous transient uniaxial extensional rheometry. *Journal of Rheology* **46**, 1419–1443 (2002).

[60] Rothstein, J. P. & McKinley, G. H. A comparison of the stress and birefringence growth of dilute, semi-dilute and concentrated polymer solutions in uniaxial extensional flows. *Journal of Non-newtonian Fluid Mechanics* **108**, PII S0377–0257(02)00134–9 (2002).

[61] Anna, S. L. & McKinley, G. H. Elasto-capillary thinning and breakup of model elastic liquids. *Journal of Rheology* **45**, 115–138 (2001).

[62] Anna, S. L. *et al.* An interlaboratory comparison of measurements from filament-stretching rheometers using common test fluids. *Journal of Rheology* **45**, 83–114 (2001).

[63] Hassager, O., Kolte, M. I. & Renardy, M. Failure and nonfailure of fluid filaments in extension. *Journal of Non-newtonian Fluid Mechanics* **76**, 137–151 (1998).

[64] Bazilevskii, A. V., Entov, V. M. & Rozhkov, A. N. Liquid filament microrheometer and some of its applications. In Oliver, D. (ed.) *3rd European Rheology Conference* (1990).

[65] Liang, R. F. & Mackley, M. R. Rheological characterization of the time and strain dependence for polyisobutylene solutions. *Journal of Non-newtonian Fluid Mechanics* **52**, 387–405 (1994).

[66] Bhardwaj, A., Miller, E. & Rothstein, J. P. Filament stretching and capillary breakup extensional rheometry measurements of viscoelastic wormlike micelle solutions. *Journal of Rheology* **51**, 693–719 (2007).

[67] Peregrine, D. H., Shoker, G. & Symon, A. The bifurcation of liquid bridges. *Journal of Fluid Mechanics* **212**, 25–39 (1990).

[68] Goldin, M., Yerushalmi, J., Pfeffer, R. & Shinnar, R. Breakup of a laminar capillary jet of a viscoelastic fluid. *Journal of Fluid Mechanics* **38**, 689–711 (1969).

[69] Grant, R. P. & Middleman, S. Newtonian jet stability. *AICHE Journal* **12**, 669–678 (1966).

[70] Kroesser, F. W. & Middleman, S. Viscoelastic jet stability. *AICHE Journal* **15**, 383–386 (1969).

[71] Bhat, P. P. *et al.* Formation of beads-on-a-string structures during break-up of viscoelastic filaments. *Nature Physics* **6**, 625–631 (2010).

[72] Sauter, U. S. & Buggisch, H. W. Stability of initially slow viscous jets driven by gravity. *Journal of Fluid Mechanics* **533**, 237–257 (2005).

[73] Rubio-Rubio, M., Sevilla, A. & Gordillo, J. M. On the thinnest steady threads obtained by gravitational stretching of capillary jets. *Journal of Fluid Mechanics* **729**, 471–483 (2013).

[74] Savart, F. Memoire sur la constitution des veines liquides lancees par des orifices circulaires en mince paroi. *Annales de chimie* **53**, 337–386 (1833).

[75] Zhang, X. G. & Basaran, O. A. An experimental study of dynamics of drop formation. *Physics of Fluids* **7**, 1184–1203 (1995).

[76] Shi, X. D., Brenner, M. P. & Nagel, S. R. A cascade of structure in a drop falling from a faucet. *Science* **265**, 219–222 (1994).

[77] Amarouchene, Y., Bonn, D., Meunier, J. & Kellay, H. Inhibition of the finite-time singularity during droplet fission of a polymeric fluid. *Physical Review Letters* **86**, 3558–3561 (2001).

[78] Cooper-White, J. J., Fagan, J. E., Tirtaatmadja, V., Lester, D. R. & Boger, D. V. Drop formation dynamics of constant low-viscosity, elastic fluids. *Journal of Non-Newtonian Fluid Mechanics* **106**, 29–59 (2002).

[79] Tirtaatmadja, V., McKinley, G. H. & Cooper-White, J. J. Drop formation and breakup of low viscosity elastic fluids: Effects of molecular weight and concentration. *Physics of Fluids* **18**, 043101 (2006).

[80] Rutland, D. F. & Jameson, G. J. Non-linear effect in capillary instability of liquid jets. *Journal of Fluid Mechanics* **46**, 267–271 (1971).

[81] Plateau, J. Recherches expérimentales et théorique sur les figures d'équilibre d'une masse liquide sans pesanteur. *Memoires de l'Academie Royale des Sciences de Belgique* **23**, 5 (1849).

[82] Lafrance, P. Nonlinear breakup of a laminar liquid jet. *Physics of Fluids* **18**, 428–432 (1975).

[83] Ardekani, A. M., Sharma, V. & McKinley, G. H. Dynamics of bead formation, filament thinning and breakup in weakly viscoelastic jets. *Journal of Fluid Mechanics* **665**, 46–56 (2010).

[84] Chandrasekhar, S. *Hydrodynamic and hydromagnetic stability* (Oxford Univeristy Press, 1961).

[85] Middleman, S. Stability of a viscoelastic jet. *Chemical Engineering Science* **20**, 1037–1040 (1965).

[86] Deen, W. *Analysis of Transport Phenomena* (Oxford Univeristy Press, USA, 1998).

[87] Eggers, J. & Dupont, T. F. Drop formation in a one-dimensional approximation of the navier-stokes equation. *Journal of Fluid Mechanics* **262**, 205–221 (1994).

[88] Garcia, F. J. & Castellanos, A. One-dimensional models for slender axisymmetrical viscous-liquid jets. *Physics of Fluids* **6**, 2676–2689 (1994).

[89] Ambravaneswaran, B., Wilkes, E. D. & Basaran, O. A. Drop formation from a capillary tube: Comparison of one-dimensional and two-dimensional analyses and occurrence of satellite drops. *Physics of Fluids* **14**, 2606–2621 (2002).

[90] Eggers, J. Universal pinching of 3d axisymmetrical free-surface flow. *Physical Review Letters* **71**, 3458–3460 (1993).

[91] Leal, L. *Advanced Transport Phenomena* (Cambridge University Press, 2007).

[92] Kowalewski, T. A. On the separation of droplets from a liquid jet. *Fluid Dynamics Research* **17**, 121–145 (1996).

[93] Rothert, A., Richter, R. & Rehberg, I. Transition from symmetric to asymmetric scaling function before drop pinch-off. *Physical Review Letters* **87**, 084501 (2001).

[94] Chen, A. U., Notz, P. K. & Basaran, O. A. Computational and experimental analysis of pinch-off and scaling. *Physical Review Letters* **88**, 174501 (2002).

[95] Campo-Deaño, L. & Clasen, C. The slow retraction method (srm) for the determination of ultra-short relaxation times in capillary breakup extensional rheometry experiments. *Journal of Non-Newtonian Fluid Mechanics* **165**, 1688–1699 (2010).

[96] Wilkes, E. D., Phillips, S. D. & Basaran, O. A. Computational and experimental analysis of dynamics of drop formation. *Physics of Fluids* **11**, 3577–3598 (1999).

[97] Chen, Y. J. & Steen, P. H. Dynamics of inviscid capillary breakup: Collapse and pinchoff of a film bridge. *Journal of Fluid Mechanics* **341**, 245–267 (1997).

[98] Day, R. F., Hinch, E. J. & Lister, J. R. Self-similar capillary pinchoff of an inviscid fluid. *Physical Review Letters* **80**, 704–707 (1998).

[99] Papageorgiou, D. T. On the breakup of viscous-liquid threads. *Physics of Fluids* **7**, 1529–1544 (1995).

[100] Doshi, P., Suryo, R., Yildirim, O. E., McKinley, G. H. & Basaran, O. A. Scaling in pinch-off of generalized newtonian fluids. *Journal of Non-newtonian Fluid Mechanics* **113**, 1–27 (2003).

[101] Doshi, P. & Basaran, O. A. Self-similar pinch-off of power law fluids. *Physics of Fluids* **16**, 585–593 (2004).

[102] Huisman, F. M., Friedman, S. R. & Taborek, P. Pinch-off dynamics in foams, emulsions and suspensions. *Soft Matter* **8**, 6767–6774 (2012).

[103] Niedzwiedz, K., Buggisch, H. & Willenbacher, N. Extensional rheology of concentrated emulsions as probed by capillary breakup elongational rheometry (caber). *Rheologica Acta* **49**, 1103–1116 (2010).

[104] Christanti, Y. & Walker, L. M. Effect of fluid relaxation time of dilute polymer solutions on jet breakup due to a forced disturbance. *Journal of Rheology* **46**, 733–748 (2002).

[105] Bousfield, D. W., Keunings, R., Marrucci, G. & Denn, M. M. Nonlinear-analysis of the surface-tension driven breakup of viscoelastic filaments. *Journal of Non-Newtonian Fluid Mechanics* **21**, 79–97 (1986).

[106] Entov, V. M. & Hinch, E. J. Effect of a spectrum of relaxation times on the capillary thinning of a filament of elastic liquid. *Journal of Non-Newtonian Fluid Mechanics* **72**, 31–53 (1997).

[107] Clasen, C., Eggers, J., Fontelos, M. A., Li, J. & McKinley, G. H. The beads-on-string structure of viscoelastic threads. *Journal of Fluid Mechanics* **556**, 283–308 (2006).

[108] Larson, R. G. *The structure and rheology of complex fluids* (Oxford University Press, 1999).

[109] Stelter, M., Brenn, G., Yarin, A. L., Singh, R. P. & Durst, F. Investigation of the elongational behavior of polymer solutions by means of an elongational rheometer. *Journal of Rheology* **46**, 507–527 (2002).

[110] Clasen, C. *et al.* How dilute are dilute solutions in extensional flows? *Journal of Rheology* **50**, 849–881 (2006).

[111] Rodd, L. E., Scott, T. P., Cooper-White, J. J. & McKinley, G. H. Capillary break-up rheometry of low-viscosity elastic fluids. *Applied Rheology* **15**, 12–27 (2005).

[112] Polyox water-soluble resins (2002). URL `www.dow.com/dowwololff/en/industrial_solution/resources/literature/index.htm`.

[113] Deboeuf, A., Gauthier, G., Martin, J., Yurkovetsky, Y. & Morris, J. F. Particle pressure in a sheared suspension: A bridge from osmosis to granular dilatancy. *Physical Review Letters* **102**, 108301 (2009).

[114] Mewis, J. & Wagner, N. *Colloidal Suspension Rheology* (Cambridge University Press, 2012).

[115] Batchelor, G. K. Sedimentation in a dilute dispersion of spheres. *Journal of Fluid Mechanics* **52**, 245–268 (1972).

[116] McKinley, G. H. & Tripathi, A. How to extract the newtonian viscosity from capillary breakup measurements in a filament rheometer. *Journal of Rheology* **44**, 653–670 (2000).

[117] Slobozhanin, L. A. & Perales, J. M. Stability of liquid bridges between equal disks in an axial gravity-field. *Physics of Fluids A-Fluid Dynamics* **5**, 1305–1314 (1993).

[118] Schummer, P. & Tebel, K. H. A new elongational rheometer for polymer-solutions. *Journal of Non-Newtonian Fluid Mechanics* **12**, 331–347 (1983).

[119] Canny, J. A computational approach to edge-detection. *IEEE Transactions On Pattern Analysis and Machine Intelligence* **8**, 679–698 (1986).

[120] Kulicke, W. M. & Clasen, C. *Viscosimetry of Polymers and Polyelectrolytes* (Springer, 2004).

[121] Flory, P. & Fox, T. Treatment of intrinsic viscosities. *Journal of the American Chemical Society* **73**, 1904–1908 (1951).

[122] Graessley, W. W. Polymer-chain dimensions and the dependence of viscoelastic properties on concentration, molecular-weight and solvent power. *Polymer* **21**, 258–262 (1980).

[123] Clasen, C. & Kulicke, W. M. Determination of viscoelastic and rheo-optical material functions of water-soluble cellulose derivatives. *Progress In Polymer Science* **26**, 1839–1919 (2001).

[124] Gier, S. & Wagner, C. Visualization of the flow profile inside a thinning filament during capillary breakup of a polymer solution via particle image velocimetry and particle tracking velocimetry. *Physics of Fluids* **24**, 053102 (2012).

[125] Meyer-Arendt, J. R. *Introduction to modern and classic optics* (Prentice Hall, 1984), 2nd edn.

[126] Goulette, T., Howard, C. D. & Davidson, M. W. Microscope optical systems. URL `www.microscopyu.com/articles/optics/index.html`.

[127] Gonzalez, R. C. & Woods, R. E. *Digital Image Processing* (Prentice Hall, 2008), 3rd edn.

[128] Marr, D. & Hildreth, E. Theory of edge-detection. *Proceedings of the Royal Society of London Series B-biological Sciences* **207**, 187–217 (1980).

[129] Huertas, A. & Medioni, G. Detection of intensity changes with subpixel accuracy using laplacian gaussian masks. *Ieee Transactions On Pattern Analysis and Machine Intelligence* **8**, 651–664 (1986).

[130] Crocker, J. C. & Grier, D. G. Methods of digital video microscopy for colloidal studies. *Journal of Colloid and Interface Science* **179**, 298–310 (1996).

[131] Clasen, C. Capillary breakup extensional rheometry of semi-dilute polymer solutions. *Korea-australia Rheology Journal* **22**, 331–338 (2010).

[132] Vadillo, D. C., Mathues, W. & Clasen, C. Microsecond relaxation processes in shear and extensional flows of weakly elastic polymer solutions. *Rheologica Acta* **51**, 755–769 (2012).

[133] Vadillo, D. C. *et al.* Evaluation of the inkjet fluid's performance using the "cambridge trimaster" filament stretch and break-up device. *Journal of Rheology* **54**, 261–282 (2010).

[134] Hoath, S. D. *et al.* Links between ink rheology, drop-on-demand jet formation, and printability. *Journal of Imaging Science and Technology* **53**, 041208 (2009).

[135] McKinley, G. H. *et al.* High deformation rate extensional rheometry of complex fluids. In *ICR 2012 - 16th International Congress on Rheology* (2012).

[136] Keshavarz, B. *et al.* Studying the effects of elongational properties on atomization of weakly viscoelastic solutions using rayleigh ohnesorge jetting extensional rheometry (rojer). *Journal of Non-Newtonian Fluid Mechanics* **222**, 171–189 (2015).

[137] Zell, A., Gier, S., Rafai, S. & Wagner, C. Is there a relation between the relaxation time measured in caber experiments and the first normal stress coefficient? *Journal of Non-newtonian Fluid Mechanics* **165**, 1265–1274 (2010).

[138] Sattler, R., Gier, S., Eggers, J. & Wagner, C. The final stages of capillary break-up of polymer solutions. *Physics of Fluids* **24**, 023101 (2012).

[139] Sharma, V., Ardekani, A. M. & McKinley, G. H. Beads on a string structures and extensional rheometry using jet break-up. In *5th Pacific Rim Conference on Rheology* (2010).

[140] Sharma, V., Serdy, J., Thefrall-Holmes, P. & McKinley, G. H. Jet extensional rheometry of complex fluids. *BSR Rheology Bulletin* **7**, 1–2 (2010).

[141] Clasen, C., Bico, J., Entov, V. M. & McKinley, G. H. 'gobbling drops': the jetting-dripping transition in flows of polymer solutions. *Journal of Fluid Mechanics* **636**, 5–40 (2009).

[142] Brandrup, J. & Immergut, E. *Polymer Handbook* (John Wiley & Sons, Inc, 1999), 4th edn.

[143] Öttinger, H. *Stochastic Processes in Polymeric Liquids* (Springer Verlag, Berlin, 1996).

[144] Bazilevskii, A. V., Entov, V. M. & Rozhkov, A. N. Breakup of an oldroyd liquid bridge as a method for testing the rheological properties of polymer solutions. *Polymer Science Series A* **43**, 716–726 (2001).

[145] Christopher, G. F. & Anna, S. L. Passive breakup of viscoelastic droplets and filament self-thinning at a microfluidic t-junction. *Journal of Rheology* **53**, 663–683 (2009).

[146] Harrison, G. M., Remmelgas, J. & Leal, L. G. The dynamics of ultradilute polymer solutions in transient flow: Comparison of dumbbell-based theory and experiment. *Journal of Rheology* **42**, 1039–1058 (1998).

[147] Harrison, G. M., Remmelgas, J. & Leal, L. G. Comparison of dumbell-based theory and experiment for a dilute polymer solution in a corotating two-roll mill. *Journal of Rheology* **43**, 197–218 (1999).

[148] Daoud, M. *et al.* Solutions of flexible polymers - neutron experiments and interpretation. *Macromolecules* **8**, 804–818 (1975).

[149] de Gennes, P. G. Dynamics of entangled polymer-solutions 1. the rouse model. *Macromolecules* **9**, 587–593 (1976).

[150] de Gennes, P. G. Dynamics of entangled polymer-solutions 2. inclusion of hydrodynamic interactions. *Macromolecules* **9**, 594–598 (1976).

[151] Rubinstein, M. & Colby, R. H. *Polymer Physics* (Oxford Univeristy Press, 2003).

[152] Oliveira, M. S. N. & McKinley, G. H. Iterated stretching and multiple beads-on-a-string phenomena in dilute solutions of highly extensible flexible polymers. *Physics of Fluids* **17**, 071704 (2005).

[153] McIlroy, C., Harlen, O. G. & Morrison, N. F. Modelling the jetting of dilute polymer solutions in drop-on-demand inkjet printing. *Journal of Non-Newtonian Fluid Mechanics* **201**, 17–28 (2013).

[154] Middleman, S. & Gavis, J. Expansion and contraction of capillary jets of newtonian liquids. *Physics of Fluids* **4**, 355–359 (1961).

[155] Gavis, J. & Modan, M. Expansion and contraction of jets of newtonian liquids in air - effect of tube length. *Physics of Fluids* **10**, 487–497 (1967).

[156] Bird, R., Armstrong, R. & Hassager, O. *Dynamics of Polymeric Liquids. Volume 1: Fluid Mechanics* (John Wiley & Sons, Inc, 1977).

[157] Harmon, D. Drop sizes from low speed jets. *Journal of the Franklin Institute* **259**, 519–522 (1955).

[158] Brenn, G., Liu, Z. B. & Durst, F. Linear analysis of the temporal instability of axisymmetrical non-newtonian liquid jets. *International Journal of Multiphase Flow* **26**, 1621–1644 (2000).

[159] Hinkley, D. V. On ratio of 2 correlated normal random variables. *Biometrika* **56**, 635–639 (1969).

[160] Hayya, J., Armstrong, D. & Gressis, N. Ratio of 2 normally distributed variables. *Management Science Series A-theory* **21**, 1338–1341 (1975).

[161] Li, J. & Fontelos, M. A. Drop dynamics on the beads-on-string structure for viscoelastic jets: A numerical study. *Physics of Fluids* **15**, 922–937 (2003).

[162] Fontelos, M. A. & Li, J. On the evolution and rupture of filaments in giesekus and fene models. *Journal of Non-newtonian Fluid Mechanics* **118**, 1–16 (2004).

[163] Bird, R., Curtis, C., Armstrong, R. & Hassager, O. *Dynamics of Polymeric Liquids. Volume 2: Kinetic Theory* (John Wiley & Sons, Inc, 1987).

[164] Wagner, C., Bourouiba, L. & McKinley, G. H. An analytical solution for capillary thinning and breakup of fene-p fluids. *Journal of Non-Newtonian Fluid Mechanics* **218**, 53–61 (2015).

[165] Bhat, P. P., Appathurai, S., Harris, M. T. & Basaran, O. A. On self-similarity in the drop-filament corner region formed during pinch-off of viscoelastic fluid threads. *Physics of Fluids* **24**, 083101 (2012).

[166] Prabhakar, R., Prakash, J. R. & Sridhar, T. Effect of configuration-dependent intramolecular hydrodynamic interaction on elastocapillary thinning and breakup of filaments of dilute polymer solutions. *Journal of Rheology* **50**, 925–947 (2006).

[167] Apelian, M. R., Armstrong, R. & Brown, R. A. Impact of the constitutive equation and singularity on the calculation of stick slip-flow - the modified upper-convected maxwell model (mucm). *Journal of Non-Newtonian Fluid Mechanics* **27**, 299–321 (1988).

[168] Vadillo, D. C. *et al.* The matching of polymer solution fast filament stretching, relaxation, and break up experimental results with 1d and 2d numerical viscoelastic simulation. *Journal of Rheology* **56**, 1491–1516 (2012).

[169] Keunings, R. On the peterlin approximation for finitely extensible dumbbells. *Journal of Non-newtonian Fluid Mechanics* **68**, 85–100 (1997).

[170] de Jong, J. *et al.* Air entrapment in piezo-driven inkjet printheads. *Journal of the Acoustical Society of America* **120**, 1257–1265 (2006).

[171] Basaran, O. A., Gao, H. J. & Bhat, P. P. Nonstandard inkjets. *Annual Review of Fluid Mechanics, Vol 45* **45**, 85–113 (2013).

[172] Windle, J. & Derby, B. Ink jet printing of pzt aqueous ceramic suspensions. *Journal of Materials Science Letters* **18**, 87–90 (1999).

[173] Smith, M. I., Besseling, R., Cates, M. E. & Bertola, V. Dilatancy in the flow and fracture of stretched colloidal suspensions. *Nature Communications* **1**, 114 (2010).

[174] Roché, M., Kellay, H. & Stone, H. A. Heterogeneity and the role of normal stresses during the extensional thinning of non-brownian shear-thickening fluids. *Physical Review Letters* **107**, 134503 (2011).

[175] White, E. E. B., Chellamuthu, M. & Rothstein, J. P. Extensional rheology of a shear-thickening cornstarch and water suspension. *Rheologica Acta* **49**, 119–129 (2010).

[176] Khandavalli, S. & Rothstein, J. P. Extensional rheology of shear-thickening fumed silica nanoparticles dispersed in an aqueous polyethylene oxide solution. *Journal of Rheology* **58**, 411–431 (2014).

[177] Van Deen, M. S. *et al.* Particles accelerate the detachment of viscous liquids. *Rheologica Acta* **52**, 403–412 (2013).

[178] Bertrand, T., Bonnoit, C., Clement, E. & Lindner, A. Dynamics of drop formation in granular suspensions: the role of volume fraction. *Granular Matter* **14**, 169–174 (2012).

[179] Zarraga, I. E., Hill, D. A. & Leighton, D. T. The characterization of the total stress of concentrated suspensions of noncolloidal spheres in newtonian fluids. *Journal of Rheology* **44**, 185–220 (2000).

[180] Maron, S. & Pierce, P. Application of ree-eyring generalized flow theory to suspensions of spherical particles. *Journal of Colloid Science* **11**, 80–95 (1956).

[181] Quemada, D. Rheology of concentrated disperse systems and minimum energy-dissipation principle .1. viscosity-concentration relationship. *Rheologica Acta* **16**, 82–94 (1977).

[182] Krieger, I. M. & Dougherty, T. J. A mechanism for non-newtonian flow in suspensions of rigid spheres. *Transactions of the Society of Rheology* **3**, 137–152 (1959).

[183] Eggers, J. Drop formation - an overview. *Zamm-zeitschrift Fur Angewandte Mathematik Und Mechanik* **85**, 400–410 (2005).

[184] Haw, M. D. Jamming, two-fluid behavior, and "self-filtration" in concentrated particulate suspensions. *Physical Review Letters* **92**, 185506 (2004).

[185] Suryo, R. & Basaran, O. A. Local dynamics during pinch-off of liquid threads of power law fluids: Scaling analysis and self-similarity. *Journal of Non-newtonian Fluid Mechanics* **138**, 134–160 (2006).

[186] Torquato, S. Statistical description of microstructures. *Annual Review of Materials Research* **32**, 77–111 (2002).

[187] Hertz, P. über den gegenseigen durchschnittlichen abstand von punkten, die mit bekannter mittlerer dichte im raume angeordnet sind. *Mathematische Annalen* **67**, 387–398 (1909).

[188] Chandrasekhar, S. Stochastic problems in physics and astronomy. *Reviews of Modern Physics* **15**, 1–87 (1943).

[189] Crosby, A. & Lister, J. R. Falling plumes of point particles in viscous fluid. *Physics of Fluids* **24**, 123101 (2012).

[190] Torquato, S., Lu, B. & Rubinstein, J. Nearest-neighbor distribution-functions in many-body systems. *Physical Review A* **41**, 2059–2075 (1990).

[191] Torquato, S. Nearest-neighbor statistics for packings of hard-spheres and disks. *Physical Review E* **51**, 3170–3182 (1995).

[192] Tembely, M., Vadillo, D., Mackley, M. R. & Soucemarianadin, A. The matching of a "one-dimensional" numerical simulation and experiment results for low viscosity newtonian and non-newtonian fluids during fast filament stretching and subsequent break-up. *Journal of Rheology* **56**, 159–183 (2012).

List of Figures

List of Tables

List of publications

Publications in international journals

- Vadillo, D., Mathues, W., Clasen, C. (2012). Microsecond relaxation processes in shear and extensional flows of weakly elastic polymer solutions. Rheologica Acta, 51 (8), 755-769.
- De Dier, R., Mathues, W., Clasen, C. (2013). Extensional flow and relaxation of semi-dilute solutions of schizophyllan. Macromolecular Materials and Engineering, 298, 944-953.
- Mathues, W., McIlroy, C., Harlen, O.G., Clasen, C. (2015) Capillary breakup of suspensions near pinch-off. Physics of Fluids (accepted)
- Mathues, W., McIlroy, C., Harlen, O.G., Clasen, C. Different scaling laws for the thinning of a weakly elastic jet. (in prep.)
- Rubio-Rubio, M., Mathues, W., Sevilla, A., Clasen, C. Experiments and modelling of the final stage pinching of particle suspension filaments. (in prep.)

Conference contributions

- Mathues, W., Clasen, C. (2012). $D \sim \exp(-t/3\lambda)$ vs. $D \sim \exp(-t/2\lambda)$: the elasto- capillary thinning behavior of weakly viscoelastic jets. The XVIth International Congress on Rheology. Lisbon (Portugal), 5-10 August 2012.
- Mathues, W., Clasen, C. (2013). Quantifying microrelaxation processes in free surface flows. MRC Annual Research Meeting. Leuven (Belgium), 26 February 2013.

- Oosterlinck, F., Bremer, L., Maljaars, L., Williams, A., Mathues, W., Clasen, C. (2013). Ropiness of yoghurts - a mechanistic study. 8th Annual European Rheology Conference. Leuven (Belgium), 2-5 April 2013.
- Cardinaels, R., Van de Velde, J., Mathues, W., Van Liedekerke, P., Moldenaers, P. (2013). A rheological characterisation of liquid egg albumen. Inside Food Symposium. Leuven (Belgium), 9-12 April 2013.
- Mathues, W., Clasen, C. (2013). The elasto-capillary thinning behavior in weakly viscoelastic jets. Belgium Polymer Group Meeting. Houffalize, 16-17 May 2013.
- Mathues, W., McIlroy, C., Harlen, O., Clasen, C. (2013). Different scaling laws for the thinning of a weakly elastic jet. The Society of Rheology 85th Annual Meeting. Montreal (Canada), 13-17 October 2013.
- Mathues, W., Clasen, C. (2013). Capillary thinning dynamics of suspensions near pinch-off. The Society of Rheology 85th Annual Meeting. Montreal (Canada), 13-17 October 2013.
- Rubio-Rubio, M., Mathues, W., Sevilla, A., Clasen, C. (2015) Experiments and modelling of the final stage pinching of particle suspension filaments. 10th Annual European Rheology Conference. Nantes (France) 14-17 April 2015.
- McIlroy, C., Mathues, W., Clasen, C., Harlen O.G. (2015) Modelling capillary breakup of particulate suspensions. 10th Annual European Rheology Conference. Nantes (France) 14-17 April 2015.

FACULTY OF ENGINEERING SCIENCE
DEPARTMENT OF CHEMICAL ENGINEERING
SOFT MATTER, RHEOLOGY AND TECHNOLOGY
Celestijnenlaan 200F box 2424
B-3001 Heverlee, Belgium
http://cit.kuleuven.be/smart